Single-Source Precursors for the Aerosol Assisted Chemical Vapour Deposition of Gallium Arsenide

Sanjayan Sathasivam

Supervised by:

Professor Claire J. Carmalt and Dr. Christopher S. Blackman

This thesis is presented to University College London in partial fulfilment of the requirements for the degree of Doctor of philosophy

I, Sanjayan Sathasivam, confirm that the work presented in this thesis is my own. Where information has been derived from other sources, I confirm that this has been indicated in the thesis.

Sanjayan Sathasivam

Abstract

This thesis describes the synthesis of single-source gallium arsenide (GaAs) precursors and the deposition of films on glass substrates using aerosol assisted chemical vapour deposition (AACVD). A range of precursors were synthesised including silyl arsine containing compounds such as $[Me_2GaAs(SiMe_2Cy)_2]_2$, $[EtGaAs(SiMe_2Cy)_2]_2$, $[Me_2GaAs(SiPh_3)_2]_2$, and $[Me_2GaAs(SiMePh_2)_2]_2$. Novel dimeric precursors, $[Me_2GaAs(H)^tBu]_2$ and $[Et_2GaAs(H)^tBu]_2$, containing tertiary butyl groups have also been synthesised from tertiarybutyl arsine and trimethyl and triethylgallium. Compounds were analysed using ^1H and ^{13}C NMR, mass spectrometry and elemental analysis. The decomposition of $[Me_2GaAs(H)^tBu]_2$ and $[Et_2GaAs(H)^tBu]_2$ was studied using thermogravimetric analysis (TGA).

Thin films of gallium arsenide were deposited on amorphous substrates using both an *in situ* approach with $As(NMe_2)_3$ and $^tBuAsH_2$ as the arsenic sources and $GaMe_3$ as the gallium source as well as with the single-source precursors $[Me_2GaAs(H)^tBu]_2$ and $[Et_2GaAs(H)^tBu]_2$.

All films were characterised using powder X-ray diffraction (XRD), scanning electron microscopy (SEM) and energy dispersive X-ray (EDX) analysis. Some of the films were further characterised using X-ray photoelectron spectroscopy (XPS), secondary ion mass spectrometry (SIMS) and high-resolution transmission electron microscopy (HRTEM) to determine crystallinity.

Acknowledgements

Firstly I would like to thank my supervisor Prof. Claire J. Carmalt to whom I owe a great deal for all the advice, encouragement and support through out my Ph.D. I would also like to thank my second supervisor Dr. Chris S. Blackman for the help, advice and patience and for all the discussions about CVD.

I am grateful to Dr. Ranga Rao Arnepalli for his guidance and assistance during the start of my Ph.D. I am also grateful to my industrial supervisors Dr. Kaushal K. Singh and Dr. Robert Visser for the discussions and advice over the three years. I am thankful to Dr. Ben Schmiege, Dr. Victor Pushparaj, Dr. Kala Pushparaj, Joe Griffith Cruz and Paul Slusser and in particular to Bhaskar Kumar, at Applied Materials who made my visits to the Santa Clara useful and enjoyable.

I wish to thank all the students and postdocs in offices 310 and 320. I would like to thank, Dr. David Pugh, Dr. Caroline Knapp, Dr. Luanne Thomas, Dr. Tegan Thomas, Dr. Geoff Hyett, Dr. Andreas Kafizas, Savio Moniz, Davinder Bhachu, Jared Crane, Peter Marchand, Dr. Rachael Hazael, Leanne Bloor, Dr. Colin Crick, Ralph Leech, Anastasia Mantalidi and Sapna Ponja. I also want to give special thanks to Mohammad Morshedi, Shabbir Khan and Mikie Kukwikila.

I am indebted to all the staff of the chemistry department who have helped me through out the years. In particular, I would like to thank Dave Knapp, Joe Nolan and Kevin Reeves. I would also like to thank Dr. Steve Firth, Martin Vickers, Jim Stevenson, Jim Percival and Bob Gollay.

Finally, I would like to thank my parents and my brothers without whom none of this would be possible.

Table of Contents

List of Figures

List of Tables

Chapter 1: Introduction

1 Introduction

This chapter provides a background to the project, giving some information on photovoltaic technology in general but focusing on gallium arsenide (GaAs) in particular. The chapter will give details of the current methods of forming GaAs thin films for photovoltaic applications as well as some device structures that are currently employed in the generation of power from light. Furthermore, the chapter will detail and discuss the precursors used in forming GaAs thin films, focusing mainly on single-source precursors. It will provide an outline of the variety of deposition techniques employed in producing GaAs thin films, but will concentrate on aerosol assisted chemical vapour deposition (AACVD) methods.

1.1.1 Photovoltaics

1.1.1.1 Basic band theory of semiconducting solids

In free atoms, electrons occupy discrete orbitals of specific energy.[1,2] In semiconducting solids however, the orbitals of neighboring atoms overlap to form bands that contain electrons not associated to any particular atom.[1] The important group of bands that form within a solid that define the material's electrical properties are the valence and conduction band.[1, 2]

At absolute zero all of the electrons occupy the energy levels of the valence band.[2] However, at ambient temperatures, a portion of electrons are thermally promoted into overlapping orbitals within the conduction band. The conduction band lies above the valence band, as it is primarily formed from higher energy empty metallic orbitals. The electrons that occupy the conduction band are considered free electrons due to their capacity to flow freely throughout the solid. Upon applying an electrical field these free electrons create an electrical current.[1]

There are three different types of solids - insulators, semiconductors and conductors (Figure 1). A region of forbidden energy levels called the bandgap separates the valence and conduction bands within insulators and semiconductors.[1,2] The bandgap energy (E_g)

is the difference between the lowest energy level in the conduction band and the highest energy level of the valence band. In conductors, there is no bandgap (Figure 1).[1,2]

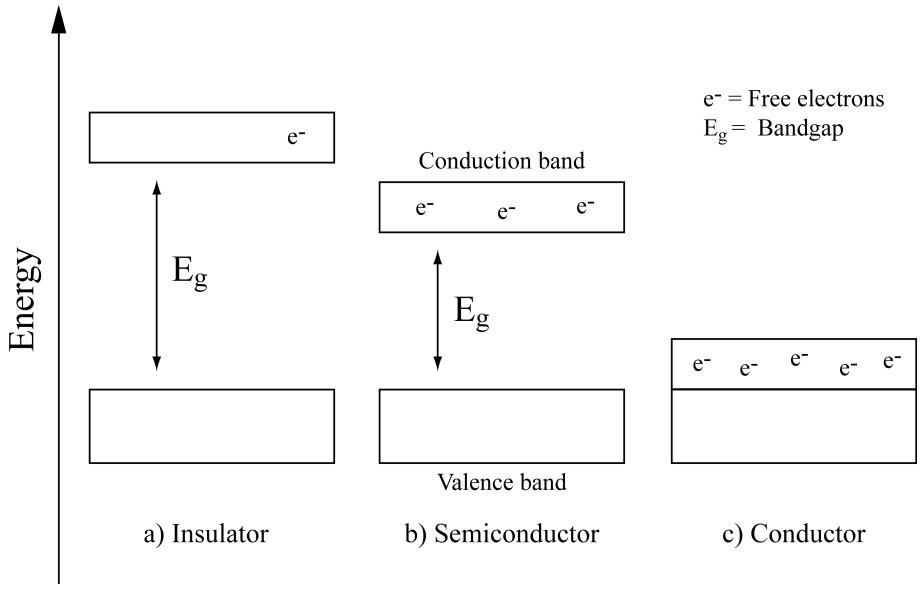

Figure 1: The bandgaps for an insulator, semiconductor and conductor.

If electrons in the valence band are given enough energy, they can overcome the bandgap energy and be excited into the conduction band. For insulators, the bandgap energy is large.[1,2] Therefore electron excitation does not occur unless a large amount of energy is introduced, hence insulators have high electrical resistance.[1,2] In conductors, however, the conduction band and the valence band overlap, therefore the high mobility of free electrons is seen even near absolute zero. Semiconductors have a bandgap energy in between that of an insulator and a conductor. Hence they behave like insulators at low temperatures and conductors at high temperatures or when energy, for example in the form of light, is supplied.[3]

1.1.1.2 Semiconductors

As mentioned above, semiconductors are materials with electrical conductivity due to electron flow in the intermediate range between that of an insulator and a conductor. Semiconductors are usually crystalline solids but can also be amorphous. A pure semiconductor (called an intrinsic semiconductor) usually has poor conductivity due to the lack of crystal defects that give rise to free electrons and holes, which are the charge carriers for electrical conductivity.[4]

In semiconductors when the minima of the conduction band and the maxima of the valence band occur at the same crystal momentum (i.e the electrons populating the states of the conduction and valence band have movement in the same vector) it is referred to as a direct bandgap material.[1] For such materials, transition of an electron from the valence to the conduction band must conserve momentum and therefore only a photon is required for electronic promotion (Figure 2).[1] Photons have high energy compared to their momentum with respect to the range of crystal momentum, therefore the momentum of the excited electron is maintained.[1,5]

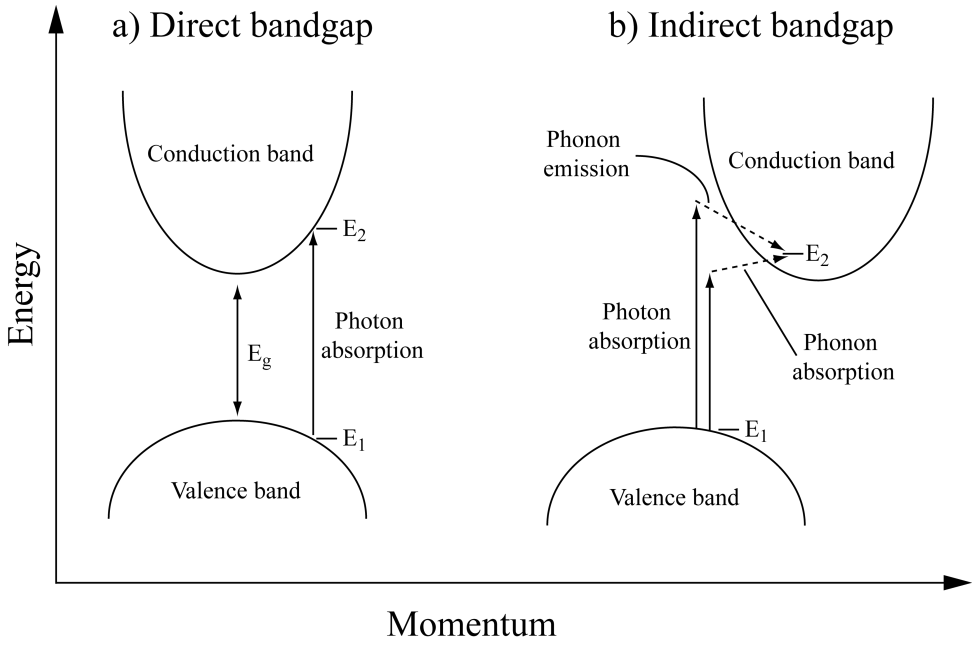

Figure 2: a) Photon absorption in a direct bandgap semiconductor such as GaAs. The photon in this example has energy equal or greater than the bandgap energy. b) Photon absorption in a material with an indirect bandgap such as Si. The diagram shows the outcome when photon energy is both above and below the bandgap energy. The emission and absorption of a phonon allows the conservation of energy and momentum of the system.

Semiconductors where the minima of the conduction band and the maxima of the valence band have different crystal momentum are referred to as indirect bandgap materials.[1] For such materials, excitation of an electron from the valence to the conduction band requires both a photon and a phonon (Figure 2).[1,5] A phonon is a

species with low energy and high momentum and is a representation of lattice vibrations.[1,5]

It is usual for semiconductors used for electrical applications to have precise amounts of impurities added to them to either increase or decrease the number of electrons in the system.[6] This is called doping and the impurities are called dopants and doped semiconductors are usually called extrinsic semiconductors.[1,7] This is because the intrinsic carrier concentrations of most semiconductors are insufficient to give current densities for useful device applications.[7]

When additional free electrons are created due to doping of the basic crystal structure with more electron rich atoms (such as adding silicon to GaAs), the semiconductor is called *n*-type (negative type).[1,3-5] In the opposite case, where 'holes' form in the space of emptied electron orbitals (such as adding Zn to GaAs), the doped semiconductor is called *p*-type (positive type). The free electrons or holes created as a result of doping are mobile charge carriers, in *n*-type the majority charge carriers are electrons and in *p*-type the majority are 'holes'. In *n*-type semiconductors electron flow is due to the free movement of electrons through the conduction band. Whereas in *p*-type semiconductors, electron flow is due to a continuous series of electron hops into vacant 'holes' within the valence band.[1,3-5]

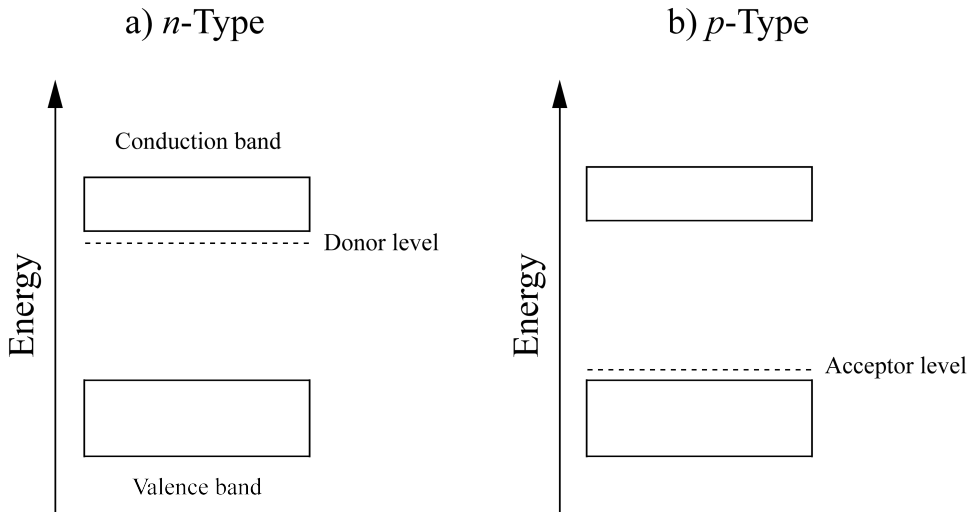

Figure 3: Relative positions of the donor and acceptor levels after doping to create an a) *n*-type and b) *p*-type semiconductor.

When an *n*-type semiconductor and a *p*-type semiconductor are brought together, the region surrounding the meeting point is called a *pn* junction. This region displays interesting electrical behavior and is the basis of and is fundamental to all semiconductor technology including photovoltaics.[7]

1.1.1.3 pn Junctions and photovoltaics

The concentration gradient that is created by placing an *n*-type semiconductor next to a *p*-type semiconductor results in a chemical potential energy that allows diffusion to take place between the two types of semiconductors.[3] Electrons will move from the higher concentration *n*-doped side to the *p*-doped side, conversely holes diffuse from the *p*-doped side to the *n*-doped side. Upon diffusion, recombination of electrons and holes takes place in the region either side of the *pn* junction, called the depletion zone.[1] The electrons that diffuse to the *p*-doped region from the *n*-doped region fall into the 'holes' and reduce the local atoms into negative ions. On the other side, the 'holes' combine with electrons and oxidise local atoms to positive ions. Hence, the depletion zone is made up of ions instead of mobile charge carriers (Figure 4).[3,5,10]

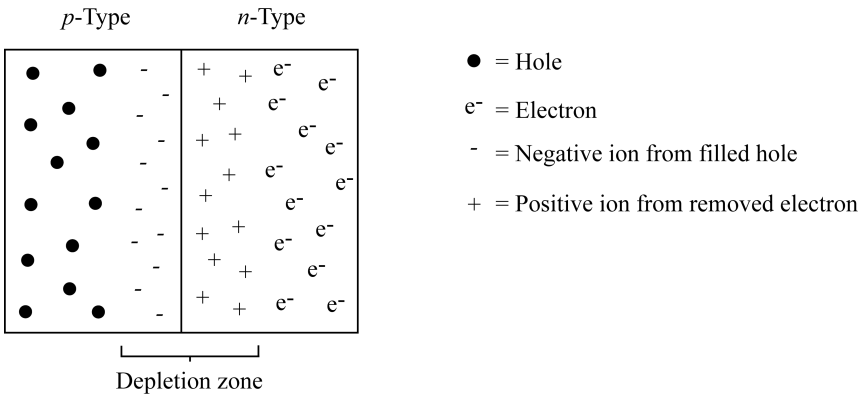

Figure 4: The depletion zone in a *pn* junction

With time, the electric field that increases in strength with diffusion of electrons and holes across the junction becomes strong enough to stop any further movement of electrons and holes. At equilibrium, when the chemical force of diffusion is equally opposite to the electrostatic force of the electric field, the diffusion of the majority carrier (electrons) of the *n*-layer into the *p*-layer is stopped.[3,5] Similarly, the diffusion of

the majority carrier of the *p*-layer (holes) is stopped from going into the *n*-layer. It is important to note that minority charge carriers, that are electrons in the *p*-layer and holes in the *n*-layer, are not limited from movement by the depletion zone. In fact, the opposite is true. When the minority carriers diffuse to the vicinity of the depletion zone, they are accelerated across the junction by the internal electric field of the depletion zone (electrons to the *n*-layer and holes to the *p*-layer).[8] However, with respect to photovoltaics, under no external stimulation the concentration of minority carriers is very low and the process has an almost insignificant effect on the system.[9,10]

The ability of the depletion zone to act as a barrier and selectively separate charges is fundamental to photovoltaics. Under photoexcitation it is the basis of the generation of electric current and power.

1.1.1.4 Photovoltaics theory

Photovoltaics are concerned with the generation of electrical power through the creation of voltage and current from the illumination of semiconductors, such as silicon and gallium arsenide, with sunlight.[3,5,9,10] A photovoltaic device is simply a semiconductor diode (the combination of a *p*-type and an *n*-type semiconductor) designed in such a way as to maximise the conversion of sunlight to power.[5]

Sunlight is electromagnetic radiation made up of photons with quantised energy. The photons behave like waves and their energy (E_λ) is dependent on the wavelength (λ) as shown in equation 1.1. Planck's constant is represented by *h* and *c* is the speed of light.

$$E_\lambda = \frac{hc}{\lambda} \qquad \textbf{(1.1)}$$

A photon with energy less than the bandgap energy (E_g) of the photovoltaic semiconductor passes straight through with minimal interaction. However, a photon with energy equal to or above the bandgap energy interacts with the device to create free electrons and 'holes'.[5,11]

An electron - hole pair is generated when an electron in the valence band is excited to the conduction band leaving behind an associated hole. For a photovoltaic device consisting of a *pn* junction, this can take place in both the *p*-layer and the *n*-layer (Figure 5).[1,5]

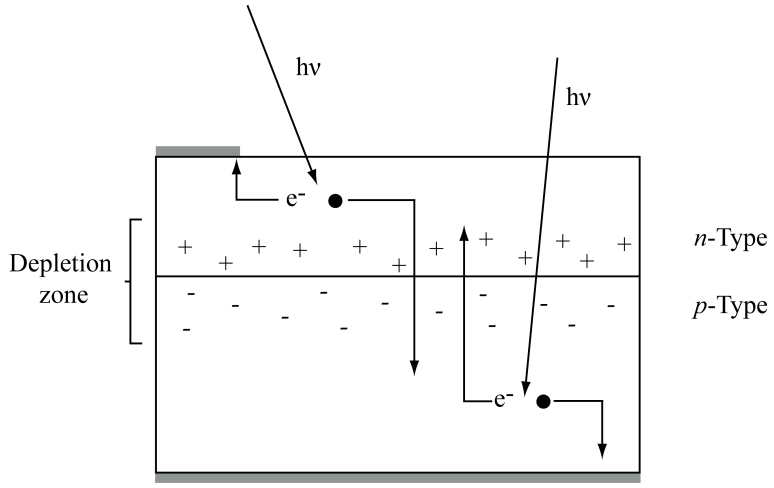

Figure 5: Charge separation in a photovoltaic device.

Once electron-hole pairs are formed there is only a brief moment before recombination (see later) takes place and the potential energy is lost as a phonon and/or photon.[12] Photovoltaic devices are designed in such a way to minimise such recombination. For example, when an electron-hole pair is formed in the *p*-layer, the electron diffuses until it is in close approximation to the depletion zone where the electric field accelerates it across the junction into the *n*-layer.[5,10,11] In the *n*-layer the number of holes present is very low and hence the chance of an electron recombining with a hole is also very low. Similarly, a hole produced in the *n*-layer by photoexcitation diffuses to the vicinity of the depletion zone where it is also pushed across the junction into the *p*-layer, again where chance of recombination is also minimal. Once accelerated across the junction, the electrons and holes are unable to return to the *p*-layer and *n*-layer respectively due to the barrier caused by the electric field of the depletion zone. Overall, electrons are encouraged to flow only in the direction of *p*-layer to *n*-layer and holes in the opposite direction of *n*-layer to *p*-layer.[11]

Hence, the charge imbalance caused by photoexcitation of a photovoltaic device results in electric current to flow from the *n*-layer to the *p*-layer *via* an external wire where they recombine with the holes. This not only allows the charge imbalance to return to equilibrium but more importantly causes a current to flow and generate electrical power. The current will continue to flow as along as photoexcitiation in either or both the *n*-layer and *p*-layer takes place.

The amount of potential energy driven through the external circuit is limited by the bandgap of the semiconductor applied in the photovoltaic device.[13] The larger the bandgap, the greater the power output as the amount of energy needed to excite an electron into the conduction band and drive it around the system is approximately equal to the energy initially received by the electron. The ideal bandgap for solar conversion is 1.5 eV as this is the optimum energy to capture and utilise as much of the solar spectrum as possible while also giving a high power output for the device.

Recombination of carriers in the photovoltaic device is a major issue in reducing carrier concentrations and thus the efficiency of photo to electrical energy conversion in the system (as photo to thermal energy occurs instead with each recombination process). Recombination is the process by which the system returns to equilibrium after it has been taken out of equilibrium by photoexcitation (Figure 6).[3]

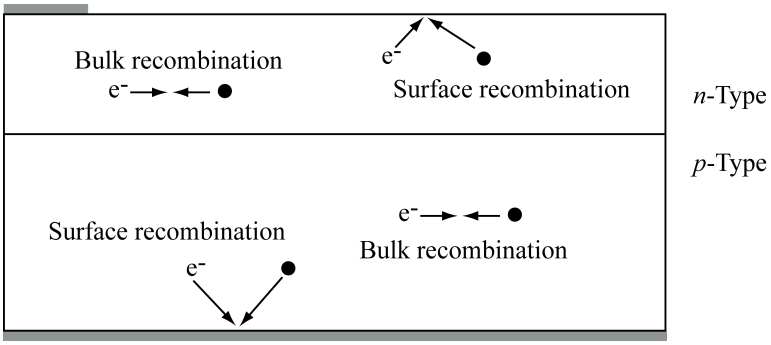

Figure 6: An overview of the types of recombination that can take place in a photovoltaic device.

Recombination can take place at the surface of the material or in the bulk.[3,12] The presence of defects and impurities within the semiconductor leads to a higher probability of recombination taking place. This is because impurities lead to energy levels in the forbidden region (band gap) between the valence and the conduction band.[12,14] These energy levels can then trap electrons as they are moving from the valence to the conduction band upon photoexcitiation, the electrons then fall back down to recombine with the hole in the valence band. The likelihood of recombination is dependent on the position of the trap energy level in the forbidden region caused by the impurities. Recombination is more likely when the trap is in the middle of the forbidden region rather than close to the valence or conduction band.[14]

The carrier lifetime of a material is the time taken for recombination to occur from the point of electron-hole pair creation. The minority carrier lifetime (as this is far more important to photovoltaic conduction than majority carrier lifetimes) for GaAs is approximately 1 x 10^{-8} seconds.[15]

In polycrystalline semiconductors the chance of recombination taking place is higher (minority carrier lifetimes are lower) than in single crystal materials. This is not only due to the presence of more defects but also due to the fact that polycrystalline materials are made up of grains with different crystalline orientations. These grains have boundaries (called grain boundaries) that act as an internal surface within the semiconductor and have a local electric field that enhances the chance of the minority carriers recombining.[14,16]

1.1.1.5 p-i-n *photovoltaic cells*

For most photovoltaic materials, upon photoexcitation, the electron hole pair is generated near the surface. From the above discussion it is evident that the most important region of the photovoltaic device is the depletion zone near the *pn* junction. The electric field created by the depletion zone separates the charge carriers and allows the photovoltaic device to function. A simple modification to the traditional *pn* junction of placing an intrinsic layer between the *n* and the *p*-layer increases the thickness of the depletion zone.[17,18] A thicker depletion zone allows charges to be separated more effectively and improves photo-electrical conversion efficiency. Solar cells made up of hydrogen alloyed amorphous silicon (a-Si:H) generally employ this method as the minority carrier lifetimes are low, therefore the quicker these charges are separated across the *pn* junction the lower the chance of recombination taking place.[5] Therefore, using a silicon based photovoltaic device that employs a *p-i-n* junction have shown respectable solar efficiencies.

1.1.1.6 Silicon

Silicon is an abundant mineral in the earth's crust and is the most widely used electronic grade semiconductor, particularly in the photovoltaic industry.[5,10] Silicon accounts for 90% of the photovoltaics produced worldwide, primarily due to its abundancy coupled with the high efficiency achieved when used in the monocrystalline form.[19,20] Crystalline silicon (c-Si) is highly efficient in converting sunlight to electricity but solar cells of c-Si are very expensive. Since c-Si has an indirect band gap, it is a poor

absorber of sunlight (as it needs a photon and phonon for excitation of electrons from the valence to the conduction band) therefore a thick silicon layer (150-300 μm) is required in the solar cell to obtain sufficient absorption for efficient energy output. The electrons that are excited to the conduction band from the valence band have a long pathway to travel before they reach the contacts and produce useful work. To avoid recombination taking place before the electrons reach the contacts, ultra pure silicon that is defect free is required to keep the excited electrons highly mobile, reduce recombination and thus keep efficiency high. The method of producing monocrstalline silicon is very slow, expensive in comparison to traditional electrical energy production methods (i.e. high cost to voltage ratio) and gives only a limited size. Furthermore, c-silicon has a band gap of 1.1 eV hence it absorbs light strongly in the infrared (IR) region and is a poor absorber in the visible region of the spectrum.[21]

Silicon in the amorphous form can be deposited as thin films.[22] However, due to its high defect density arising from dangling bonds, a-silicon is useless as a photovoltaic material (in crystalline materials defects are atoms out of place in the lattice but in amorphous materials defects are coordination defects that arise when atoms have too many or too few bonds). However, passivation of the dangling bonds through alloying with hydrogen, dramatically improves its properties for photovoltaic application. This is achieved conveniently by plasma enhanced CVD (PECVD) of silane (SiH_4). Hydrogen alloyed amorphous silicon (a-Si:H) is useful as a thin film photovoltaic material due to its tunable bandgap (ranging from 1.1 to 3.7 eV depending on the amount of hydrogen and other impurity incorporation) that is easily achieved by changing the deposition conditions. It can also be doped easily using boron (from diborane) for *p*-type character and phosphorus (from phosphine) for *n*-type.[23] After deposition (with or without doping) the average crystallite size within the films is small, but upon annealing the crystallites act as seeds in the formation of larger crystallites for the remainder of the film. Furthermore, it has a high absorption coefficient in the wavelength range of interest therefore only films of about 1 μm thickness are required. Hence this is one of the reasons why unlike c-Si, a-Si:H is much cheaper to produce.

Though a-Si:H has much lower solar efficiencies than silicon in the crystalline form, only 0.1 g of a-Si is required to generate 1 W of electricity. It is possible to use thin films because they have a higher absorption coefficient than bulk materials (such as 300 μm thick c-Si) therefore they are able to absorb light more efficiently. Also, a-Si:H has

a band gap of 1.7 eV, thus it absorbs strongly in the visible region.[5]

There are disadvantages to using a-Si:H in photovoltaic solar cells. They have low efficiency in power generation relative to c-Si due to many defects arising from dangling/twisted bonds and large grain boundaries.[5,19]

In summary, silicon based photovoltaic devices are widely used primarily due to silicon's abundance. The highly efficient c-Si based solar cells are expensive as large amounts of especially produced, ultra pure monocrystalline silicon is required to compensate for poor absorption. a-Si:H based solar cells are cheap as they use a small amount of low grade silicon but they have very lower efficiencies due to defects and large grain boundaries. The high cost to efficiency ratio of silicon based photovoltaic devices has driven research to develop alternative semiconductors that would give higher efficiency, stability and reproducibility at a fraction of the cost of crystalline silicon based photovoltaics.

1.1.1.7 Thin film photovoltaics

The future of photovoltaic technology lies with semiconductors with direct bandgaps such as GaAs. As these materials are able to absorb light much more efficiently than c-Si, only a thin layer of the active material is required to achieve the same level of efficiency obtained from bulk c-Si. Thin film photovoltaics require 30-300 times less semiconductor material than c-Si and can be produced using a variety of techniques such as chemical vapor deposition (CVD), molecular beam epitaxy (MBE) and vapour phase epitaxy (VPE).[5,19,20,21,24]

GaAs is an important semiconductor in the electronics industry. Its wide variety of applications is second only to silicon. GaAs is the preferred material/technology for integrated optoelectronics due to its reliability and simplicity.[25] GaAs has potential to be extremely useful in high speed telecommunications, as GaAs light emitting diodes (LEDs) have been manipulated to emit around 1.5 micron wavelengths and can be pulsed at terahertz rates due to their high electron mobility.[25,26] Also, the high pulse rates available with GaAs allows it to be applied in ultra high radio frequency and fast electronic switching devices. GaAs creates less noise than other semiconductors such as silicon, hence it is being used in weak signal amplification. Furthermore, GaAs is highly applicable in microwave frequency integrated circuits as silicon is highly resistive at these frequencies.

GaAs is a III-V semiconductor material with a direct bandgap of 1.43 eV.[15, 27] This is near the optimum for conversion of light to power because the bandgap is small enough that the majority of light in the solar spectrum is absorbed but not too low such that the energy of the excited electrons cannot do any useful work. At a film thickness of about 2 μm it is able to absorb 97% of AM1 radiation (air mass coefficient 1, the spectrum of light from the directly overhead sun after traveling through the earth's atmosphere and reaching sea level).[13] GaAs also has a high absorption coefficient (compared to silicon) therefore only a thin layer is required for practical use. Furthermore, its higher carrier concentration allow it to be a much more efficient photovoltaic material.[28] Thin film GaAs photovoltaic devices display efficiencies of 27.6%, whereas crystalline silicon devices demonstrate 25% and amorphous silicon 10%.[29]

A disadvantage associated with GaAs is its higher cost. This is because gallium is very rare (with a crustal abundance of 19 parts per million and an annual production of only 182 tonnes) and is only obtained as the by-product of smelting other metals such as zinc and aluminium.[30] Arsenic on the other hand is abundant but unfortunately poisonous and as such there are stringent handling issues.[31,32] GaAs is more difficult to handle mechanically than silicon, this also contributes to the overall higher costs when dealing with GaAs.[15,33]

Furthermore, GaAs films are usually grown epitaxially on lattice matched wafers made of single crystal GaAs or germanium, which are expensive to manufacture. Another factor to the high cost of GaAs is the production methods that are currently available. GaAs is much more difficult to grow and optimise than silicon and hence its development as ubiquitous photovoltaic device has been limited. First developed in 1960, GaAs photovoltaic devices showed efficiencies of just 3% but due to its high resistance to heat and radiation damage it was used in space applications by Russia.[34] Owing to the lack of epitaxial growth technology, further development of GaAs based photovoltaic technology was not made until the 1980s when growth techniques such as metal organic vapour phase epitaxy (MOVPE) and molecular beam epitaxy (MBE) were used to grow films on GaAs and germanium wafers.[34]

GaAs in the pure form is an intrinsic semiconductor therefore *p* and *n* type layers are achieved through doping.

1.1.2 Fabrication techniques

GaAs solar cells are produced using chemical vapour deposition (CVD) or molecular beam epitaxy (MBE).[35,36,37,38,39,46]

CVD is a technique widely used in the semiconductor industry to produce thin films of high quality and purity. Unlike physical vapour deposition techniques (PVD) such as sputtering, CVD involves chemical reactions either in the gas phase or on the substrate. In general CVD involves the transport of the precursor(s) from either the gas, liquid or solid phase into the gas phase. Followed by transport to the substrate where energy is supplied to allow chemical reactions to take place and a thin film to form.

There are three different forms of energy that can be supplied, thermal, plasma and photon.[40] Thermally activated CVD processes will be described in detail since this is the type of technique employed in this work (Figure 7). The pressure of the system can be atmospheric or reduced pressure.

There are many different types of CVD such as atmospheric pressure CVD (APCVD), low pressure CVD (LPCVD) and plasma enhanced CVD (PECVD) but here the focus will be on a specialised form of CVD called aerosol assisted chemical vapour deposition (AACVD) as this is method used to grow thin films in this project.

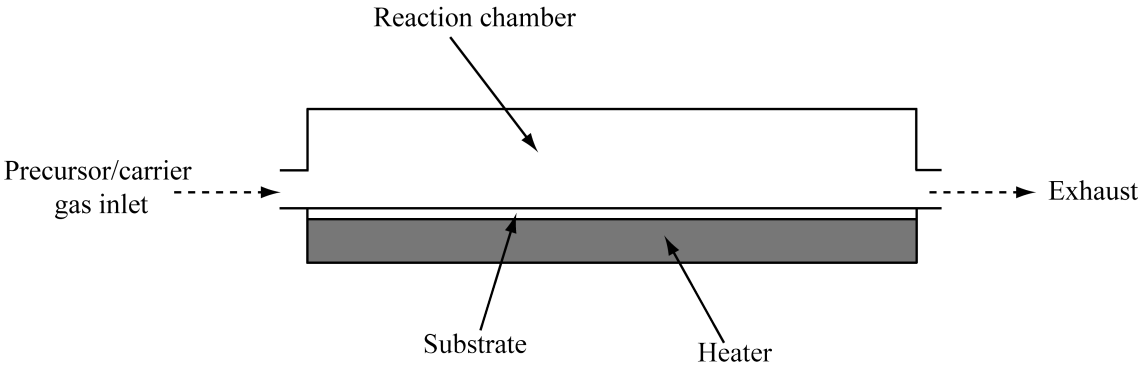

Figure 7: Diagram of a CVD reactor.

Molecular precursors in the CVD chamber in the gas phase undergo several steps to form high quality thin films, as shown in Figure 8.

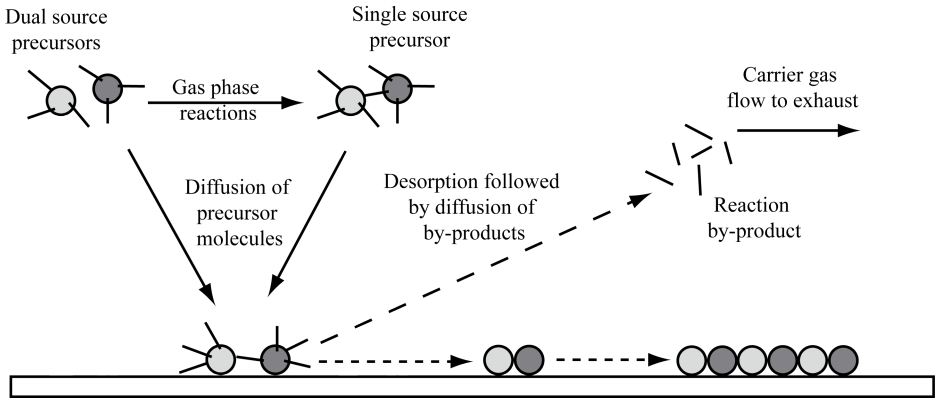

Figure 8: Overview of CVD process.

If there are, for example, two different types of molecular precursors (like trimethylgallium ($GaMe_3$) and tertiarybutylarsine ($^tBuAsH_2$)) as opposed to a single source precursor (like $[Me_2GaAs(H)^tBu]_2$) then upon entry into the CVD reaction chamber gas phase reactions can occur. These reactions result in the formation of a single source precursor or other intermediate products. These species then diffuse through the reaction chamber and adsorb onto the substrate where surface reactions and decomposition take place to give the desired product (GaAs in this example). The adatoms then diffuse to find the lowest energy site on the heated substrate, at the same time by-products from the surface reaction desorb from the substrate and enter the gas phase where they are taken to the exhaust by the carrier gas. Once the adatoms find the lowest energy site, nucleation takes place to form a thin film.

The precursors used in CVD can be a solid, liquid or a gas. If the precursors are gaseous under ambient conditions, then the transport of the precursor to the reaction chamber is fairly simple where the gas can be transported (with or without a carrier gas) over the heated substrate.

If the precursors are liquid then they can be injected into a vaporisation chamber to convert them to the gaseous state before a carrier gas is used to transport them to the CVD chamber. Alternatively, if the liquid precursors are highly volatile then they can simply be heated above boiling point and then the vapour transported to the chamber. In AACVD reactions, liquid precursors can be suspended with or without a solvent in the gas phase in the form of aerosols and then transported using a carrier gas.

This is also possible with solid precursors, which can be dissolved in a suitable solvent and then converted to aerosol droplets. Solid precursors of a suitable volatility and those that have an appropriate melting and boiling point can be heated to obtain the gaseous state.

The flow of the precursor gas (and carrier gas) through the reaction chamber can be understood using fluid mechanics. In general, the Reynolds (R_e) number characterises the motion of the gaseous species through the CVD reactor and in most CVD reactions the flow of the gas is laminar (**Eq 1.2**).[41] Laminar flow is the flow of a gas in parallel layers with no crosscurrents perpendicular to the direction of flow.[40,41] The other two type of flow are turbalent flow, whereby the gas undergoes irrigular changes in velocity and direction resulting in a slower movement through the reactor and transitional flow, which is a combination of turbulent and laminar flow.[41,42] Laminar flow exists when R_e is below 2300, turblent flow when R_e is above 4000. Transient flow occurs when when R_e is between 2300 and 4000.[42,41]

The Reynolds number is defined as shown in equation **1.2**.

$$R_e = \frac{\rho u_x}{\mu} \qquad \textbf{(1.2)}$$

Where, ρ is the density of the gas, u is the flow density, x is the distance from the gas inlet and μ is the viscosity of the gas. When R_e is low the flow of the gas is laminar. In such cases the velocity of the gas at the substrate surface in the CVD chamber is zero. The boundary between this zero velocity volume of gas and the volume of gas with velocity directly above it is called the boundary layer. For CVD to take place, the precursor gases that are in motion must diffuse into the boundary layer and adsorb (using Van der Waals like bonding) to the surface of the substrate as shown in Figure 9.[40]

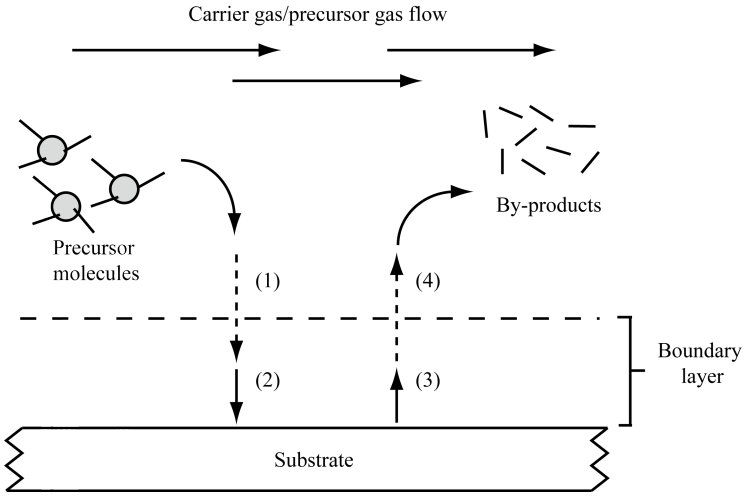

Figure 9: Diagram showing 1) the diffusion of precursor molecules through the boundary layer followed by 2) adsorption and reaction of precursor on the substrate then 3) desorption of adsorbed and 4) diffusion of the by products out of the boundary layer.

1.1.2.1 Thermodynamics and kinetics of CVD

Chemical vapour deposition is a chemical reaction in equilibrium. The reactants are in the gas phase and the products are in the solid phase. During the CVD process, non-equilibrium is forced upon the system by increasing the amount of reactants in the system and maintaining this until the end of the reaction. At this situation the system will attempt to equilibrate by depositing a film, i.e. taking the reactants out of the gas phase and forming the products, a solid film.

The difference in Gibbs free energy between the product and the reactants is the driving force for thin film deposition. The more negative the change in Gibbs free energy the more drive there is to form the film. Therefore, thermodynamics determines whether or not deposition takes place. It also determines the maximum rate of deposition.

The activation energy for the CVD reaction is another important factor that determines whether or not the reaction will take place. The activation energy is the kinetic barrier for a reaction; there must be enough energy to overcome the activation for an exothermic reaction to take place. The rate of the reaction or deposition is limited by the rate-determining step, the slowest step in any CVD process.

If the rate of deposition is considered as a function of substrate temperature then one of three factors can be rate determining depending on the temperature (Figure 10):

1) At very low temperature ranges the rate-determining step is the surface reaction. This is because the surface reaction is dependent on the temperature of the substrate and at low temperatures the reaction is very slow. If the temperature is increased, the deposition rate will increase.
2) After a certain point, when the substrate temperature is high enough, the rate of deposition is no longer affected by temperature but rather by the mass transfer of precursors *via* diffusion through the boundary layer. Therefore, the partial pressure of precursors above the boundary layer is the most important factor in the rate of the deposition at this stage.
3) At very high temperatures, the deposition rate decreases with temperature. This is because the temperature of the system is sufficiently high, that gas phase reactions become predominant and the precursors fully decompose in the gas phase to leave solid particles. These particles are then affected by thermophoresis. This is the process whereby solid particles in temperature gradient move down the temperature gradient. Since the substrate is the hottest region in the reaction chamber, the particles move away form the substrate and the film thickness decreases. Other reasons for a decrease in deposition rate with increasing temperature at very high temperatures include, deposition on the walls of the reactor and desorption of adsorbed species from the substrate.

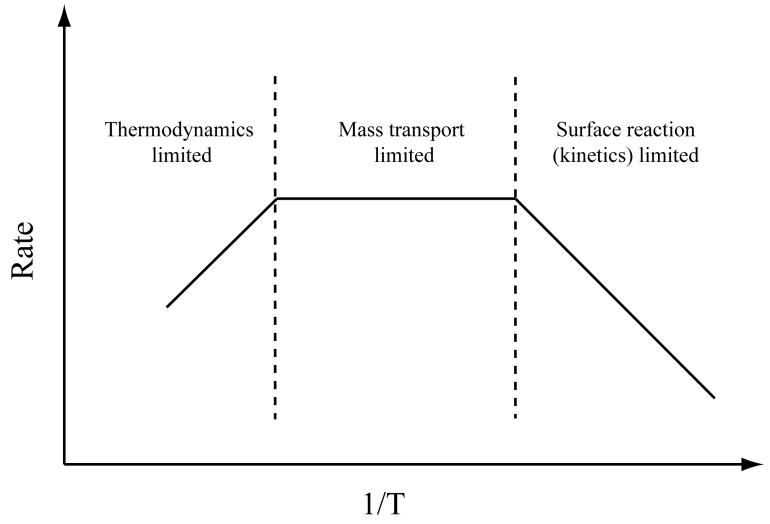

Figure 10: The change in the rate-determining step with temperature.

1.1.2.2 Aerosol assisted CVD

Aerosol assisted CVD (AACVD) is a specialised form of CVD where the precursor or precursors are transported to the reaction chamber using an aerosol mist.[43] Due to this innovative method of precursor transportation, solid and liquid precursors that are involatile can be used in CVD. This is useful as it allows the use of many precursors previously incompatible due to low volatility. The only requirement on solid precursors is that they are soluble in a suitable solvent and they or their decomposition products have a vapour phase.

Furthermore, since volatility and thermal stability of the precursors is generally not an issue in most cases, the cost to produce device quality thin films can be lower than traditional CVD methods.[43]

The aerosol mist can be generated using an ultrasonic atomiser, a pneumatic sprayer or an electrostatic atomiser. However, the most popular method is ultrasonic aerosol generation, which involves the use of a piezoelectric transducer that vibrates at a high frequency when an electric field is applied. The ultrasonic sound waves created by the transducer travel through the precursor solution and disturb the surface, causing fine droplets to form. The size of these droplets is given by Lang's equation (**1.3**).[44]

$$d = 0.34\left(\frac{2\pi\gamma}{\rho f^2}\right)^{1/3} \qquad (\mathbf{1.3})$$

Where the diameter (d) of the droplets is dependent on the excitation frequency (f), the density (ρ) and surface tension (γ) of the liquid/solution. From the equation it is clear that the size of the droplets decreases as the frequency of ultrasonic vibration increases. Typically, the finer the droplets, the higher the quality of the deposited film, as evaporation of the solvent and vaporisation of the precursor can take place more readily. Only when the precursor is in the gas phase can true CVD occur.

In this project, the piezoelectric transducer used had an operational frequency of 20 kHz, and therefore for toluene (the solvent used throughout this project) the diameter of the droplets was 59.3 μm at 25 ^{o}C.

After generation of the aerosol droplets they are carried into the CVD reactor using an inert gas such as nitrogen or argon. Once in the reactor the size of the droplets decreases

with time until the solvent is fully evaporated. This is followed by vaporisation of the precursors and then the conventional CVD process, described in section 1.1.2, can take place. [45]

Aerosol assisted CVD could be employed for the deposition of GaAs using both novel single source precursors and dual source precursors that are currently available. Furthermore, as AACVD does not require ultra high vacuums it is a technique that operates at low running costs.

1.1.2.3 Current GaAs fabrication techniques

The usual method of GaAs thin film fabrication is by metal organic chemical vapour deposition (MOCVD).[36,37,38,39,40,46] This technique is also referred to as metal organic vapour phase epitaxy (MOVPE), metal alkyl VPE (MAVPE) and organometallic CVD (OMCVD).

MOCVD involves the epitaxial growth of a thin film on a crystalline substrate from metal organic precursors. Growth can also take place on non-crystalline substrates but in these cases the growth is not epitaxial. For GaAs growth, the gallium source is usually trimethyl or triethylgallium ($GaMe_3$ or $GaEt_3$), whereas the arsenic source can be the arsine (AsH_3), or tertiary butyl arsine ($^tBuAsH_2$). The precursors undergo pyrolysis (decomposition of a species using thermal energy) upon a heated substrate within a cold wall CVD reactor. Hydrogen carrier gas is used either in the pure form or mixed with nitrogen. The reactions that occur for trimethylgallium and arsine have been well studied and these studies show that reactions can occur *via* two routes. If the reactions/pyrolysis takes place in the gas phase then it is said to be homogeneous. The pyrolysis is heterogeneous when it occurs on the substrate surface.

The overall decomposition of trimethylgallium and arsine is shown in (**1.4**):

$$Ga(CH_3)_{3\,(g)} + AsH_{3\,(g)} \longrightarrow GaAs_{(s)} + 3\,CH_{4\,(g)} \qquad (\mathbf{1.4})$$

However, computational and theoretical studies have revealed a much more complicated decomposition pathway. The homogeneous and heterogeneous pyrolysis

pathway for trimethylgallium is described below in equations (**1.5**) - (**1.8**).

Homogeneous

$$Ga(CH_3)_3 \longrightarrow Ga(CH_3)_2 + \cdot CH_3 \quad (\mathbf{1.5})$$

$$Ga(CH_3)_2 \longrightarrow Ga(CH_3) + \cdot CH_3 \quad (\mathbf{1.6})$$

Dimethylgallium is a stable decomposition product of trimethylgallium and therefore further decomposition occurs *via* the heterogeneous route. The heterogeneous route takes place after adsorption of the species onto the substrate, according to equations (**1.7**) and (**1.8**).

Heterogeneous

$$Ga(CH_3)_3 \longrightarrow \text{Substrate-}Ga(CH_3) + 2 \cdot CH_3 \quad (\mathbf{1.7})$$

$$Ga(CH_3)_2 \longrightarrow \text{Substrate-}Ga(CH_3) + \cdot CH_3 \quad (\mathbf{1.8})$$

The methyl radicals can then take part in reactions with arsine, the hydrogen carrier gas and other by-products to produce methane. Arsine pyrolysis purely takes place at the substrate and thus is wholly heterogeneous. The stepwise pyrolysis of arsine is given in equations (**1.9**) - (**1.11**).

$$AsH_3 \longrightarrow \text{Substrate-AsH} + H_2 \quad (\mathbf{1.9})$$

$$AsH_2 \longrightarrow \text{Substrate-AsH} + \cdot H \quad (\mathbf{1.10})$$

$$AsH \longrightarrow \text{Substrate-AsH} \quad (\mathbf{1.11})$$

GaAs films then grow after surface reactions between adsorbed gallium and arsenic species takes place, as shown in equations (**1.12**) and (**1.13**)

$$\text{Substrate-Ga}(CH_3)_3 + \text{Substrate-AsH} \longrightarrow \text{GaAs} + CH_4 \quad (\mathbf{1.12})$$

$$\text{Substrate-Ga}(CH_3)_3 + \text{Substrate-As} \longrightarrow \text{GaAs} + \cdot CH_3 \quad (\mathbf{1.13})$$

Another possibility for GaAs formation is *via* the formation of a gas phase adduct between the Lewis acid ($GaMe_3$) and Lewis base (AsH_3) pairs. The stability of the adduct [$GaMe_3\{AsH_3\}$] in the CVD chamber is dependent on the temperature of the system. Given the low thermal stability of this adduct, it can readily break down to form GaAs at the high deposition temperatures in which CVD is conducted.

The use of arsine as the arsenic source for the growth of GaAs has long been a problem.[47,48] This is due to its extreme toxicity. In MOCVD systems it is stored in pressurised cylinders that could cause widespread contamination if there was a leak. Furthermore, the pyrolysis of arsine requires temperatures above 550 ^{o}C to achieve reasonable rates of deposition.[47] Therefore, efforts have been made to find other arsenic sources for MOCVD. These include trimethylarsine, diethylarsine and tertiarybutyl arsine. Of these tertiarybutyl arsine has shown the most promise due to its reduced toxicity and lower pyrolysis temperature compared to arsine.[48]

The use of hydrogen carrier gas aids pyrolysis by hydrogenolysis of the precursors and decomposition products in MOCVD. As well as reducing the reaction time under atmospheric pressure MOCVD, it also promotes the formation of methane as the major by-product. Conversely, using nitrogen carrier gas results in ethane as the major by-product of pyrolysis of the precursors. This is unfavourable as ethane pyrolyses more easily (as it can undergo β-hydride elimination) than methane and thus can increase carbon contamination in the films.[49,50,51]

GaAs films of the *n*-type can be obtained by MOCVD through doping with silicon using silane gas as the dopant precursor. *p*-Type layers are achieved by doping with either zinc (using diethyl zinc precursor) or carbon (using carbon tetrabromide).[34]

The reactor design of an MOCVD system is crucial in obtaining high quality films, hence much research has gone into developing optimised reactor systems. The

uniformity, growth efficiency and reproducibility are all factors affected by the MOCVD reactor design. One of the major components of a sophisticated MOCVD rig (such as those used to grow GaAs) is the "gas handling system". This dictates the timing and composition of the vapour entering the reactor. It is essential that this system is airtight as oxygen contamination results in unintended oxides and overall degradation of the photovoltaic properties of the film. Furthermore, accurate control of the flow rate, temperature and pressure is needed to obtain high quality epitaxial films. For precursors to be compatible with MOCVD they must be volatile. Hence, in the case of growing GaAs films, the ubiquitous precursors are trimethyl gallium ($GaMe_3$) or triethyl gallium ($GaEt_3$) as the gallium source and arsine (AsH_3) or tert-butyl arsine ($^tBuAsH_2$) as the arsenic source. Safety is of paramount concern as large amounts of toxic gases such as arsine are used. Therefore, the use of MOCVD in producing GaAs thin films can be expensive.

Molecular beam epitaxy (MBE) is an alternative route to GaAs thin films. This enables the growth of high quality and very pure epitaxial layer of the semiconductor, but requires an ultra high vacuum that can be difficult to achieve without the use of high-end pumping equipment. Thus, it is expensive and cannot easily be used to grow materials with high vapour pressures.[52] MBE is a controlled evaporation of different elements under high vacuum onto a temperature controlled single crystal substrate.[53] MBE produces single crystal layers of uniform and precise thickness with minimal mismatch of chemical bonds at the substrate-layer interface. It is also possible to integrate highly precise/sensitive electron probe and optical instruments (*via* high energy electron diffraction) to monitor film growth as it is taking place.[54] This allows great reproducibility. In MBE the pressure is kept very low, typically 1×10^{-10} Torr, so that the molecules in the chamber travel in a straight line to the substrate without colliding with each other.[55]

MBE is an expensive technique because it involves some stringent mechanical and electrical demands. Due to the very high vacuum levels required it is a slow process and is not ideal for mass production.[56] It requires pure gallium and arsenic (in the form of arsine) to grow the films. These methods require high temperature and/or low pressures, which contribute significantly to the high cost of producing GaAs photovoltaics and severely adds to the cost/ wattage ratio.

1.1.3 GaAs based photovoltaic devices

GaAs photovoltaics are rarely based on a simple *pn* junction design.[57,58,59] This is due to many factors that would limit the efficiency of such a device. Since GaAs has a high absorption coefficient, a large amount of charge carriers would be produced near the surface where recombination is more likely.[57] Furthermore, GaAs is a direct bandgap material hence charge carriers are easily created but the opposite is also true, i.e. recombination of charge carriers takes place very easily compared to indirect materials such as silicon.[15,12,13]

These problems are overcome by creating a heteroface junction device.[57] A *pn* junction is a homojunction as it is made up of two materials (they can be the same material) with equal bandgaps but different doping. A heterojucnction is the junction between two materials with unequal bandgaps.[48] Therefore a heteroface junction can be created using a *p*-type material $Al_xGa_{1-x}As$ placed next to the *p*-type GaAs of a GaAs *pn* junction system. $Al_xGa_{1-x}As$ layer can be referred to as a window layer as it has a higher bandgap than GaAs therefore it is transparent to light below its bandgap.[60,61,62] It is compatible with GaAs because they are very well lattice matched and it helps improve the photovoltaic efficiency by dramatically reducing the recombination of charge carriers at the front surface of the *p*-type GaAs. Hence, a typical GaAs single junction photovoltaic device is made up of several layers (Figure 11). [60,62,63,64]

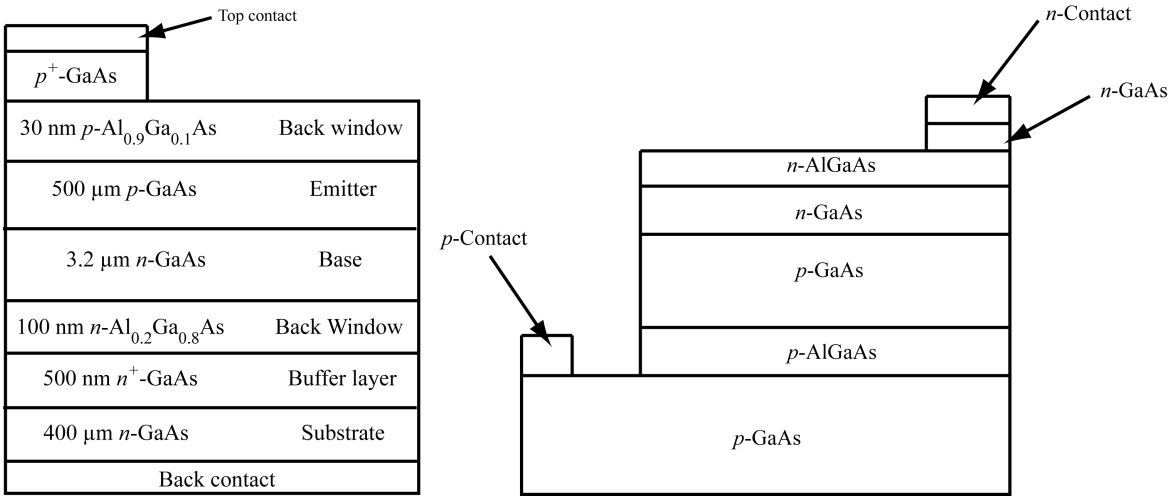

Figure 11: A single junction GaAs photovoltaic devices.

1.1.3.1 GaAs on amorphous substrates

The current method of GaAs fabrication using MOCVD or MBE involves epitaxial film growth on lattice-matched substrates such as GaAs or germanium.[14,63] These substrates are single crystal and are expensive to manufacture. Furthermore, they are very thick but the diameter is limited. Amorphous substrates such as glass present an alternative option. Glass is very easy and cheap to manufacture and can be made into large sizes, allowing the deposition area to be large. The main issue is in the quality of the GaAs films produced. Due to the substrate being amorphous the film deposition cannot be epitaxial, therefore polycrystalline GaAs films are formed when deposited on glass.[65]

For instance polycrystalline GaAs films have been grown on quartz using trimethylgallium and arsine in a chemical beam expitaxy system (CBE) reported by Imaizumi *et. al*.[65] CBE is a hybrid system between MBE and MOCVD, in that like MBE it uses very high vacuum conditions and like MOCVD it employs molecular precursors, such as trimethylgallium. In the experiments, the deposition temperature was limited to 500 ^{o}C by the glass substrate. Since the pyrolysis of arsine requires at least 550 ^{o}C the precursor was pre-cracked at 1000 ^{o}C before going into the deposition chamber. As typical with dual-source CVD growth of GaAs, ten times more arsine was used compared to trimethylgallium to obtain stoichiometric films.

Polycrystalline films using glass have also been grown using MBE.[66] Films were grown at 400 ^{o}C or at lower temperatures in two stages; firstly a seed layer at 250 ^{o}C followed by the GaAs film on top at 400 ^{o}C, 300 ^{o}C and 250 ^{o}C. All films were polycrystalline in nature with some having a preferred orientation in the (111) direction. As expected, the crystallinity of the films improved when annealed at 800 ^{o}C.[66] Another example of polycrystalline films on glass was shown by Kalem *et. al*.[67] Films were grown again in two stages, with a seed layer at 400 ^{o}C followed by the actual film at 580 ^{o}C. The films showed good polycrystallinity and were strain free. The grain sizes observed were well below 1 μm in diameter.

Norton *et. al.* used a low-pressure chemical vapour deposition system with arsine, triethylgallium and hydrogen carrier gas to grow polycrystalline films on glass.[68] The deposition was activated using two mercury lamps. The temperature was maintained at 240 ^{o}C. Polycrystalline films were obtained with preferred orientation in the (220) and (311) direction.

1.1.4 Molecular precursors to GaAs

There are a wide selection of single-source precursors to GaAs ranging from simple 1:1 adducts to complex clusters. This section will focus on a few interesting and CVD applicable precursors however Cowley *et. al.*, Wells and Neumuller *et. al.* and provide detailed reviews.[74,75,76,93]

Adducts with a 1:1 ratio of gallium to arsenic have been researched and developed as they are less air sensitive and easier to handle and purify than their dual-source counterparts (for example AsH_3 and $GaMe_3$).[69,70,71] These Lewis acid–base adducts, of the type $[GaR_3\{AsR'_3\}]$, have been synthesised and characterised by Schulz *et. al.* from simple reactions whereby the products precipitate out as white solids immediately when the reagents are mixed in a glove box as shown in equation (**1.14**) .[72]

$$R_3Ga + AsR'_3 \rightarrow [GaR_3\{AsR'_3\}] \qquad R = Et, {}^tBu; R' = SiMe_3, {}^iPr \qquad (\mathbf{1.14})$$

However, dissociation of the arsine moiety can easily occur resulting in the need for excess reagents (e.g. AsR_3) during deposition experiments. This is due to the donor-acceptor bonds being weak compared to the other bonds (Ga-C, As-H).

The key feature of single-source precursors is that all the necessary bonds required in the film are pre-existent in the precursor. Unlike the weak donor-acceptor linkage present in adducts, precursors of the type $[R_2GaAsR_2']_n$ (n = 1, 2, 3 etc), contain strong two centre-two electron sigma bonds. Deposition can be carried out at a lower temperature and cost due to the strong pre-existent Ga-As bonds. This feature of single-source precursors has encouraged researchers to synthesise such precursors for the growth of GaAs films of device quality. As already mentioned GaAs films are expensive to manufacture due to costly growth techniques currently employed, as well as requiring costly single crystal substrates.

Two of the most successful types of single-source precursors that been used to produce epitaxial films of GaAs are shown in Figure 12.[69,73,74,75,76] The trimeric version of **1** also exists and is capable of producing GaAs films.

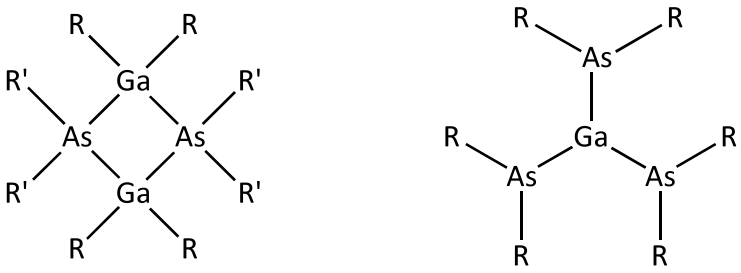

1 **2**

Figure 12: The two different types of GaAs precursors commonly synthesized. R and R' = alkyl groups.

The alkyl groups (R and R') are carefully selected to promote facile β–hydride and/or radical elimination reactions during decomposition of the GaAs precursor. This helps to reduce the decomposition temperature (to between 400 and 590 ^{o}C) and reduce production cost.

Alkyl groups such as *tert*-butyl, isopropyl and ethyl that contain β-hydrogen atoms can readily undergo β–hydride elimination (Scheme 1).[77] The products of such eliminations are a hydride and an alkene.[78]

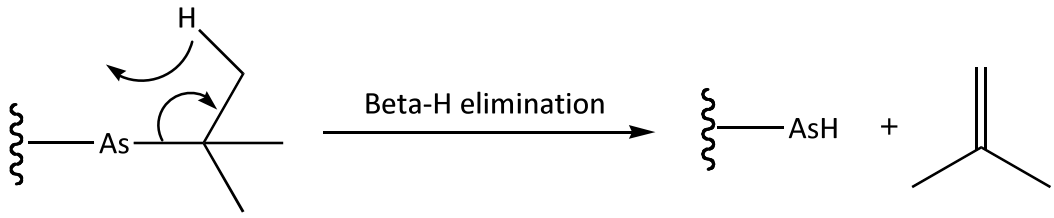

Scheme 1: *Tert*-Butyl arsine ligand undergoing β-hydride elimination.

The most basic type of decomposition that often takes place in single-source precursors with alkyl ligands is homolysis to produce hydrocarbon free radicals.[78] Depending on the mean free path, these radicals can recombine in the gas phase to produce stable products. However, the most probable outcome for the radicals are reactions between surface bound species and a gas phase species or reactions at the surface of the substrate between two surface bound species.[78] The ease at which a ligand undergoes homolysis depends on the stability of the resultant radical. If homolysis takes place to produce a tertiary radical then the temperature required for decomposition of that ligand would be lower than the temperature required for a ligand that produces a primary or secondary

radical.[74] Therefore selecting radical stabilising ligands can also help reduce deposition temperature and cost.

Another decomposition route is the intramolecular reaction of ligands attached to the same metal centre to produce saturated hydrocarbons. These hydrocarbons are then likely to dissociate *via* homolysis.[78]

Single-source precursors based around the structure of **1** have been synthesized by Cowley *et. al.*[69,79] The formation of LiCl was used as the driving force for the formations of the dimers **3**, **4** and **5** (equation **1.15**). In fact salt elimination is a tactic often employed to synthesise not only GaAs but also many other semiconductor precursors. This reaction proceeds to result in dimeric products as opposed to trimers, due to the bulky nature of the *tert*-butyl ligands on the arsenic atoms.

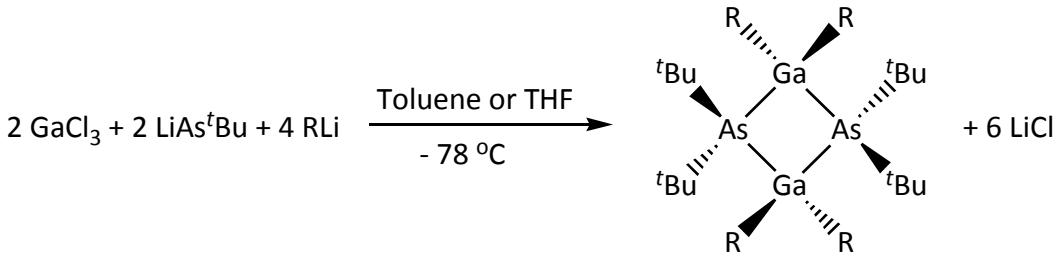

(**1.15**)

3, R = Me

4, R = Et

5, R = ^{n}Bu

GaAs films have been grown on α-Al_2O_3 (0001), GaAs (100), and GaAs (111) substrates *via* low pressure MOCVD using precursors **3** and **4**. Optimum film growth was obtained using a temperature of 525 ^{o}C, pressure of 1×10^{-4} Torr and either H_2 or He as the carrier gas when growing the GaAs film from precursor **3**.[74,80,81]

Recently, precursor **5** has been used in a low pressure CVD system to grow GaAs thin films on silica substrates.[82] Hector *et. al.* report that polycrystalline films were formed with the correct stoichoimetry at higher temperatures.

Using the sterically less demanding isopropyl group allows the formation of the trimer **6** (equation **1.16**).[75] The lack of steric hindrance around the arsenic also allows the reaction to proceed *via* the simpler alkane elimination mechanism and salt formation is not required to drive the reaction.[83,84] Though the alkane elimination reactions are higher yielding and easier to work up than salt elimination, they do require harsher conditions to overcome the kinetic energy barrier.

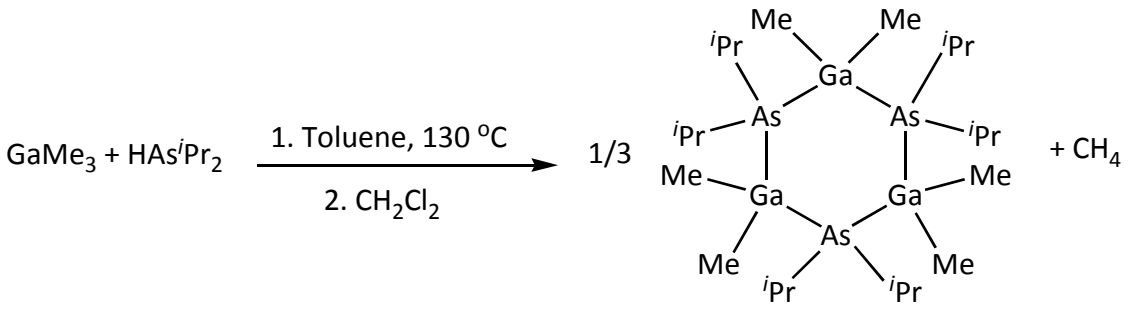

6 (**1.16**)

Cowley *et. al.* report that film growth was possible with the trimeric precursor (**6**) but the results were not reproducible.

The successfully grown films from **3** and **4** were of good quality and analysis showed that carbon contamination was generally low from both precursors but with less than 1000 ppm with precursor **4** in particular.[81] This indicates relatively clean decomposition pathways as a result of the carefully chosen organic ligands. Pyrolysis studies using mass spectrometric analysis carried out on both dimers (**3**, **4**) and the trimer (**6**) gave evidence of the predicted *β*–hydride and free radical modes of decomposition (Scheme 2).[81,85,86]

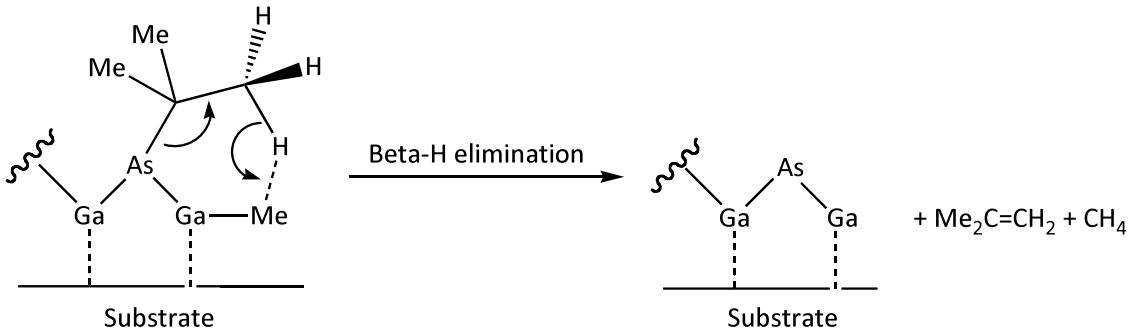

Scheme 2: Decomposition taking in precursor 3 on the substrate via β–hydride elimination.

Pyrolysis analysis on trimer **6** shows the formation of non-stiochiometric gallium and arsenic species, such as diarsines (R_4As_2), even at low temperatures.[86] At higher temperatures triisopropylarsine and trimethylarsine were detected. Diarsine or trialkylarsine species were not formed upon pyrolysis of the dimers **3** and **4**, which could explain why GaAs films were possible with precursors **3** and **4** but not **6**.[74,80,81,86]

Thin film deposition of GaAs has also been carried out *via* CBE using precursors **3** and **4**. Temperature and pressure play an important role in the crystallinity of the films obtained. When a study of film growth from **3** at various temperatures and pressures was undertaken the results showed that low pressure was necessary to reduce the gas phase heating of the precursor before it reached the substrate. Temperatures above 475 ^{o}C were needed to remove all the hydrocarbon ligands and obtain epitaxial film with precursor **3** however precursor **4** only required a deposition temperature of 400 ^{o}C to obtain epitaxial films.[74]

Although films obtained from both precursor **3** and **4** were epitaxial, Hall effect measurements showed films from **3** to be of superior quality with less defects. The only difference between the two precursors is that **3** has methyl ligands on the Ga while **4** has ethyl, therefore this could be the cause for the difference in the final quality of the film. Ga-Me decomposes at higher temperature than Ga-Et due to the lack of β-hydrogens on Me. Hence Ga-Me groups prevent Ga from reacting with itself forming inhomogeneous films. Ga-Et quickly undergoes β-hydride elimination to give Ga-H and finally free Ga *via* desorption of hydrogen. The free Ga can then react with each other rather than with arsenic to give defective films.[74,80,81] This problem could be limited if the concentration of As was increased so that Ga adatoms on the surface of the substrate favour reacting with As rather than with themselves.

Compounds with a 1:3 stoichiometry of Ga:As, such as **2** (Figure 12) were very efficient precursors to GaAs.[74] These were synthesised using salt elimination as the driving force for the reaction as in equation **1.17**. The monomeric compound **7** has a trigonal planar geometry around the Ga and As atoms.[74]

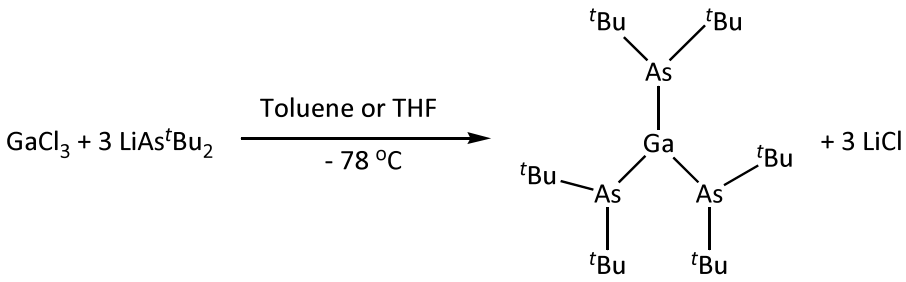

(**1.17**)

7

The excess of arsenic enables high quality GaAs films to be deposited from **7** because the excess arsenic promotes reactions between Ga and As while limiting reactions between free Ga that result in inhomogeneous films, such as those obtained when using precursor **4**. Furthermore, carbon contamination is very low due to the lack of Ga-C bonds in the compound.[86]

Another monomeric compound with a 1:3 ratio of Ga to As is compound **8**. The reaction proceeds *via* silyl halide elimination as shown in equation **1.18**.[87] This is a highly efficient technique for the synthesis of GaAs precursors that was developed by Wells *et. al*.[76]

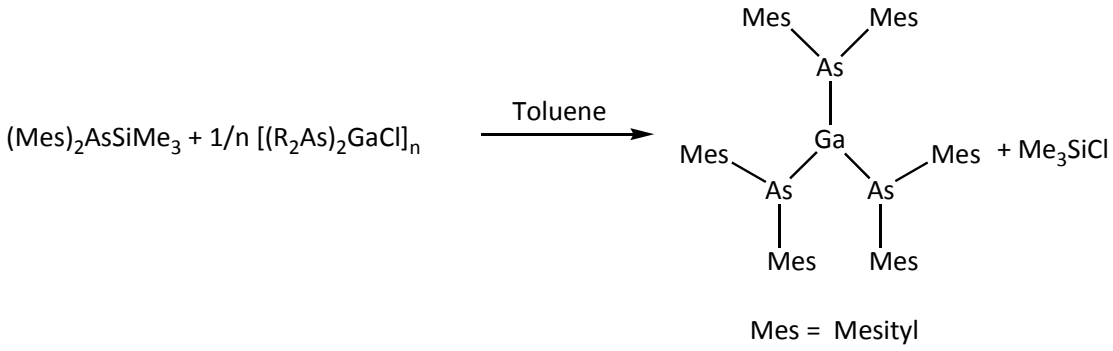

8 (**1.18**)

This method of precursor preparation was developed due to the lack of efficiency in getting the alkane elimination to proceed when bulky and sterically hindered substituents were attached to the gallium or arsenic atoms. The driving force for these reactions is the formation of the strong Si-Cl bond.[74,76,88]

The first reported case of GaAs precursors formed *via* silylarsines was by Wells *et. al.* in 1986.[87] The precursors were synthesised by reacting halogallanes with secondary trimethylsilylarsines in hydrocarbon solvents to yield monomeric (**8**), dimeric (**11**, **12**) and oligomeric (**9**, **10**), compounds (equations **1.18** – **1.20**).[81]

$$GaCl_3 + R_2AsSiMe_3 \xrightarrow[\text{Heat}]{\text{Toluene or THF}} 1/n\ (Cl_2GaAsR_2)_n + Me_3SiCl$$

9, R = Me_3SiCH_2 (**1.19**)

10, R = Mesityl

$$RGaCl_2 + As(Me_3SiCH_2)_2 \xrightarrow[\text{Heat}]{\text{Toluene or THF}} 1/n\ [R(Cl)GaAs(CH_2SiMe_3)]_2 + Me_3SiCl \quad (n = 2, 3)$$

11, R = Me (**1.20**)

12, R = Ph

The silyl arsines (e.g. compound **13**) used by Wells *et. al.* were synthesised using arsenate (As_2O_3) *via* a reaction using Grignard's reagent (Scheme 3).[76]

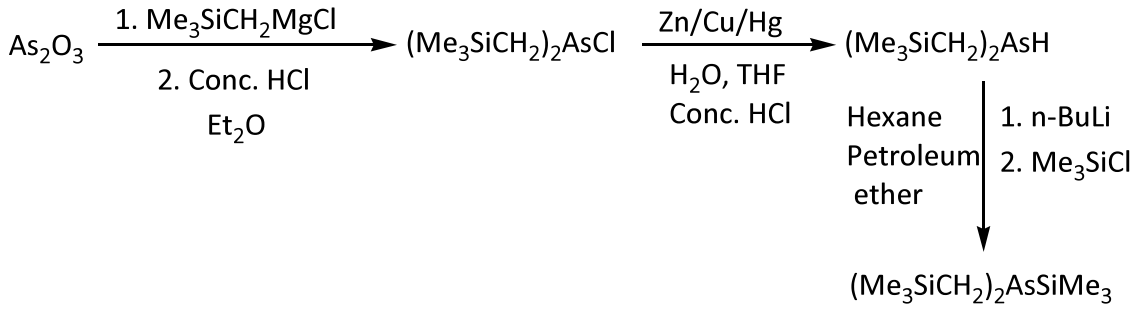

13

Scheme 3: Silyl arsines via silyl chloride.

Simpler and more convenient routes to silyl arsines that involve the use of less toxic reagents have since been reported. One such example is by Carmalt *et. al*.[89] Their technique involves the synthesis of a range of homoleptic silylarsines (**14-16**) from the reaction of readily available silyl chlorides with trisodium arsenide (Scheme 4).

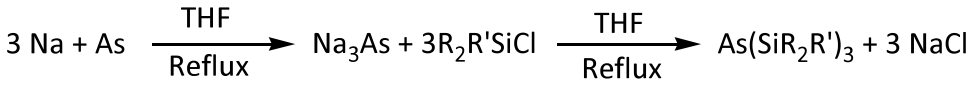

14, R = Me, R'= Cy

15, R = Me, R' = Ph

16, R = Ph, R' = Ph

Scheme 4: Homoleptic silylarsines *via* sodium arsenide

Further work carried out by Wells *et. al.* with the use of homolyeptic arsines include precursors (equation **1.21**) (**17**) that have been used to produce nanocrystalline GaAs via *β*-hydride elimination when thermolysis was carried out.[90] The precursor was heated to 400 ^{o}C under static vacuum for 5 h. A dark grey GaAs film formed on the walls of the sublimator and cold finger. The volatiles were analysed to be $HSiMe_3$, C_2H_4, CH_4, and H_2 using IR spectroscopy thus showing both homolysis and *β*-hydride elimination had taken place.

This dimer (**17**) is very similar in structure to **4** that was produced by Cowley *et. al. via* the salt elimination route (equation **1.15**). The only difference between the two is that **4** contains *tert*-butyl ligands on the arsenic while **17** contains trimethylsilane. As the trimethylsilane ligand lacks *β*-hydrogens it reacts via homolysis during decomposition and the temperature required to grow GaAs films from **17** is higher than that required for **4**. Detailed pyrolysis analysis has not been carried out on **17**, but judging from the lack in quality of the film obtained from the CBE of **4**, it is likely that the ethyl ligands on Ga would give rise to Ga islands and inhomogeneous films here as well.

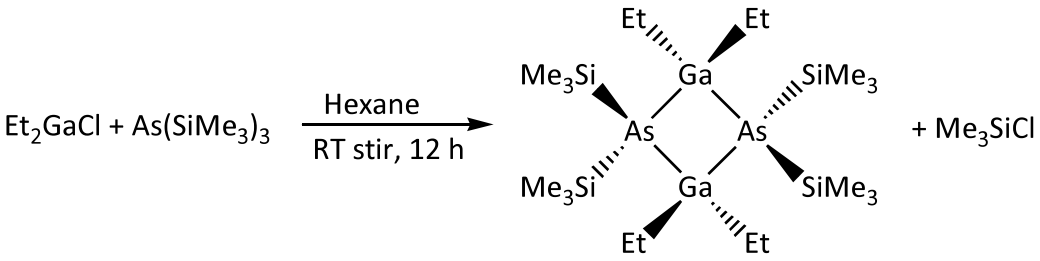

(**1.21**)

17

The analogous compound to **17** with methyl groups on Ga, namely $[Me_2GaAs(SiMe_3)_2]_2$, instead of ethyl has been synthesised using the same methodology, but CVD or pyrolysis analysis were not been carried out.[91]

Nanocrystalline GaAs has also been obtained from trimeric gallane complexes (**18**). These were prepared by dehydrosilylation from the reaction of $[H_3Ga\{NMe_3\}]$ with a homoleptic silylarsine (Equation 1.22).[92] The trimer spontaneously decomposes at room temperature and must be stored below -30 ^oC.

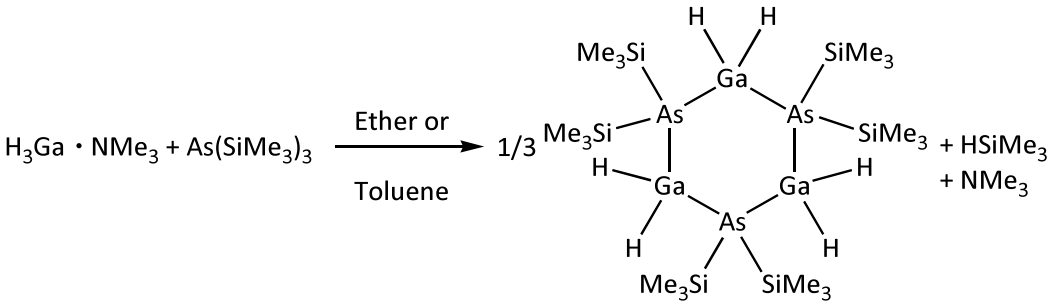

(**1.22**)

18

Other interesting GaAs single-source precursors include gallacyclopentane (**20**). Compound **20** was synthesised *in situ* by the addition of [LiAs^{t}Bu$_2$] with $GaCl_3$ and [Li$(CH_2)_4$Li], with the reaction proceeding *via* an intermediate (**19**) (Scheme 5). Film growth using this precursor has yet to be reported. The cyclic substituent on gallium lacks *β*-hydrogen hence decomposition *via* *β*-hydride elimination is not possible. Furthermore, the substituent does not favour homolysis too strongly either as relatively unstable primary radicals would be produced. Thus CVD of such a precursor (**20**) is likely to require high temperatures and lead to carbon contaminated films.

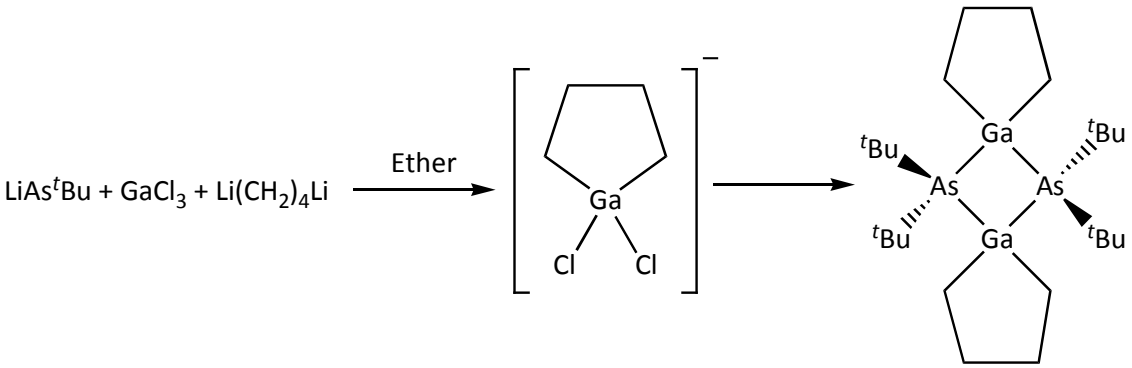

19 **20**

Scheme 5: GaAs precursor containing cyclic substituents.

More complex cyclic compounds are rare but structures have been reported.[93] Neumuller *et. al.* reported the synthesis of (**21**) via the mixture of $GaCl_3$ with [Li$_2$As^{t}Bu] at -78 ^oC (equation **1.23**).[94] The isolated crystals of **21** were stabilised by THF molecules.[94] Such ionic species are likely to have very low volatility thus making them

only suitable for AACVD and other similar techniques where volatility of the precursor is not a concern.

$$6\ GaCl_3 + 4\ Li_2As^tBu \xrightarrow[2.\ THF/\ Toluene]{1.\ Et_2O,\ -78\ ^oC} [Li(THF)_4]_2[(GaCl_2)_6(As^tBu)_4].THF + 6\ LiCl$$

21

(**1.23**)

Another GaAs cluster, $[(PhAsH)(R_2Ga)(PhAs)_6(RGa)_4]$ (where R = Me_3SiCH_2) (**22**), that has been reported shows the presence of As-As bonds. The compound was synthesised through the elimination of $SiMe_4$ and the As-As linkages formed most likely through the evolution of H_2.[95]

1.1.5 Conclusion

Gallium arsenide is an important photovoltaic material as it has a direct band gap of 1.43 eV that is near the optimum for solar conversion. Its high absorption of light along with high heat and radiation resistance results in high solar efficiencies compared to other materials. However due to high material costs and expensive fabrication techniques it is currently limited to space and military applications. Fabrication methods such as MOCVD and MBE are expensive, as they require high vacuums and high temperatures. They also require expensive substrates that are destroyed in the post deposition process during device fabrication. Furthermore, the process uses high purity, volatile dual-source precursors (AsH_3, $^tBuAsH_2$, $GaMe_3$, $GaEt_3$) that are difficult to handle due to their toxicity and pyrophoricity.[96]

We have attempted to overcome this issue by depositing films of polycrystalline GaAs using a specialised form of CVD called AACVD. The goal is to minimise the fabrication cost by using a chemical process under atmospheric and relatively low temperature conditions. As AACVD uses molecular precursors dissolved in solvent, the requirements on precursor purity is not so stringent. Also, we have avoided the use of expensive single crystal substrates in an attempt to minimise the watt/cost ratio. This is possible by developing a novel photovoltaic stack that is a hybrid between an amorphous silicon and GaAs device (Figure 13).

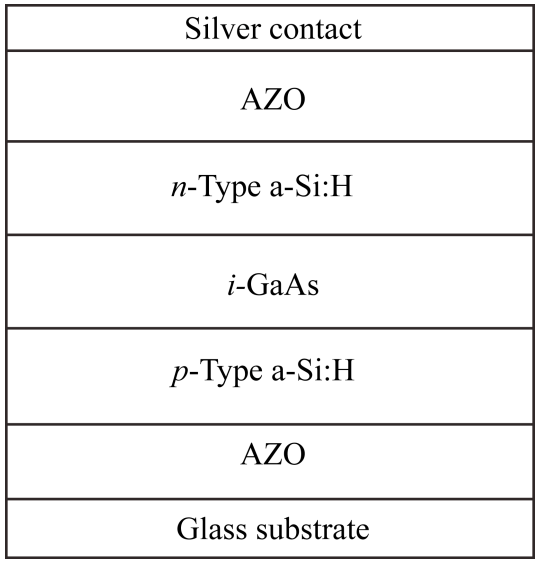

Figure 13: The hybrid a-Si:H device stack with a polycrystalline intrinsic GaAs layer. *p*-Type and *n*-type a-{H)Si layers are obtained *via* boron and phosphorus doping respectively. The device has aluminium doped zinc oxide (AZO) electrodes.

A typical a-Si:H solar device is composed of three layers of silicon (*p*-layer, *i*-layer and *n*-layer) of slightly different composition to make a *p-i-n* junction. A *p-i-n* junction device is very similar to a traditional p/n junction devices but with an intrinsic layer in the middle to enhance absorption of the solar spectrum.

Amorphous Si solar cells are very easy and cheap to manufacture. However, their low efficiency (10%) as a result of their poor absorption in the 650-900 nm wavelength region of the solar spectrum has hindered their commercial success. We have attempted to improve the overall efficiency of an a-Si:H solar cell by enhancing the absorption in the 650-900 nm region. This can be achieved by replacing the intrinsic a-Si:H layer in the *p-i-n* junction with an intrinsic GaAs layer. GaAs has very high absorption in the 650 -900 nm range. Therefore it is envisioned that a good efficiency of light to power conversion is possible at low cost.

Chapter 2

2 Experimental technique

2.1.1 Introduction

This chapter details the experimental techniques used to synthesise thin films *via* AACVD and gives a brief introduction and background to the analytical techniques used to analyse the thin films.

2.1.2 Aerosol Assisted Chemical Vapour Deposition (AACVD)

All the films made during this project were synthesised using an AACVD reactor (Figure 14). The cold wall AACVD reactor contains a semicircular graphite block upon which the glass substrates sit. The graphite block was heated using a rod heater and the temperature is monitored using two thermocouples. A glass top plate was used to obtain laminar flow of the precursor/carrier gas fluid mixture. This is placed 12 mm above the bottom plate. The aerosol entered the AACVD reactor *via* a brass baffle that promotes a flat, horizontal flow of aerosol across the width of the reactor.

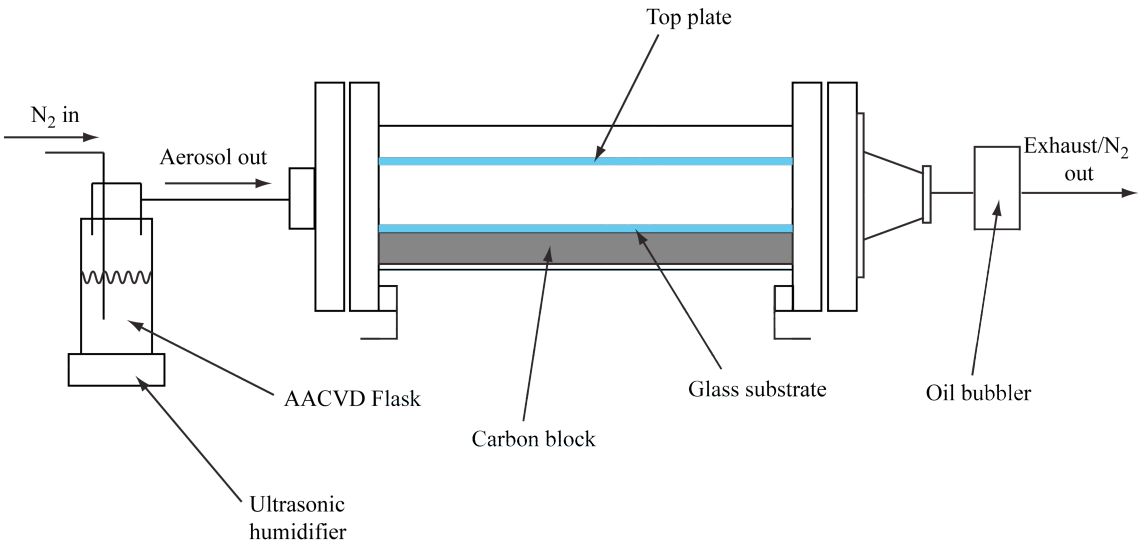

Figure 14: Schematic of an AACVD reactor.

It was very important to avoid oxygen contamination in the films, therefore modifications to the standard AACVD rig were made so that all metal-to-metal joints had PTFE gaskets to achieve airtight seals. The rig was confirmed to be airtight by pressurising it with nitrogen and checking for leaks with a gas flow meter. The exhaust was connected to an oil bubbler to avoid any back draft of air into the reactor.

The aerosol was generated inside a glass flask using a Vicks ultrasonic humidifier, which contains a piezoelectric transducer that operated at 20 mHz therefore producing aerosol droplets 59.3 μm in diameter. The droplets were carried into the reaction chamber using a nitrogen carrier gas supplied by BOC. The nitrogen, which was oxygen free with 99.9% purity, was passed over vacuum dried molecular sieves (dried monthly, under vacuum at 400 ^{o}C for 3 hours) to remove any water.

The glass substrates made from borosilicate glass with no barrier coating were used to grow the films and as the substrate. They were 148 mm x 45 mm x 0.7 mm and supplied by corning glass. They were cleaned using isoproponal and acetone solvents and dried using a heat gun before being placed into the reactor at room temperature. The reactor was sealed and heated to the required temperature under nitrogen gas flow, which was controlled using a gas flow meter. After deposition, the reactor was cooled naturally to room temperature under a flow of nitrogen and films removed and stored.

2.1.3 Material Characterisation Techniques

A range of analytical techniques were used to characterise the films and to determine their properties.

2.1.3.1 Powder X-ray Diffraction

Powder X-ray diffraction is a powerful tool that can be used to characterise solid crystalline materials such as thin films. Information obtained from XRD includes the phase identity, preferred orientation, crystallinity and crystallite size.[97,98, 99]

When a monochromatic X-ray beam of a particular wavelength interacts with a polycrystalline sample, it is scattered by the electrons of the atoms that make up that sample. If the scattered X-rays have only undergone a change in momentum (as opposed to change in momentum and wavelength (inelastic scattering)) the X-rays are said to be elastically scattered.

In crystalline materials the atoms are arranged in a periodic manner and in layers or planes (lattice planes) a particular distance apart (d). This d spacing of a lattice (a lattice is defined as the regular three dimensional arrangement of atoms in space) is unique to that lattice and all crystalline materials have different orientations of the planes all with unique d spacing (Figure 15).[99,100]

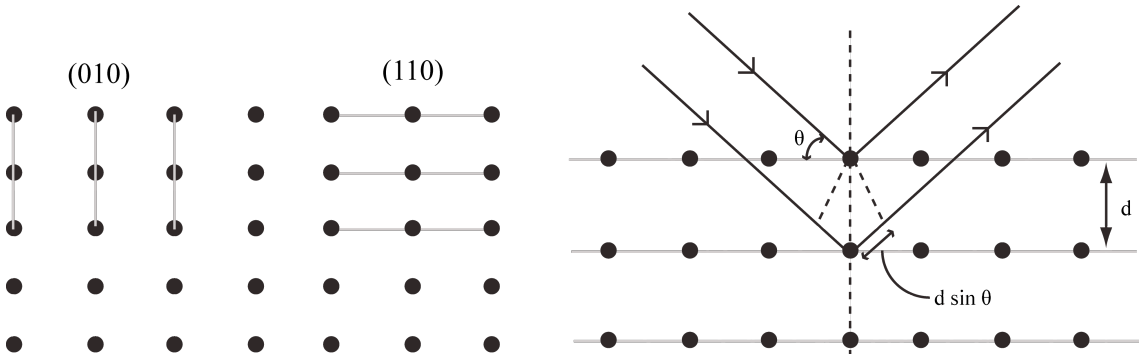

Figure 15: Left - A two dimensional representation of a crystal lattice orientated I different directions. Right – The interaction of X rays with different planes of a lattice within a crystalline material.

$$n\lambda = 2d\sin\theta \qquad (\mathbf{2.1})$$

Therefore, if a d spacing of various orientated planes within a crystal is determined it is possible to identify the crystalline material by a technique called indexing, which essentially involves determining the peak position in a XRD diffractogram and matching it to a standard data set.

Therefore upon interaction with an X-ray of a suitable wavelength (λ) some of the X-rays are diffracted from one plane and some from the adjacent planes directly below. This diffraction takes place at an angle equal to the angle of incidence, which is labelled θ. The elastically diffracted X-rays from different planes of the lattice of the crystalline materials interfere constructively when Bragg's law is observed and when the scattered X-rays are in phase (i.e. diffracted waves differ by only a complete number of wavelengths (n)).[99]

By changing the angle of incidence, θ, so that Bragg's law is always observed allows in phase and constructive diffraction by different d spacings of the different lattice plane

of the crystalline material. These diffracted X-rays are collected by a dectector and an XRD diffractogram is produced unique to the material.[99, 100]

Powder XRD for this project was carried out on a Bruker D4 diffractometer with Bragg-brentano θ-2θ reflection geometry using a post sample monochromator. It uses a $Cu_{K\alpha}$ X ray source with a wavelength of 0.154056 nm, a voltage of 30 kV and current of 40 mA. Powder XRD was also carried out using Bucker D8 X-ray diffractometer with $Cu_{K\alpha1}$ and $Cu_{K\alpha1}$ radiation of wavelength 0.154056 and 0.154439 nm respectively emitted with an intensity ratio of 2:1, a voltage of 40 kV and current of 40 mA. The instrument broadening was determined using a alumina flat plate from the National Institute of Standards and Technology (NIST). Peak positions were compared to patterns from the Inorganic Crystal Structure Database (ICDS).

2.1.3.2 Raman Spectroscopy

Raman spectroscopy depends on the Raman effect that takes place when a sample is exposed to monochromated light from a laser. It is a material characterisation tool that inspects the vibrational modes within a sample. Only vibrational modes that give a change in the polarisability of a bond are Raman active, this is one of the selection rules. The majority of light that interacts with the sample is scattered elastically, i.e at the same energy as the incident light. However a small fraction is scattered inelastically at energies below and above the energy of the incident light. This occurs because the incident light excites the molecule from the ground to an excited electronic state. After illumination, if a molecule returns not to the original state it was excited from but to a higher state then it has undergone Stokes type scattering. Similarly, if the molecule returns to a higher state than the original state before excitation it has undergone anti-stokes type scattering. Calculating the change in energy between the incident light and the scattered light gives information regarding the vibrational energy levels of the molecule.

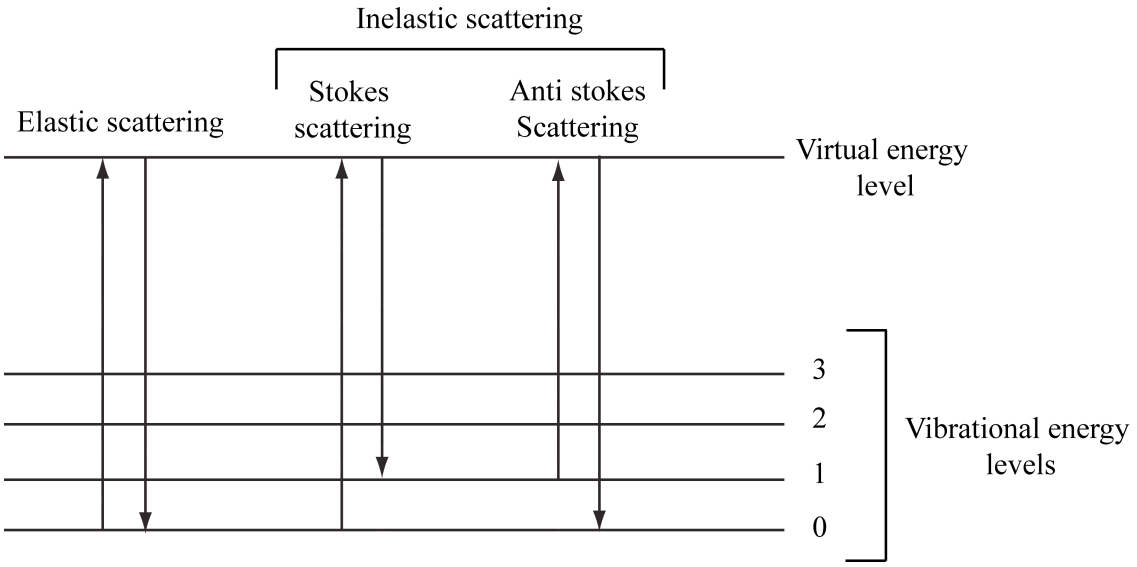

Figure 16: Energy level diagram showing the different types of light scattering and the different types of inelastic scattering.

Raman spectroscopy was preformed using a Renishaw 1000 spectrometer equipped with a 514.5 nm laser. Peaks were fitted to a Gaussian model using CasaXPS software.

2.1.3.3 Scanning Electron Microscopy (SEM)

In SEM, a finely focused high-energy electron beam probes the sample. The beam interacts with the sample and is able to cause the emission of two different types of electrons.

The electrons that are ejected from the atoms of the sample due to inelastic interactions with the electron beam are called secondary electrons. These have very little energy and hence can only escape from the sample and reach the detector if they are created near the surface. Furthermore, secondary electrons created near the peaks in the surface escape more readily than those created in troughs. Therefore due to the dependence of secondary electrons on the topography of the sample it is possible to build a high-resolution and magnification image of the morphology of the sample. The amount of secondary electrons produced by the sample is independent of the atomic number of the atoms of that sample; hence it is not possible to do elemental analysis.

SEM images were taken on a JEOL JSM-6301F Field Emission instrument with acceleration voltage ranging from 3 to 10 kV. The probe current range was 6 to 8 μm.

The images were captured using SEMAfore software. Sample preparation involved cutting the films down to coupons 10 mm x 10 mm or less and sticking them on stainless steel holders using conductive carbon tape. Contacts from the top of the film to the carbon tape were made using a solution of silver paint. Once dried the samples were coated with a fine layer of carbon or gold to avoid charging. SEM images show in Figures 28 – 31 were carried out by members of the analytical team at Applied Materials Inc., California, USA.

2.1.3.4 Energy Dispersive X Ray Spectroscopy (EDX)

Upon interaction between the sample and the focused electron beam, electrons are knocked from the outer shell of the atoms (with respect to the Bohr model) that make up the sample. At this point the atoms are in an excited state and they return to the ground state by the various transformations that involve the dropping of electrons from the outer shell to the inner shell filling the vacancy. As the electrons drop energy is released in the form of X-rays that have an energy equal to the energy difference between the two shells. Hence the energy is unique to the element and therefore it is possible to characterise the elemental make up of a material by collecting these X-rays with a detector.

Depending on the acceleration voltage used for the electron beam, the spectrum that is given can have various peaks or lines corresponding to the same element. These lines are labelled depending on the atomic shell where the electron has been removed from and also on the shell from which the outer electron is dropping. If the vacancy is created in the K shell and an electron drops from either the L, M or N shell then the spectrum has Kα, Kβ or Kγ lines respectively. Similarly if an electron is knocked from the L shell and an electron drops from the M or N shell to fill the vacancy then the lines are Lα or β. As mentioned above, depending on the strength of the electron beam and on the elements being analysed, it is possible to have all the lines in the spectrum.

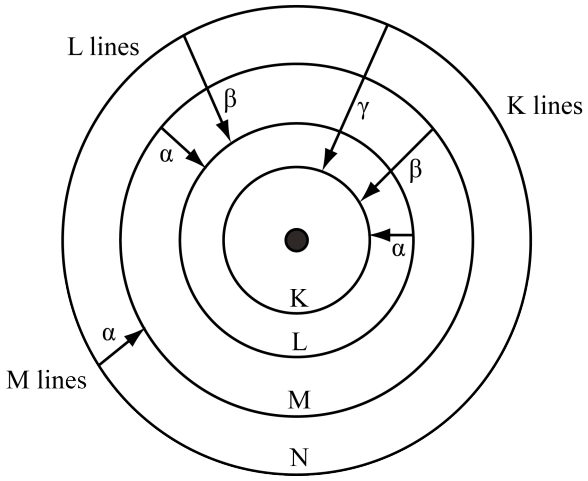

Figure 17: The energy of the emitted X-rays as a result electron transfer from a higher energy shell to a lower energy shell enables the identification of the elements of the samples being analysed.

EDX was carried out on a JEOL JSM-6301F Field Emission instrument with acceleration voltage ranging from 20 kV. Sample preparation involved cutting the films down to coupons 10 mm x 10 mm or less and sticking them on stainless steel holders using conductive carbon tape. Contacts from the top of the film to the carbon tape were made using a solution of silver paint. Once dried the samples were coated with a fine layer of carbon or gold to avoid charging.

2.1.3.5 High Resolution Transmission Electron Spectroscopy

HRTEM is a sophisticated technique that enables the imaging of a sample at the atomic scale. Due to its high resolution it is possible to directly determine the features of the sample such as crystallite size. It involves the acceleration of a beam of electrons through a very thin sample that results in the formation of an image due to the interaction (diffraction) of the electrons with the sample. As a result of the wave/particle properties of electrons they can be used to behave like a wave such as X-rays. The advantage of using electrons instead of X-rays is that they have a much smaller wavelength. The electrons in the TEM instrument are generated by thermonic emission and accelerated and focused using an electric potential and electrostatic/electromagnetic lenses respectively. The focused beam of electrons interacts with the sample as it passes through it and it contains information about the phase, periodicity and electron density of the material. Importantly it is possible of form a very high resolution image of the sample on a layer of photographic film.

The TEM instrument used in this project was a FEI Titan FEG-TEM with a 0.8 angstrom resolution in TEM mode and 1.4 Angstrom STEM resolution. Characterisation was preformed by members of the CAMCOR technical team at the University of Oregon, Oregon, USA.

2.1.3.6 X-Ray Photoelectron Spectroscopy

In XPS, X-rays (with photon energy of 200 to 2000 eV) are used to eject core level electrons from the atoms that make up the surface (1-10 nm) of the solid sample. The ejected electrons are then collected by a detector and the kinetic energy distribution of these electrons is studied. It is possible to calculate the binding energy of the ejected electron by calculating the difference in energy between the neutral atom and the ionised atom of a particular sample. Each element has a characteristic binding energy for the electrons in the core atomic orbital and will give a peak in the XP spectrum at a specific binding energy. Also, the intensity of the peaks indicates the concentration of a particular element in the sample. Therefore using XPS it is possible to quantify the surface composition of the sample.[101]

XPS was carried out on Thermofisher Scientific K-Alpha XPS system with Avantage software. The base pressure in the chamber was $1x10^{-8}$ Torr. Samples were sputtered using a 2kV argon ion gun, the sputtering rate was 1 angstroms per second (calibrated using a SiO_2 standard and a relative sputter factor of GaAs of 1.3). High resolution scans were recorded for Ga $3d_{5/2}$, As $3d_{5/2}$, O 1s and C 1s. The peaks were modeled using CasaXPS software with binding energies calibrated to carbon (284.5 eV). XPS was carried out by members of the analytical team, Applied Materials Inc., California, USA.

2.1.3.7 Secondary Ion Mass Spectroscopy

SIMs is a very sensitive technique used to analyse trace elements in solid samples such as thin films at concentrations as low as one parts per million or billion. The high-energy (1-30 KeV) primary ion beam (usually Ar^+) collides with the solid sample in a vacuum. Upon interaction with the sample, sputtering of the surface takes place whereby neutral, charged and incident ions are ejected in the form of atoms and molecules. The ejected species are analysed using a mass spectrometer.

SIMS was carried out by Evans analytical Group, California, USA.

Chapter 3

3 Single-source precursor synthesis

3.1.1 Introduction

With respect to precursor and CVD growth of thin films there are two options, dual-source or single-source. The dual-source route employs the use of multiple precursors each being the root of an element required in the film. For example, the growth of GaAs *via* a dual-source method would typically use trimethylgallium as the gallium source and arsine as the arsenic source. Though good quality films can be achieved *via* this method the process can be difficult as the two precursors have different vapour pressures and decomposition temperature. Hence it can be a challenge to obtain stoichoimetric films.

Conversely, single-source precursors contain all the required elements for the film within a single compound thus eliminating problems, such as non stoichiometry. Furthermore, they generally decompose at lower temperatures as they already contain the bonds required in the film. This chapter details the synthesis of single-source gallium arsenide precursors.

3.1.2 Single-source precursor synthesis

Trisodium arsenide (**23**) was synthesised in high yield (94%), from the 48 h reflux of sodium metal with arsenic powder as shown in equation **3.1**. Since **23** is toxic and highly air sensitive, powder XRD was carried out with the black powder in a sealed glass tube to minimize decomposition. XRD confirms the presence of trisodium arsenide as shown in Figure 18.

$$3\,Na + As \xrightarrow[\text{Reflux, 48 h}]{\text{Toluene}} Na_3As \qquad (\mathbf{3.1})$$

23

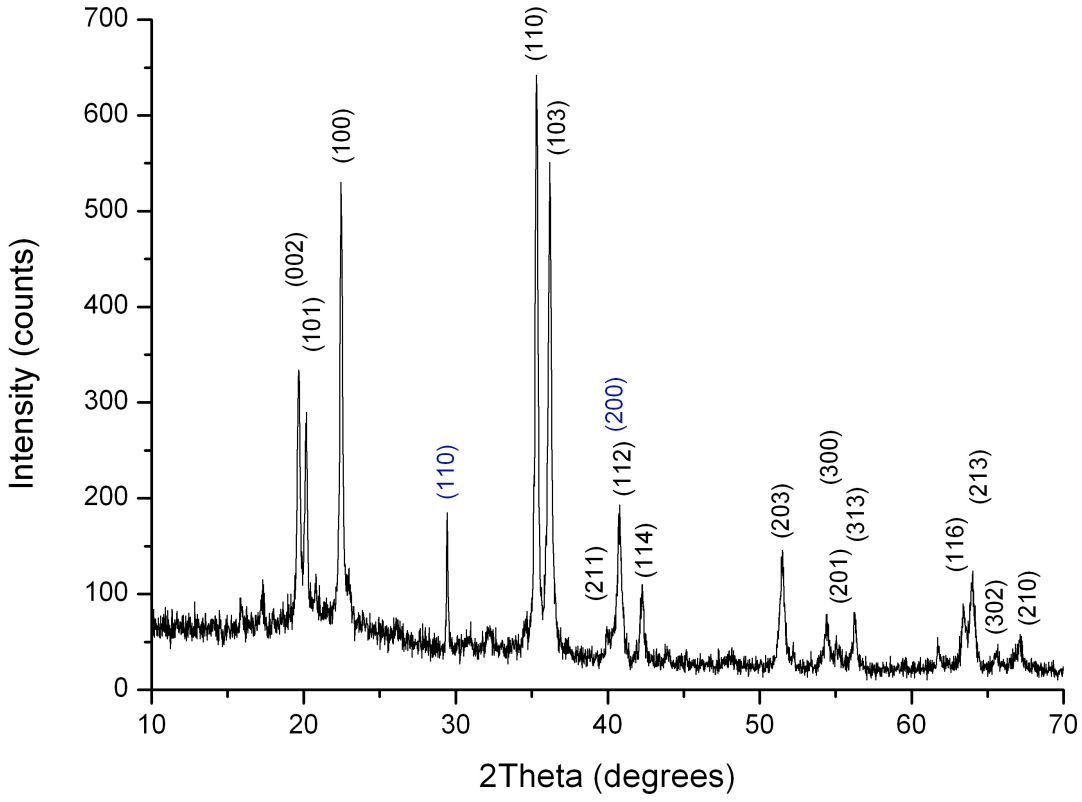

Figure 18: Powder XRD pattern for Na_3As (23) synthesised from sodium and arsenic. The *hkl* values in blue are the peaks for unreacted sodium metal in the powder.

Capillary XRD carried out in transmission mode showed that the synthesised product of the above reaction was indeed Na_3As. However, the product does contain some sodium impurities as indicated by the two peaks at 29.40° and 40.55°, which is due to unreacted sodium remaining behind after the reaction has taken place.

Homoleptic silylarsines, of the type $As(SiR_3)_3$, are a key class of reagents for the synthesis of the GaAs precursors. These were synthesised by reacting trisodium arsenide (**23**) with silyl chlorides in a 1:3 ratio (equation **3.2**) according to literature procedures.[102] On addition of three equivalents of $R_2R'SiCl$ to a slurry of Na_3As in THF the black mixture was refluxed for 16 hours. After the reactions had gone to completion in THF, the solvent was removed *in vacuo* and the black solid extracted with toluene. This was to remove the NaCl, which is soluble in THF but completely insoluble in toluene. After work up a yellow oil (**24**-**38**) or yellow solid (**29**) were isolated. All the homoleptic silylarsines were synthesised in good yield apart from compound **30** possibly due to an impure batch of Na_3As (**23**). The ^1H and ^{13}C NMR analysis of these

compounds corresponds (singlet peaks at 0.29, 0.49 and 0.49 ppm in the ^{1}H NMR spectra seen for compounds **24**, **25** and **26** respectively for the Si-Me group) with reported literature data.[102]

$$Na_3As + 3\ R_2R'SiCl \xrightarrow[\text{Reflux, 16 h}]{\text{THF}} As(SiR_2R')_3 + 3\ NaCl \quad (\mathbf{3.2})$$

24-29

24, R = Me, R' = Cy, 83%

25, R = Me, R' = Ph, 79%

26, R = Ph, R' = Me, 84%

27, R = Ph, R' = Ph, 92%

28, R =Ph, R' = ^{t}Bu, 81%

29, R = Me, R' = ^{t}Bu, 27%

Some of the homoleptic silylarsines were reacted with gallium reagents such as $GaCl_3$, $GaMe_3$, Et_2GaCl (**30**) and $GaEt_3$ to produce dimeric GaAs precursors. Diethylgallium chloride (**30**) was synthesised *via* a comproportionation reaction to yield a colourless liquid in a 97% yield (equation **3.3**). Evidence for the formation of the product **30** was given by a quartet at 0.90 ppm corresponding to the CH_2 group attached to the gallium and a triplet at 1.30 ppm corresponding to the CH_3 group of the ethyl ligand on the metal in its ^{1}H NMR spectrum.

$$2\ GaEt_3 + GaCl_3 \xrightarrow[\text{-78 }^oC, 2\text{ h}]{\text{Hexane}} 3\ Et_2GaCl \quad (\mathbf{3.3})$$

30

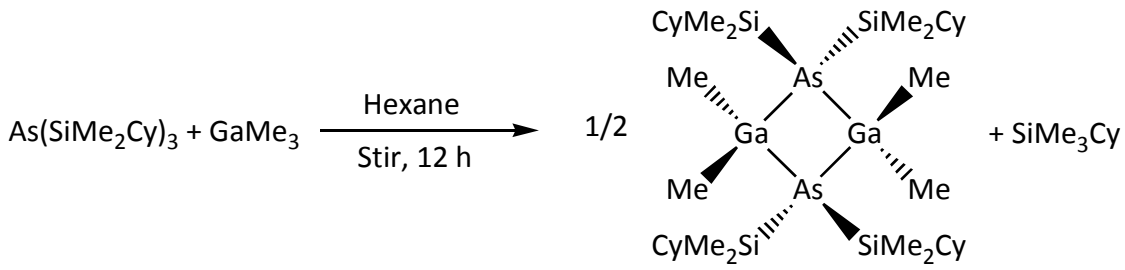

24 **31** (**3.4**)

The dimeric compound **31** was obtained by slowly adding $GaMe_3$ to $As(SiMe_2Cy)_3$ (**24**). Both reagents were dissolved in hexane and kept at -78 ^oC to avoid any decomposition (equation **3.4**). The reaction proceeds *via* the elimination of Me_3SiCy, which is easily removed *in vacuo*. A colour change from yellow to orange/brown was observed once the reaction had gone to completion. ^1H NMR peaks corresponding to the methyl groups attached to the silicon were observed at 0.90-1.10 ppm and the cyclohexyl group at 1.75-2.00 ppm for **31**. The synthetic route to **31** was identical to that used by Wells and coworkers for the synthesis of the analogous compound $[Et_2GaAs(SiMe_3)_2]_2$ and similar yields were obtained.[103] Compound **31** is more sterically hindered than $[Et_2GaAs(SiMe_3)_2]_2$ with bulkier organic groups. This was to increase the solubility of the precursor as it is intended for AACVD, whereas $[Et_2GaAs(SiMe_3)_2]_2$ was synthesised for MOCVD. Furthermore, the cyclohexyl ligands on **31** should also promote homolysis to take place more readily and thus reduce the deposition temperature as it decomposes to form a relatively stable secondary radical. This precursor does not contain any substituents with β-hydrogens on the gallium. This was to avoid the formation of Ga islands and inhomogeneous film growth as observed by Cowely *et al*. during their detailed comparisons of two similar precursors, $[Me_2GaAs^tBu_2]_2$ and $[Me_2GaAs^tBu_2]_2$**.** Colourless crystals were obtained when compound **31** was dissolved in hexane and kept below -20 ^oC for 4 weeks. In order to confirm the formation of a dimeric compound the structure of **31** was determined by single crystal X-ray crystallography (Figure 19).

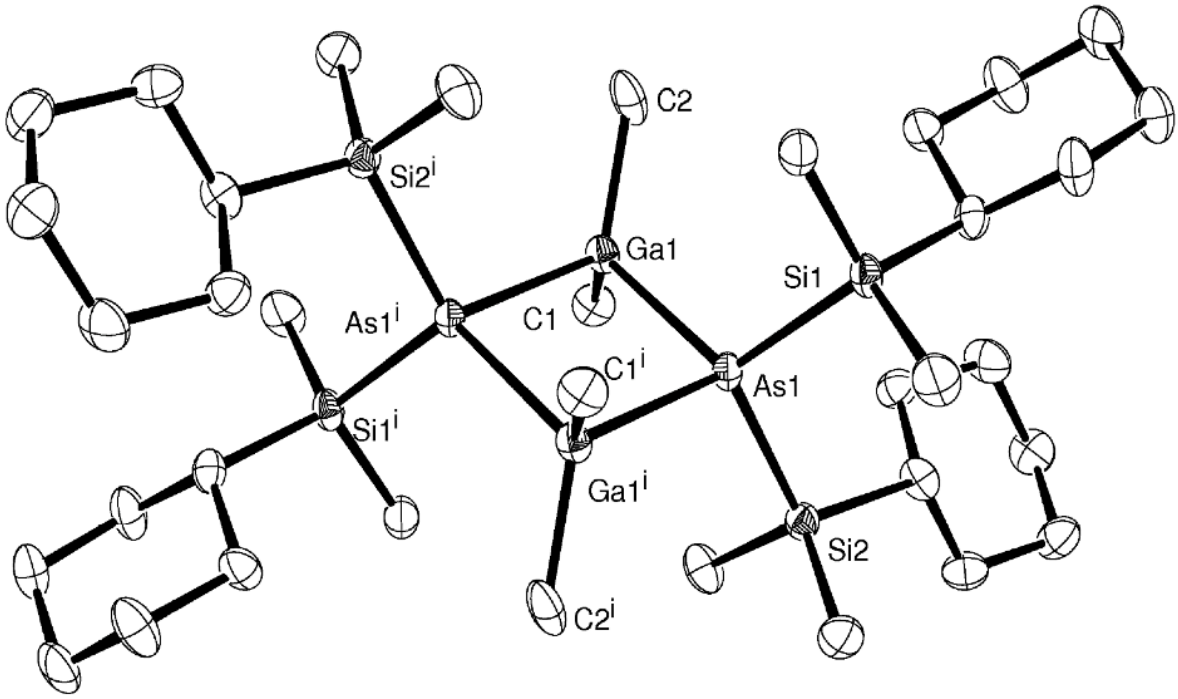

Figure 19: ORTEP representation of 31 with thermal ellipsoids at 50% for probability and H atoms removed for clarity.

$[Me_2GaAs(SiMe_2Cy)_2]_2$ (**31**)	
Empirical formula	$C_{42}H_{94}As_2Ga_2Si_4$
Formula weight	1000.81
Temperature	150(2) K
Wavelength	0.71073 Å
Crystal system	Triclinic
Space group	P-1
Unit cell dimensions	a = 9.145(4) Å α= 91.398(8)°
	b = 9.835(5) Å β= 90.664(8)°
	c = 14.547(7) Å γ = 103.042(8)°
Volume	1274.0(11) $Å^3$
Z	1
Density (calculated)	1.304 Mg/m^3
Absorption coefficient	2.466 mm^{-1}

$[Me_2GaAs(SiMe_2Cy)_2]_2$ (**31**)					
Bond lengths (Å)					
Ga (1)-As(1)	2.5218(14)	Ga(1)-C(1)	1.979(9)	Si(1)-As(1)	2.343(2)
Ga(1)-As(1^i)	2.5328(15)	Ga(1)-C(2)	1.957(9)	Si(2)-As(1)	2.355(3)
Bond Angles (^{o})					
As(1)-Ga(1)-As(1^i)	87.55(5)	Ga(1)-As(1)-Ga(1^i)	92.45(5)		
C(2)-Ga(1)-C(1)	115.5(4)	Si(1)-As(1)-Si(2)	109.44(9)		
C(2)-Ga(1)-As(1)	112.5(3)	Si(1)-As(1)-Ga(1)	116.49(7)		
C(1)-Ga(1)-As(1)	112.3(3)	Si(2)-As(1)-Ga(1^i)	109.55(6)		
C(2)-Ga(1)-As(1^i)	111.1(3)				
C(1)-Ga(1)-As(1^i)	114.6(3)				

Table 1: Crystallographic data for 31 with Selected bond lengths (Å) and bond angles (^{o}).

The crystal structure of **31** shows that a distorted tetrahedral geometry is adopted around the gallium, arsenic and silicon atoms. The average Ga-As bond length is 2.5273(15) Å, which is slightly shorter than the average Ga-As bond length (2.5432(6) Å) in $[Et_2GaAs(SiMe_3)_2]_2$. The average As-Si bond lengths were also shorter in **31** (2.349(3) Å) compared to $[Et_2GaAs(SiMe_3)_2]_2$ (2.3599(11) Å). This trend was also followed with the bond angles with, the As-Ga-As bond angle in **31** being 87.55^o but in $[Et_2GaAs(SiMe_3)_2]_2$ it is 87.77^o.[103] The four membered ring in the centre of the dimer is constrained as the As-Ga-As (87.55^o) and Ga-As-Ga (92.45^o) are smaller than expected. The shorter bond lengths and smaller bond angles of **31** compared to $[Et_2GaAs(SiMe_3)_2]_2$ can be attributed to the more sterically hindered nature of **31**.

Thermogravametric analysis (TGA) was also attempted on this precursor (**31**) to determine it's melting point and decomposition temperature but this was unsuccessful and not informative due the precursor being highly air and moisture sensitive.

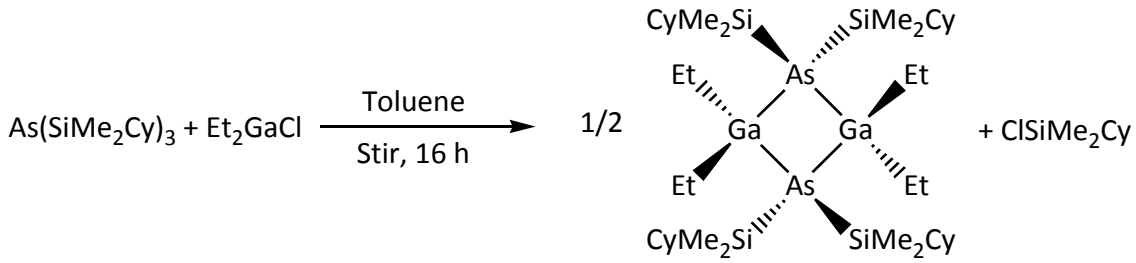

24 **32** (**3.5**)

The reaction of dimethylcyclohexylsilylarsine (**24**) with diethylgallium chloride in hexane resulted in the isolation of $[Et_2GaAs(SiMe_2Cy)_2]_2$ (**32**). Diethylgallium chloride was used instead of triethylgallium to discourage the formation of a 1:1 adduct such as $[GaEt_3\{As(SiMe_3Cy)_3\}]$ since the elimination of the chlorosilane is expected to be more facile. On the addition of Et_2GaCl to $As(SiMe_2Cy)_3$ the mixture was stirred in hexane for 16 h to ensure the reaction went to completion (equation **3.5**). After work-up of the reaction mixture, a colourless oil resulted and, unfortunately attempted recrystallisations in hexane did not yield crystalline material. However, FT-IR analysis of **32** shows the Si-CH_3 peak at 1252.82 cm^{-1}. The ^1H NMR of **32** shows a quartet and triplet at 0.90 ppm and 1.39 ppm, respectively, corresponding to the CH_3CH_2- and CH_3CH_2- protons of Et-Ga group in a 2:3 ratio. Multiple peaks are also seen between 0.90-1.10 and 1.75-2.00 ppm corresponding to Me-As and Cy-As respectively. TGA of **32** was not informative due to the precursor decomposing in the TAG pan by reaction with air and moisture.

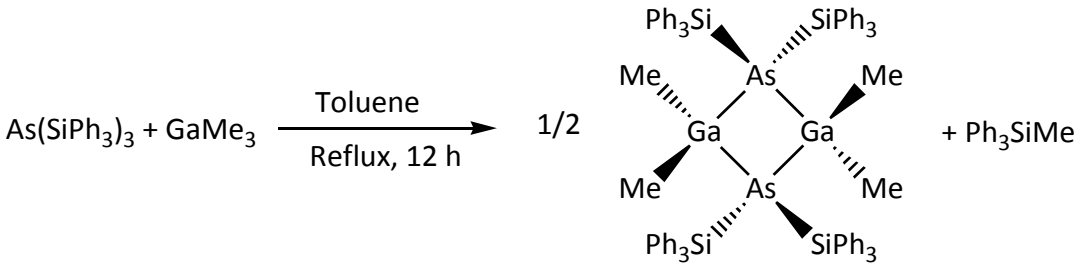

27 **33** (**3.6**)

The triphenyl silylarsine, $As(SiPh_3)_3$, (**27**) was found to be insoluble in hexane and hence the reaction was carried out in toluene. Therefore, trimethylgallium was dissolved in toluene and added dropwise to **27.** The resulting yellow solution was refluxed for 12 h and the solvent removed to obtain a brown solid (equation **3.6**). Elemental analysis carried out on the solid suggests the formation of the expected compound $[Me_2GaAs(SiPh_3)_2]_2$ (**33**). The isolation of **33** was confirmed by ^1H NMR spectroscopy, which shows the presence of the methyl group attached to the gallium at 0.41 ppm and multiplets at 7.00-7.50 ppm corresponding to $SiPh_3$ in the expected ratio. Chemical ion (positive) mass spectrometry was carried out on **33** but the molecular ion was not found. Only a low yield of **33** was obtained, this could be due to the electronic properties of the triphenyl silylarsines. The electronic withdrawing nature of the phenyl groups on the silicon makes the Si-Me bond in the by-product of the reaction weak. The formation of this bond is a factor in driving the reaction forward and hence the reaction may not have gone to completion.

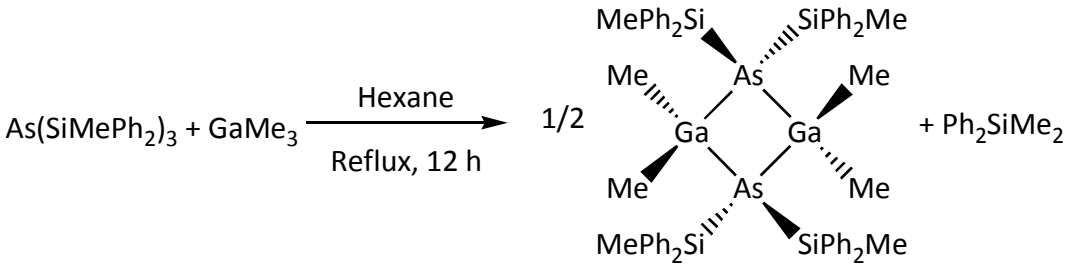

26 **34** (**3.7**)

The reaction between $GaMe_3$ and $As(SiMePh)_3$ (equation **3.7**) was stirred for 16 hours at room temperature, but there was no colour change to indicate that reaction had taken place. Therefore, the reaction was refluxed for a further 12 h at this point. The ^1H NMR analysis carried out on the resulting product (**34**) indicates the presence of methyl groups attached to a gallium at 0.41 ppm, and the methyl and phenyl groups on the silicon at 0.80 ppm and 7.20-2.30, 7.65-7.70 ppm respectively. However, the ratio of the Me group on the gallium is lower than expected, the reasons for which are unclear since the starting materials are colourless liquids and the product is yellow oil a reaction has clearly taken place. Furthermore, $GaMe_3$ is very volatile and would have been

removed *in vacuo* with the solvent if it remained unbound to any other species. Since the methyl groups attached to the gallium appears in the NMR it must be attached to the arsine group. It is not likely that the 1:1 adduct, $[Me_3Ga\{As(SiMePh_2)_3\}]$, has formed as, this would result in the number of gallium methyl groups being more than expected in the NMR spectrum. Mass spectrometry carried out on **34** does not show the presence of the molecular ion. The most likely case is the formation a mixture of products including **34**. Recrystallisation in hexane is being attempted to determine the structure of the product. TGA analysis was not possible due to the highly sensitive nature of 34 to moisture and air.

The synthesis of another class of GaAs precursors was attempted using *tert*-butyl arsine. Firstly, several gallium compounds were synthesised in an attempt to couple them with the arsine. The gallium amides, **35** and **36**, were synthesised under ambient conditions in high yield, the reactions proceed *via* the formation of the LiCl (Equations **3.8** and **3.9**). The formation of **35** was confirmed by a peak at 2.59 ppm corresponding to the methyl group on the non-bridging nitrogens of the dimer and a peak at 2.97 ppm corresponding to the methyl groups on the bridging nitrogens in the proton NMR. The formation of **37** was confirmed by a peak at 2.46 ppm for the methyl groups on the non bridging nitrogens and a peak at 2.92 for the methyl groups on the bridging nitrogens.

$$GaCl_3 + 3\ Li(NMe_2) \xrightarrow[\text{Stir, 12 h}]{\text{Hexane}} 1/2\ [Ga(NMe_2)_3]_2 + 3\ LiCl \quad (\mathbf{3.8})$$

35

$$GaCl_3 + 2\ Li(NMe_2) \xrightarrow[\text{Stir, 12 h}]{\text{Hexane}} 1/2\ [ClGa(NMe_2)_2]_2 + 2\ LiCl \quad (\mathbf{3.9})$$

36

Tert-butyl is seen as a very good ligand for CVD as it decomposes via homolysis to a relatively stable tertiary radical. It is also capable of undergoing β-hydride elimination. As a result *tert*-butyl substituted precursors are able to give GaAs films at lower deposition temperatures. With this in mind, the strategy was to make

$[(Me_2N)_2GaAs^tBuH]_2$, a precursor that should in theory be highly soluble yet without the presence of large organic groups that could result in carbon contamination in the GaAs film.

$$[Ga(NMe_2)_3]_2 + 2\ H_2As^tBu \xrightarrow[\text{Stir, 16 h}]{\text{Hexane}} [(NMe_2)_2GaAs^tBuH]_2 + HNMe_2 \qquad (\mathbf{3.10})$$

35 **37**

Gallium amide (**35**) was mixed with excess *tert*-butyl arsine very slowly at reduced temperature to prevent any decomposition, as shown in equation **3.10**. After the reaction was stirred for 16 h, the solution had turned yellow and a white precipitate had formed. The solution was separated from the precipitate and the solvent removed to obtain a yellow solid. Upon analysis of the solid using NMR spectroscopy it was impossible to confirm the structure of the product. Mass spectrometry was unable to find the molecular ion. Interestingly, elemental analysis carried out on the compound shows the presence of chlorine.

The gallium amide (**35**) used in this reaction was not entirely pure. Therefore, during the synthesis of **35**, it is possible that a mixture of products had formed including $[Ga(NMe_2)_3]_2$, $[ClGa(NMe_2)_3]$ and $[Cl_2Ga(NMe_2)]_2$ (equation **3.9**). When this batch of gallium amide was reacted with As^tBuH_2 the adduct $[Ga(NMe_2)_2Cl\{As^tBuH_2\}]$ may have formed.

$$[Ga(NMe_2)_3]_2 + 2\ H_2As^tBu \xrightarrow[\text{2. Reflux, 4.5 h}]{\text{1. Hexane/stir, 16 h}} [(NMe_2)_2GaAs^tBuH]_2 + HNMe_2$$

35 **38** (**3.11**)

In an effort to produce compound **38** and avoid the adduct, pure gallium amide (**35**) was produced. This was then reacted with *tert*-butyl arsine as indicated in equation **3.11**. ^1H NMR analysis on the product showed that the desired compound **39** had not formed.

Singlet peaks in the proton NMR were observed at 1.66, 1.70, 1.90, 2.06, 2.19, 2.78, 2.81 and 2.86 ppm suggests the formation of a mixture of products.

Therefore another type of precursor to GaAs was attempted using amido arsine and trimethylgallium. The two reagents were mixed, with a slight excess of the arsine and refluxed in dichloromethane for 18 hours, as shown in equation **3.12** The expected product was the dimer **39** formed *via* the elimination of the trimethylamine.

$$As(NMe_2)_3 + GaMe_3 \xrightarrow[\text{Reflux, 18 h}]{CH_2Cl_2} 1/2\,[Me_2GaAs(NMe_2)_2]_2 + NMe_3$$

39 (**3.12**)

However, upon analysis of the product it was realised that the intended product **39** had not formed. Instead a simple ligand transfer has taken place to yield $[Me_2Ga(NMe_2)]_2$ (**40**) and $[MeAs(NMe_2)_2]$, with the latter being removed *in vacuo* with the solvent on workup of the reaction (equation **3.13**). This was confirmed by ^{1}H NMR where two single peaks corresponding to $GaMe_2$ at -0.12 ppm and $GaNMe_2$ at 2.26 ppm of equal intensity were observed. Also, the elemental analysis, which found C, 32.58; H, 8.34; N, 9.26% corresponds to what is expected for $[Me_2Ga(NMe_2)]$ C, 33.38; H 8.41; N, 9.74%. Further conclusive evidence was obtained by single crystal X-ray crystallography (Figure 20).

$$As(NMe_2)_3 + GaMe_3 \longrightarrow 1/2\,[Me_2Ga(NMe_2)]_2 + MeAs(NMe_2)_2$$

40 (**3.13**)

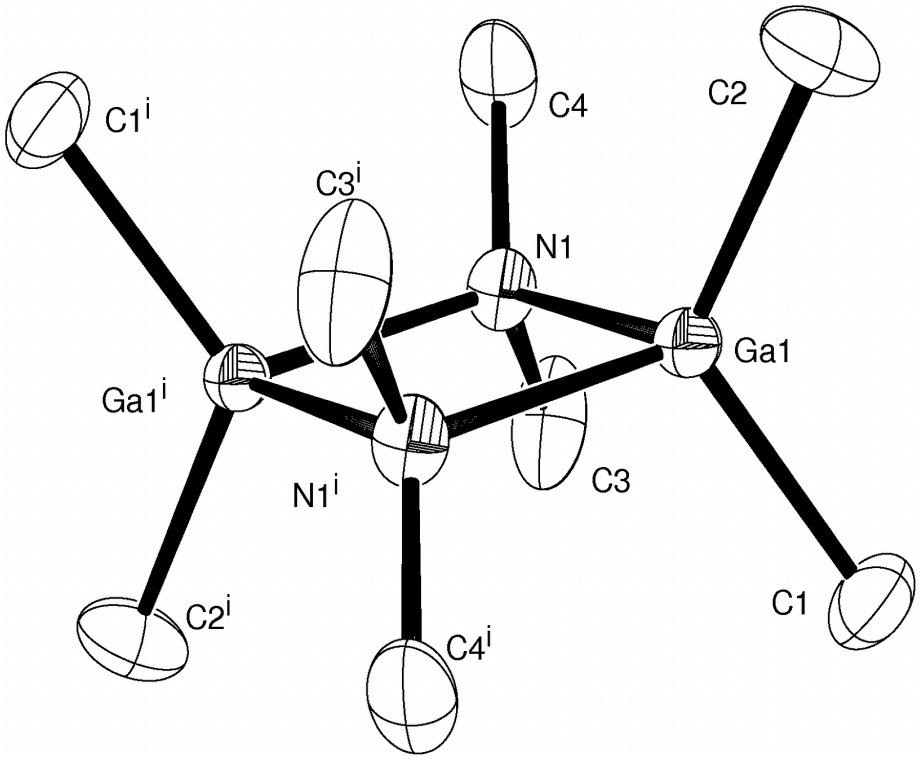

Figure 20: ORTEP representation of 40 with thermal ellipsoids at 50% for probability and H atoms removed for clarity

$[Me_2NGaMe_2]_2$ (**31**)	
Empirical formula	$C_8H_{24}Ga_2N_2$
Formula weight	287.73
Temperature	120(2) K
Wavelength	0.71073 Å
Crystal system	Monoclinic
Space group	$P\text{-}2_{1/n}$
Unit cell dimensions	a = 7.4426(2) Å α= 90°
	b = 8.0294(3) Å β= 99.386(2)°
	c = 11.2896(2) Å γ = 90°
Volume	665.63(3) $Å^3$

Table 2: Crystallographic data for 40

$[Me_2NGaMe_2]_2$ (**40**)			
Bond Lengths (Å)			
C(1)-Ga(1)	1.969(2)	N(1)-Ga(1)	2.0180(15)
C(2)-Ga(1)	1.966(2)	N(1)-Ga(1)#1	2.0202(17)
C(3)-N(1)	1.480(3)	Ga(1)-N(1)#1	2.0202(17)
C(4)-N(1)	1.472(3)	Ga(1)-Ga(1)#1	2.9125(4)
Bond Angles (°)			
C(4)-N(1)-C(3)	109.41(19)	C(1)-Ga(1)-N(1)	110.05(9)
C(4)-N(1)-Ga(1)	114.47(14)	C(2)-Ga(1)-N(1)#1	111.68(9)
C(3)-N(1)-Ga(1)	113.30(13)	C(1)-Ga(1)-N(1)#1	110.66(9)
C(4)-N(1)-Ga(1)#1	113.28(13)	N(1)-Ga(1)-N(1)#1	87.69(7)
C(3)-N(1)-Ga(1)#1	113.32(14)	C(2)-Ga(1)-Ga(1)#1	121.11(8)
Ga(1)-N(1)-Ga(1)#1	92.31(7)	C(1)-Ga(1)-Ga(1)#1	118.84(7)
C(2)-Ga(1)-C(1)	120.05(11)	N(1)-Ga(1)-Ga(1)#1	43.87(5)
C(2)-Ga(1)-N(1)	112.08(9)	N(1)#1-Ga(1)-Ga(1)#1	43.81(4)

Table 3: Selected bond lengths and angles for 40.

Gallium monoamides, of type $[R_2GaNR'_2]_n$ (R = halide, allyl, aryl) have been previously reported and most are dimeric or trimeric depending on the substitutent steric requirements as well as entropy factors and ring strain. Compounds of this type have been prepared *via* various methods including amine elimination and salt metathesis. Amido compounds of gallium have been reviewed in detail by Carmalt.[104]

A similar observation has been reported previously in the literature for the reactions of $AlMe_3$ with Me_2AsNMe_2, $MeAs(NMe_2)_2$ and $As(NMe_2)_3$.[105,106] These reactions were studied as a function of time at room temperature as well as low temperature and analysed using $^1H/^{13}C$ NMR. The immediate formation of a 1:1 adduct was observed in all cases although numerous competing side reactions involving aminoarsine/adduct exchange also occurred. Both an Al-As bonded adduct, $[Me_3Al\{As(NMe_2)_3\}]$, as well as the mono and bis Al-N adducts, $[(Me_2N)_2AsNMe_2.AlMe_3]$ and $[Me_2NAs(NMe_2.AlMe_3)_2]$ were observed. The bis adduct readily decomposes and the Al-As bonded adduct dissociates at low temperature. The Al-N bonded adducts were

found to decompose by a pathway that transfers a methyl group from the Al to the As atom, cleaving the As-N bond and yielding species of the type $[Me_xAs(NMe_2)_{3-x}]$ (x = 1-3) similar to compound **40**. The end products of the reaction of $AlMe_3$ and $As(NMe_2)_3$ were found to include $[Me_2AlNMe_2]_2$ Me_2AsNMe_2, $MeAs(NMe_2)_2$ or Me_3As.

Based on the previous study of $Me_3Al/As(NMe_2)_3$ it seemed likely that reactions involving $As(NMe_2)_3$ and $GaMe_3$ would undergo ligand transfer. To investigate this further a time variable ^1H and ^{13}C NMR study of the reaction of $As(NMe_2)_3$ and $GaMe_3$ in C_6D_6 was undertaken.[105,106]

Therefore, precursors $As(NMe_2)_3$ and $GaMe_3$ were mixed in 1:1 ratio in deuterated benzene in an airtight NMR tube. The course of the reaction was followed by monitoring the disappearance of reactant peaks from $As(NMe_2)_3$ and $GaMe_3$ and the appearance of new peaks corresponding to new reaction products.

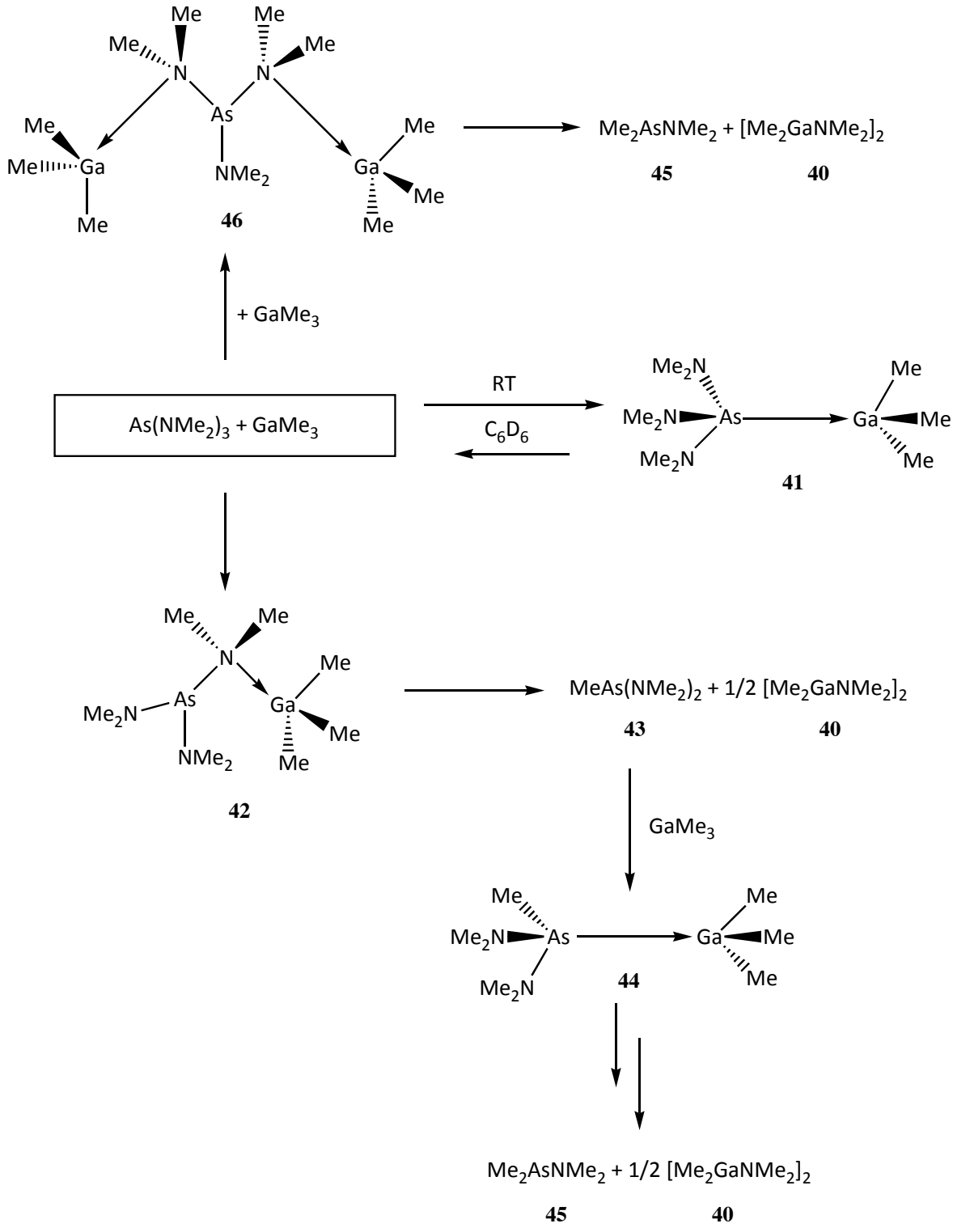

Scheme 6: Schematic showing the possible products of the NMR reaction experiment.

The $^{1}H/^{13}C$ NMR spectra taken after 5 minutes of mixing $Me_3Ga/As(NMe_2)_3$ show peaks indicating the immediate formation of the 1:1 adduct $[Me_3Ga\{As(NMe_2)_3\}]$ **(41)**. The peak at -0.13 ppm in ^{1}H NMR and at -5.2 ppm in the ^{13}C NMR indicates that the $GaMe_3$ (which unreacted has a ^{1}H shift of 0.14 ppm and ^{13}C shift of -1.1 ppm) has reacted with the arsine and formed adduct **41** (Scheme 6). Relating this to work carried out by Krannich *et al*. on related aluminium reactions supports the formation of a As-Ga bonded adduct, $[Me_3Ga\{As(NMe_2)_3\}]$. Furthermore, the major peak in the ^{1}H NMR in the $As(NMe_2)_3$ region (after 5 minutes of mixing) was observed at 2.42 ppm which represents an upfield shift of 0.21 ppm, as the peak for unreacted $As(NMe_2)_3$ appears at 2.61 ppm. The major peak in the ^{13}C NMR in the As-NMe_2 region for the mixture was at 40.3 ppm, whereas unreacted $As(NMe_2)_3$ has a single peak at 39.5 ppm. Though the shift is small (downfield by 0.81 ppm) it still supports the hypothesis for an initial 1:1 adduct formation. Table 4 provides a summary of the ^{1}H and ^{13}C NMR data for $GaMe_3$, $As(NMe_2)_3$ and compounds **40** - **45**.

In the ^{1}H NMR of the $Me_3Ga/As(NMe_2)_3$ mixture taken after 5 minutes there were also minor peaks assignable unreacted to $GaMe_3$ and $As(NMe_2)_3$. It is likely that adduct **41** readily dissociates at room temperature and so the presence of free $GaMe_3$ and $As(NMe_2)_3$ was expected.

Due to the presence of additional peaks as a result of unreacted reagents, the ^{1}H spectra, were studied over a longer time period. After 45 minutes of the reagents mixing in the NMR tube, the $^{1}H/^{13}C$ NMR spectra showed very little difference to the initial NMR obtained after 5 minutes. However, some minor peaks were present in the ^{1}H NMR (45 mins) at -0.18 ppm, 0.87 ppm, 1.04 ppm, 2.16 ppm, 2.22 ppm and 2.30 ppm. In the ^{13}C NMR for the 45 min solution, there were no new peaks compared to the 5 minute spectrum, suggesting that these new products were in low concentrations after 45 minutes. However, decomposition of **41** and consumption of $As(NMe_2)_3$ proceeds with time (see below) resulting in mixtures of Me_2AsNMe_2 (**43**), $MeAs(NMe_2)_2$ (**45**), $As(NMe_2)_3$ and $[Me_2GaNMe_2]_2$ (**40**) as well as other species.

In order to investigate the competing reactions, further $^{1}H/^{13}C$ NMR spectra were taken after 17.5 hours of the $Me_3Ga/As(NMe_2)_3$ solution being in the NMR tube. Both $^{1}H/^{13}C$ spectra look similar to the 5 minute/45 minute experiment and the 1:1 adduct is still present. However further peaks were apparent at 0.88 ppm and 1.04 ppm in the ^{1}H

NMR and at 12.8 ppm and 14.2 ppm in ^{13}C NMR, which correspond to Me-As bond formation. This suggests that ligand scrambling has occurred between $GaMe_3$ and $As(NMe_2)_3$ to form $MeAs(NMe_2)_2$ (**43**) and $MeAs(NMe_2)_2$ (**45**) based on the previous work by Krannich *et al*.[105,106] Peaks were also observed in ^1H NMR (17.5 hours) at 2.17 ppm and 2.22 ppm corresponding to As-NMe_2 (**43** and **45**) groups and -0.13 ppm corresponding to Me-Ga groups (**41**). There was also peaks at -6.2 ppm for Me-Ga in the ^{13}C NMR suggesting the formation of another adduct, $[(Me_2N)_2AsNMe_2{:}GaMe_3]$ (**42**). This adduct explains some of the intensity ratios observed in the ^1H NMR. The initial adduct, $[Me_3Ga\{As(NMe_2)_3\}]$ (**41**) was still present as the major product and $[(Me_2N)_2AsNMe_2{:}GaMe_3]$ the minor. In fact it is likely that compounds **43** and **45** are formed *via* the N-bonded adduct **42**, as depicted in Scheme 6. Decomposition of **42** would initially result in the formation of $MeAs(NMe_2)_2$ (**43**) and **40**, $[Me_2GaNMe_2]_2$. However, further reactions of **43** with any unreacted $GaMe_3$ would initially result in the adduct $[\{MeAs(NMe_2)_2\}GaMe_3]$ (**44**) (not detected) which on decomposing would yield Me_2AsNMe_2 (**45**) and **40**. Alternatively, **45** could be the result of decomposition of the bis Ga-N bonded adduct **46** (Table 4). In the 17.5 hour experiment there is a peak at -0.94 ppm which cannot be assigned to any species.

The ^1H and ^{13}C NMR spectra of the $Me_3Ga/As(NMe_2)_3$ mixture after 24 hours looks very similar to those observed after 17.5 hours. The intensity of the peaks had not changed from 17.5 hours to 24 hours, however the unassigned peak observed at -0.94 ppm in the 17.5 hour spectrum is not present in the 24 hour spectrum. The ^{13}C NMR spectra look exactly the same for both time experiments.

After 44 hours the major product in the $Me_3Ga/As(NMe_2)_3$ reaction mixture was the N-bonded adduct $[(Me_2N)_2AsNMe_2{:}GaMe_3]$ **42** rather than the As-bonded adduct **43**. Therefore peaks at -0.14, 2.17 ppm and 2.22 ppm in ^1H NMR have increased in intensity and corresponds to Me-Ga, As-NMe_2 and As-μ-NMe_2 respectively (assigned based on analogous Al compound reported by Krannich *et al*.[105,106] Similarly, a peak at -6.20 ppm for Me-Ga and 39.5 and 43.4 ppm for As-NMe_2 were observed in ^{13}C NMR. An additional peak was observed in the ^{13}C NMR at 20.5 ppm, which could not be assigned.

In the 45 minute NMR experiment there was also a peak at 2.17 ppm in the ^1H NMR corresponding to the NMe_2 group present in the dimeric compound $[Me_2Ga(NMe_2)]_2$

(**40**). This peak increases in intensity throughout the NMR experiment suggesting that the concentration of compound **40** is increasing with time. However, a peak at -0.23 ppm corresponding to Ga-Me in **40** was not observed in ^{1}H NMR until after a spectrum was recorded after two weeks. $^{1}H/^{13}C$ NMR spectra were also collected after 44 hours, 1 week and 2 weeks. It is possible that **40** has also formed an adduct which would cause a shift to this peak. However, in the ^{13}C NMR (44 hours) the peaks corresponding to **40** at -10.5 ppm (for the GaMe groups) and 43.4 ppm (NMe_2 groups) were present in spectra run from 44 hours onwards.

Also, peaks at 1.94 ppm and 2.49 ppm in the ^{1}H NMR for the one week experiment were not present in the previous experiments. However a peak at -0.17 ppm seen in the 44 hour NMR experiment has fully disappeared in the one week experiment. This peak is present in the 24 hour experiment but the intensity is very small. Interestingly, a peak seen at 2.49 ppm in the 1 week experiment is not seen in any of the other experiments. This peak is in the region corresponding to NMe_2 group. The intensity of the minor peaks has increased further in the ^{1}H NMR and there are also new peaks observed at -0.25 ppm and -0.11 ppm.

After one month there were no peaks in the ^{1}H and ^{13}C NMR spectra corresponding to the adducts seen previously, [$Me_3Ga{:}As(NMe_2)_3$] (**41**) and [$(Me_2N)_2AsNMe_2GaMe_3$] (**42**) (indicated by the disappearance of the -6.20 ppm and 14.1 ppm peaks in the ^{13}C NMR). Both the ^{1}H and ^{13}C NMR spectra for the 1 month experiment was clearer than previous spectra with less peaks observed. After 1 month, the major product was the dimeric compound $[Me_2Ga(NMe_2)]_2$ (**40**) as seen by peaks at -0.23 and 2.18 ppm in the ^{1}H NMR corresponding to Me_2Ga- and -NMe_2 respectively. The ^{13}C NMR also provides evidence for the formation of **40** as seen by peaks at -10.5 and 43.4 ppm. The other identifiable remaining species were **43** and **45** (Table 4).

	δ_C (ppm)			δ_H (ppm)		
Compound	Me_2N	MeAs	MeGa	Me_2N	MeAs	MeGa
$As(NMe_2)_3$	39.5			2.61		
$GaMe_3$			-1.1			0.14
40	43.4		-10.5	2.18		-0.23
41	40.3		-5.2	2.42		-0.13
42	42.1		-6.2	2.17		-0.14
				2.22		
43	Not detected			2.17	0.88	
44	Not detected					
45	Not detected			2.22	1.04	

Table 4: ^{1}H and ^{13}C NMR data for compounds 41 to 46.

Therefore, analysis of the room temperature NMR spectral data for the $Me_3Ga/As(NMe_2)_3$ reaction suggests that $As(NMe_2)_3$ initially forms a Ga-As bonded adduct, **41** and the mono Ga-N bonded adduct **42**. Additional peaks also suggest that the bis Ga-N bonded adduct **46** may form as a very minor product. Similar adducts were observed to form in the reaction of $Me_3Al/As(NMe_2)_3$ and related $BH_3.THF/As(NMe_2)_3$ systems.[105,106,107] The Ga-As adduct **41** is expected to be relatively unstable to dissociation and hence $GaMe_3$ and $As(NMe_2)_3$ would also be present. The Ga-N bonded adducts decompose *via* a pathway that cleaves the As-N bond with transfer of a methyl group from Ga to As. The actual mechanism could not be determined from these NMR studies but it is possible that it involves a four-membered transition state species with simultaneous bond cleavage and formation of the As-Me bonds. The Ga-N bonded adducts decompose to yield $MeAs(NMe_2)_3$, $Me_2As(NMe_2)$ and $[MeGaNMe_2]_2$ thus supporting the formation of **40**, the structure of which was determined *via* X-Ray

crystallography. The reaction of $As(NMe_2)_3$ and $GaMe_3$ is further complicated by the presence of compounds **41**-**46** which can also take part in separate exchange averaging, competing side reactions and decomposition, hence the presence of other minor peaks in the NMR which were difficult to assign. Many of these reactions are depicted in Scheme 6. The final products of these reactions were $[Me_2GaNMe_2]_2$ and $Me_xAs(NMe_2)_{3-x}$.

These solutions based NMR studies are important as they can offer an insight into the types of species present in the AACVD reactions involving $Me_3Ga/As(NMe_2)_3$ described in Chapter 4. It is possible that adduct formation and scrambling of ligand are key to these compounds eventually decomposing to GaAs.

The amino and silyl arsine based single-source compounds (**31**-**34**) were found to be poor precursors for AACVD. Many attempts were made to deposit GaAs thin films using these compounds but to no avail as it was difficult to transfer the precursor across in the aerosol into the CVD chamber.

Therefore another route was attempted to synthesise precursors using tertiary butyl arsine (^{t}BuAsH$_2$) and $GaMe_3/GaEt_3$. A 21 hour stir of ^{t}BuAsH$_2$ and GaR_3 (R = Me, Et) at 80 ^{o}C in toluene resulted in a yellow solution (equation **3.14**). A yellow solid was obtained when the solvent was removed in *vacuo*. Colourless crystals were obtained when the yellow solid was dissolved in minimum solvent and cooled to below room temperature. Single crystal X-ray diffraction was attempted but with no success as the diffraction pattern could not be solved. The Signer method, which is a technique to determine the molecular mass of a species with reference to a standard (in this case ferrocene), was attempted to determine the molecular mass of **47** and **48** but with no success as they kept decomposing.[108]

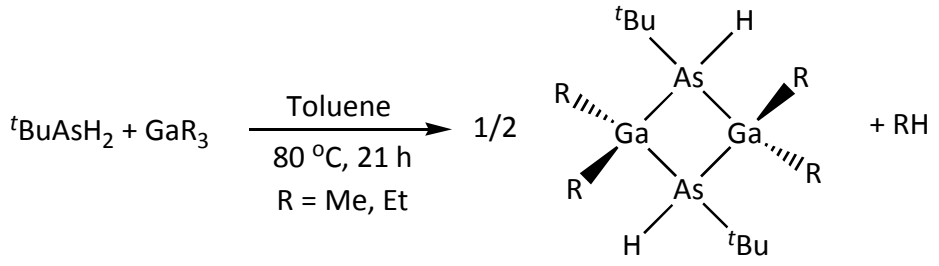

47, R = Me (**3.14**)

48, R = Et

The ^{1}H NMR of $[Me_2GaAs(H)^tBu]_2$ **47** showed 4 major peaks, two of which (0.02 ppm and 0.08 ppm) correspond to the two methyl groups on the gallium. Both of these peaks intergrate to 3 protons with respect to the AsH peak observed at 2.56 ppm, which is equivalent to 1 proton. The peak for the tertiary butyl group appeared at 1.43 ppm and corresponds to 9 protons as expected. Minor peaks were observed at 0.47 ppm, 1.35 ppm and 1.58 ppm which are believed to correspond to rearranged products in the NMR solvent possibly the trimer $[Me_2GaAs(H)^tBu]_3$. Mass spectrometry carried out on $[Me_2GaAs(H)^tBu]_2$ did not show the molecular ion but the presence of other fragments such as $[MeGaAs(H)^tBu]_2$ at 437, $[GaAs(H)^tBu]_2$ at 435 and $[MeGa(H)^tBu]_2$ at 451 were observed. Elemental analysis carried out on **47** found 28.9% carbon and 6.6% hydrogen which matches with the expected values of 30.93% carbon and 6.93% hydrogen. The analysis therefore supports the formation of **47** although same impurities maybe present.

The ^{1}H NMR for $[Et_2GaAs(H)^tBu]_2$ (**48**), shows the expected peaks at 0.86-1.01 corresponding to the $-CH_2$ of the ethyl groups attached to the gallium and a peak at 1.35 ppm for the ^{t}Bu group. There are also peaks at 1.39-1.47 ppm and 2.31 corresponding to the $-CH_3$ group of the ethyl attached to the gallium and to the AsH group respectively and all in the correct ratio. Mass spectrometry carried out on **48** does not show the molecular ion but it does however show the peaks for some fragments including $[Et_2GaAs(H)C(CH_3)]_2$ at 493.

3.1.3 Conclusion

Single-source precursors are excellent route to thin films as they contain all the required elements of the film contained in the precursor, usually in the desired ratio. This is advantageous as it reduces the deposition temperature and enables the production of stiochiometric films. Therefore a variety of single-source compounds have been synthesised as precursors to GaAs.

Trisodium arsenide (**23**), was synthesised by the reaction of sodium with arsenic powder (Equation **3.1**). Then it was then reacted with a range of silyl chlorides to produce silyl arsines of the type $As(SiR_2R'_3)$ (equation **3.2**), these were then coupled with trimethygallium, triethylgallium and diethylgallium chloride to produce single source precursors: $[Me_2GaAs(SiMe_2Cy)_2]_2$ (**31**), $[Et_2GaAs(SiMe_2Cy)_2]_2$ (**32**), $[Me_2GaAs(SiMePh_2)_2]_2$ (**33**) and $[Me_2GaAs(SiPh_3)_2]_2$ (**34**).

The synthesis of precursors *via* the reaction of $As(NMe_2)_3$ and $GaMe_3$ was attempted but due to ligand scrambling reactions taking place only $[Me_2NGaMe_2]_2$ (**41**) was isolated. NMR studies revealed a range of adducts being formed in solution with one of the final products being **41** (Scheme 6).

Another class of single-source precursors of the type $[R_2GaAs(H)^tBu]_2$ **47** and **48,** were also synthesised as they contained tertiary butyl groups that are know to undergo β-hydride elimination, which is ideal for AACVD.

3.1.4 General Procedure

All reactions were carried out under moisture- and oxygen-free, nitrogen atmosphere using standard Schlenk techniques or in an Mbraun Unilab glovebox. All reagents were purchased from Aldrich or Alfa Aesar and used as received without any modifications. Trimethylgallium, triethylgallium, tert-butylarsine and $As(NMe_2)_3$ were purchased from SAFC Hitech and used as received without any modifications. All solvents were stored in alumina columns and dried with anhydrous engineering equipment.

All yields quoted are isolated yields. ^1H NMR spectra were recorded at 400 MHz or 500 MHz and ^{13}C NMR at 100 MHz or 125 MHz on Oxford instrument 400/ Bruker AMX 500 (respectively) at ambient temperature. Deuterated benzene was distilled from solutions of sodium benzophenone ketyl. The chemical shifts (δ) for ^1H and ^{13}C are quoted in ppm relative to residual signals of the solvent. Coupling constants (*J*) are expressed in Hz and approximated to the nearest 0.5 Hz. Microanalytical data were obtained at University College London (UCL). The elemental analysis was carried out using Elemental Analyser (CE-440) (Exceter Analytical Inc.). FT-IR spectra were recorded on a Perkin Elmer Spectrum RX I instrument, over the range 4000-400 cm^{-1} either neat or in nujol between KBr disks. Mass spectra were obtained on a VG70-SE mass spectrometer using chemical ionisation (CI) with methane reagent gas. For crystal structures, geometric and intensity data were obtained on Bruker SMART APEX CCD diffractometer using graphite-monochromated Mo-Kα radiation (λ_1 = 0.71073 Å) at 150(2) K. Data reduction and integration was carried out with SAINT+[109] and absorption corrections applied using SADABS.[110] All solutions and refinements were performed using PLATON[111] and the WinGX package and all software packages within.[112] Hydrogen atoms were placed in geometrically assigned positions with fixed bond lengths of 0.95 Å (aromatic CH) and 0.98 Å (CH_3). These were refined using a riding model with a $U_{iso}(H)$ value of 1.2 U_{eq} (CH) or 1.5 U_{eq} (CH_3) of the parent atom.

3.1.5 Na_3As (23)

Sodium lumps (3.68 g, 160.2 mmol) were added to arsenic powder (4.00 g, 53.4 mmol) in THF (*ca.* 40 mL). The black mixture was refluxed. After 48 hours the black sodium arsenide powder was allowed to settle and the solvent decanted. The remaining solvent was removed *in vacuo* to yield a fine black powder (7.23 g, 50.2 mmol, 94%).

3.1.6 As(SiMe$_2$Cy)$_3$ (24)

Chlorocyclohexyldimethylsilane (5.53 g, 31.3 mmol) in THF (*ca.* 15 mL) was added dropwise to a stirring suspension of trisodium arsenide (1.50 g, 10.42 mmol) in THF (*ca.* 20 mL). The mixture was refluxed for 16 h. The solvent was removed *in vacuo* and the black solid washed with dry toluene (*ca.* 40 mL). The solid was allowed settle and the yellow solution was decanted off and dried *in vacuo* to yield a yellow oil (4.33 g, 8.7 mmol, 83%). ^{1}H NMR (C_6D_6): δ 0.29 (s, 18 H, Si*Me*$_2$Cy), 1.10-1.90 (m, 33H, SiMe$_2$*Cy*). ^{13}C{^{1}H} NMR (C_6D_6): δ -0.5 (Si*M*e$_2$Cy), 26.6 (SiMe$_2$*Cy*), 26.8 (SiMe$_2$*Cy*), 27.8 (SiMe$_2$*Cy*), 28.2 (SiMe$_2$*Cy*). IR (neat, cm^{-1}): 3086.8 (vw), 3027.9 (vw), 2913.2 (vs), 2849.2 (vs), 2667.4 (w), 1941.2 (vw), 1605.1 (w), 1496 (w), 1477.1 (vs), 1405.5 (s), 1354.8 (m), 1326.9 (m), 1292 (m), 1252.7 (vs), 1188.4 (m), 1169.9 (s), 1101.7 (vs), 1072.2 (s), 1038.1 (s), 996.2 (s), 910.76 (s), 889.5 (vs), 853.6 (vs), 840.5 (vs), 818.4 (vs), 801.5 (vs), 782.9 (vs), 728.9 (s), 694.4 (m), 667.6 (m), 653.7 (s), 510.9 (vs), 483.1 (vs), 428.6 (w).

3.1.7 As(SiMe$_2$Ph)$_3$ (25)

Chlorodimethylphenylsilane (3.05 g, 17.9 mmol) in THF (*ca.* 15 mL) was added dropwise to a stirring suspension of trisodium arsenide (0.80 g, 5.6 mmol) in THF (*ca.* 20 mL). The mixture was refluxed for 16 h. The solvent was removed *in vacuo* and the black solid washed with dry toluene (*ca.* 40 mL). The solid was allowed to settle and the yellow solvent was decanted off and concentrated to yield a yellow oil (2.11 g, 4.4 mmol, 79%). Anal. Calc. for $C_{24}H_{33}AsSi_3$: C, 59.97; H, 6.92.% Found: C, 55.43; H, 6.82%. ^{1}H NMR (C_6D_6): δ 0.49 (s, 9 H, Si*Me*Ph$_2$), 7.21-7.23 (m, 18 H, SiMe*Ph$_2$*), 7.67-7.69 (m, 12 H, SiMe$_2$*Ph*). ^{13}C{^{1}H} NMR (C_6D_6): δ 2.0 (Si*M*e$_2$Ph), 129.0 (*m*-C of SiMe$_2$*Ph*), 133.9 (*p*-C of SiMe$_2$*Ph*), 140.2 (*o*-C of SiMe$_2$*Ph*). IR (cm^{-1}): 3063.6 (vw), 2958(vs), 2925.2 (vs), 2854.6 (vs), 2361.8 (w), 2343.9 (w), 1946.9 (vw), 1876.9 (vw), 1815.4 (vw), 1586.0 (vw), 1460.3 (s), 1426.3 (m), 1377.5 (s), 1311.9 (vw), 1300.4 (vw), 1250.0 (m), 1191.6 (vw), 1155.2 (vw), 1109.9 (m), 1093.7 (m), 162.9 (w), 1040.6 (w), 998.6 (vw), 965.0 (vw), 872.7 (w), 832.2 (s), 805.5 (s), 772.2 (m), 735.7 (s), 699.6 (s), 69.6 (m), 495.1 (vw), 470.8 (w).

3.1.8 As(SiMePh$_2$)$_3$ (26)

Chloro(methyl)diphenylsilane (3.76 g, 16.1 mmol) in THF (*ca.* 15 mL) was added dropwise to a stirring suspension of trisodium arsenide (0.76 g, 5.3 mmol) in THF (*ca.*

20 mL). The mixture was refluxed for 16 h. The solvent was removed *in vacuo* and the black solid washed with dry toluene (*ca.* 40 mL). The solid was allowed to settle and the yellow solvent was decanted off and concentrated to yield a yellow oil (2.94 g, 4.4 mmol, 84%). ^{1}H NMR (C_6D_6): δ 0.49 (s, 18 H, Si*Me*Ph_2), 7.23-7.28 (m, 33H, $SiMe_2$*Ph*), 7.61-7.63 (m, 2 H, SiMe*Ph*$_2$) . ^{13}C{^{1}H} NMR (C_6D_6): δ 0.6 (Si*M*ePh_2), 130.5 (*o*-C of SiMe*Ph*$_2$), 134.2 (*m/p*-Cs of SiMe*Ph*$_2$). IR (cm^{-1}): 3070.6 (m), 3050.6 (m), 2963.3 (m), 1958.0 (w), 1888.1 (w), 1818.2 (w), 1776.2 (w), 1655.9 (w), 1590.1 (m), 1546.9 (w), 1479 (m), 1429.1 (vs), 1406.5 (m), 1381.8 (w), 1337.1 (w), 1304.9 (w), 1258.7 (s), 1189.8 (m), 1119.8 (vs), 1110 (vs), 1027.6 (m), 917.5 (w), 798.7 (vs), 783.2 (vs), 730.1 (vs), 696.5 (vs), 675.2 (m), 517.3 (vs), 474.6 (s), 436.1 (s).

3.1.9 As(SiPh$_3$)$_3$ (27)

Chlorotriphenylsilane (2.46 g, 8.3 mmol) in THF (*ca.* 15 mL) was added dropwise to a stirring suspension of trisodium arsenide (0.40 g, 2.8 mmol) in THF (*ca.* 20 mL). The mixture was refluxed for 16 h. Solvent was removed *in vacuo* and the black solid washed with dry toluene (*ca.* 40 mL). The solid was allowed to settle and the yellow solution was decanted off and concentrated to yield a yellow solid (2.73 g, 3.2 mmol, 92%). Anal. Calc. for $C_{54}H_{45}AsSi_3$: C, 76.02; H, 5.32%. Found: C, 72.74; H, 5.24%. ^{1}H NMR (C_6D_6): δ 7.02-7.25 (m, 45 H, Si*Ph*$_3$). ^{13}C{^{1}H} NMR (C_6D_6): δ 129.3 (Si*Ph*$_3$), 136.9 (Si*Ph*$_3$). IR (cm^{-1}): 3042.0 (vw), 2958 (s), 2923.4 (s), 2854.5 (s), 2728.3 (vw), 2677.9 (vw), 2358.7 (w), 2341.7 (w), 2070.1 (w), 1958 (w), 1893.7 (w), 1821 (w), 1776.2 (w), 1664.3 (vw), 1586.5 (w), 1567.3 (w), 1464 (s), 1427.5 (s), 1378.1 (s), 1328.7 (vw), 1305.1 (w), 1260.2 (m), 1185.3 (m), 1157.4 (w), 1104.3 (s), 1093.7 (s), 1027.8 (m), 998.3 (m), 979.0 (vw), 920.3 (w), 853.1 (vw), 802.6 (m), 733.6 (s), 697.4 (vs), 676.0 (s), 619.6 (w), 553 (w), 52.5 (w), 500.7 (vs), 493.9 (vs), 455.5 (w).

3.1.10 As(Si^{t}BuPh$_2$)$_3$ (28)

Tert-butyldiphenylarsine (5.73 g, 20.9 mmol) in THF (*ca.* 15 mL) was added dropwise to a stirring suspension of trisodium arsenide (1.00 g, 6.9 mmol) in THF (*ca.* 20 mL). The mixture was refluxed for 16 h. The solvent was removed *in vacuo* and the black solid washed with dry toluene (*ca.* 40 mL). The solid was allowed to settle and the yellow solution was decanted off and concentrated *in vacuo* to yield a yellow oil (4.48 g, 5.6 mmol, 81%). ^{1}H NMR (C_6D_6): δ 1.14 (s, 27 H, As(Si^{t}*Bu*Ph$_2$)), 1.22 (s, 12.5 H), 7.25-7.28 (m, 30 H, As(Si^{t}Bu*Ph*$_2$)), 7.89-7.91 (m, 5 H), 7.94-8.00 (m, 12 H). ^{13}C{^{1}H}

NMR (C_6D_6): δ 26.4 (Si*C*$(CH_3)_3$, 29.2 (SiC(*C*$H_3)_3$), 128.9, 135.4, 136.8, 137.7 (As(Si^{t}Bu*Ph*$_2$)). IR (cm^{-1}, nujol): 3072 (w), 3050.5 (w), 2924.4 (vs), 2856.3 (vs), 1952.4 (w), 1893 (w), 1815.4 (w), 1773.4 (w), 1655.9 (vw), 1588.9 (w), 1486.5 (s), 1468.9 (vs), 1427.9 (vs), 1390.3 (m), 1378.1 (m), 1363.8 (m), 1328.7 (vw), 1309.1 (vw), 1261.9 (w), 1195.8 (s), 1111.7 (vs), 1097.2 (vs), 1068.5 (w), 1029.9 (w), 999.3 (m), 936.1 (w), 883.9 (vw), 811.7 (s), 734.9 (vs), 700 (vs), 681.8 (m), 623.9 (m), 613.4 (m), 586.9 (s), 545.8 (s), 495.8 (s), 480.2 (vs), 455.3 (m), 414.2 (s).

3.1.11 As(Si^{t}BuMe$_2$)$_3$ (29)

Tert-butylchlorodimethylsilane (4.71 g, 31.1 mmol) in THF (*ca.* 15 mL) was added dropwise to a stirring suspension of trisodium arsenide (1.50 g, 10.4 mmol) in THF (*ca.* 20 mL). The mixture was refluxed for 16 h. The solvent was removed *in vacuo* and the black solid washed with dry toluene (*ca.* 40 mL). The solid was allowed to settle and the colourless solution was decanted off and concentrated to yield a white crystalline solid. (1.18 g, 2.80 mmol, 27%). Anal. Cal. for $C_{18}H_{45}AsSi_3$: C, 51.39; H, 10.78%. Found: C, 42.51; H, 10.99%. ^{1}H NMR (C_6D_6): δ 0.50 (s, 18 H, Si*Me*$_2$^{t}Bu), 1.17 (s, 27 H, SiMe$_2$*^{t}Bu*). ^{13}C{^{1}H} NMR (C_6D_6): δ 1.5 (Si*Me*$_2$^{t}Bu), 19.9 (SiMe$_2$*^{t}Bu*), 27.5 (SiMe$_2$*^{t}Bu*). IR (cm^{-1}): 2954.7 (vs), 2926.2 (vs), 2854.7 (vs), 2733.9 (vw), 2705.9 (vw), 1463 (s), 1401.6 (w), 1378.5 (m), 1358.5 (m), 1254.2 (m), 1242.8 (m), 1197.2 (vw), 1183.2 (vw), 1093.3 (m), 1021 (m), 1003.5 (m), 936.8 (w), 833.4 (s), 815.7 (s), 792.7 (vs), 759.9 (s), 724.5 (w), 683.8 (m), 666.2 (m), 568.4 (m).

3.1.12 Et$_2$GaCl (30)

Gallium trichloride (1.50 g, 8.5 mmol) in hexane (*ca.* 20 mL) at -78 ^{o}C was added dropwise to $GaEt_3$ (2.67 g, 17.0 mmol), also in hexane (*ca.* 20 mL) at -78 ^{o}C. The mixture was stirred at -78 ^{o}C for 2 h and then allowed to reach room temperature slowly. The solvent was removed *in vacuo* to afford a colourless liquid (4.05 g, 24.8 mmol, 97%). ^{1}H NMR (C_6D_6): δ 0.90 (q, *J* = 8.0 Hz, 6 H, Ga*CH*$_2$CH$_3$), 1.30 (t, *J* = 8 Hz, 9 H, GaCH$_2$*CH*$_3$). ^{13}C{^{1}H} NMR (C_6D_6): δ 8.8 (GaCH$_2$*CH*$_3$), 10.9 (Ga*CH*$_2$CH$_3$). IR (cm^{-1}, nujol): 3369.2 (w), 3182.1 (vw), 2958 (vs), 2918.8 (vs), 2854 (vs, nujol), 2728.3 (vw, nujol), 2672.3 (vw), 2363.9 (vw), 2336.1 (vw), 1618.2 (vw), 1463.4 (s), 1377.6 (m), 1303.5 (vw), 1261.5 (vw), 1202.8 (vw), 1152.4 (vw), 1076.9 (w), 1009.7 (w), 965 (vw), 945.5 (vw), 892.3 (vw), 800.9 (w), 722 (w), 699.3 (vw), 668.9 (w), 581.1 (w), 514.7 (vw).

3.1.13 $[Me_2GaAs(SiMe_2Cy)_2]_2$ (31)

Trimethyl gallium (1.40 g, 8.0 mmol) dissolved in hexane (*ca.* 10 mL) at -78 °C was added dropwise to a solution of $As(SiMe_2Cy)_3$ (4.0 , 8.0 mmol) in hexane (*ca.* 30 mL) at -78 °C. The orange solution was allowed to reach room temperature and stirred overnight. The solution was concentrated in vacuo and placed in the freezer to recrystallise. After 4 weeks, a small amount of colourless crystals had formed. The orange solution was separated from the crystals and concentrated *in vacuo* to yield an oil (3.30 g, 3.6 mmol, 90%). ^{1}H NMR (C_6D_6): δ 0.58 (s, 12 H, Ga*Me*$_2$), 1.62 (s, 24 H, Si*Me*$_2$Cy), 0.90-1.10, 1.75-2.00 (m, 44 H, SiMe$_2$*Cy*). ^{13}C{^{1}H} NMR (C_6D_6): δ 0.4 (Me_2Ga), 28.0 (SiMe$_2$*Cy*), Other peaks: 28.2, 28.8. IR (cm^{-1}, nujol): 2958 (vs), 2923.7 (vs), 2853.8 (vs), 1463 (s), 1401.4 (vw), 1378 (m), 1292.3 (vw), 1258.7 (w), 1248.4 (m), 1180.4 (vw), 1167.7 (vw), 1095.2 (m), 1037.8 (w), 1026.6 (w), 994 (w), 909.1 (vw), 886 (m), 849.8 (w), 836.3 (w), 791.1 (m), 769.2 (w), 749.7 (vw), 723.6 (vw), 641.9 (m), 558.1 (m), 526.6 (m), 506.3 (vw).

3.1.14 $[Et_2GaAs(SiMe_2Cy)_2]_2$ (32)

Diethylgallium chloride (0.98 g, 6.0 mmol) dissolved in toluene (*ca.* 15 mL) at -78 °C was added dropwise to $As(SiMe_2Cy)_3$ (3.0 g, 6.0 mmol) in toluene (*ca.* 30 mL) also at -78 °C. The orange solution was allowed to reach room temperature and stir overnight. The solvent was removed *in vacuo* to afford a red/brown oil (1.81 g, 3.7 mmol, 62%). ^{1}H NMR (C_6D_6): δ 0.30 (s, 24 H, Si*Me*$_2$Cy), 0.90 (q, *J* = 8 Hz, 8H, Ga*CH*$_2$CH$_3$), 1.10-1.30, 1.70-1.90 (m, 44 H, SiMe$_2$*Cy*), 1.39 (t, *J* = 8Hz, Ga*CH*$_2$CH$_3$). ^{13}C{^{1}H} NMR (C_6D_6): -1.0 (Ga*CH*$_2$CH$_3$), 9.1 (Si*Me*$_2$Cy), 26.3, 26.7, 27.5, 28.0 (SiMe$_2$*Cy*), 27.0 (GaCH$_2$*CH*$_3$). IR (cm^{-1}): 2923.1 (vs), 2850.1 (s), 2661.1 (vw), 2610.6 (vw), 2363.8 (vw), 2341.7 (vw), 2039.2 (vw), 1602.8 (vw), 1447.2 (s), 1413.6 (w), 1381.8 (w) 1353.8 (w), 1325.9 (vw), 1291.7 (vw), 1252.8 (s), 1188.7 (w), 1169.8 (w), 110.8 (m), 1071.5 (m), 1037.3 (m), 997.2 (m), 962.2 (vw), 942.7 (vw), 910.5 (w), 890 (m), 853.9 (s), 840.9 (s), 818.4 (m), 801.8 (s), 782.3 (s), 728.6 (vw), 716.1 (vw), 693.7 (vw), 667.8 (m), 654 (m), 573.6 (w), 520.9 (m), 483.1 (m).

3.1.15 $[Me_2GaAs(SiPh_3)_2]_2$ (33)

Trimethylgallium (0.10 g, 0.9 mmol) in toluene (*ca.* 10 mL) at -78 °C was added dropwise to $As(SiPh_3)_3$ (0.75 g, 0.9 mmol) in toluene (*ca.* 20 mL) also at -78 °C. The yellow solution was allowed to reach room temperature slowly and then refluxed for 12

h. The solvent was removed *in vacuo* to afford a orange/brown solid (0.18 g, 0.7 mmol, 30%). Anal. Calc. for $C_{76}H_{72}As_2Ga_2Si_4$: C, 65.81; H, 5.23%. Anal. Calc. for $C_{83}H_{80}As_2Ga_2Si_4$ ($[Me_2GaAs(SiPh_3)_2]_2.PhCH_3$): C, 67.40%, H, 5.45%. Found: C, 68.61; H, 5.44%. ^{1}H NMR (C_6D_6): δ 0.41 (s, 12 H, Ga*Me*$_2$), 7.00-7.50 (m, 60 H, Si*Ph*$_3$). $^{13}C\{^1H\}$ NMR (C_6D_6): δ 1.7 (Ga*Me*$_2$), 125.5, 130.1, 136.3, 135.6 ($SiPh_3$). IR (cm^{-1}): 3047.6 (vw), 2958 (vs), 2922.4 (vs), 2853 (vs), 2728.3 (vw), 2666.7 (vw), 2358.5 (vw), 1955.2 (vw), 1893.7 (vw), 1815.4 (vw), 1773.4 (vw), 1658.7 (vw), 1586.3 (vw), 1567 (vw), 1463.7 (vs), 1427.8 (s), 1377.8 (s), 1304.4 (vw), 1260.6 (m), 1185.4 (w), 1158.4 (w), 1117.4 (m), 1093.8 (s), 1027.5 (m), 998.4 (m), 886.8 (w), 859 (w), 801.1 (m), 733.6 (s), 697.9 (vs), 675.8 (m), 621 (vw), 595.8 (vw), 552.4 (w), 501.5 (vs), 493.7 (vs).

3.1.16 $[Me_2GaAs(SiMePh_2)_2]_2$ (34)

Trimethyl gallium (0.20 g, 1.7 mmol) in hexane (*ca.* 10 mL) at -78 °C was added dropwise to $As(SiMePh_2)_3$ (1.16 g, 1.7 mmol) in hexane (*ca.* 20 mL), which was also kept at -78 °C. The pale yellow solution was allowed to reach room temperature and stirred overnight. No colour change in the solution indicated that the reaction had not taken place, hence it was refluxed for 16 h at 75 °C. The solvent was removed *in vacuo* to yield a yellow oil. ^{1}H NMR (C_6D_6): δ 0.41 (s, 2.5 H, Ga*Me*$_2$), 0.80 (s, 12 H, Si*Me*Ph_2), 7.20-7.30, 7.65-7.70 (m, 40 H, SiMe*Ph*$_2$). $^{13}C\{^1H\}$ NMR (C_6D_6): δ 0.6 (Si*Me*Ph_2), 130.5, 134.2, 134.7, 135.1, 135.3 (SiMe*Ph*$_2$).

3.1.17 $[Ga(NMe_2)_3]_2$ (35)

A fine slurry of $Li(NMe_2)$ (3.20 g, 62.7 mmol) in hexane (*ca.* 40 mL) was added dropwise to a solution of $GaCl_3$ (3.00 g, 17.0 mmol) in hexane (*ca.* 10 mL) at -78 °C. The cream coloured mixture was allowed to reach room temperature and stirred overnight. The resulting solid was allowed to settle and the solvent was filtered into a clean flask. The solvent was then removed *in vacuo* to produce an off-white solid (2.50 g, 6.2 mmol, 73%). Anal. Calc. for $C_{12}H_{36}Ga_2N_6$: C, 35.68; H, 8.98; N, 20.81%. Found: C, 35.38, H, 9.08; N, 21.33%. ^{1}H NMR (C_6D_6): δ 2.59 (s, 24 H, N*Me*$_2$), 2.97 (s, 12 H, μ-N*Me*$_2$). $^{13}C\{^1H\}$ NMR (C_6D_6): δ 43.8 (μ-N*Me*$_2$). IR (cm-^{1}): 2924.4 (vs), 2765.3 (s), 1462.9 (vs), 1406.4 (w), 1377.7 (s), 1303.5 (vw), 1255.8 (s), 1228.7 (m), 1169.3 (s), 1127.3 (m), 1065.9 (m), 1039.7 (m), 967.9 (s), 899 (s), 802.8 (vw), 722.4 (m), 562.4 (m), 540 (m), 501.8 (s).

3.1.18 $[ClGa(NMe_2)_2]_2$ (36)

A fine slurry of $Li(NMe_2)$ (1.83 g, 35.9 mmol) in hexane (*ca.* 130 mL) at -78 ^oC was added dropwise to $GaCl_3$ (3.00 g, 17.0 mmol) also in hexane (*ca.* 25 mL) at -78 ^oC. The mixture was allowed to reach room temperature and stirred overnight. The resulting solid was allowed to settle and the solvent was filtered into a fresh flask where it was concentrated *in vacuo* to produce a white solid (2.55 g, 6.6 mmol, 76%). Anal. Calc. for $C_8H_{24}Cl_2Ga_2N_4$: C, 24.85; H, 6.26, N, 14.49%. Found: C, 22.99; H, 5.81; N, 13.47%. ^1H NMR (C_6D_6): δ 2.46 (s, 12 H, N*Me*$_2$), 2.92 (s, 12 H, μ-N*Me*$_2$). IR (nujol, cm^{-1}): 2924.1 (vs), 2853.4 (vs), 2780.2 (s), 1612.1 (vw), 1459.8 (vs), 1409.8 (vw), 1377.7 (m), 1265.2 (s), 1231.3 (m), 1173.6 (s), 1125 (s), 1072 (m), 1034.7 (s), 973.3 (vs), 894.1 (vs), 802 (w), 758 (w) 722 (w), 568.2 (s), 518.9 (s).

3.1.19 $[(Me_2N)_2GaAs(H)^tBu]_2$ (37)

Tert-butylarsine (0.66 g, 4.9 mmol) was dissolved in hexane (*ca.* 10 mL) and added dropwise to $[Ga(NMe_2)_3]_2$ (1.00, 2.5 mmol) in hexane (*ca.* 20 mL) at -78^oC. The solution was allowed to reach room temperature and stirred for 16 h. This resulted in the formation of a white precipitate within the yellow solution. The solution was separated from the precipitate via filtration. The solvent was removed from the filtrate *in vacuo* to yield a yellow solid (0.69 g, 1.2 mmol, 48 %). Anal. Calc. for $C_{16}H_{44}As_2Ga_2N_4$: C, 33.03; H, 7.62; N, 9.63%. Found: C, 26.74; H, 5.98; N, 7.54; Cl, 9.12%. (The adduct $[Ga(NMe_2)_2Cl\{As^tBuH_2\}]$ has anal. cal. for $C_8H_{23}AsClGaN_2$ of C 29.33, H 7.08, N 8.56, Cl 10.83%). ^1H NMR (C_6D_6): Peaks observed: δ 1.66 (s), 1.70 (s), 1.73 (s), 1.90 (s), 2.06 (s), 2.19 (s), 2.78 (s), 2.81 (s), 2.86 (s). $^{13}C\{^1H\}$ NMR (C_6D_6): δ 33.6, 35.0, 36.8, 37.2, 37.3, 38.0, 43.1, 43.5, 44.1, 46.7. IR (cm^{-1}, nujol): 3249.3 (vw), 2958 (vs), 2923.9 (vs), 2853.8 (vs), 2765.1 (w) 2067.2 (w), 1462.1 (s), 1378 (m), 1361.1 (m), 1260.8 (m), 1222.4 (vw), 1154.4 (m), 1125.9 (m), 1093.7 (w), 1035 (m), 1020.7 (m), 953.9 (m), 892.7 (s), 804.4 (m), 758.1 (vw), 721.7 (w), 548.3 (vw), 478.5 (w).

3.1.20 $[(Me_2N)_2GaAs(H)^tBu]_2$ (38)

Tert-butylarsine (0.17 g, 1.3 mmol) was dissolved in hexane (*ca.* 15 mL), cooled in hexane and added dropwise to $[(Ga(NMe_2)_3]_2$ (0.25 g, 0.6 mmol) in hexane (*ca.* 10 mL) at -78^oC. The solution was allowed to reach room temperature and stirred for 16 h, which resulted in the solution changing from colourless to yellow. The solution was then refluxed for 4.5 h. White precipitate formed in the orange/brown solution. The

precipitate was allowed to settle, the orange/brown solvent filtered to a fresh flask and concentrated *in vacuo* to yield a yellow solid (0.20 g, 0.3 mmol, 56%). ^{1}H NMR (C_6D_6): δ 0.29 (s, 12 H), 0.88 (t, *J* = 5 Hz, 0.6 H), 1.40 -2.10 (m, 18 H). ^{13}C{^{1}H} NMR (C_6D_6): δ 1.5 (Ga*(NMe$_2$)$_2$*). Peak at 23.0 was also observed. IR (nujol, cm^{-1}): 2960.7 (vs), 2924.4 (vs), 2853 (vs), 2763.3 (w), 2705.9 (vw), 2067.2 (vw), 1801.4 (vw), 1642 (vw), 1457.9 (s), 1412.6 (w), 1378.1 (w), 1359.6 (m), 1261.2 (vs), 1153.2 (s), 1095.4 (vs), 1020 (vs), 961.7 (w), 886.2 (w), 801.4 (vs), 703.7 (w), 660 (vw), 542.7 (vw), 467.1 (vw).

3.1.21 [Me$_2$Ga(NMe$_2$)]$_2$ (39)

As(NMe$_2$)$_3$ (2.71 g, 13.1 mmol) in CH_2Cl_2 (*ca.* 20 mL) at -78 ^{o}C was added dropwise to $GaMe_3$ (1.0 g, 8.7 mmol) in CH_2Cl_2 also at -78 ^{o}C. The colourless solution was allowed to reach room temperature slowly, then refluxed for 18 h. The solvent was removed *in vacuo* to yield a white solid (3.80 g, 7.2 mmol, 83%). The solid was redissolved in CH_2Cl_2 and placed in the fridge to recrystallise. Anal. Calc. for $C_4H_{24}Ga_2N_2$: C, 33.39; H, 8.41; N, 9.74%. Found: C, 32.58; H, 8.34; N, 9.26%. ^{1}H NMR (C_6D_6): δ -0.12 (s, 12 H, Ga*Me$_2$*), 2.26 (s, 12 H, Ga*(NMe$_2$)$_2$*). ^{13}C{H} NMR (C_6D_6): δ -10.5 (Ga*Me$_2$*), 43.4 (Ga*(NMe$_2$)$_2$*).

3.1.22 [Me$_2$GaAs(H)^{t}Bu]$_2$ (47)

^{t}BuAsH$_2$ (1 g, 7.50 mmol) in toluene (15 mL) was cooled to -78 ^{o}C. This was then added dropwise to a solution of $GaMe_3$ (0.86g, 7.5 mmol) in toluene (15 mL) also cooled to -78 ^{o}C. The colourless solution was allowed to reach room temperature and then heated to 80 ^{o}C for 21 hours. The solvent was removed in *vacuo* to obtain a yellow solid. The solid was dissolved in minimum toluene and reduced to below room temperature to yield colourless crystals. Anal. Calc. for $C_{12}H_{32}As_2Ga_2$: C, 30.95; H, 6.93. Found: C, 28.9; H, 6.60% ^{1}H NMR ($CDCl_3$): δ 0.02 (s, 3 H, Ga*Me$_2$*), 0.08 (s, 3 H, $GaMe_2$), 1.40 (s, 9 H, As*^{t}Bu*), 2.54 (s, 1 H, As*H*). ^{13}C{^{1}H} NMR ($CDCl_3$): δ 33.4 (*^{t}Bu*As). IR (Neat, cm^{-1}) 2947.9 (s), 2924.6 (s), 2883.9 (s), 2854.9 (s), 2123.2 (m), 1454.7 (s), 1390 (w), 1363.1 (s), 1260.4 (m), 1209 (vw), 1188 (w), 1154.8 (s), 1097.5 (m), 1018.4 (m), 935.5 (vw), 860.1 (vw), 715.7 (vs).

3.1.23 [Et$_2$GaAs(H)^{t}Bu]$_2$ (48)

^{t}BuAsH$_2$ (1 g, 7.50 mmol) in toluene (15 mL) was cooled to -78 ^{o}C. This was then added dropwise to a solution of $GaEt_3$ (1.17 g, 7.5 mmol) in toluene (15 mL) also cooled to -78 ^{o}C. The colourless solution was allowed to reach room temperature and

then heated to 80 ^{o}C for 21 hours. The solvent was removed in *vacuo* to obtain a yellow oil. ^{1}H NMR (C_6D_6): δ 0.86-1.01 (m, 8 H, Ga*CH*$_2$CH$_3$), 1.35 (s, 9 H, As^{t}Bu), 1.39-1.47 (m, 12 H, GaCH$_2$*CH*$_3$), 2.31 (s, 1H, AsH) ^{13}C{^{1}H} 7.8 (CH$_2$*CH*$_3$), 11.6 (*CH*$_2$CH$_3$), 12.4 (*C*(CH$_3$)$_3$), 33.9 (C*(CH*$_3$*)*$_3$). IR (Neat, cm-1) 2933.1 (s), 2889.7 (s), 2862.4 (s), 2116.1 (m), 1559.9 (vw), 1455.8 (s), 1417.7 (m), 1364.6 (s), 1260.8 (w), 1231.1 (w), 1183.3 (vw), 1160.9 (s), 1096 (w), 1018.7 (vw), 994.6 (s), 958.3 (m), 930.69 (m), 850.22 (s), 813.31 (s), 725.64 (s).

Chapter 4

4 GaAs thin films *via in situ* AACVD using $As(NMe_2)_3$ and $GaMe_3$

4.1.1 Introduction

This section details the deposition of gallium arsenide *via* AACVD and the analysis of polycrystalline GaAs thin films on glass using an *in situ* approach. The precursors used for this study were $As(NMe_2)_3$ and $GaMe_3$.

4.1.2 The precursors

Carbon contamination from the arsenic precursor is a major problem when depositing GaAs films. Hence, trialkyl arsines are generally avoided, as they are a source of carbon in the film. This is a result of direct As-C bonds in the molecule in the absence of As-H bonds that can promote β-hydride elimination (such as tertiary butyl arsine). In GaAs films grown *via* MBE and CBE the high temperatures needed to break the As-C bond has limited the use of many arsenic precursors. Another method to avoid carbon contamination is to use precursors without any direct As-C bonds. Tris(dimethylaminoarsine), $As(NMe_2)_3$, is an example of such a precursor.

Tris(dimethylaminoarsine) is a liquid precursor that is used in many MOCVD techniques due to its high volatility and relatively low decomposition temperature (450 ^oC) compared to tertbutyl arsine (550 ^oC) and arsine. Indeed, GaAs films have been grown with undetectable carbon levels at 450 ^oC using trimethylgallium as the gallium source. No pre-cracking was required. The major decomposition products of $As(NMe_2)_3$ have been found to be dimethylamine, hydrogen and aziridine. Furthermore, $As(NMe_2)_3$ has been shown to turn gallium rich films arsenic rich at low temperatures (400 ^oC) and low pressures (ca. 10^{-7} torr).

In-situ mass spectrometry studies in low pressure MOMBE suggest that the low levels of carbon found in films grown when using $As(NMe_2)_3$ is due to the reaction of adsorbed hydrogen atoms with surface carbon molecules. These hydrogen atoms originate from the amine during β-hydride elimination (Figure 21) and thus this

suggests that the low carbons levels are not due to the formation of $AsMe_3$ from the reaction of $As(NMe_2)_3$ with $GaMe_3$.[113]

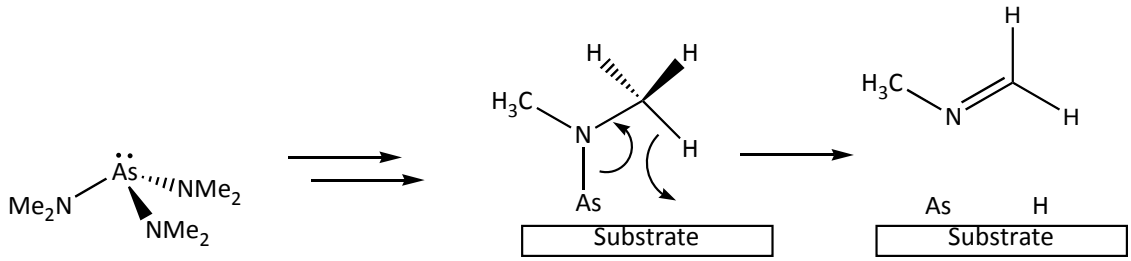

Figure 21: The heterogeneous decomposition of $As(NMe_2)_3$ *via* hydride elimination.

As mentioned earlier, tris(dimethylaminoarsine) is often used with trimethylgallium in the production of GaAs thin films. Typical methods such as MOCVD, MOVPE, MBE and CBE employ a dual-source approach whereby the two precursors do not come in contact with one another until the reaction chamber where the substrate is heated.

However, with the AACVD system employed here, the reagents are mixed in a flask prior to entering the CVD chamber in aerosol form. Therefore, there is an opportunity for ligand transfer to take place. This was indeed true, as rearrangement was observed to have taken place as shown by the NMR experiments carried out in Chapter 3. The possibility of ligand rearrangement was studied *via* solution phase reactions in order to understand the reactions taking place in the AACVD flask as shown in equation **4.1** and described in Chapter 3.

$$As(NMe_2)_3 + GaMe_3 \xrightarrow[18\ ^oC]{CH_2Cl_2} 1/2\ [Me_2NGaMe_2]_2 + MeAs(NMe_2)_2$$

(**4.1**)

The reaction of $As(NMe_2)_3$ with $GaMe_3$ in dichloromethane resulted in the formation of $[Me_2NGaMe_2]_2$ after heating at 18 ^oC. The arsenic compound $MeAs(NMe_2)_2$ was also formed but was removed *in vacuo* during workup. Recrystallisation of $[Me_2NGaMe_2]_2$ in minimum solvent (dichloromethane) at -15 ^oC yielded colourless crystals. The ^1H NMR spectrum of $[Me_2NGaMe_2]_2$ showed two singlet peaks at 2.15 ppm and -0.23 ppm corresponding to NMe and GaMe respectively in a 1:1 ratio. Single crystal X-ray crystallography was performed on the colourless crystals to confirm the structure and

formation of $[Me_2NGaNMe_2]_2$. When the two reagents were mixed at reduced temperature in toluene and then allowed to reach room temperature some minor ligand scrambling takes place. With time this scrambling is more prevalent and hence could be occurring in the AACVD flask.

4.1.3 Film Deposition

Depositions were carried out on glass substrates using AACVD via an *in-situ* approach whereby, $As(NMe_2)_3$ was mixed with $GaMe_3$ in toluene. The two reagents were mixed at reduced temperature and then allowed to reach room temperature in the AACVD flask before deposition was started.

A 1.5:1 ratio of $As(NMe_2)_3$ to $GaMe_3$ was required to obtain close to stoichoimetric GaAs in the films. An increase in the amount of $As(NMe_2)_3$ ratio above 1.5 did not result in any change of film stiochiometry. The films were grown under a range of temperatures (450 ^oC, 500 ^oC and 550 ^oC) in toluene (20 mL) at a carrier gas flow rate of 0.5 L min^{-1} (Table 5). The films were continuous but appeard textured and appeared grey/black in reflected light. They were also adherent to the substrate passing the Scotch tape test but were scratched by stainless steel and brass stylus, which is typical for GaAs films.

Condition	$As(NMe_2)_3$ / g	$GaMe_3$ /g	Temp. / ^oC	Solvent	Volume / mL	Dep. Time / mins
1	1.08	0.4	450	Toluene	20	90
2	1.08	0.4	500	Toluene	20	90
3	1.08	0.4	550	Toluene	20	90

Table 5: The deposition conditions used to grow GaAs films from a solution of $As(NMe_2)_3$ and $GaMe_3$ in CH_2Cl_2.

4.1.4 Analysis

4.1.4.1 Powder X-Ray Diffraction (XRD)

Polycrystalline GaAs is a cubic crystal structured material that shows an XRD pattern with five peaks from the [111], [200], [220], [311] and [222] planes between a 2θ range

of 20 to 60° as shown in the standard stick pattern in Figure 22.[114] The [111] plane is the most intense followed by [220] and [311]. There is very little diffraction from the [200] and [222] planes therefore they show very low intensity.

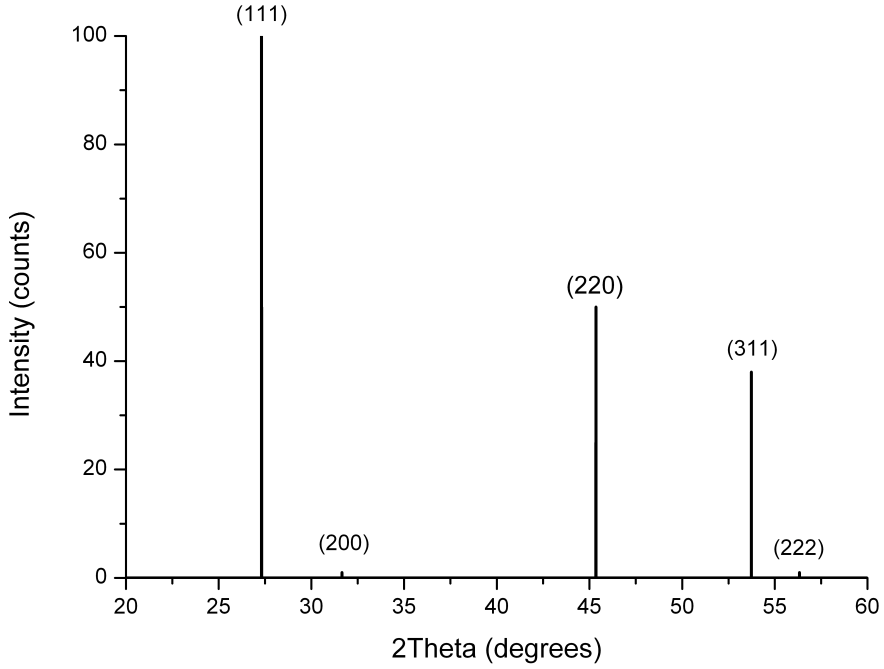

Figure 22: Standard XRD stick pattern for cubic GaAs. There are five peaks corresponding to diffraction from the [111]. [200], [220], [311] and [222] *hkl* planes.

Films grown from $As(NMe_2)_3$ and $GaMe_3$ in toluene solution were polycrystalline at 500 °C and 550 °C. These films were polycrystalline with peaks corresponding to cubic GaAs [111], [220] and [311] (Figure 23). The intensity of the peaks also matches that of the standard therefore indicating a lack of preferred orientation. The films grown at 450 °C were only partially crystalline, i.e. the predominant 'peak' is the broad amorphous hump due to glass around 30° but on top of this hump it is possible to see small peaks corresponding to GaAs (Figure 23). The lack of crystallinity in these films is due to two reasons. Firstly, the temperature of deposition of 450 °C is insufficient to crystallize enough of the film such that the disordered and amorphous component of the film is far more prevalent than the ordered/crystalline content of the film. Secondly, the films are very thin, such that during XRD analysis a large proportion of the amorphous substrate was analysed which dwarfs the peaks from the GaAs film.

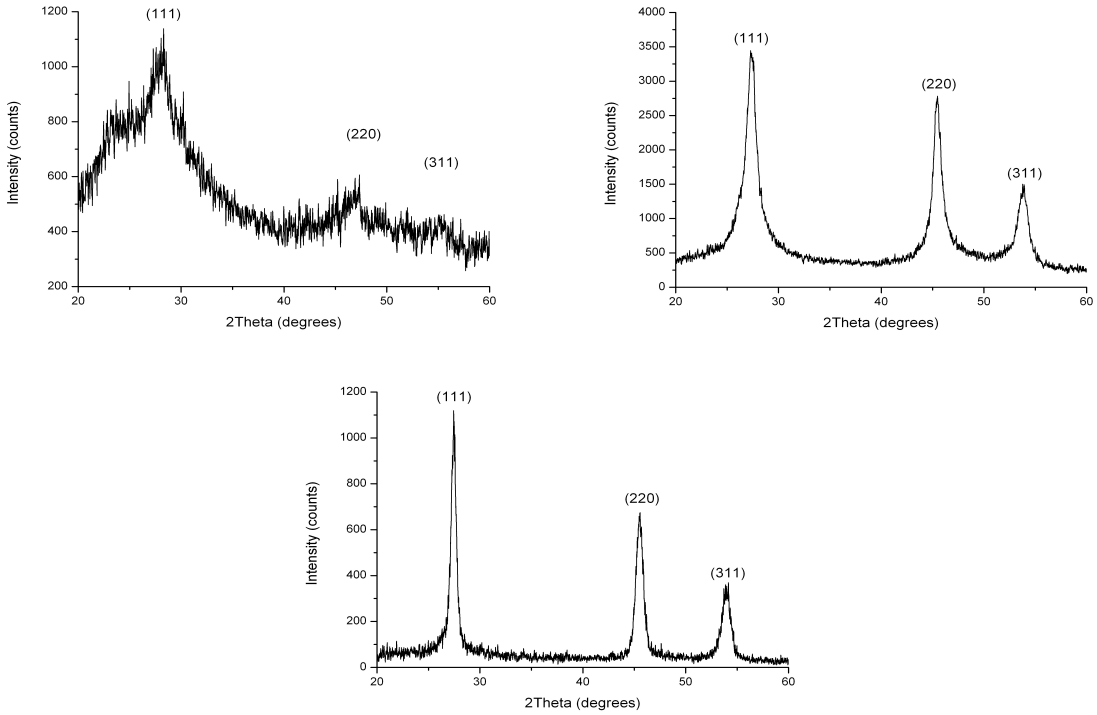

Figure 23: XRDs for films grown under condition 1 at 450 °C (top left), condition 2 500 °C (top right) and condition 3 550 °C (bottom centre).

The crystallite size of the films grown under conditions **2** and **3** were calculated using the Scherrer equation.[97,98]

$$B(2\theta) = \frac{K\lambda}{L\cos\theta} \qquad \textbf{(4.2)}$$

Where L is full width half maximum (FWHM) of the corresponding peak, θ is the angle corresponding to peak and λ is the wavelength of X-Rays. K is the Scherrer constant (constant of proportionality) and is dependent on the method of peak width determination (in this case Full Width Half Maximum), the shape of the crystallites (usually spherical shape is assumed) and the size distribution in the film.[115] The most common value for K is 0.94 for spherical crystals with cubic unit cell.[116] It should be noted that this leads to a relatively large error being associated with the dimensions of the crystallites determined *via* the Scherrer equation.[97]

There are two factors that cause broadening of an XRD peak.

- The size of the crystallites (the smaller the crystallites the greater the peak broadening)
- Instrument resolution (which in turn is effected by detector resolution, slit width and wavelength spread from monochromator)

The broadening of the XRD peaks caused by the instrument was determined by measuring a standard sample (corundum, aluminium oxide) under the exact same conditions as the GaAs samples. The standard is highly crystalline and has micron (assumed infinite) size crystallites therefore any broadening observed is solely due to the instrument.[97]

Three peaks with similar 2θ values to the peaks of interest in the samples ((111), (220) and (311)) were selected from the diffraction pattern of the standard. Then a pseudo–Voigt function (which is a simple linear combination of the Gaussian function with the Lorentz function) was used to fit the shape of the peaks and hence determine the FWHM. Instrument broadening was calculated to be 0.07994°, 0.05495° and 0.06478° at 27.47°, 45.59° and 53.99° 2θ values.

Out of the three samples, only two (grown under condition **2** and **3**) were crystalline enough to determine the crystallite size using the Scherrer equation (**4.2**). Three of the most intense peaks (at 2θ values of 27.52°, 45.59°, 53.98°) were selected to carry out the calculation. Again, a pseudo-Voigt function was used to determine the FWHM of the peaks and from these values the broadening due to the instrument was taken away to obtain FWHM values that are purely due to the sample. In this case the peaks are more Lorentizian than Gaussian, therefore simply taking the broadening due to instrument away from broadening due to sample is sufficient.[97]

Using the Scherrer equation the crystallite sizes were very small (Table 6). The average crystallite size of the film grown under condition **2** at 500 °C is 6 (± 1) nm, whereas for the film grown under condition **3** at 550 °C it is 11 (± 1) nm. If crystallite sizes were determined using the Scherrer equation without taking the instrument broadening into account the calculated crystallite sizes are 5 (± 2) nm and 10 (± 1) nm (for condition **2** and **3** respectively). This indicates that for this particular prowder X-Ray diffractometer, the broadening due to instrument does not underestimate the size of the crystallites by a significant amount.

The increase in crystallite size with increasing temperature is as expected. The higher the deposition temperature the more crystalline the films and therefore the larger the crystallites. This is because higher deposition temperature gives more energy to the adatoms on the substrate to find the lowest energy site before nucleation to grow the films and thus form films with larger crystallites and reduced grain boundaries.

	Condition **2**					
hkl	Bragg Angle 2θ/°	Peak Width 'β'/°	Instrument resolution/°	Corrected 'β'	Diameter /nm	Ave. Carystal lite Size / nm
111	27.48	1.84	0.080	1.760	5	6(±1)
220	45.83	1.21	0.055	1.155	7	
311	54.21	1.68	0.065	1.615	6	
	Condition **3**					
111	27.49	0.93	0.080	0.850	10	11(±1)
220	45.69	0.75	0.055	0.695	12	
311	54.09	0.97	0.065	0.905	10	

Table 6: The crystallite size of a film grown under condition 2 (top) and 3 (bottom) calculated using the Scherrer equation (4.2).

The results obtained from the Scherrer equation calculations suggest that these films are less crystalline than films grown using the $^{t}BuAsH_2$ and $GaMe_3$ *in-situ* AACVD approach and using the single-source precursors ($[R_2GaAs(H)^{t}Bu]_2$ where R = Me, Et) where the crystallite sizes were larger (Chapter 6).

4.1.4.2 Raman

Raman spectroscopy was used to further characterise the resulting GaAs films since GaAs shows characteristic Raman peaks.

The Raman spectra (modeled using a Gaussian function) showed the expected peaks for GaAs (Figure 24) having both a longitudinal optical (LO) phonon mode at 275.4 cm^{-1} and the transverse optical (TO) phonon mode at 252.4 cm^{-1}. The peaks were however shifted to lower wavenumbers than what is observed in bulk GaAs (LO of 291 cm^{-1} and

TO of 268 cm^{-1}) this is most likely due to strain in the GaAs lattice and/or defects as well as local heating effects induced by the 514.5 nm laser and other thermal effects. The poor crystallinity of the samples as confirmed by XRD (Table 6) has also resulted in the peaks being broad. The broadening of the Raman peak(s) with decreasing crystallinity is due to the breakdown of the q=0 selection rules that occur when long range order (i.e. crystallinity) is lost. When these selection rules breakdown, all modes of vibration become allowed resulting in broadening of the peaks. As the amount of amorphous content in the films increase the peaks become broader.[117]

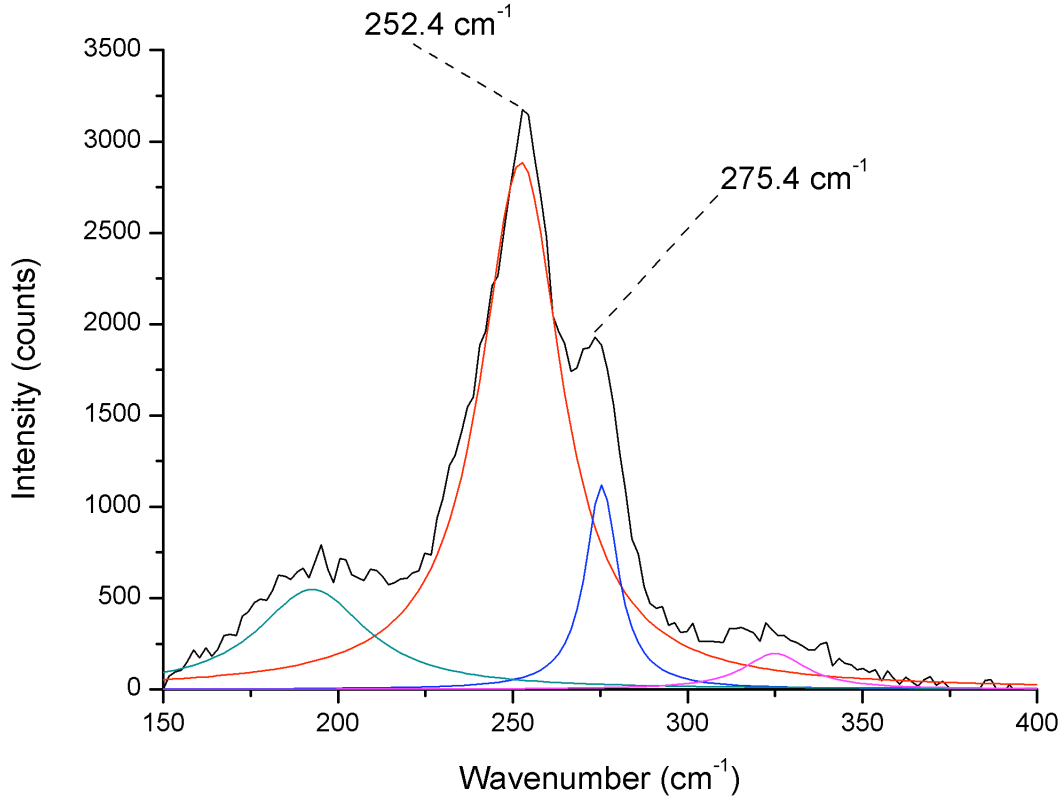

Figure 24: Raman spectra of a film grown under condition 2 at 500 °C. The LO peak appears at 275.4 cm^{-1} and the TO at 252.4 cm^{-1}.

4.1.4.3 Energy Dispersive X-Ray (EDX) analysis

Energy dispersive X-ray (EDX) analysis was utilised to obtain composition analysis of the films. Prior to carrying out EDX on the samples analysis was carried out on a GaAs standard that was know to be stoichiometric (Table 7). The results indcate that the EDX is over estimating the gallium concentration (and underestimating the arsenic concentration) by 1.6% with a standard deviation of 0.1%.

Ga / Atomic %	As / Atomic %
51.6 ± 0.1	48.4 ± 0.1

Table 7: Average EDX results showing the Ga to As ratio in a GaAs standard.

The EDX results of the samples grown under condition **1**, **2** and **3** show that the films become more stoichiometric with increasing temperature. Films grown under condition **1**, i.e. at 450 ^{o}C, were non-stoichimetric with a gallium excess of on average 25 atomic percent (Table 8). Again, this could be due to the films being very thin as they were only grown at 450 ^{o}C deposition temperature. When the deposition is kinetic controlled as opposed to mass flow controlled the deposition temperature determines the thickness of the films (Chapter 1).

It is common for a native oxide layer to form on the surface of GaAs thin film or wafers after a few seconds of exposure to a non-inert atmospheres. Many oxides of Ga and As such as Ga_2O_3 and As_2O_3 form on the surface of the films but it is predominately Ga_2O_3. If the GaAs films are thin then upon exposure to air during storage or analysis a larger portion of the films will be oxidized than if the film was thick. Since the majority of the oxide is Ga_2O_3 the EDX analysis would give results that show the film to be Ga rich. Arsenic oxides are also formed on the surface, but arsenic could also react with the moisture in the atmosphere to produce arsine, which would then leave the film as a gas, helping the films to be As deficient.

Therefore this gives rise to EDX results that show an excess of gallium in the films. Also, the non-stoichoimetry indicated by EDX could be a result of the films being amorphous as indicated by XRD and Raman (Figure 23 and Figure 24).

Condition **1**		
Region	Gallium / Atomic %	Arsenic / Atomic %
1	64.7	35.3
2	64.1	35.9
3	61.6	38.4
4	60.1	39.9
Average	**62.6 ± 2.2**	**37.4 ± 2.2**

Condition **2**		
Region	Gallium / Atomic %	Arsenic / Atomic %
1	53.2	46.8
2	52.9	47.1
3	53.0	47.0
4	55.5	44.5
Average	**53.7 ± 1.2**	**46.3 ± 1.2**

Condition **3**		
Region	Gallium / Atomic %	Arsenic / Atomic %
1	53.2	46.9
2	53.0	47.1
3	52.4	47.6
Average	**52.8 ± 0.4**	**47.2 ± 0.4**

Table 8: Tables showing the composition of the films grown under the three different conditions.

4.1.4.4 Scanning Electron Microscopy (SEM)

The morphology of the films was investigated using scanning electron microscopy (SEM) and images were taken in secondary electron mode with 5 kV. Samples were coated with gold prior to images being taken to avoid charging, as these samples are non-conducting. The films appear very compact and but have large-scale morphology issues. The featured morphology has arisen due to island type growth rate that has taken place as a result of many reasons, possibly a high growth or due to the decomposition pathway of the precursors in the CVD reaction chamber (Figure 25).

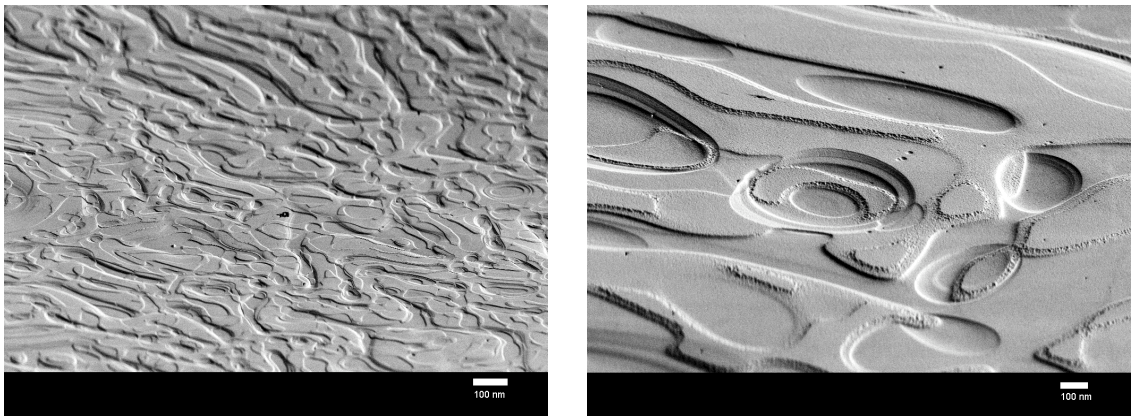

Figure 25: SEM images of film grown under condition 2 at 500 ^{o}C.

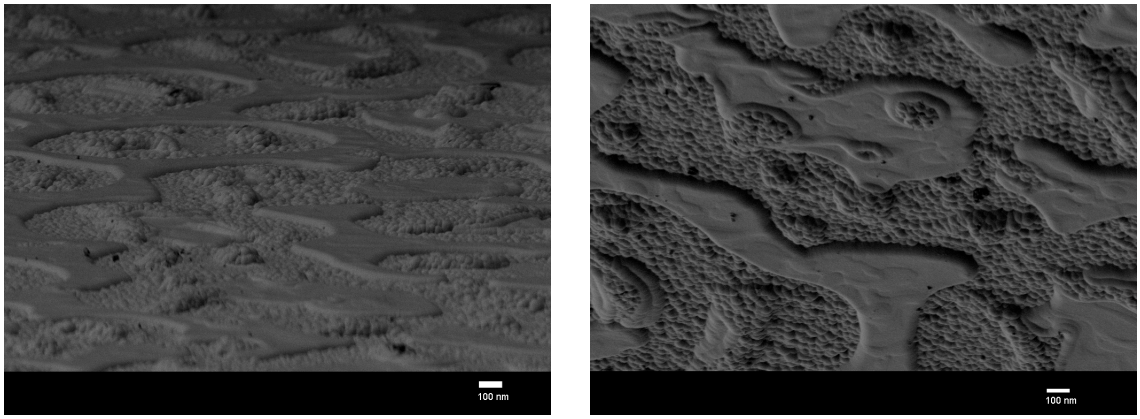

Figure 26: SEM images of films grown under condition 3 at 550 ^{o}C.

This growth phenomenon is also seen under condition **3**, which uses a deposition temperature of 550 ^{o}C as shown in Figure 26. In comparison to the films grown at 500 ^{o}C (condition 2) the images show larger and more defined features. The growth rate of the films is higher with increasing temperature; therefore it suggests that these structured films are most likely due to the high growth rate (Chapter 1).

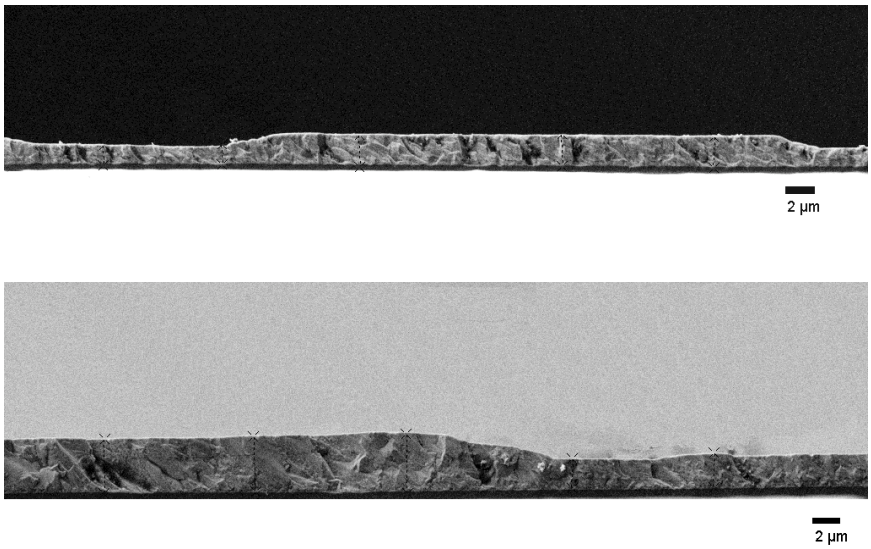

Figure 27: Side on SEM images of a film grown under condition 2 at 500 ^{o}C. There is a variation in thickness between 2 µm to 6 µm along the films.

Films grown under condition **2** and **3** were both thick ranging from 2 to 7 µm. Film thickness is dependent on the position analysed as there is a thickness gradient across the substrate. This is due to the CVD reactor design, which causes the films to be thicker near the inlet. Furthermore, due to the morphology of the films there were large and sudden changes in thickness as observed in Figure 27. The sudden changes in thickness are less prevalent in samples grown under condition **3** as seen in Figure 28.

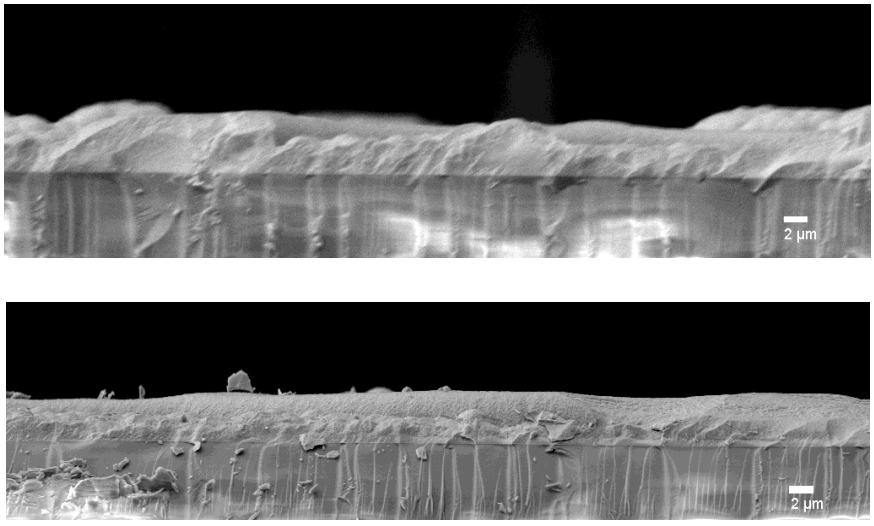

Figure 28: Shows side on SEM images of film grown under condition 3. The top image had thickness range 5 – 7 µm whereas bottom it was 4.5-5.5 µm.

4.1.4.5 High Resolution Transmission Electron Spectroscopy (HRTEM)

The crystallinity of the films grown under condition **2** (Table 5) were analysed using high-resolution transmission electron microscopy (HRTEM). The darkfield HRTEM image (Figure 29) shows the absence of convex features on the top region of the film, this is indicative of a film with minimum or no columnar growth. A lack of columnar growth means there are grain boundaries in both the vertical and lateral direction.

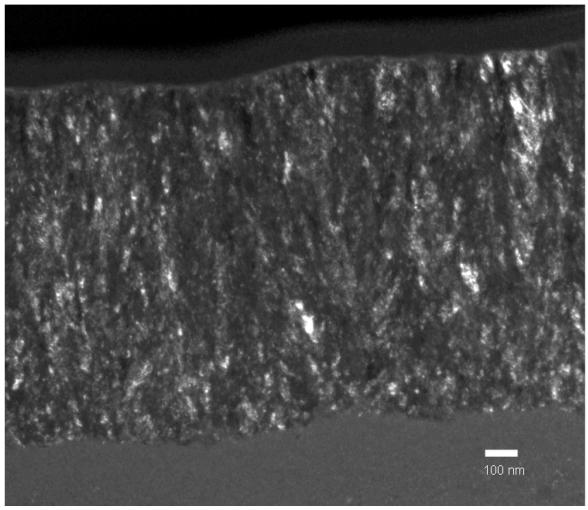

Figure 29: Darkfield TEM image of a film grown under condition 2 at 500 °C.

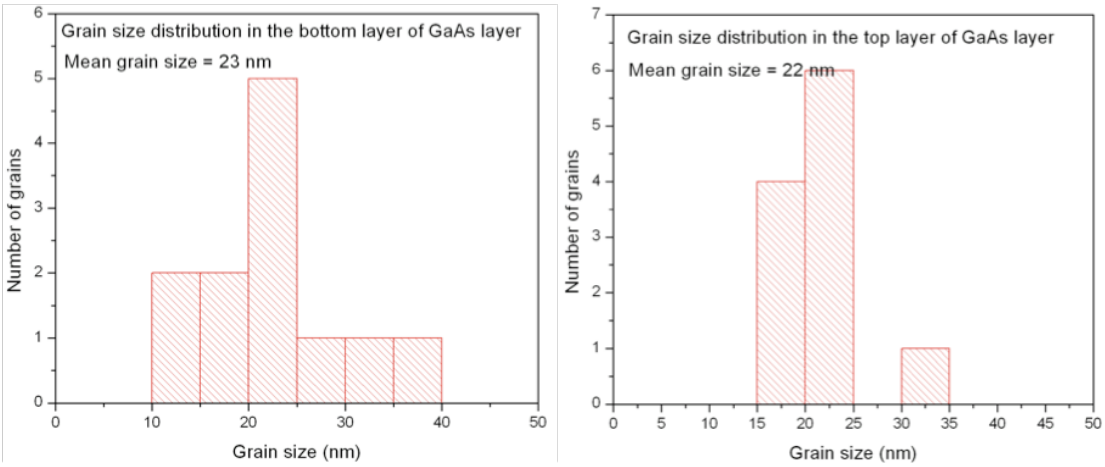

Figure 30: Grain size distribution in the top (left) and bottom (right) region of a film grown under condition 2 at 500 °C.

The grain size distribution near the top and bottom regions of the film grown under condition **2** were very similar. The average grain size is 22 nm near the top and 23 nm near the bottom. This is the opposite of what is expected, the grain size should increase

with thickness. This is because; the first few nanometers of GaAs is grown on the amorphous substrate therefore there is no lattice match hence the size of the initial grains will be small. But as the film thickness increases with deposition time, the there is more lattice match as the previous GaAs layers on the amorphous substrate act as a template therefore giving rise to larger grains near the top region of the film than the bottom. The crystallite size observed by the HRTEM is larger than those given using the Scherrer equation (Table 6), this is not unexpected as mentioned earlier the grain size estimation *via* the Scherrer equation has a much larger error associated with it compared direct determination methods such as HRTEM.

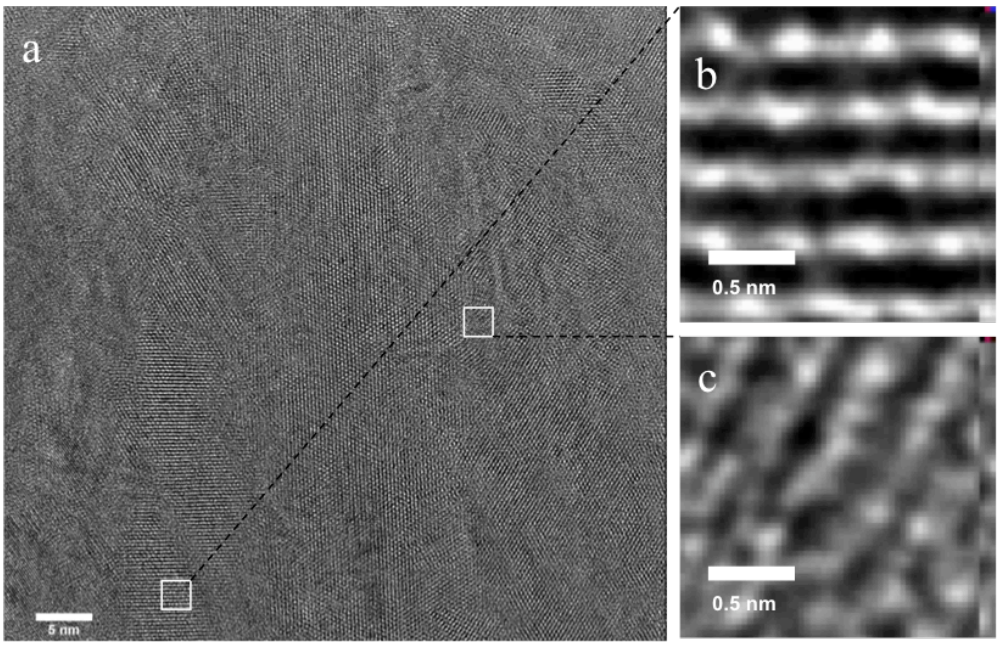

Figure 31: a) HRTEM of the central region of a film grown under condition 2 at 500 ^{o}C. There are many grain boundaries as expected with polycrystalline films. b) A magnified image showing the well spaced lattice fringes indicating good crystallinity. c) A magnified image of a less crystalline region of the film.

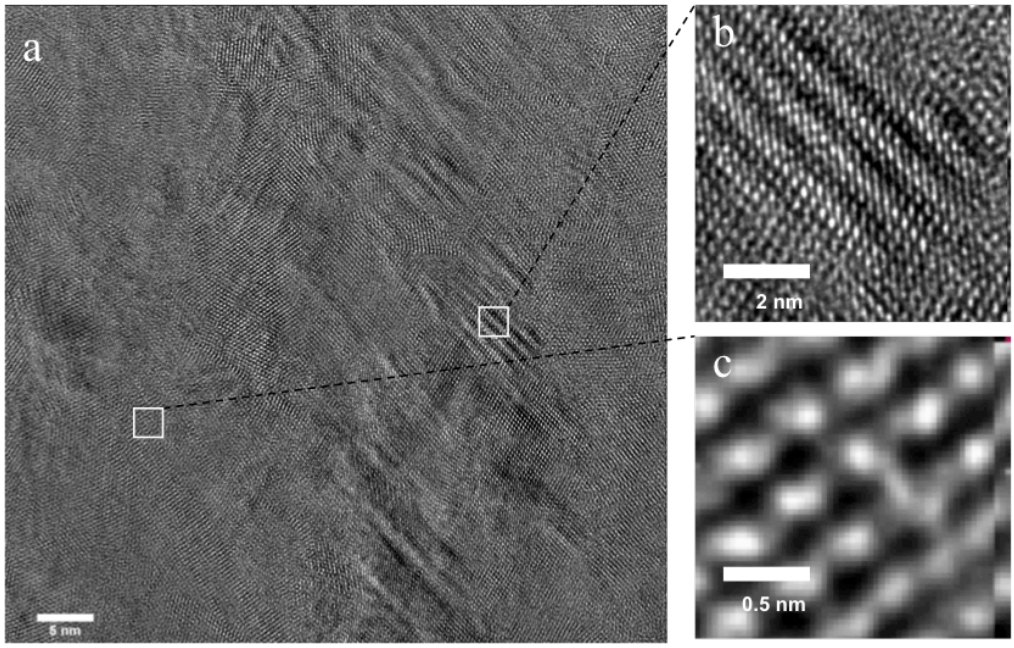

Figure 32: a) HRTEM image of the top region of a film grown under condition 2 at 500 ^{o}C. Again there are many grain boundaries, which is indicative of a polycrystalline film. b) and c) A magnified regions of the film show regions of good crystallinity with well spaced lattice finges.

The HRTEM of a film grown under condition **2** of regions near the centre and top of the film show there to be many grain boundaries, which is typical of polycrystalline films. In both cases there are regions of the film that are very crystalline and regions that are poorly crystalline. The crystalline regions are very well ordered with well spaced lattice fringes as shown in Figure 31 and Figure 32.

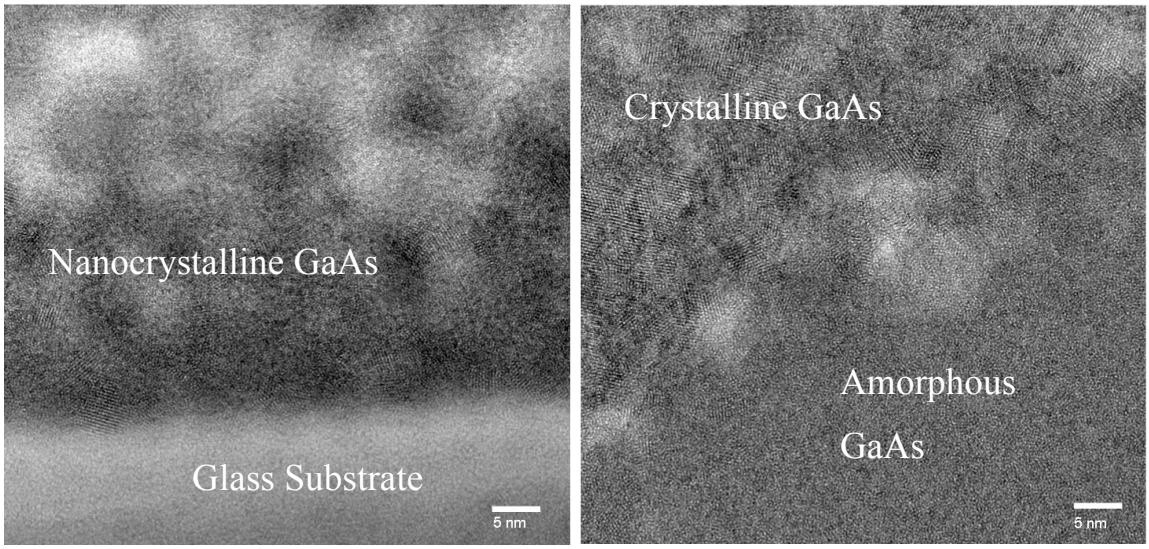

Figure 33: HRTEM image showing amorphous, nanocrystalline and crystalline regions of the film grown under condition 2 at 500 ^{o}C. The amorphous and nanocrystalline regions are close to the amorphous substrate.

There are also amorphous regions within the film especially near the glass substrate. Furthermore, unlike what is observed in the other precursor systems (see chapter 5 and 6) there are a few layers of nanocrystalline GaAs on the glass followed by crystalline GaAs (Figure 37)

4.1.4.6 Energy Dispersive X-ray (EDX) mapping

The change in the crystallographic nature of the film is more obvious from the EDX mapping study The STEM image on the left of Figure 34 shows there to be several distinct layers in the film analysed. The EDX maps on the right show that the gallium content is uniform throughout the film and that there is no carbon contamination apart from the surface of the film. Also, there is no silicon from the glass substrate that has diffused into the film, this is evident from the lack of colour in the EDX map. The arsenic content however is not so uniform throughout the film, there are some regions with poor arsenic content in particular in the darker region near the bottom of the film. This was also the same region where the oxygen content is high, suggesting that maybe this region near the glass substrate is rich in gallium oxide.

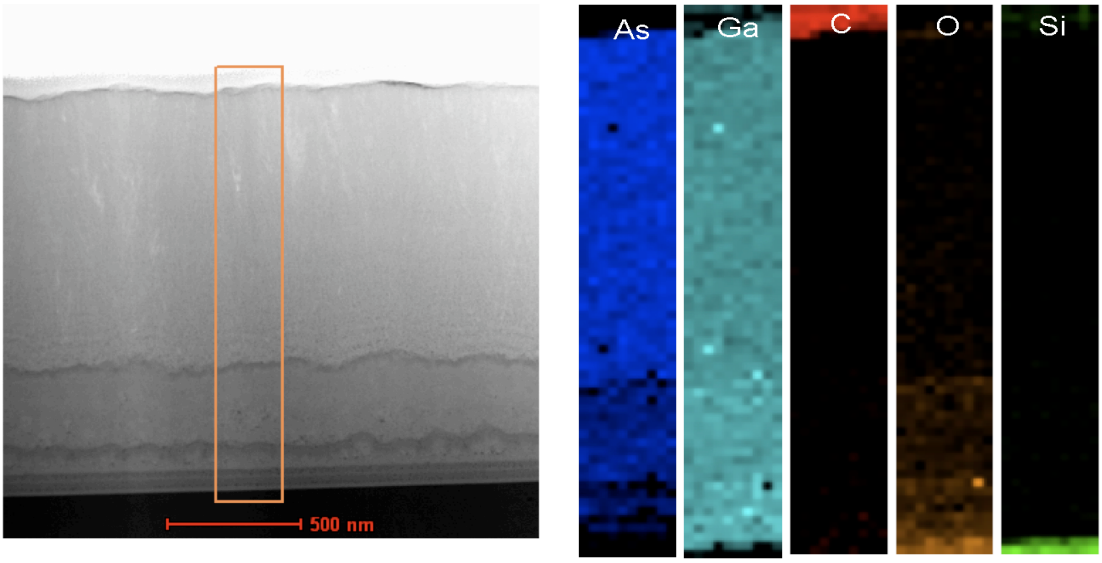

Figure 34: EDX mapping of a film grown under condition 2 at 500 °C. The STEM image on the left has an orange box, which represents the region of the film where EDX mapping (right) was carried out.

Comparing the HRTEM images with the STEM and EDX map (Figure 34) it is clear that the regions lacking in arsenic but high in oxygen near the substrate, have regions that are nanocrystalline with grain sizes only a few nanometers large and amorphous.

4.1.4.7 X-Ray Photoelectron Spectroscopy (XPS)

X-ray photoelectron spectroscopy was carried out to determine the surface chemistry of a film grown under condition **2** (Table 5). The surface sensitivity of XPS allows the determination of oxidation states, contaminant levels as well as the native oxide composition. The peaks observed after XPS analysis were modeled and the binding energy values compared to literature values to determine the identity of the components of the film and the native oxide layer. The data obtained for the depth profiling were not deconvulated as sputtering leads to unreliable results due the sputtering rate being element dependent.

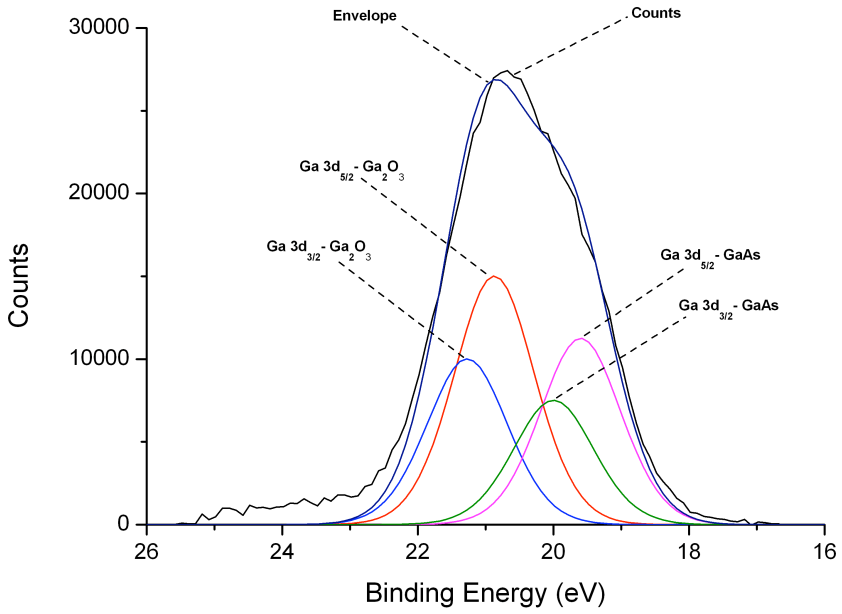

Figure 35: XPS peak for Ga 3d deconvulated to Ga $3d_{5/3}$ and Ga $3d_{3/2}$ for Ga_2O_3 and GaAs.

The most predominant peak for the Ga 3d spectra is the peak corresponding to the Ga in the +3 oxidation state in the form of Ga_2O_3 at binding energy 20.84 eV.[118] This peak also has a slight shoulder at 19.68 eV that corresponds to Ga in the form of GaAs. This is expected, as the surface of GaAs is prone to a native oxide.

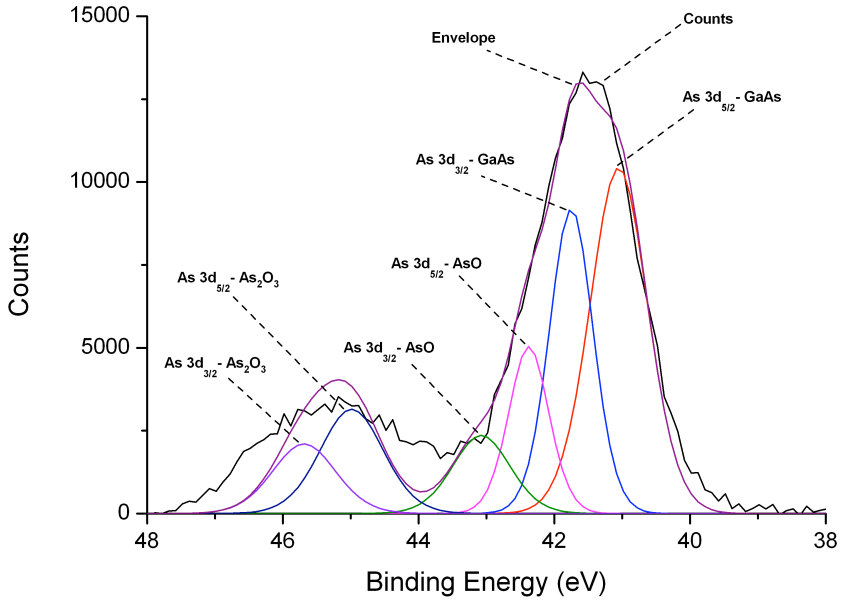

Figure 36: XPS peak for As 3d deconvulated to Ga 3d 5/3 and Ga 3d 3/2 for GaAs, As_2O_3 and AsO.

The peak of As 3d in the XPS spectra can be deconvulated to three different As 3d 5/2 and As 3d 3/2 peaks. The peak at binding energy 41.05 eV corresponds to As in the form of GaAs. The other peaks at 42.37 eV and at 44.99 eV correspond to AsO and As_2O_3.[119,120]

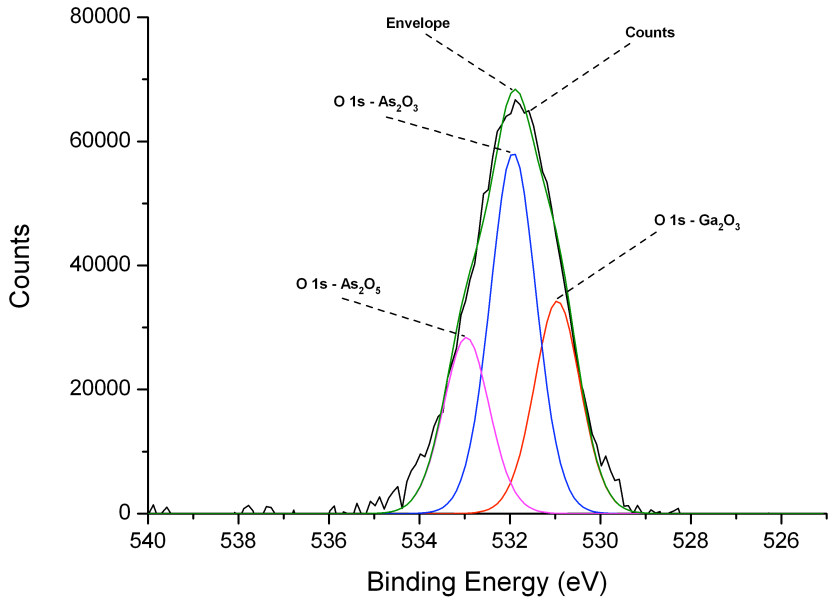

Figure 37: The XPS peak for O 1s deconvulated to Ga_2O_3 and As_2O_3.

The O 1s peak can be deconvulated to three different environments corresponding to Ga_2O_3 at 530.95 eV, As_2O_3 at 531.93 eV and As_2O_5 at 532.96 eV. A peak for AsO observed in the As 3d spectrum is not observed in the O 1s spectrum.

The XPS peak for carbon can be deconvulated to show a peak at 284.50 eV corresponding to graphitic carbon and a smaller peak at 288.79 corresponding to other forms of carbon species containing double bonds to oxygen and carbon (Figure 38).

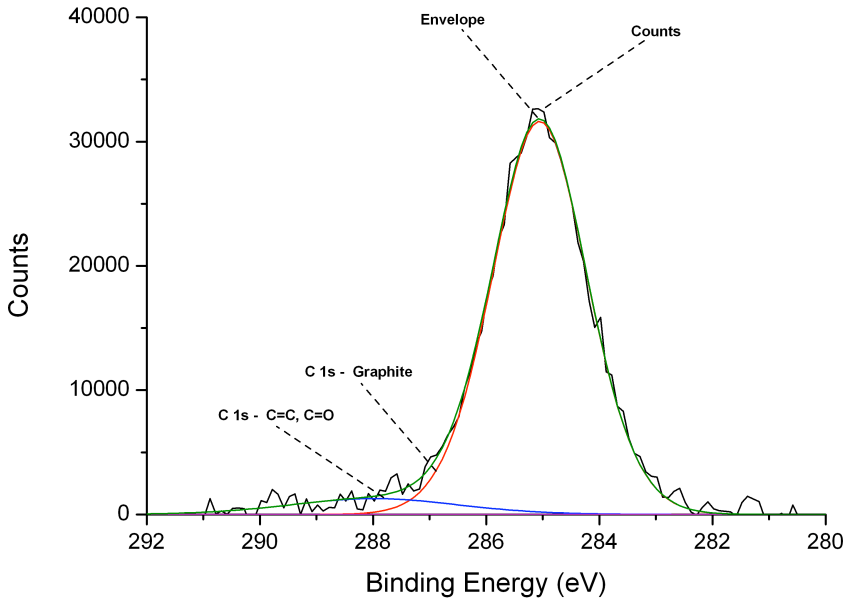

Figure 38: XPS peak for C 1s deconvulated to graphitic carbon and compounds with carbon-carbon and carbon-oxygen double bonds.

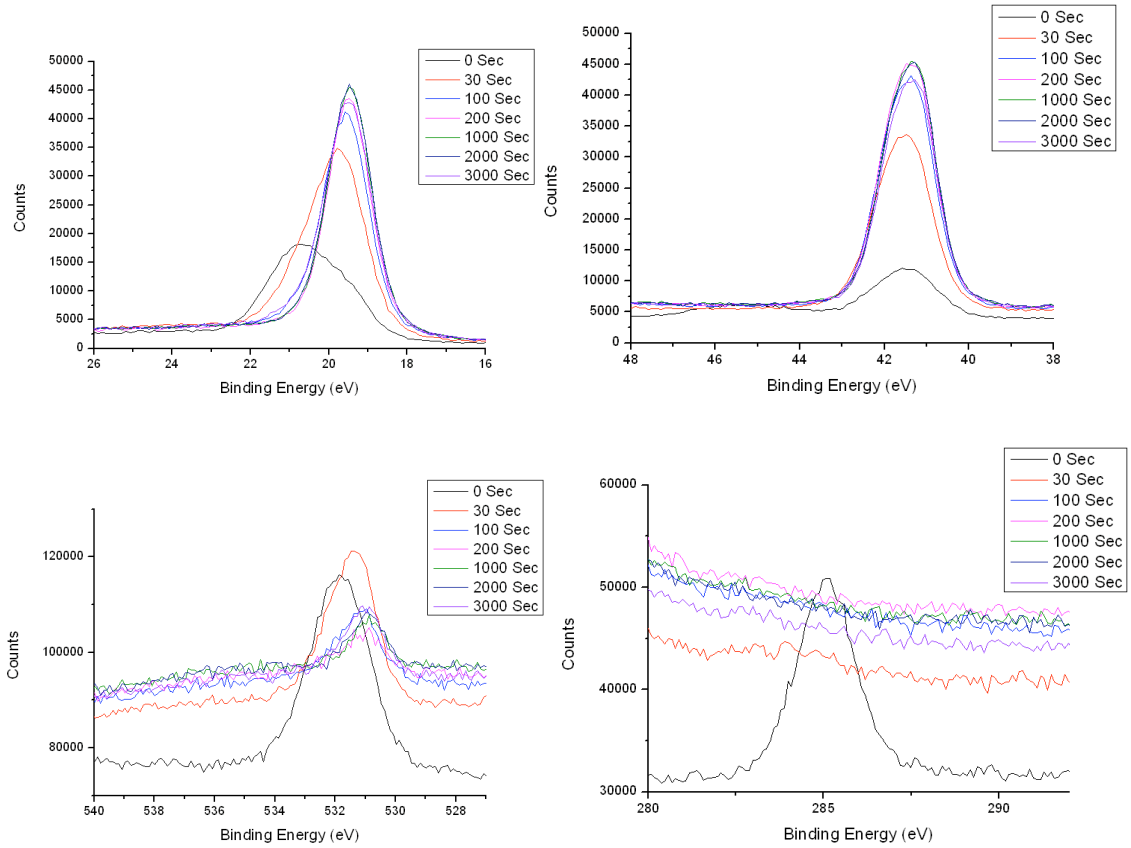

Figure 39: XPS depth profiling. Top left Ga 3d, top right As 3d peak. Bottom left O 1s and bottom right is C 1s.

Depth profiling reveals that the oxide peak seen in the As 3d spectra disappears after 30 seconds of sputtering. This indicates that oxygen contamination is only on the surface. The energy of the As (GaAs) peak is 41.5 eV, which corresponds to what is seen in literature for GaAs. The gallium peak corresponding to GaAs is the only peak observed after 30 seconds of sputtering again indicating that the majority of the contaminants are surface bound. The peak for gallium oxide seen on the surface at 21 eV shifts to 19.5 eV when the sample has been sputtered for 30 seconds.

Therefore, the depth profiling XPS indicates that gallium oxide is only surface bound however looking at the EDX mapping shown earlier (Figure 34) it is clear there is still some oxygen contamination present in the bulk of the film near the substrate. This is not show in the XPS perhaps due to the sputtering not going deep enough into the film even after 3000 seconds.

The depth profiling for oxygen shows the peak for chemisorbed oxygen on the surface at 532 eV binding energy shifts to 531 eV after 30 seconds of sputtering, the peak shifts further to 530 eV after 100 seconds of sputtering.

The depth profiling spectra for carbon (Figure 39) shows that there is no carbon contamination after the first 30 seconds of sputtering as it shows the peak observed at 286 eV when the surface is analysed disappears after sputtering. This confirms what is seen in the EDX mapping (Figure 34).

4.1.4.8 Secondary Ion Mass Spectrometry (SIMS)

Secondary ion mass spectrometry was carried out on a film grown under condition **2** at deposition temperature of 500 ^{o}C with depth profiling until the substrate was reached. Arsenic was chosen as the reference element due to its relative sensitivity factor (RSF) (1×10^{21} atoms per cm^3) being higher than that of gallium (1×10^{24}). The concentrations of oxygen remained fairly stable at 4.66×10^{21} atoms per cm^3 from the top surface to the about 2.4 μm into the film, after which point there is a sudden jump to 4.37×10^{23} atoms per cm^3 when the substrate is reached and there is very little film left (Figure 40). The carbon concentration is lower at 3.41×10^{20} atoms per cm^3 and reduces to below 0.5×10^{20} atoms per cm^3 at a depth of 2.25 μm (Figure 40).

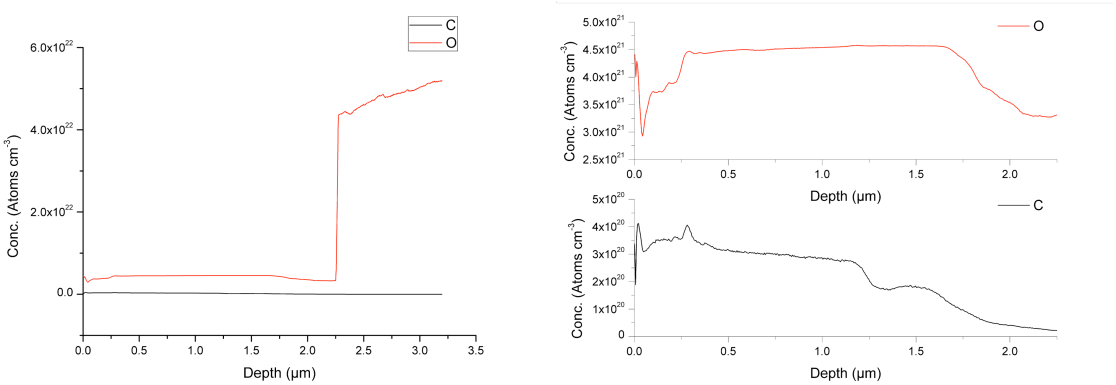

Figure 40: Left - Graph showing the levels of carbon and oxygen contamination in a film grown under condition 2 at 500 °C. Right – A detailed view of the change in carbon and oxygen between depth 0 – 2.25 μm.

Conclusion

Films were grown using $As(NMe_2)_3$ and $GaMe_3$ at a range of temperatures from 450, 500, 550 °C. Films at 450 °C were less crystalline than those grown at 500 °C and 550 °C. The crystallinity of the films increase with temperature as indicated by the crystallite size (determined by the Scherrer equation).

SEM images showed the films to have a structured morphology with large and sudden variations in thickness. This is not ideal for photovoltaic applications where, films with uniform thickness are required.

EDX shows the films to have 1:1 ratio of Ga to As when grown at 500 and 550 °C, but not at 450 °C. This is most like due to the film at the lower temperature (450 °C) being thin and the native oxide leading to the films to be Ga rich. STEM images taken of a film grown under condition **2** at 500 °C show that the film was polycrystalline with lots of grain boundaries. EDX mapping carried out indicate that Ga is bound to As throughout the film and that oxygen and carbon impurities are only surface bound. This is further supported by XPS analysis.

4.1.5 Experimental Methods

Nitrogen (99.9%, BOC) carrier gas was passed through activated sieves to remove moisture. Tris(dimethylamino)arsine (99%, Strem Chemicals Inc.) and Trimethylgallium (99.999%, SAFC Hitech Ltd.) were both used as bought. Toluene was stored in alumina columns and dried with anhydrous engineering equipment.

$As(NMe_2)_3$ (1.08 g, 5.2 mmol) was dissolved in toluene (10 mL) at -78 ^oC. $GaMe_3$ (0.4 g, 3.5 mmol) was dissolved in toluene (10 mL) at -78 ^oC. The $As(NMe_2)_3$ in toluene solution was added dropwise to the $GaMe_3$/toluene solution and the solution allowed to reach room temperature before deposition was carried out at 450, 500 and 550 ^oC. On completion of deposition the reactor was cooled under nitrogen until room temperature. The films were stored under air.

Chapter 5

5 GaAs thin films via *in situ* AACVD using $^{t}BuAsH_2$ and $GaMe_3$

5.1.1 Introduction

Gallium arsenide thin films were grown *via* AACVD in toluene using an *in situ* approach with tertiary butyl arsine as the arsine source and trimethyl gallium as the gallium source. The polycrystalline films were then analysed using material and optical characterisation techniques.

5.1.2 The Precursors

Tertiary butyl arsine is widely used in CVD as an alternative to arsine (AsH_3) as an arsenic source in the production of GaAs, InAs and other arsenic containing semiconductor materials. This is due to its reduced toxicity compared to AsH_3 and lower deposition temperatures required to grow films with similar properties. Like AsH_3, tertiary butyl arsine yields films with low carbon contamination, in spite of a direct As-C bond within the molecule, due to the presence of beta hydrogens that allow facile elimination of the organic group.

Trimethylgallium is a primary precursor for films containing gallium as it is volatile, non-toxic and produces films with low carbon contamination. However, its pyrophoric nature makes it difficult to handle.

5.1.3 Film Deposition

Thin films were grown using an *in situ* approach by mixing a solution of $^{t}BuAsH_2$ in toluene at -78 ^{o}C with a solution of $GaMe_3$ in toluene. The mixture was then allowed to reach room temperature and then the AACVD was undertaken. Various ratios of $^{t}BuAsH_2$ and $GaMe_3$ (ranging from 1.5:1 to 3:1 $^{t}BuAsH_2$ to $GaMe_3$ respectively) were tried at different temperatures in an effort to obtain stoichoimetric films, as shown in Table 9. The main aim, as with all films in this project was to deposit polycrystalline thin films with good crystallinity, large crystallite size and void of any contamination.

The films produced *via* the *in situ* route using $^{t}BuAsH_2$ and $GaMe_3$ were smooth, adherent and appeared grey/blue in colour under reflected light. They were adherent to

the substrate passing the Scotch tape test but were scratched by a stainless steel and brass stylus.

Condition	$^{t}BuAsH_2$ / g	$GaMe_3$ / g	$^{t}BuAsH_2$:$GaMe_3$	Temp. / ^{o}C	Solvent	Volume / mL	Dep. Time / mins
4	0.5	0.29	1.5:1	500	Toluene	30	120
5	0.5	0.29	1.5:1	550	Toluene	30	120
6	0.5	0.21	2:1	500	Toluene	30	120
7	0.5	0.21	2:1	550	Toluene	30	120
8	0.74	0.21	3:1	500	Toluene	30	120
9	0.74	0.21	3:1	550	Toluene	30	120

Table 9: Table showing the deposition conditions used for the *in situ* AACVD growth of GaAs from $^{t}BuAsH_2$ and $GaMe_3$

5.1.4 Analysis

5.1.4.1 Powder X-Ray Diffraction (XRD)

Film crystallinity was investigated using, X-ray powder diffraction (XRD). XRD of the films grown under the six different conditions confirms that they were polycrystalline GaAs. The patterns match well to the standard XRD pattern for polycrystalline GaAs (Figure 22). Peaks corresponding to cubic GaAs [111], [220] and [311] were observed at 27.3^{o}, 45.4^{o}, 53.7^{o} respectively (Figure 41, Figure 42 and Figure 43). The small shoulder on the [111] peak at 27.3^{o} corresponds to graphitic carbon.

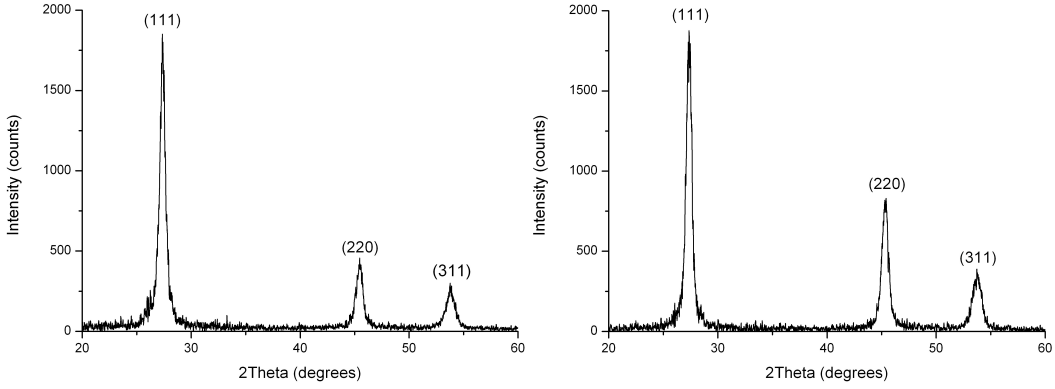

Figure 41: Powder XRD pattern for sample grown under condition 4 (left) and 5 (right), at 500 and 550 ^{o}C respectively with $^{t}BuAsH_2/GaMe_3$ ratio was 1.5:1 in the solution.

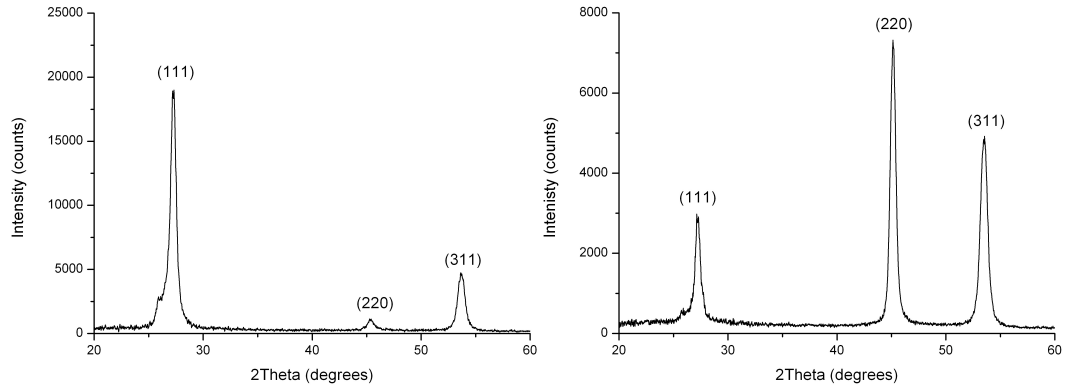

Figure 42: Powder XRD pattern for sample grown under condition 6 (left) and 7 (right), at 500 and 550 ^{o}C respectively with $^{t}BuAsH_2/GaMe_3$ ratio was 2:1 in the solution.

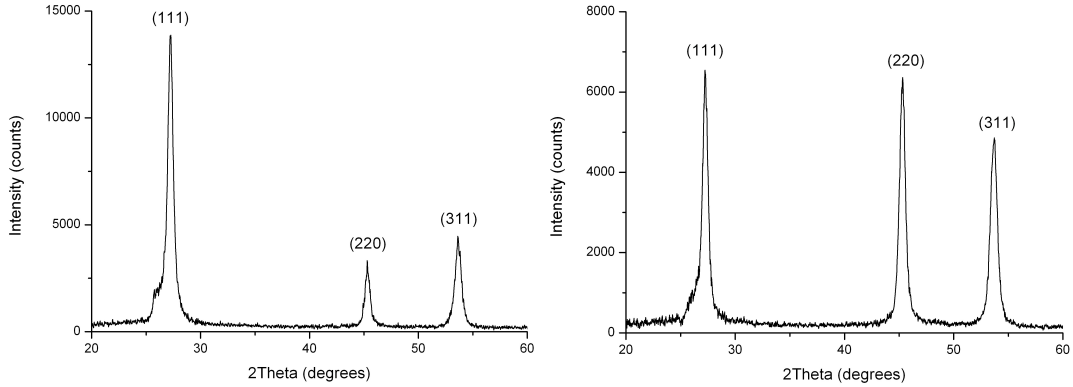

Figure 43: Powder XRD pattern for sample grown under condition 8 (left) and 9 (right), at 500 and 550 ^{o}C respectively with $^{t}BuAsH_2/GaMe_3$ ratio was 3:1 in the solution.

The expected trend of an increase in crystallinity with increasing deposition temperature was observed in the films obtained from these experiments. This is indicated by the decrease in the average full width half maximum (FWHM) of the peaks with increasing deposition temperature. This observation is true for all conditions apart from **8** and **9** where the film grown at 500 ^{o}C (condition **8**) is more crystalline than that grown at 550 ^{o}C (condition 9).

Condition	FWHM / ^{o}			Average FWHM / ^{o}
	(111)	(220)	(311)	
4	0.746	0.760	1.013	0.840 ± 0.15
5	0.578	0.699	0.986	0.754 ± 0.21
6	0.633	0.700	0.780	0.704 ± 0.07
7	0.552	0.605	0.716	0.624 ± 0.08
8	0.596	0.500	0.640	0.579 ± 0.07
9	0.601	0.658	0.739	0.666 ± 0.07

Table 10: The average FWHM of the peaks in the XRD pattern for the films grown under the six different conditions.

The crystallite size of the polycrystalline films was also calculated using the Scherrer equation using Corundum/aluminium oxide as the standard to determine the extent of peak broadening caused by the instrument. Under all six conditions the films have small crystallites under 20 nm in diameter, which is small compared to the crystallites observed in films grown using the single-source precursor $[Me_2GaAs(H)^{t}Bu]_2$ (**47**), obtained from the reaction between $^{t}BuAsH_2$ and $GaMe_3$ (see chapter 6). The average crystallite as worked out from the Scherrer equation for the single-source films was 18 nm for films grown at 500 ^{o}C and 34 nm for films grown at 550 ^{o}C. However these crystallite sizes are larger than those observed for the films obtained *via* the other dual source/ *in situ* method of $As(NMe_2)_3$ and $GaMe_3$.

Condition	Average crystallite size / nm
4	11 ± 2
5	13 ± 3
6	14 ± 3
7	16 ± 2
8	17 ± 2
9	14 ± 2

Table 11: The average crystallite size of the films grown under the six different conditions.

As expected, there is an increase in crystallite size with increasing deposition temperature. This is because normal grain growth is determined by the minimization of the total free energy through the reduction in the number of grain boundaries and hence the energy associated with grain boundaries.[121] Higher deposition temperatures allow the adatoms on the substrate to find the lowest energy site before nucleation (as they have more kinetic energy) and therefore films with larger grains are produced.

Slightly larger grains were also obtained when the $^{t}BuAsH_2$ to $GaMe_3$ ratio increases (Figure 44 and Table 11). For example, at 500 ^{o}C the average crystallite goes from 11 ± 2 nm at 1.5:1 ($^{t}BuAsH_2$: $GaMe_3$) to 17 ± 2 nm when the $^{t}BuAsH_2$: $GaMe_3$ ratio is 3:1. This was most likely due to the films becoming more stoichoimetric with increasing $^{t}BuAsH_2$ in excess.

It must be noted that the error associated with the Scherrer equation is significant enough that it is difficult to distinguish between values with the same order of magnitude. However, the Scherrer equation gives a good indication of the trends in crystallite size with varying conditions such as deposition temperature and precursor concentration(s).

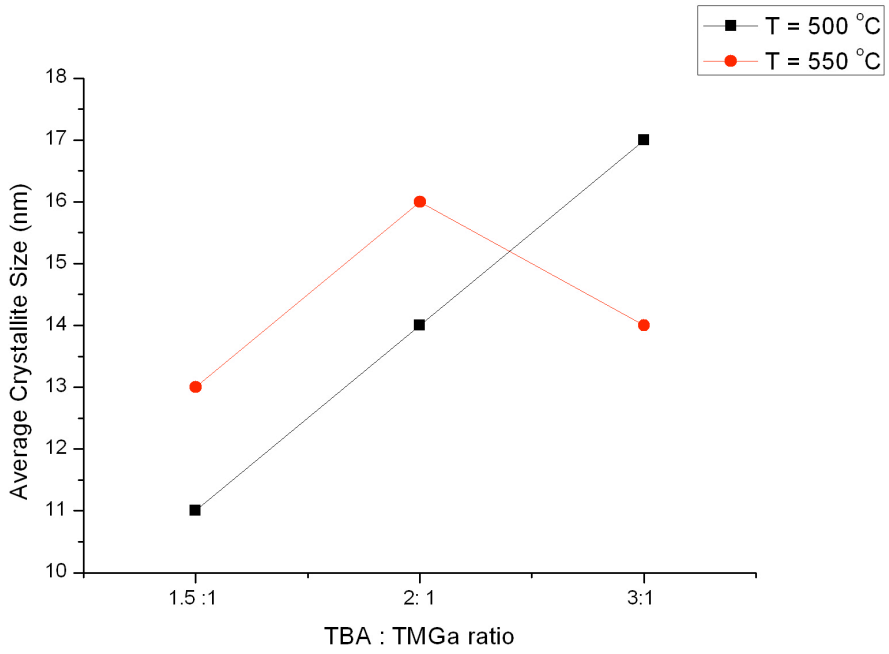

Figure 44: The change in crystallite size with $^{t}BuAsH_2$ to $GaMe_3$ ratio for the two temperature regimes tested.

	Condition **4**					
hkl	Bragg Angle 2θ/°	Peak Width 'β'/°	Instrument resolution/°	Corrected 'β'	Diameter/ nm	Ave. Crystallite Size / nm
111	27.34	0.746	0.080	0.666	12	11(±2)
220	45.41	0.760	0.055	0.705	12	
311	53.79	1.013	0.065	0.948	9	
	Condition **5**					
111	27.35	0.578	0.080	0.498	16	13(±3)
220	45.33	0.699	0.055	0.644	13	
311	53.74	0.986	0.065	0.922	10	
	Condition **6**					
111	27.24	0.633	0.080	0.553	15	13(±2)
220	45.28	0.700	0.055	0.645	13	
311	53.64	0.780	0.065	0.715	12	
	Condition **7**					
111	27.23	0.552	0.080	0.472	17	16(±2)
220	45.15	0.605	0.055	0.550	16	
311	53.50	0.716	0.065	0.651	14	
	Condition **8**					
111	27.25	0.596	0.080	0.516	16	17(±2)
220	45.30	0.500	0.055	0.445	19	
311	53.62	0.640	0.065	0.575	15	
	Condition **9**					
111	27.24	0.601	0.080	0.521	16	14(±2)
220	45.31	0.658	0.055	0.603	14	
311	53.70	0.739	0.065	0.674	13	

Table 12: Table showing the change in crystallite size in the films grown under the six different deposition conditions.

Though the XRD shows the expected peaks of the films for polycrystalline GaAs compared to the standard (Figure 22), it is apparent that the intensity of the peaks were not as expected. Therefore indicating that there is preferred orientation in the films. Furthermore there is a change in preferred orientation with change in deposition temperature and ^{t}BuAsH to $GaMe_3$ ratio. The crystallographic preferred orientation can be determined by calculating the intensity ratio (α) for each peak in each pattern, according to:

$$\alpha = \frac{I_{(h'k'l')}}{\sum I_{(hkl)}} \qquad \textbf{(5.1)}$$

Where $I_{(h'k'l')}$ is the intensity of the peak of interest and $\Sigma_{(hkl)}$ is the sum of intensities of all the peaks in the diffractorgram. If this is applied the randomly orientated GaAs standard pattern shown in Figure 22 the values are as follow:

(111)	(200)	(220)	(311)	(222)
0.53	0.01	0.26	0.20	0.01

Table 13: The intensity ratio (α) for the (111), (200), (220), (311) and (222) peaks for the standard GaAs.

Table 14 shows the extent of preferred orientation for each peak observed from the films. The most intense peak for films grown under condition **4**,**5**,**6** and **8** is the (111) as in the standard (Figure 11) however the relative intensity of the (111) is much more compared to the other peaks in the films grown under condition **4**,**5**,**6** and **8** than in the standard. This shows that there is preferred orientation in these samples for the (111) plane. Films grown under condition **1** and **3** have the most preferred orientation in the (111) direction.

The films grown under condition **7** (550 ^{o}C using a 2:1 ratio of $^{t}BuAsH_2$ and $GaMe_3$) and **9** (550 ^{o}C using a 3:1 ratio of $^{t}BuAsH_2$ and $GaMe_3$) have preferred orientation in the (220) and (311) directions. This suggest that using these precursors, a deposition temperature of 550 ^{o}C leads to preferred orientation in the (220) and (311) planes where

as lower deposition temperature of 500 ^{o}C leads to preferred orientation in the (111) direction.

Condition	(111)	(220)	(311)
4	0.71	0.18	0.11
5	0.61	0.27	0.13
6	0.76	0.05	0.19
7	0.19	0.48	0.32
8	0.56	0.13	0.18
9	0.43	0.42	0.32

Table 14: Intensity ratio (α) for the (111), (220) and (311) peaks showing the changes in preferred orientation with deposition condition.

5.1.4.2 Energy Dispersive X-Ray (EDX) analysis

EDX analysis was carried out to determine the stoichoimetry of the thin films grown under the different conditions. The results indicate only a small change in Ga to As ratio in the films with changes in $^{t}BuAsH_2$ to $GaMe_3$ ratio in the precursor solution.

Condition **4**			Condition **5**		
Regions	Gallium / Atomic %	Arsenic / Atomic %	Regions	Gallium / Atomic %	Arsenic / Atomic %
1	58.4	41.6	1	54.8	45.2
2	57.6	42.4	2	53.9	46.1
3	57.8	42.2	3	55.4	44.6
Average	**57.9(±0.4)**	**42.1(±0.4)**	**Average**	**54.7(±0.8)**	**45.3 (±0.8)**
Condition **6**			Condition **7**		
Region	Gallium / Atomic %	Arsenic / Atomic %	Regions	Gallium / atomic %	Arsenic / atomic %
1	54.2	45.8	1	54.1	45.9
2	54.0	46.0	2	54.5	45.5
3	54.1	45.9	3	54.5	45.5
Average	**54.1(±0.1)**	**45.9(±0.1)**	**Average**	**54.4(±0.2)**	**45.6(±0.2)**

Condition **8**			Condition **9**		
Region	Gallium / Atomic %	Arsenic / Atomic %	Region	Gallium / Atomic %	Arsenic / Atomic %
1	53.1	46.9	1	53.1	46.9
2	53.4	46.7	2	53.0	47.0
3	53.6	46.4	3	53.2	46.8
4	53.3	46.7	4	53.4	46.6
Average	**53.3(±0.2)**	**46.7(±0.2)**	**Average**	**53.2(±0.2)**	**46.8(±0.2)**

Table 15: EDX results for various spots on the films grown under the 6 different conditions. The average values are given at the bottom of each table in bold.

There were two variables that were changed for the six experiments, namely deposition temperature and $^{t}BuAsH_2$ to $GaMe_3$ ratio (Table 5). A change in deposition temperature from 500 ^{o}C to 550 ^{o}C does not have any effect on the gallium to arsenic atomic ratio for films that are sufficiently thick like in these cases. The limiting factor is the extent of $^{t}BuAsH_2$ excess; there is roughly a 5% decrease in the Ga excess in the films when the $^{t}BuAsH_2$ to $GaMe_3$ ratio is increased from 1.5:1 to 3.1. The change in Ga:As ratio in the film observed when going from 1.5:1 to 2:1 or 2:1 to 3:1 is within the error of the instrument therefore it can be assumed the change is negligible.

5.1.4.3 Scanning Electron Microscopy (SEM)

SEM images were taken at various magnifications in secondary electron mode to give an overall picture of the morphology. The images indicate that there is some structured film growth in some cases (condition **4**) resulting in non-ideal morphology that contain many boundaries within groups of crystallites.

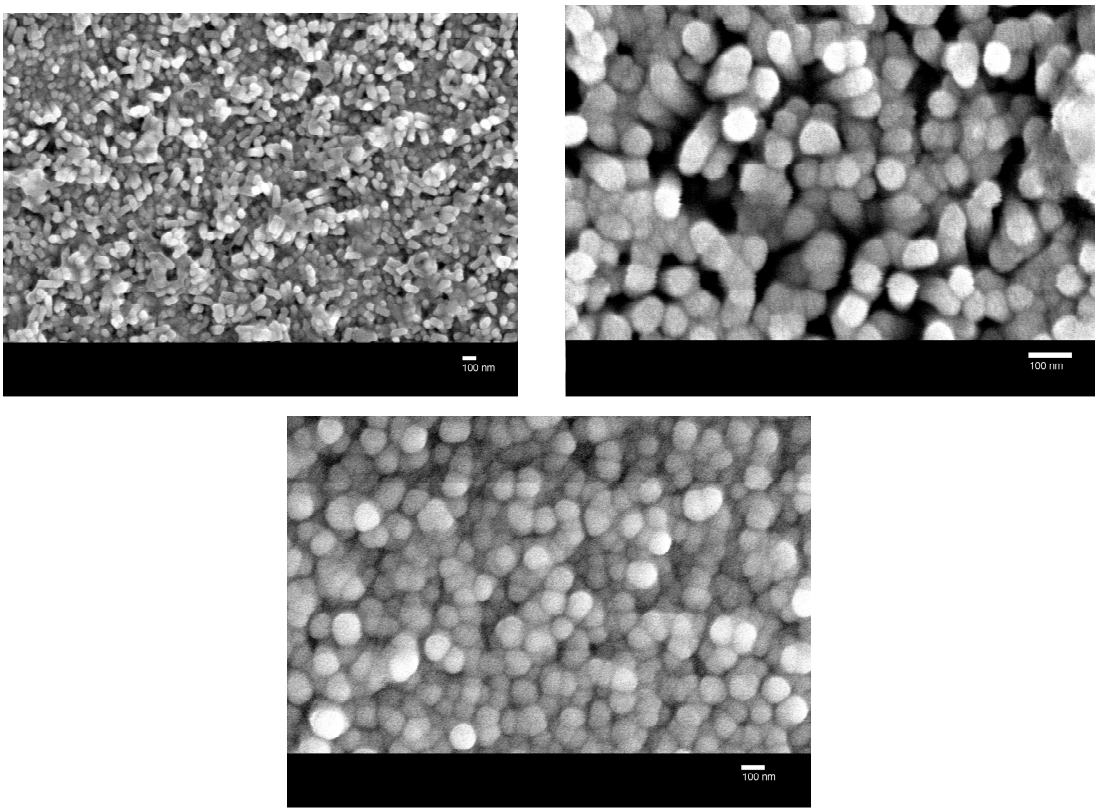

Figure 45: SEM image of films grown under condition 4, 500 ^{o}C using 1.5:1 ratio of $^{t}BuAsH_2$ and $GaMe_3$ in toluene. The images show the films to have almost needle-like features most likely in the (111) direction as indicated by the XRD preferred intensity calculations.

The morphology of the films grown under condition **4** have spherical grains (cluster of crystallites) as shown in Figure 45. In regions of the substrate (i.e the centre) where the films are the thickest, due to this being the hottest part of the substrate, these spheres have grown to almost needle-like features in probably the (111) direction as indicated by the XRD preferred orientation study (Table 14). This is different to what was observed for the films grown using the single-source precursor $[Me_2GaAs(H)^{t}Bu]_2$ (**47**) (Chapter 6) where the morphology is very flat, compact and almost featureless.

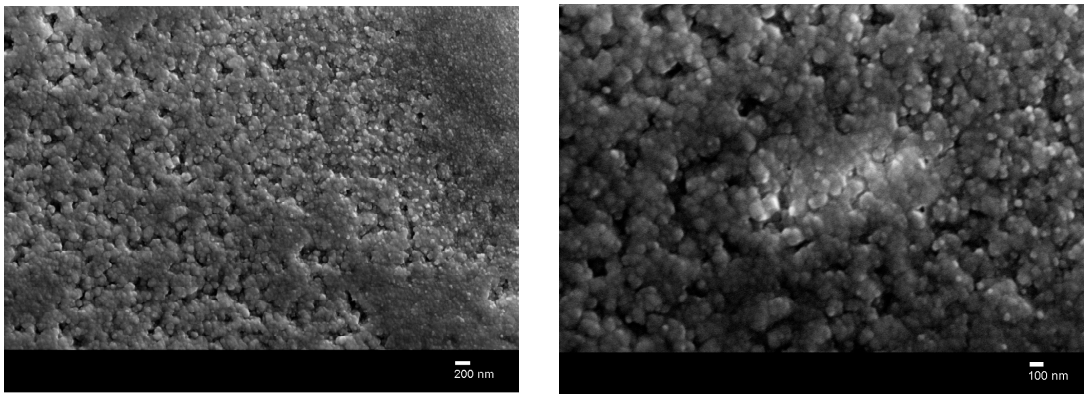

Figure 46: SEM images of films grown under condition 5, 550 ^{o}C with 1.5:1 ratio of $^{t}BuAsH_2$ and $GaMe_3$ in toluene. The needle like features seen previously has coalesced together to form a more uniform and smooth film.

The morphology of the films grown under condition **5 (**Figure 46**)** were not as featured and it appears that the spherical or needle-like features observed in films grown under condition **4** (Figure 45) have coalesced together to form larger and flatter regions. From the image taken at higher magnification it is possible to see that the spherical morphology is still present but in larger clusters. This has occurred under this condition because the higher deposition temperature has allowed nucleation of the adatoms to take place at lower energy sites on the substrate, as the species are more mobile due to their higher kinetic energy. This in turn has resulted in larger nucleated features.

5.1.4.4 High Resolution Transmission Spectroscopy (HRTEM)

HRTEM was preformed on films grown under condition **8** and **9** to obtain detailed information about the structure within the bulk of the film as well as grain/crystallite size information.

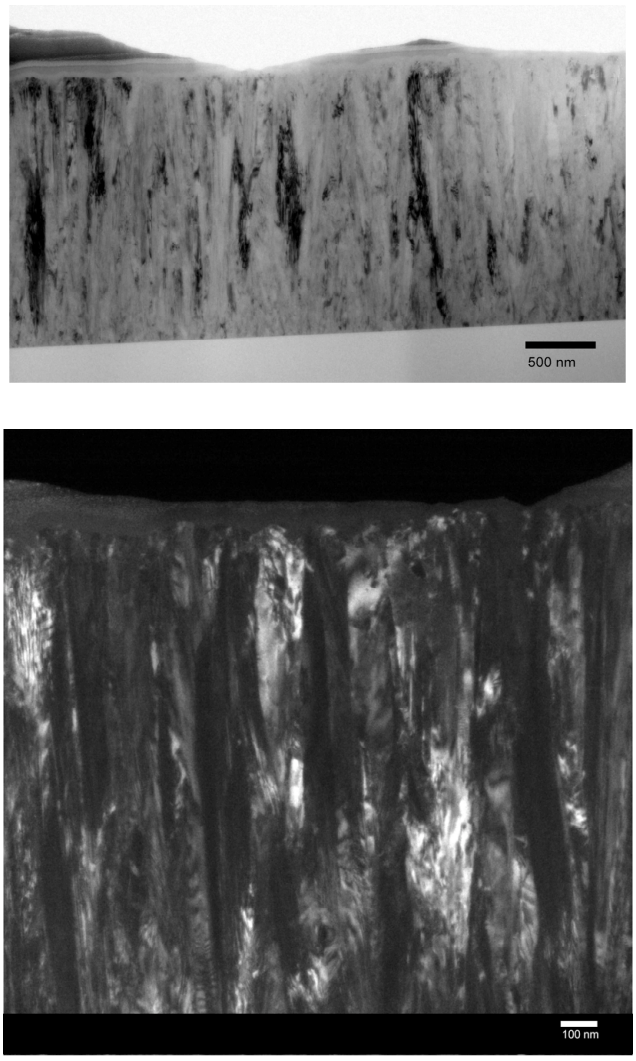

Figure 47: HRTEM light field (top) and dark field (bottom) of a film grown under condition 8, 500 ^{o}C using 3:1 ratio of $^{t}BuAsH_2$ and $GaMe_3$ in toluene.

The thickness of a sample film grown under condition **8** was determined using side on TEM. The TEM images reveal that the film was roughly 1.9 μm and the darkfield image in Figure 47 shows that there is good columnar growth present. This is ideal for photovoltaic applications as it means that there are less grain boundaries in the vertical direction. Films grown under condition **9** were even thicker at 2.7 μm (Figure 48), since they were grown at the higher temperature of 550 ^{o}C. There is less columnar growth here (Figure 48) than seen in the previous film grown under condition **8** (Figure 47) and

this is unusual because with increasing temperature of a system prone to columnar grown should exhibit more columnar structure. This was unexpected and could just be in this particular sample analysed. The columnar structure observed in the film grown under condition **8** is the best seen for the films analysed, even better than the films grown using the single-source precursor, $[Me_2GaAs(H)^{t}Bu]_2$ (**47**) (Chapter 6).

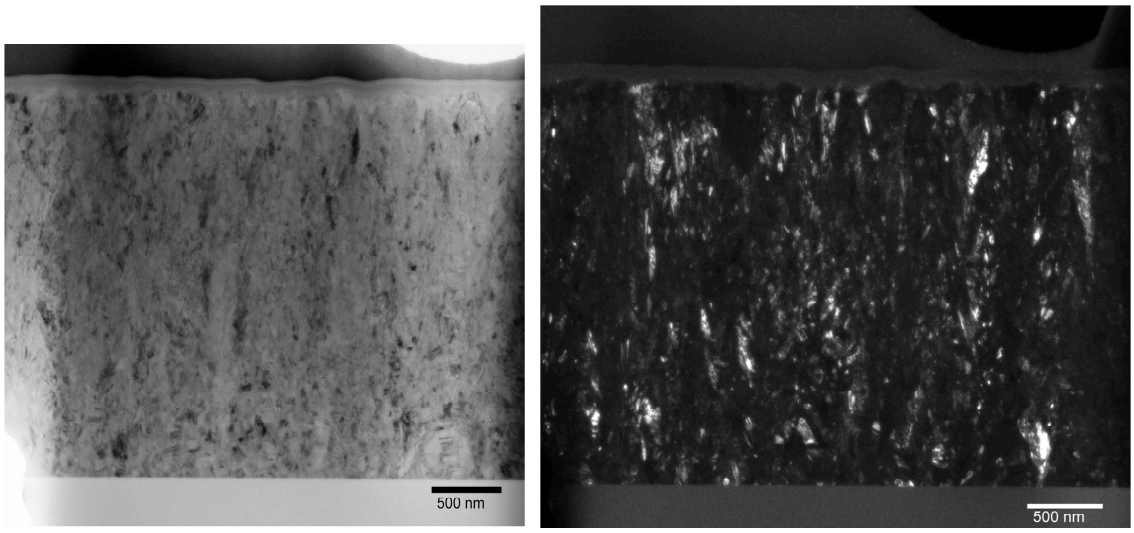

Figure 48: Lightfield (left) and Darkfield (right) image of a film grown under condition 9, 550 ^{o}C with 3:1 ratio of $^{t}BuAsH_2$ and $GaMe_3$ in toluene.

The grain distribution in the films grown under Condition 8 and 9 (Figure 49 and Figure 50) are as expected with larger grains found near the top of the film than at the bottom. This is because the bottom layers act as templates and provide a more crystalline surface for growth as opposed to the amorphous substrate. For films grown under condition 8 (Table 5) the average grain size in the bottom region is 30 nm and the average near the top is 66 nm (Table 11). The distribution near the top is more varied, i.e. there are grains 20 nm big as well as grains 160 nm. The distribution range in the lower region is not as wide and is only between 10-55 nm. HRTEM analysis shows the grain size in the films to be larger than the grain sizes calculated using the Scherrer equation (17 nm) (Table 11), however this is not unexpected as there are many assumptions and errors associated with the Scherer technique for grain size determination.

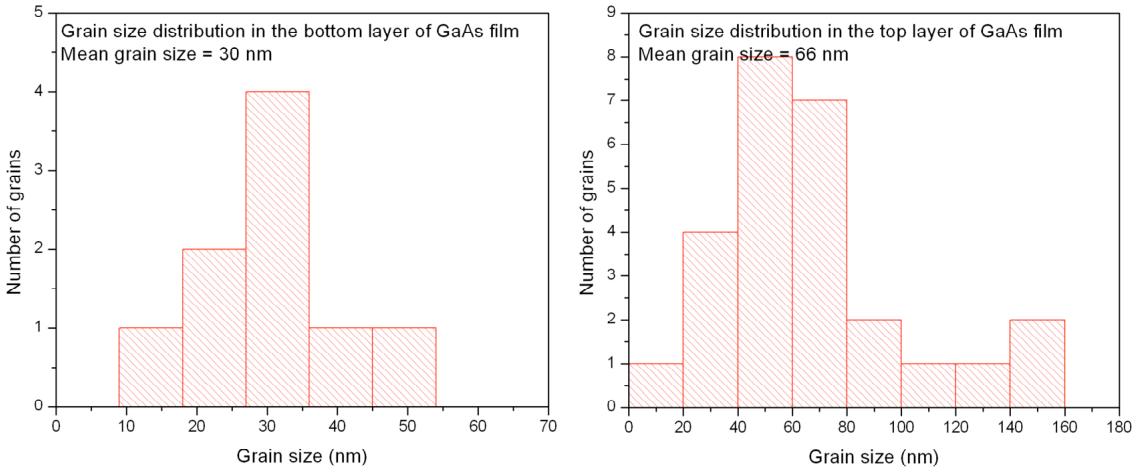

Figure 49: Shows the grain distribution in both the bottom (left) and top (right) region of the sample film grown under condition 8.

The grain size distribution in the film grown under condition **9** is much more even with both the bottom and top regions having similar grain sizes (Figure 50). The average grain size in the bottom region is 46 nm and the average grain size in the top region is 50 nm. This could be due to lack of columnar grown observed in the film. Also, films grown at 500 ^{o}C (condition **8**) have a larger grain sizes than that grown at 550 ^{o}C (condition **9**).

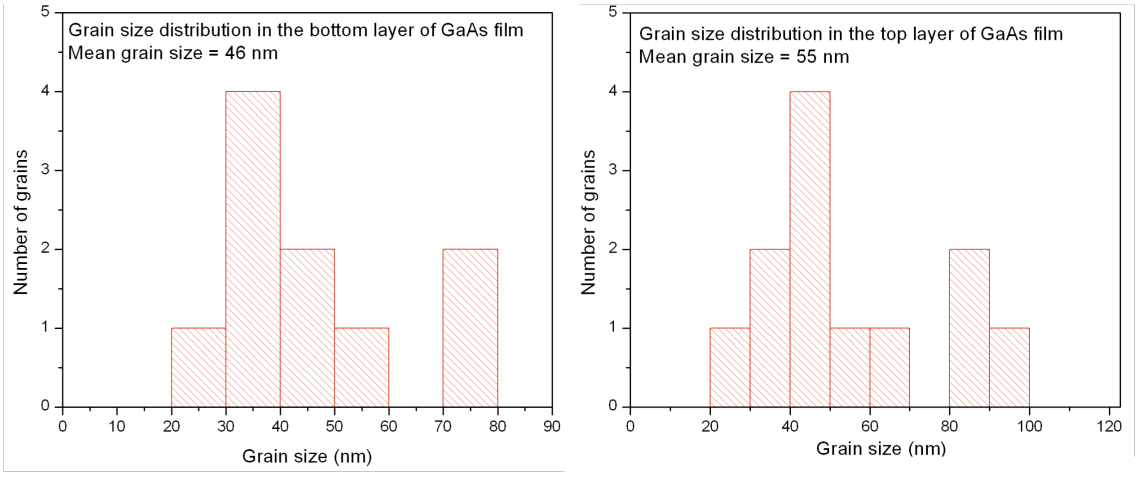

Figure 50: The grain size distribution in the top (left) and bottom (right) of film grown under condition 9.

In general the grain sizes determined using HRTEM are much larger than those calculated using the Scherrer equation. The HRTEM data is more reliable as it is a direct method for determining the grain size.

HRTEM images of the top and central regions of the films grown *via* condition **8** and **9** (Figure 51 and Figure 52) show there to be many grain boundaries as expected due to the small grain size within the polycrystalline films.

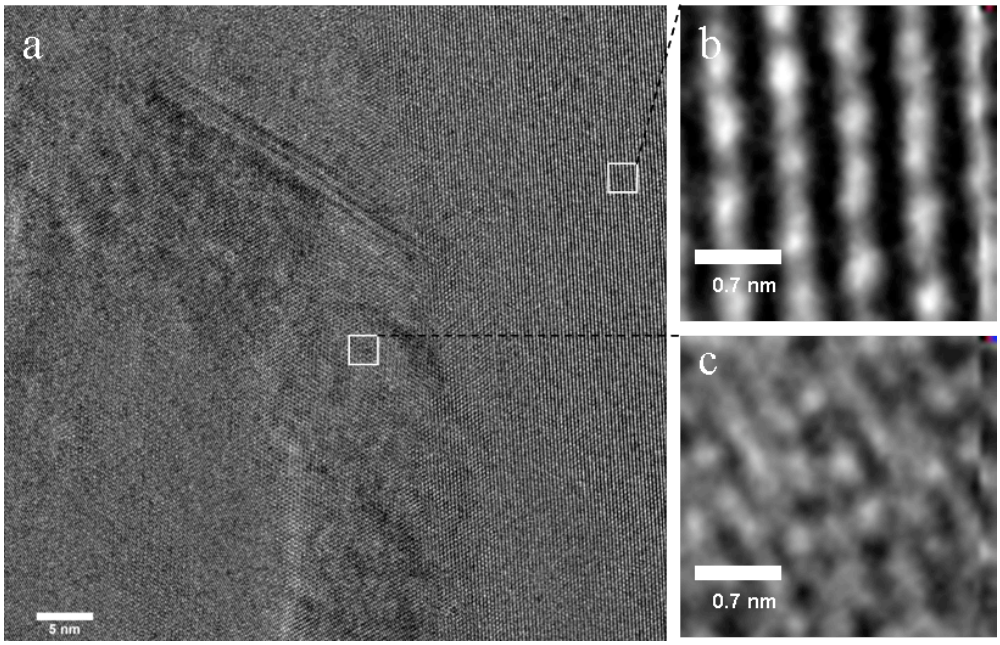

Figure 51: HRTEM of the top region of a film grown under condition 8 at 500 ^{o}C using 3:1 ratio of $^{t}BuAsH_2$ and $GaMe_3$ in toluene. There are many grain boundaries in the film. b) The magnified image of a more crystalline region shows that the lattice fringes are well spaced. c) A magnified image of a less crystalline region of the film, where the lattice fringes are difficult to make out.

The HRTEM of the top region of a film grown under condition **8** show that the lattice fringes are well spaced in the highly crystalline regions of the film but they are less well defined than seen in the HRTEM images of the previous films grown using $As(NMe_2)_3$ and $GaMe_3$ under the same temperature (Figure 31, Chapter 4). The poorly crystalline regions of the sample show a lack of definition in the lattice fringes.

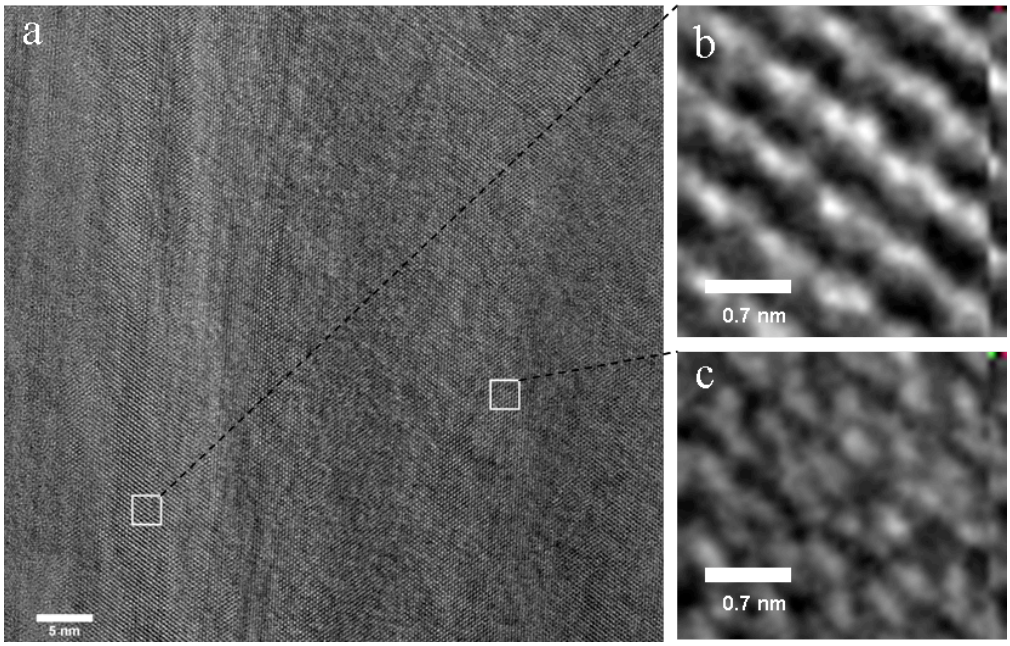

Figure 52: HRTEM of the central region of a film grown under condition 9 at 550 ^{o}C using 3:1 ratio of $^{t}BuAsH_2$ and $GaMe_3$ in toluene. There are many grain boundaries film, more than in the top region of the film. b) The magnified image of a more crystalline region shows that the lattice fringes are not well spaced. c) A magnified image of a less crystalline region of the film.

In the central region the film shown in Figure 52 appears less crystalline with the lattice fringes less well defined than for the film grown under condition 8 (Figure 51). Comparing the top and central regions of the film grown under condition **8** using HRTEM (Figure 51 and Figure 52) it is possible to see that the central region is less crystalline. This is due to the grains in the central region of the films being smaller in size than the top region, as indicated by the grain size distribution study shown in Figure 49.

Film grown under condition **9**, at 550 ^{o}C, was also analysed using HRTEM (Figure 53 and Figure 54). The top region is more crystalline than the central as expected due to the size of the crystallites being larger near the top. In both regions the lattice fringes are well defined and separated. The film grown under condition **9** are more crystalline than that grown under condition **8** as expected due to the higher temperature of deposition.

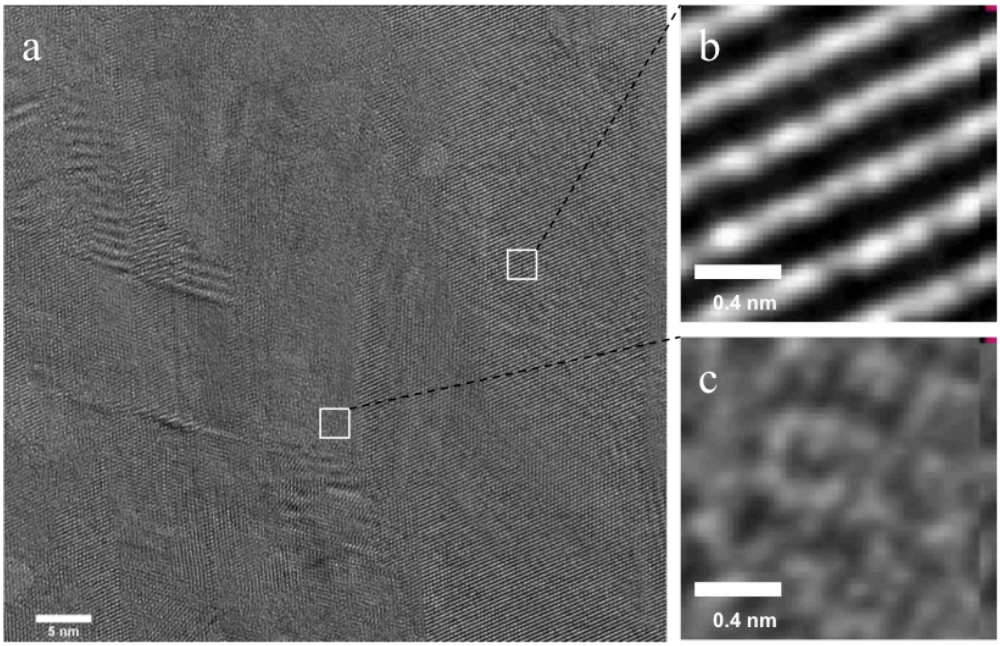

Figure 53: HRTEM image of the top region of a film grown under condition 9, 550 ^{o}C using 3:1 ratio of $^{t}BuAsH_2$ and $GaMe_3$ in toluene. b) A magnified image of a crystalline region of the film shows that it is indeed highly crystalline with well sperated lattice fringes. c) A magnified image of a less crystalline region of the film with lack of lattice definition.

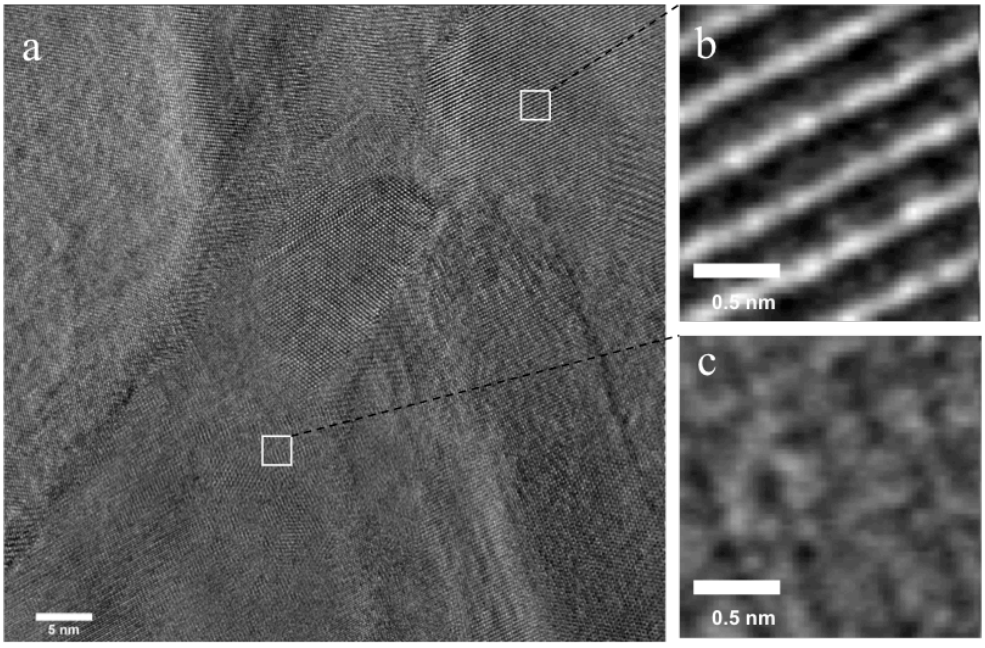

Figure 54: HRTEM image of the top region of a film grown under condition 9, 550 ^{o}C using 3:1 ratio of $^{t}BuAsH_2$ and $GaMe_3$ in toluene. b) A magnified image of a crystalline region of the film showing well spaced lattice fringes. c) A magnified image of a less crystalline region of the film.

5.1.4.5 Energy Dispersive X-Ray (EDX) mapping

EDX mapping was undertaken to test the purity of the films from the top to the bottom. A region of the film was analysed and tested for the arsenic, gallium, carbon, oxygen and silicon content. The results are displayed in the profile below.

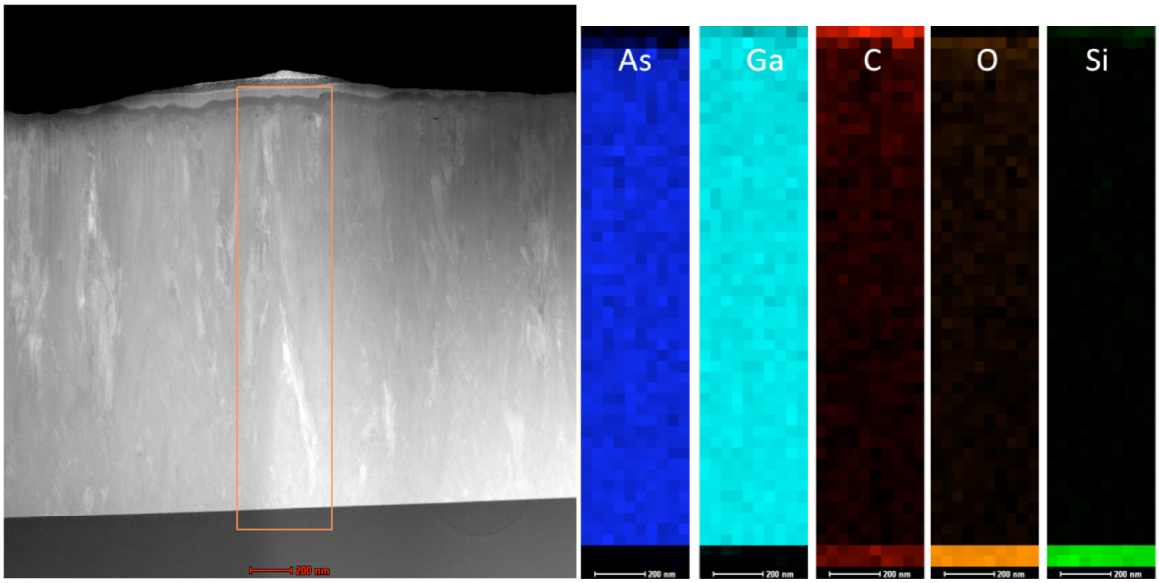

Figure 55: EDX mapping of a film grown under condition 8, 500 ^{o}C using 3:1 ratio of $^{t}BuAsH_2$ and $GaMe_3$ in toluene.

The region indicated on the STEM image on the left of Figure 55 was analysed and it showed that the gallium and arsenic distribution in the film was very uniform. Apart from carbon and oxygen contamination on the very top of the film there was no other contamination.

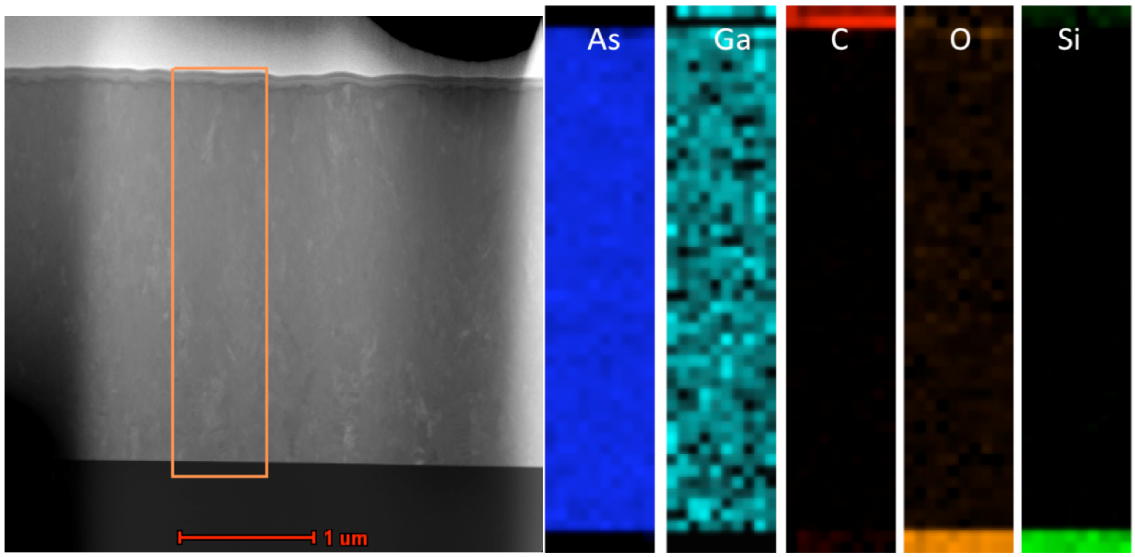

Figure 56: EDX mapping of a film grown under condition 9, 550 oC using 3:1 ratio of $^{t}BuAsH_2$ and $GaMe_3$ in toluene.

Similar to the results from condition **8** films (Figure 55), the EDX mapping of the region of the film shown in orange in the STEM image indicate that there is no contamination within the film, only on the surface of the films. The EDX mapping shows that they were very uniform in the distribution of Ga and As. Also there is minimal contamination apart from the top region where the film has been exposed to air and has formed a native oxide layer. This means that the contamination is post deposition as seen in the literature.

5.1.4.6 X-Ray Photoelectron Spectroscopy (XPS)

XPS along with depth profiling was performed to get a more detailed understanding of the structure of the films. XPS was only performed on the film grown under condition **8**. Deconvolution of the peaks observed showed the presence of GaAs along with the expected native oxide species, such as Ga_2O_3 and As_2O_3. Deconvolution of the sputtered regions was not attempted due to the error associated with the technique as a result of the differing sputtering rates of the gallium and arsenic.

.

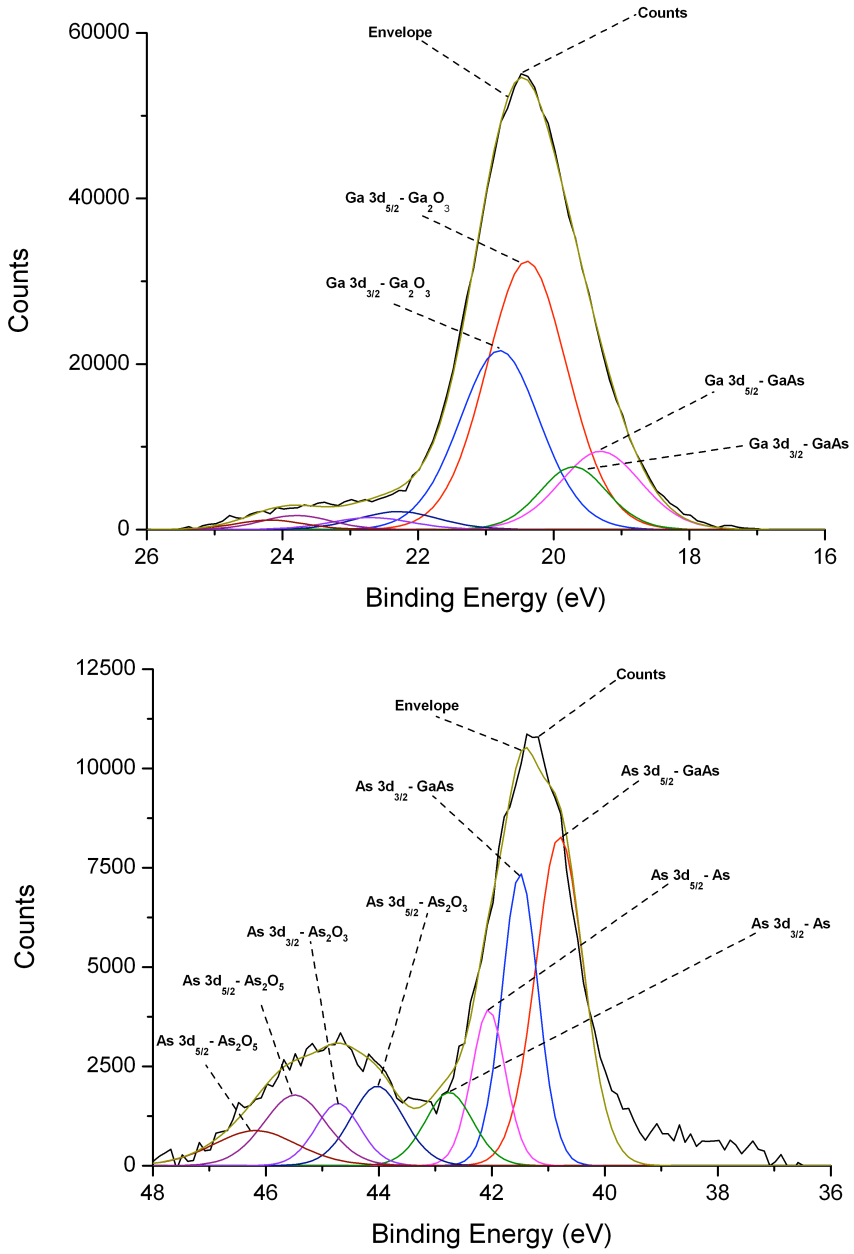

Figure 57: XPS spectra of the Ga 3d peak of a GaAs surface of sample grown under condition 8 (left) and XPS spectra of the As 3d peak of a GaAs surface of a sample also grown under condition 8 (right).

The Ga 3d peak was deconvulated to the Ga $3d_{5/2}$ and the Ga $3d_{3/2}$ (Figure 57). The position of the Ga $3d_{5/2}$ at a binding energy of 20.40 eV corresponds to Ga in the +3 oxidation state in the form of Ga_2O_3. This matches well with literature values.[122] The other Ga $3d_{5/2}$ peak at 19.31 eV is also at an oxidation state of +3 and corresponds to Ga attached to As, i.e. GaAs (Figure 57).[123]

The As 3d envelope was resolved into four different doublets, corresponding to GaAs (As 3d $_{5/2}$ with a binding energy of 40.49 eV)[124], As (with the As $3d_{5/2}$ binding energy of 41.75 eV)[125], As_2O_3 (with As 3d $_{5/2}$ with a binding energy of 43.72 eV) and As_2O_5 (with As 3d $_{5/2}$ binding energy of 45.18 eV) as shown in Figure 57.[126]

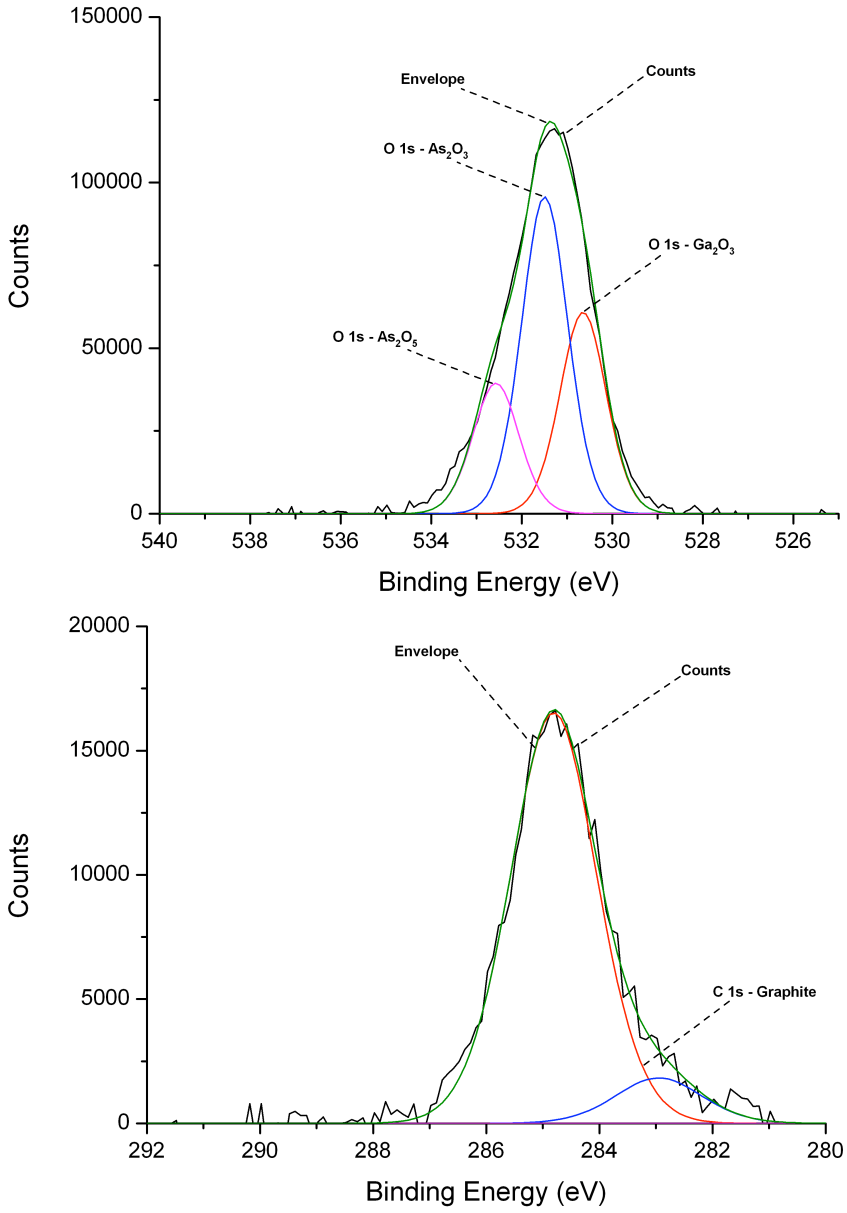

Figure 58: XPS spectra of the O 1s peak of a GaAs surface of a sample grown under condition 8.

The XPS peak for O 1s can be deconvoluted to three peaks corresponding to, Ga_2O_3 with a peak at 530.52 eV, As_2O_3 eV with a peak at 531.32 eV and As_2O_5 with a peak at 532.24 eV as reported in the literature.[127,128,129]

The XPS peak for C 1s can be deconvoluted into two peaks corresponding to graphitic carbon at 284.81 eV. The standard value for grahitic carbon is 284.5 eV, therefore the data can be calibrated to this value. The other peak appears at 282.65 eV and can be assigned to carbon bonded to silicon. This may be from contamination from silicon grease commonly used in the laboratory.[130]

Depth profiling shows that the arsenic oxide peaks seen at 42.17 eV and 44.13 eV binding energies disappears upon sputtering for 30 seconds, however the peak for Ga_2O_3 at 20.40 eV only disappears after sputtering for 1000 seconds (Figure 59). This indicates that there is oxygen contamination deep into the film, which was not revealed by EDX mapping shown earlier. The peak for oxygen at around 530 eV, corresponding to Ga_2O_3, As_2O_5 and As_2O_3 also takes 1000 seconds of sputtering before it disappears. This confirms what is seen in the Ga 3d spectra earlier. As predicted by the EDX mapping the carbon contamination is only surface bound, and the peak at 285 eV disappears after only 30 seconds of sputtering.

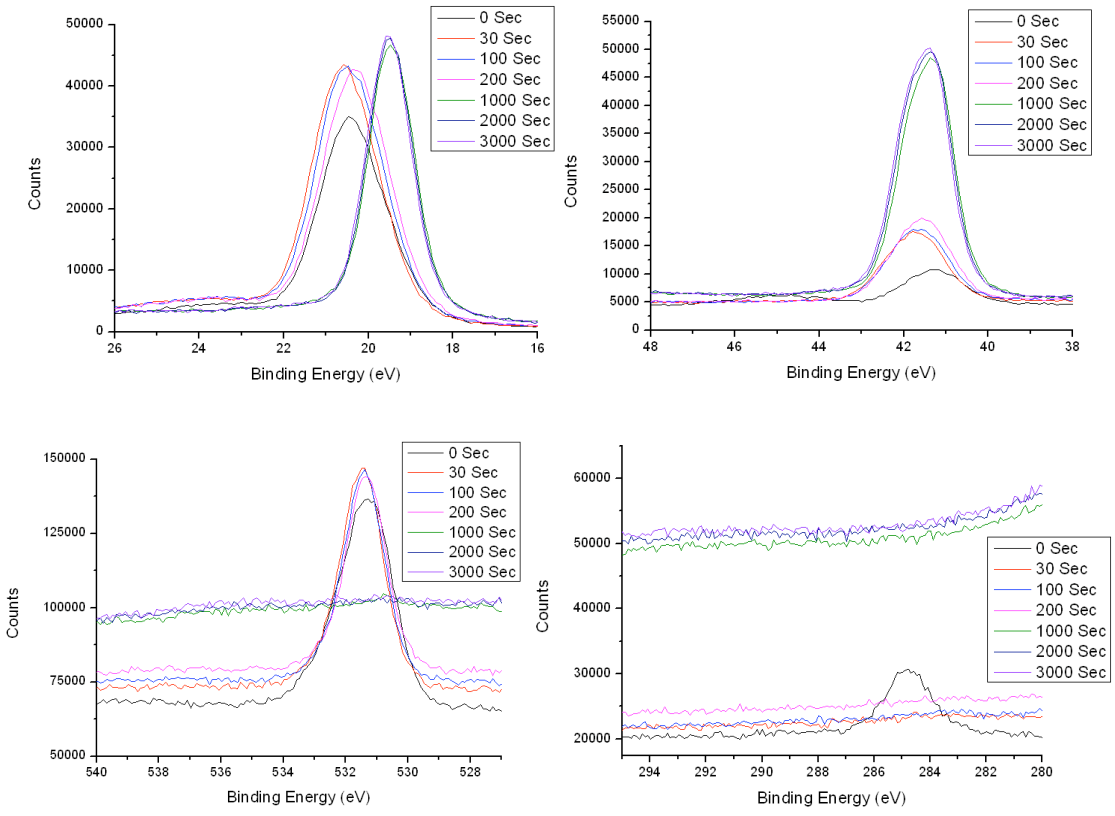

Figure 59: XPS depth profiling of Ga 3d peak (top left), As 3d peak (top right) depth, O 1s (bottom left), C 1s (bottom right) peaks.

5.1.4.7 Secondary Ion Mass Spectrometry

As a final measure of contaminant determination, secondary ion mass spectrometry was carried out to determine the concentration of carbon and oxygen within the film grown under condition **8** and **9**. The results are show in Figure 60. The atomic concentration of oxygen starts at $3.05x10^{21}$ atoms per cm^3 and remains at this level until 120 nm into the film. Then there is a sharp decrease to $4.30x10^{20}$ atoms per cm^3 at a film dept of 370 nm from the surface and the oxygen levels remain at this concentration until the substrate is reached at 1.75 μm into the film.

The carbon concentration in the film is much lower than oxygen and is only a surface phenomenon (Figure 60). On the surface of the film the concentration is $7.33x10^{20}$ atoms per cm^3 and it remains at this level only a few nanometers (40 nm) into the film. After which it stabilises at $1.97x10^{19}$ atoms per cm^3.

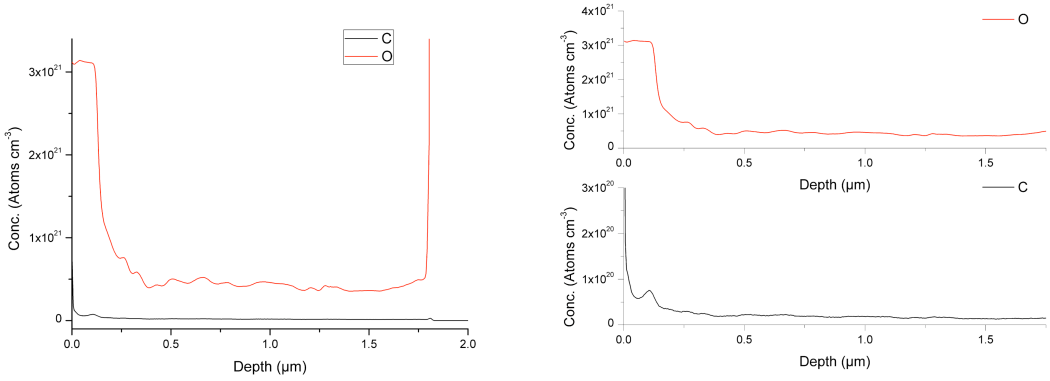

Figure 60: Graph showing the levels of carbon and oxygen contamination in a film grown under condition 8.

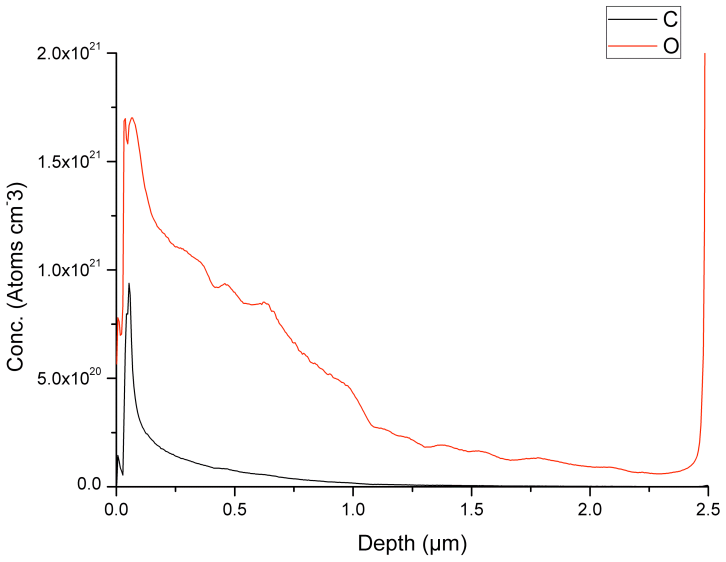

Figure 61: Graph showing the levels of carbon and oxygen contamination from SIMS analysis in a film grown under condition 9.

As seen in Figure 61 the concentration of oxygen starts at $1.69x10^{21}$ atoms per cm^3 and steadily drops to $2.94x10^{20}$ atoms per cm^3 which at film thickness of 1.1 µm. Then there is a further decrease in oxygen concentration until the glass substrate is reached at 2.4 µm.

The carbon concentration within the film follows the same pattern, however after the initial carbon concentration of $9.39x10^{20}$ atoms per cm^3 on the surface of the film, there is a sudden decrease to $3.00x10^{20}$ atoms per cm^3 after 100 nm followed by a gradual decrease to $1.07x10^{19}$ atoms per cm^3 at 1 µm deep into the film. After this point it remains at this level until the substrate is reached (Figure 61).

Comparing SIMS results of the two films grown under condition **8** and **9** (Table 5) shows that although the oxygen concentration starts off lower for films grown under condition **8** ($1.69x10^{21}$ atoms per cm^3) than under condition 6 ($3.05x10^{21}$ atoms per cm^3) it remains at $1.69x10^{21}$ atoms per cm^3 deep into the films and only reduced to $2.94x10^{20}$ atoms per cm^3 after 1 micron of etching. Whereas in film grown under condition **8**, the oxygen concentration reduces to $4.30x10^{20}$ atoms per cm^3 after a depth of 320 nm. The higher levels of contamination may explain the smaller crystallite sizes seen with both HRTEM and the Scherrer calculations.

5.1.5 Conclusion

Polycrystalline GaAs thin films were produced on glass substrates using an *in situ* approach using $^{t}BuAsH_2$ and $GaMe_3$. The films were grown at both 500 and 550 ^{o}C with varying ratios of the arsenic and gallium precursors (1:1 to 3:1). Analysis of the films showed that the films had good columnar growth that is ideal for photovoltaic applications. Oxygen and carbon contamination was only surface bound as revealed by the EDX mapping. Furthermore, all gallium atoms were bonded to arsenic atoms within the film. XPS studies showed that the surface of the films was contaminated with the native oxides (Ga_2O_3, Ga_2O_5 and As_2O_3) after sputtering these species as well as carbon compounds were eliminated.

The morphology of the films studied *via* SEM showed the films to be composed of spherical clusters that joined together to produce smooth and continuous films.

Over all the films produced from this precursor system were very good giving with good polycrystallinity and morphology. They also had low contamination levels. However stoichiometry was still an issues as films were arsenic deficient in spite of excess $^{t}BuAsH_2$ usage. This problem was overcome by syntheisising single source precursor from these precursors that contains the preformed Ga-As bond needed in the films.

5.1.6 Experimental Methods

Nitrogen (99.9%, BOC) carrier gas was passed through activated sieves to remove moisture. Tertiary butylarsine (99.99, Strem HAFC Hitech Ltd.) and Trimethylgallium (99.999%, SAFC Hitech Ltd.) were both used as bought. Toluene was stored in alumina columns and dried with anhydrous engineering equipment.

5.1.6.1 Condition 4 and 5

$^{t}BuAsH_2$ (0.5 g, 3.73 mmol) was dissolved in toluene (10 mL) at -78 ^{o}C. $GaMe_3$ (0.29 g, 2.53 mmol) was dissolved in toluene (10 mL) at -78 ^{o}C. The $^{t}BuAsH_2$ in toluene solution was added dropwise to the $GaMe_3$/toluene solution and the solution allowed to reach room temperature before deposition was carried out at 500 and 550 ^{o}C. On completion of deposition the reactor was cooled under nitrogen until room temperature. The films were stored under air.

5.1.6.2 Condition 6 and 7

$^{t}BuAsH_2$ (0.5 g, 3.73 mmol) was dissolved in toluene (10 mL) at -78 ^{o}C. $GaMe_3$ (0.21 g, 1.83 mmol) was dissolved in toluene (10 mL) at -78 ^{o}C. The $^{t}BuAsH_2$ in toluene solution was added dropwise to the $GaMe_3$/toluene solution and the solution allowed to reach room temperature before deposition was carried out at 500 and 550 ^{o}C. On completion of deposition the reactor was cooled under nitrogen until room temperature. The films were stored under air.

5.1.6.3 Condition 8 and 9

$^{t}BuAsH_2$ (0.74 g, 5.52 mmol) was dissolved in toluene (10 mL) at -78 ^{o}C. $GaMe_3$ (0.21 g, 1.83 mmol) was dissolved in toluene (10 mL) at -78 ^{o}C. The $^{t}BuAsH_2$ in toluene solution was added dropwise to the $GaMe_3$/toluene solution and the solution allowed to reach room temperature before deposition was carried out at 500 and 550 ^{o}C. On completion of deposition the reactor was cooled under nitrogen until room temperature. The films were stored under air.

Chapter 6

6 GaAs thin films via AACVD using $[R_2GaAs(H)^tBu]_2$

6.1.1 Introduction

This section details the deposition and characterization of polycrystalline GaAs thin films on amorphous substrates (glass). Films were deposited using the novel single-source precursors, $[Me_2GaAs(H)^tBu]_2$ and $[Et_2GaAs(H)^tBu]_2$, *via* aerosol-assisted chemical vapour deposition (AACVD) on borosilicate glass substrates under a range of conditions.

6.1.2 Aim

The overall target was to produce polycrystalline GaAs thin films with the correct stoichoimetry which cover 100% of the substrate after deposition. The films need to have the correct functional properties, such as band gap, so that photovoltaic devices can be made from them. Contaminants such as carbon and oxygen need to be minimised.

6.1.3 Precursor

The single-source precursors, $[R_2GaAs(H)^tBu]_2$ (R = Me, Et), were prepared from the reaction of trimethylgallium or triethylgallium and tertiary butylarsine in toluene at 80 ^oC, as shown in equation **6.1**. After work up, a yellow solid was isolated that forms colourless crystals when dissolved in minimum toluene and cooled to below room temperature. The ^1H NMR of $[Me_2GaAs(H)^tBu]_2$ (**47)** showed peaks corresponding to the two methyl groups on the gallium at 0.024 ppm and 0.084 ppm. Both of these peaks intergrate to 3 protons with respect to AsH peak observed at 2.56 ppm. The peak for the tertiary butyl group appeared at 1.43 ppm and corresponds to 9 protons as expected. The ^1H NMR for $[Et_2GaAs(H)^tBu]_2$ (**48**), shows the expected peaks at 0.86-1.01 corresponding to the $-CH_2$ of the ethyl groups attached to the gallium and a peak at 1.35 ppm for the ^{t}Bu group. There are also peaks at 1.39-1.47 ppm and 2.31 corresponding to the $-CH_3$ group of the ethyl attached to the gallium and to the AsH group respectively.

$$^tBuAsH_2 + GaR_3 \xrightarrow[80\ ^oC,\ 21\ h]{\text{Toluene}} 1/2\ [R_2GaAs(H)^tBu]_2 + RH \quad (\mathbf{6.1})$$

R = Me, Et

47, R = Me

48, R = Et

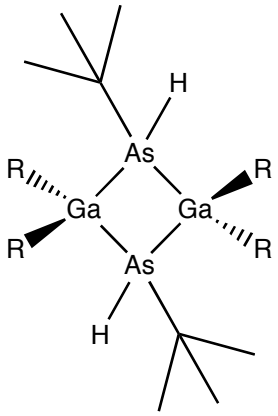

R = Me, Et

Figure 62: Proposed structure for the $[R_2Ga(H)^tBu]_2$.

Thermal decomposition of the single-source precursors was studied using thermogravimetic analysis (TGA). Excluding the loss of small amounts of solvent that take place initially (7% and 3% respectively for **47** and **49**) there were three major mass losses that take place. Both precursors fully decompose around 300 ^oC, with the ethyl derivative, $[Et_2GaAs(H)^tBu]_2$ (**48**), decomposing at a slightly lower temperature of 275 ^oC than the corresponding methyl complex, $[Me_2GaAs(H)^tBu]_2$ (**47**). Above these temperatures there is residual mass loss until 600 ^oC.

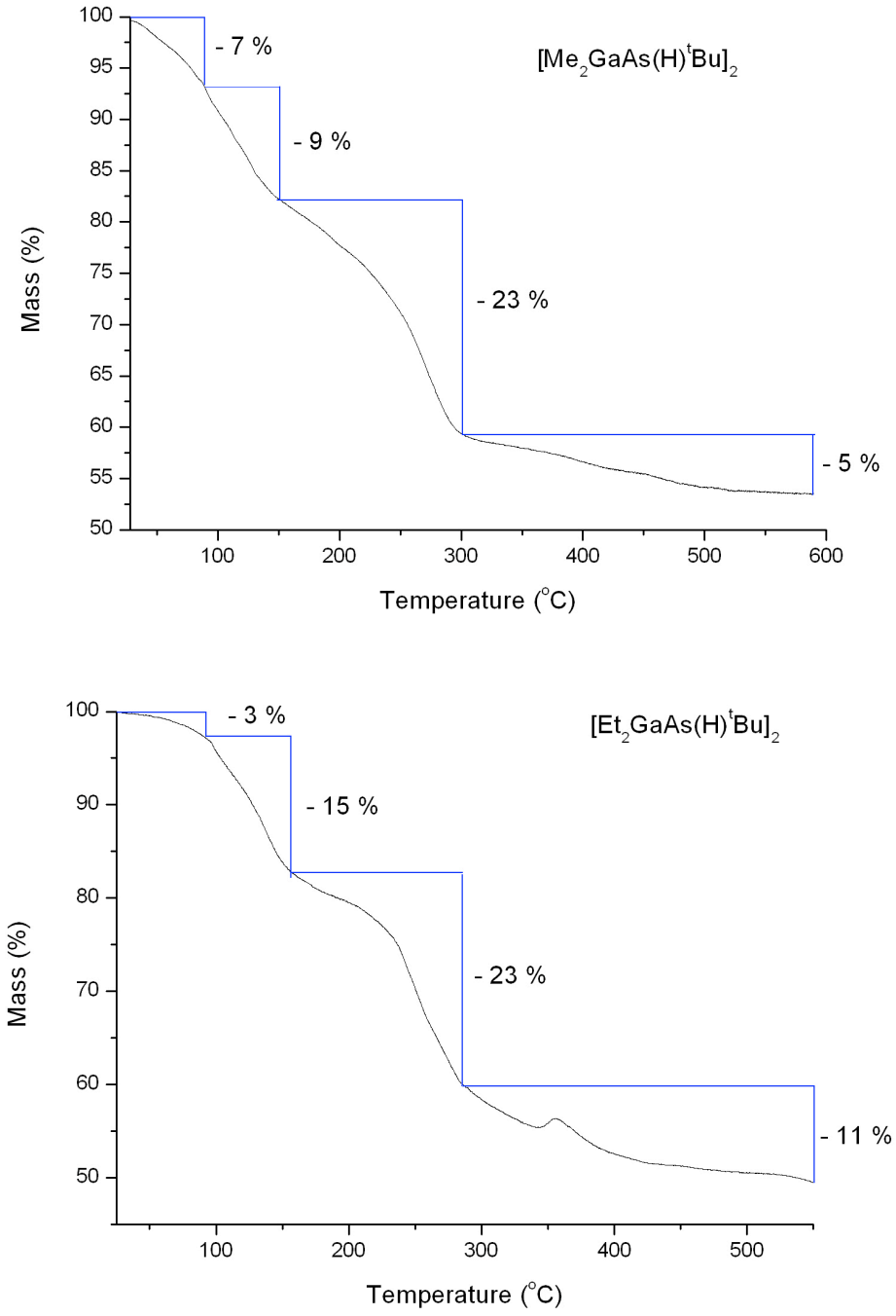

Figure 63: TGA of both precursors $[Me_2GaAs(H)^tBu]_2$ (top) and $[Et_2GaAs(H)^tBu]_2$ (bottom).

The molecular mass of $[Me_2GaAs(H)^tBu]_2$ is 465.67, therefore 62% of the precursor is GaAs, while the remaining 38% belong to the organic ligands. Each *tert*-butyl group and the H that take part in β-hydride elimination contribute to 13% of the mass. A methyl group contributes 3%. In TGA, the organic ligands should be removed leaving only the GaAs behind in the pan. So in this case the mass loss should be roughly 38%, but the actual mass loss observed is about 10% more at 47%. A similar outcome is

observed for $[Et_2GaAs(H)^tBu]_2$ but to a lesser extent, the actual mass loss is only 4% more than expected.

This observation is partly due to residual solvent removal. Also, the higher than expected mass loss may also be due to sublimation that could be occurring inside the TGA pan.

6.1.4 Chemical Vapour Deposition

Aerosol assisted chemical vapour depositions were carried out using the two precursors ($[Me_2GaAs(H)^tBu]_2$ (**47**) and $[Et_2GaAs(H)^tBu]_2$) (**49**) at a range of temperatures to determine whether the films produced were of sufficient quality (with respect to crystallinity, coverage and stiochoimetry) to proceed in this particular direction.

Condition	Precursor	Mass / g	Temp. / ^oC	Solvent	Volume / mL	Dep. Time / mins
10	$[Me_2GaAs(H)^tBu]_2$	0.5	400	Toluene	30	120
11	$[Me_2GaAs(H)^tBu]_2$	0.5	450	Toluene	30	120
12	$[Me_2GaAs(H)^tBu]_2$	0.5	500	Toluene	30	120
13	$[Et_2GaAs(H)^tBu]_2$	0.5	400	Toluene	30	120
14	$[Et_2GaAs(H)^tBu]_2$	0.5	450	Toluene	30	120
15	$[Et_2GaAs(H)^tBu]_2$	0.5	500	Toluene	30	120

Table 16: The conditions used in the initial AACVD experiments carried using the two precursors.

AACVD depositions were carried out using $[Me_2GaAs(H)^tBu]_2$ or $[Et_2GaAs(H)^tBu]_2$ in toluene (30 mL) at 400 ^oC, 450 ^oC and 500 ^oC to obtain GaAs films on glass substrates (Table 16).

6.1.5 Coverage

When the $[Me_2GaAs(H)^tBu]_2$ (**47**) precursor was used the substrate coverage increased with temperature whereas with the $[Et_2GaAs(H)^tBu]_2$ (**48**) precursor the opposite was

observed (Figure 64). With $[Me_2GaAs(H)^tBu]_2$, the best coverage was achieved at 500 °C with 70% of the substrate covered. Using $[Et_2GaAs(H)^tBu]_2$ at 400 °C, however, produced the best over substrate coverage of 85% (average).

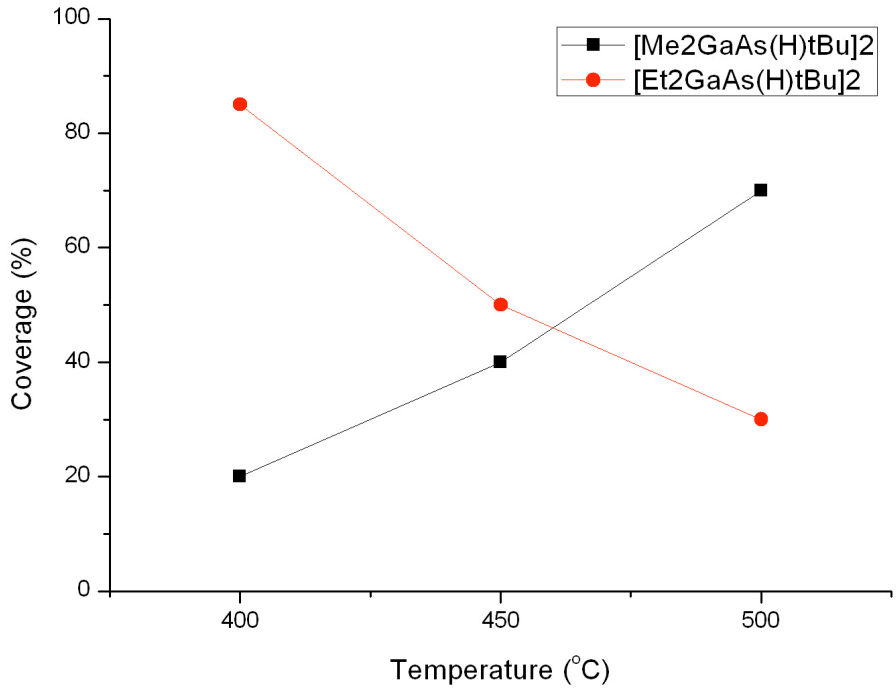

Figure 64: Graph showing the variation in substrate coverage with temperature for both precursors.

The results from these initial CVD depositions back up what was observed in the TGA experiments. Both precursors were able to decompose at 400 °C. However, due to the presence of β-hydrogens in the ethyl ligands of the $[Et_2GaAs(H)^tBu]_2$ this precursor was able to decompose much more readily at 400 °C than $[Me_2GaAs(H)^tBu]_2$, therefore leading to very good coverage of the substrate. The $[Me_2GaAs(H)^tBu]_2$ precursor requires more thermal energy (500 °C) to decompose fully and achieve the same level of substrate coverage. This is most likely due to the inability of the methyl ligands on the gallium centres to under go β-hydride elimination. At 400 and 450 °C most of the $[Me_2GaAs(H)^tBu]_2$ precursor has passed though the CVD reactor without decomposing, hence leading to very thin films that cover the substrate.

With the $[Et_2GaAs(H)^tBu]_2$ (**48**) precursor, 400 ^oC was sufficient to fully decompose the compound such that the film covers most of the substrate. At 450 ^oC or 500 ^oC, the temperature was too high such that the precursor decomposes soon after it enters the CVD reactor therefore giving rise to films that cover only a portion of the substrate (near the gas inlet). With the amount of precursor (0.50 g) used for these experiments, it was fully depleted before it has a chance to encounter the majority of the substrate. Therefore thick films near the inlet were observed for $[Et_2GaAs(H)^tBu]_2$ at 450 ^oC and 500 ^oC. The films at 500 ^oC were thicker than those at 450 ^oC as expected because the area of deposition decrease with temperature but the amount of precursor that decomposes to give a film remains the same.

Examples from literature show that during dual-source CVD, ethyl groups on gallium (like in $GaEt_3$) are able to undergo clean intramolecular cleavage while methyl groups (like in $GaMe_3$) require the presence of excess surface hydrogen. However, there have been some reports showing that the use of triethylgallium can lead to gallium island formation in the films.

6.1.5.1 Stoichiometry

These films were intended for photovoltaic applications therefore it was essential that they meet the strict requirements such as low grain boundaries, low contamination, high crystallinity and stoichiometry. The GaAs films are to be the intrinsic absorber in the *p-i-n* junction device structure hence the films need to be non conducting and thus the Ga to As ratio need to be as close to 1:1 as possible. Non-stoichiometry in the films can result in intrinsic doping which can lead to the films being conducting.

The stoichiometry in the films was determined using energy dispersive X-ray (EDX) analysis. The EDX results show that the films grown using the $[Me_2GaAs(H)^tBu]_2$ precursor at 500 ^oC had the correct stoichiometry (Ga : As, 1 : 1, 52.57 : 47.43). The other two conditions of 400 ^oC and 450 ^oC produced films that were gallium rich (Ga:As, 1.5:1, 60.20: 39.80). This is due in part to the presence of a relatively large native oxide layer on the surface of these films. It is common for a native oxide layer to form on the surface of GaAs thin film or wafers (Table 17) after a few seconds of exposure to a non-inert atmospheres. Many oxides of Ga and As such as Ga_2O_3 and As_2O_3 form on the surface of the films but it is predominately Ga_2O_3. If the GaAs films are thin then upon exposure to air during storage or analysis a larger portion of the films

will be oxidized than if the film was thick. Since the majority of the oxide is Ga_2O_3 the EDX analysis would give results that show the film to be Ga rich. Arsenic oxides are also formed on the surface, but arsenic could also react with the moisture in the atmosphere to produce arsine, which would then leave the film as a gas, helping the films to be As deficient.

The films grown using the ethyl precursor, $[Et_2GaAs(H)^tBu]_2$, were stoichiometric (Ga : As, 1:1, 50.10 : 49.90) when the deposition temperature is 450 °C and 500 °C as the films were sufficiently thick and hence the native oxide layer was relatively very thin. At 400 °C, the temperature at which the best coverage of the substrate was achieved, the films were non-stoichiometric and Ga rich, as seen with the $[Me_2GaAs(H)^tBu]_2$ analogue also at 400 °C.

Ga / Atomic %	As / Atomic %
51.6 (±0.1)	49.4(±0.1)

Table 17: Table showing the typical EDX results for a GaAs wafer that is known to be 1:1 GaAs.

6.1.5.2 Crystallinity

The films grown from $[Me_2GaAs(H)^tBu]_2$ (**47**) and $[Et_2GaAs(H)^tBu]_2$ (**48**) under the six different conditions were analysed for crystallinity using XRD.

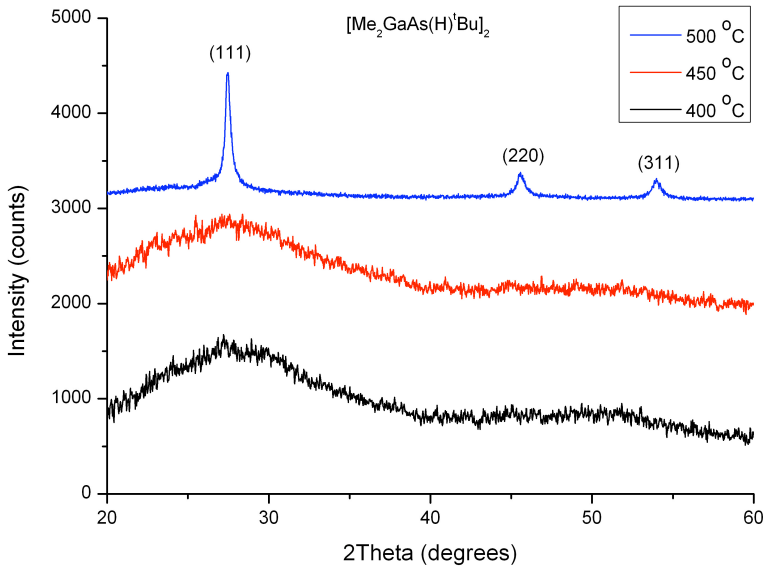

Figure 65: Powder XRD showing the crystalline nature of films grown under condition 10 (black), 11 (red) and 12 (blue).

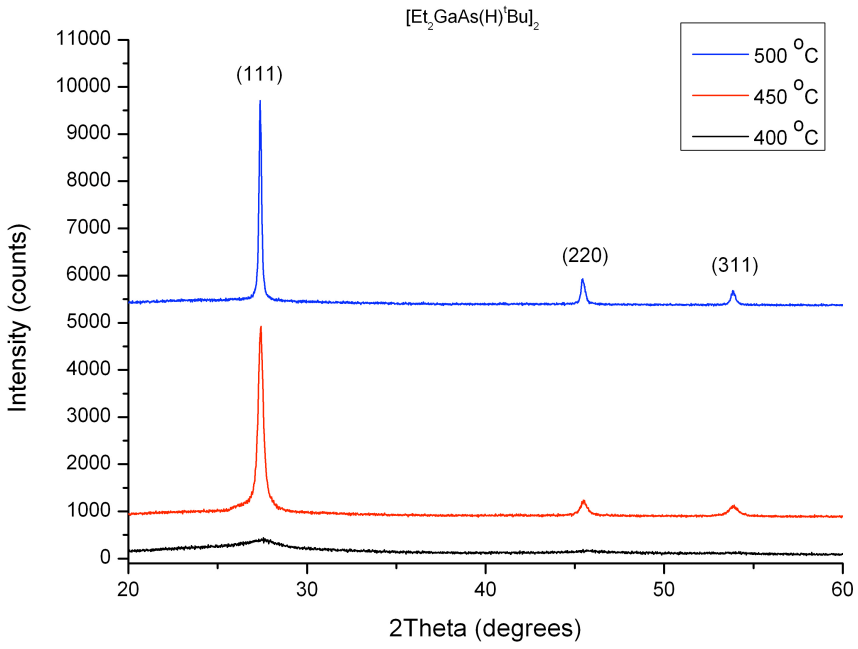

Figure 66: Powder XRD showing the crystalline nature of films grown under condition 13 (black), 14 (red) and 15 (blue).

Films grown from $[Me_2GaAs(H)^tBu]_2$ were only crystalline when deposited at 500 °C. These films were polycrystalline with peaks corresponding to cubic GaAs [111], [220] and [311] at 27.3°, 45.4° and 53.7° respectively. There was no diffraction pattern for films grown at 400 °C and 450 °C apart from a broad hump around 28°, which is indicative of amorphous materials. From these studies, a minimum temperature of 500 °C is required to grow crystalline films using the methyl precursor on glass.

With depositions using the $[Et_2GaAs(H)^tBu]_2$ precursor, there was an increase in crystallinity with temperature. Films grown at 450 °C and 500 °C were both crystalline, whereas films deposited at 400 °C were amorphous. As opposed to the previous system, 450 °C was sufficient to grow crystalline films using the ethyl precursor.

The increase in crystallinity with temperature trend observed in this study is typical of any films grown *via* CVD, and is due to two effects. The higher the deposition temperature, the more energy there is on the substrate surface to allow the adsorbed molecules to decompose efficiently and for the resulting atoms/molecules to find the lowest energy site or sites before nucleating to grow the film. This happens repeatedly during the deposition to form a film with long-range order (and thus crystallinity). The

higher the temperature, the more long range order there is and therefore the more crystalline the film. At low temperatures, the ad-atoms do not have sufficient energy to move fast enough to find the lowest energy site on the substrate before nucleation takes place, thus they nucleate soon after adsorption to the substrate resulting in films with poor long range order and crystallinity. If the temperature is too low then the films lack any order and are amorphous such as films grown under conditions **10**, **11** and **13** (Table 16).

The other effect for the observed increase in crystallinity of the films with an increase in temperature is due to film thickness. The higher the temperature, the more energy there is to decompose the precursors and therefore form thicker the films. The thicker the film the more crystalline material (as opposed to the amorphous substrate) there is to analyse *via* XRD.

There is also another trend in crystallinity observed in this study, that films produced using $[Et_2GaAs(H)^tBu]_2$ are crystalline at lower temperatures than those produced using the methyl equivalent precursor ($[Me_2GaAs(H)^tBu]_2$). The precursor, $[Et_2GaAs(H)^tBu]_2$ (**49**) is able to give crystalline films at 450 ^oC whereas $[Me_2GaAs(H)^tBu]_2$ requires 500 ^oC for the films to be crystalline. This is as expected and was suggested to some degree by the TGA due to the ability of ethyl groups on the Ga centres in $[Et_2GaAs(H)^tBu]_2$ to undergo facile beta hydride elimination.

6.1.5.3 Summary

Out of all six conditions that were studied only **12**,**14** and **16** were crystalline and stoichoimetric. And out of these three conditions only condition **12** (grown using $[Me_2GaAs(H)^tBu]_2$ in 30 mL of toluene at 500 ^oC) had sufficient coverage of the substrate (on average 70%) to be useful for device fabrication. Therefore the $[Me_2GaAs(H)^tBu]_2$ precursor was chosen over the $[Et_2GaAs(H)^tBu]_2$ precursor for further study and optimisation.

6.1.6 Introduction

6.1.6.1 The Precursor

Considering the earlier study, $[Me_2GaAs(H)^tBu]_2$ (Figure 67) was used as the precursor to carry forward and do CVD optimisation. It is an ideal precursor for CVD in particular AACVD as it contains some of the key features that are crucial for successful deposition of thin films with good functional properties.

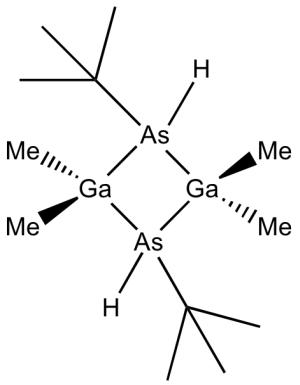

47

Figure 67: Structure of the single-source precursor.

In AACVD the precursor is transported to the heated substrate as an aerosol mist. Therefore, it is crucial that solid precursors intended for AACVD are soluble in a range of solvents. This precursor displays excellent solubility in a wide range of organic solvents, both polar (e.g. diethyl ether) and non-polar (e.g. hexane). This is due to the presence of organic groups around the gallium/arsenic centres. The groups maximize solubility in a wide range of solvents but also minimize carbon contamination in the films by undergoing facile elimination. The arsenic centre of the dimeric precursor is bound to a tert-butyl group and hydrogen. This is ideal for two reasons:

- Tertiary butyl groups undergo β-hydride elimination readily and thus eliminate cleanly to minimise contamination. The adjacent hydrogen (also on the As) aid the β-hydride elimination process.
- The *tert* butyl is a large organic ligand that helps solubility of the dimer in organic solvents.

The precursor, $[Et_2GaAs(H)^tBu]_2$, with ethyl groups on the Ga instead of methyl groups does decompose more cleanly (Figure 62) due to the ability of the ethyl groups to

undergo β-hydride elimination. But this produces films with poor substrate coverage (see Figure 64, Figure 65 and Figure 66) at the required temperatures (500 °C and above). It is important that films cover a sufficient area of the substrate so that analysis can be carried out and photovoltaic devices be made.

6.1.6.2 Film Deposition

AACVD depositions were carried out using $[Me_2GaAs(H)^tBu]_2$ (0.50 g, 1.26 mmol) in toluene (15 mL and 30 mL) at 500 °C and 550 °C to obtain polycrystalline GaAs thin films on glass using a flow rate of 0.5 L min^{-1} was adopted. The initial AACVD study undertaken on this precursor (along with $[Et_2GaAs(H)^tBu]_2$) showed that a temperature of at least 500 °C was required to obtain good coverage and crystallinity.

Films were grown at two different temperatures, 500 °C and 550 °C. Two different concentrations were also studied, 0.5 g in 15 mL of toluene and 0.5 g in 30 mL of toluene (Table 18). Films deposited from $[Me_2GaAs(H)^tBu]_2$ under these conditions were smooth, continuous and appeared grey/blue in colour under reflected light. They were adherent to the substrate, passing the Scotch tape test but were scratched by stainless steel and brass stylus which is typical for GaAs thin films.

Good coverage of the substrate was obtained with both temperatures but as expected better coverage was achieved at 500 °C (the first *ca.* 70% of the substrate) than at 550 °C (the first *ca.* 35% of the substrate). Films deposited at 550 °C have a higher thickness gradient than those deposited at 500 °C.

Condition	$[Me_2GaAs(H)^tBu]_2$ / g	Temp. / °C	Solvent	Volume / mL	Dep. time / min
16	0.5	500	Toluene	15	60
17	0.5	550	Toluene	15	60
12	0.5	500	Toluene	30	120
18	0.5	550	Toluene	30	120

Table 18: Table showing the conditions used to grow films using $[Me_2GaAs(H)^tBu]$ (47).

6.1.7 Analysis

6.1.7.1 Energy Dispersive X-Ray Diffraction (EDX)

Energy dispersive X-ray (EDX) analysis was carried out to determine the overall composition of the thin films and to confirm the stoichoimetry. The films were stoichimetric at all temperatures and concentrations studied, with an average gallium to arsenic ration of 1:1 as shown in Table 19.

Condition **16**			Condition **17**		
Region	Ga / Atomic %	As / Atomic %	Region	Ga / Atomic %	As / Atomic %
1	52.6	47.4	1	51.4	48.6
2	52.6	47.4	2	51.8	48.2
3	51.9	48.1	3	52.1	47.9
Average	**52.4(±0.4)**	**47.6(±0.4)**	**Average**	**51.7(±0.4)**	**48.3(±0.4)**
Condition **12**			Condition **18**		
Region	Ga / Atomic %	As / Atomic %	Region	Ga / Atomic %	As / Atomic %
1	52.9	47.1	1	51.2	48.8
2	53.1	46.9	2	52.4	47.6
Average	**53.0**	**47.0**	3	51.9	48.1
			4	51.8	48.2
			Average	**51.8(±0.5)**	**48.2(±0.5)**

Table 19: The EDX results for various spots on some of the films grown under the four different conditions. The average values are in bold.

6.1.7.2 Powder X-Ray Diffraction (XRD)

X-ray powder diffraction (XRD) of the films grown under the 4 different conditions confirms the presence of polycrystalline GaAs for all films (Figure 68 and Figure 69). Peaks corresponding to cubic GaAs [111], [220], [311], [400], [331] and [422] were observed at 27.3°, 45.4°, 53.7°. 66.0°, 72.9° and 83.7° 2θ values, respectively. There are

three other peaks ([200] at 31.6°, [222] at 56.3° and [420] at 75.0°) expected in this 2θ angle range (20 -90°) that were not visible due to their very low intensity.

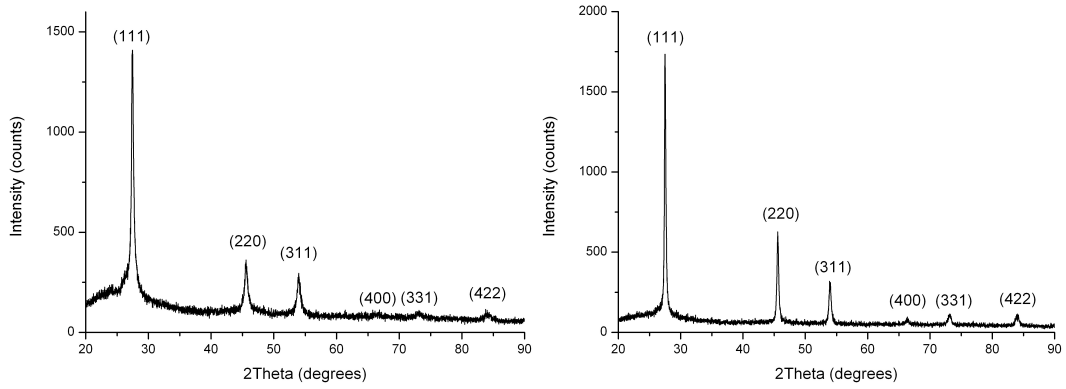

Figure 68: XRD pattern of films grown under condition 16 (left) and 17 (right).

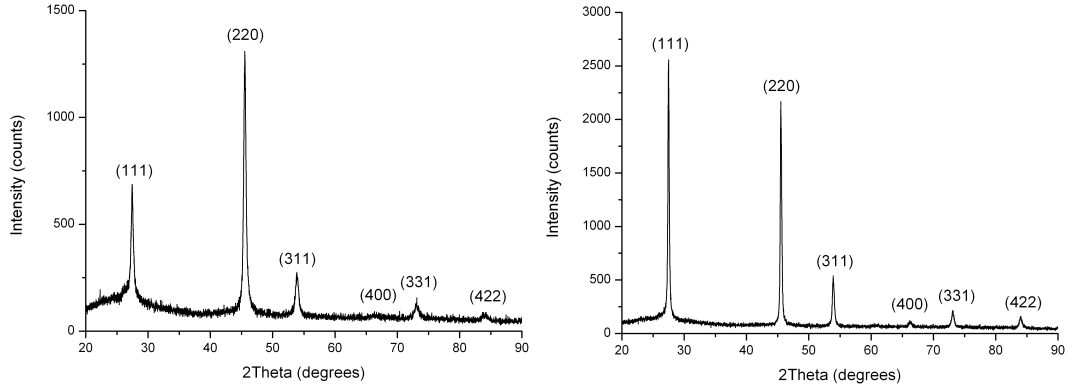

Figure 69: XRD pattern of films grown under condition 12 (left) and 18 (right).

The diffraction peaks (Figure 68 and Figure 69) were narrow indicating that the films have good crystallinity. The intensity of the peaks was greater for the thicker films grown at higher temperature and/or using a less concentrated solution. Diffractograms for the films grown at the lower temperature (500 °C) show a larger background hump, which is probably due to more amorphous substrate being analysed for thinner films.

If the average FWHM of the 3 most prominent peaks is taken as an indicator of the crystallinity, then films grown under condition **18** are the most crystalline with a FWHM of 0.29° and condition **16** the least with FWHM of 0.50°. The most crystalline films were grown using 550 °C and 0.042 mmol/mL concentration (Table 20).

Condition	FWHM / ^{o}			Average FWHM / ^{o}
	(111)	(220)	(311)	
16	0.37	0.52	0.61	0.50(±0.1)
17	0.25	0.30	0.42	0.33(±0.1)
12	0.42	0.44	0.60	0.49(±0.1)
18	0.23	0.27	0.36	0.29(±0.1)

Table 20: Table showing the uncorrected FWHM of the 3 prominent peaks for selected XRD diffractograms of the films grown using condition 16,17, 12 and 18.

The XRD patterns of the films show that there is a degree of preferred orientation compared to randomly orientated GaAs standard (Figure 70).

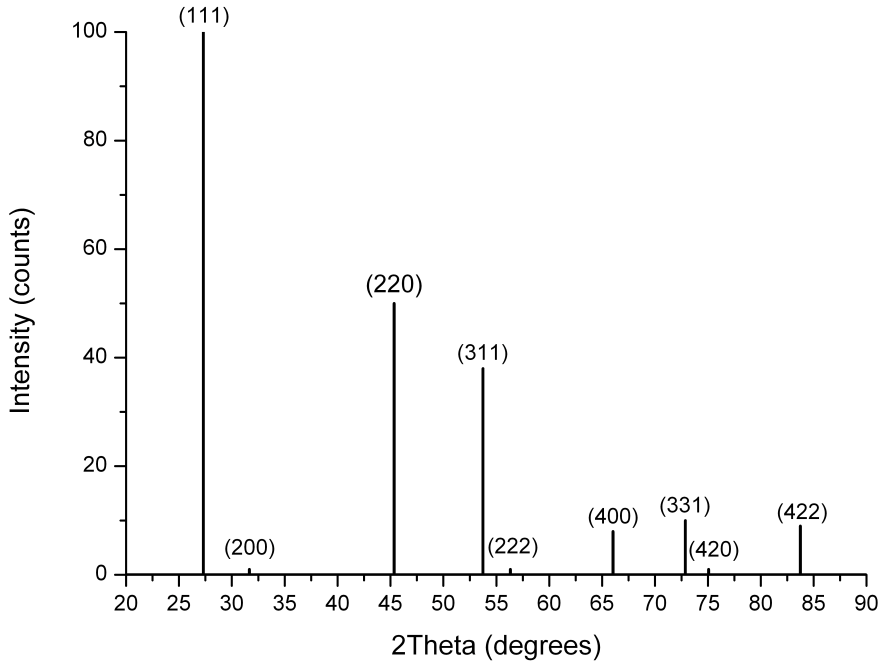

Figure 70: XRD pattern of a randomly oriented GaAs polycrystalline standard with the 2 theta range 20 to 90 ^oC.

The crystallographic preferred orientation (α) with respect to each peak was calculated using Equation 5.1 (Chapter 5). For the standard it is shown in Table 21.

(111)	(200)	(220)	(311)	(222)	(400)	(331)	(420)	(422)
0.44	0.01	0.26	0.20	0.01	0.04	0.05	0.01	0.03

Table 21: Shows the crystallographic preferred orientation (α) in a randomly oriented GaAs standard.

The films grown under condition **16** and **17** show a preferred orientation in the (111) plane as seen earlier in the majority of films for the *in situ* system (Chapter 5). The films grown under condition **12** and **18** show preferred orientation in the (220) plane this most likely due to the slower growth of the film as these films were grown using 30 mL of toluene compared to 15 mL used for condition **16** and **17**.

Condition	(111)	(200)	(220)	(311)	(222)	(400)	(331)	(420)	(422)
16	0.59	0	0.15	0.12	0	0.04	0.05	0	0.05
17	0.58	0	0.21	0.11	0	0.03	0.04	0	0.04
12	0.27	0	0.51	0.11	0	0.03	0.05	0	0.04
18	0.44	0	0.38	0.09	0	0.02	0.04	0	0.03

Table 22: Intensity ratio (α) showing the extent of preferred orientation in the (111) and (220) planes.

The XRD peaks for films deposited at 550 ^oC (conditions **17** and **18**) were more intense and narrower, which is indicative of larger grain/crystallite size. The peak width is inversely proportional to crystallite size, i.e. as the crystallite size decreases the peaks get broader. The crystallite size was calculated using the Scherrer (Equation 4.2, Chapter 4).

The results show for the four samples show an increase in crystallite size with temperature and deposition time (Table 23). Increasing the temperature by 50 ^oC from 500 to 550 ^oC results in a 100% increase in crystallite size (on average from 18 nm and 20 nm to 34 nm and 40 nm respectively). Furthermore, decreasing the concentration of the precursor solution by 50% shows only a small increase (roughly 15%) in crystallite size (from 18 nm and 34 nm to 20 nm and 40 nm respectively). These crystallite sizes

are of the same order of magnitude to other reports of GaAs grown on amorphous substrates.

	Condition **16**					
hkl	Bragg Angle 2θ/°	Peak Width 'β'/°	Instrument resolution/°	Corrected 'β' /°	Diameter/ nm	Ave. Crystallite Size / nm
111	27.47	0.405	0.080	0.325	25	18(±6)
220	45.59	0.612	0.055	0.557	15	
311	53.99	0.670	0.065	0.605	15	
	Condition **17**					
111	27.52	0.253	0.080	0.173	47	34(±11)
220	45.59	0.332	0.055	0.277	31	
311	53.98	0.420	0.065	0.355	25	
	Condition **12**					
111	27.452	0.444	0.0799	0.364	22	20(±4)
220	45.533	0.437	0.0550	0.382	23	
311	53.901	0.617	0.0648	0.552	16	
	Condition **18**					
111	27.493	0.231	0.0799	0.151	54	40(±13)
220	45.539	0.280	0.0550	0.225	38	
311	53.944	0.380	0.0648	0.315	28	

Table 23: The crystallite size of the films grown under the four different conditions as determined by the Scherrer equation.

Compared to the grain sizes calculated for the films gown using the *in situ* approach of either $As(NMe_2)_3$ and $GaMe_3$ or $^tBuAsH_2$ and $GaMe_3$ the single source approach produced films with larger crystallites. This is ideal for photovoltaic applications.

Generally micron size crystallites are reported from films grown expitaxially on gallium arsenide or germanium substrates *via* MOCVD or MBE. These kinds of crystallite sizes are not possible on non-lattice matched amorphous substrates such as glass because the structural and thermal properties of glass and GaAs are not very similar and as a result

of the strain caused by the mismatch can lead to small crystallite/grain size result, as well as defects in the films.

6.1.7.3 Raman

Micro Raman of the samples produced expected results for GaAs when excited with 514.5 nm laser. Measurements were carried out at room temperature at a rough penetration depth of 100 nm. GaAs is a zinc blende polar material with space group F-43m and therefore shows two first order Raman bands with two active modes of vibration. These are a longitudinal optical (LO) phonon mode at 291 cm^{-1} and a doubly degenerate transverse optical (TO) phonon mode at 268 cm^{-1}.[131] This indeed what was observed for the films gown under the four different conditions, a LO at 286.78 cm^{-1} and a TO at 263.80 cm^{1}. However, these peaks were shifted, both the LO and TO by roughly 4 cm^{-1} to lower wavenumbers. This could be due to local heating effects induced by the laser upon excitation, other thermal effects, disorder and strain in the GaAs Lattice. Thermal effects are likely to be the major cause of the shift.

The peaks have a bandwidth of 10.8 cm^{-1}, which indicates good crystallinity of the samples. Typical Raman line widths of the TO and LO for GaAs films grown *via* a variety of techniques range from 3 to 12 cm^{-1}.

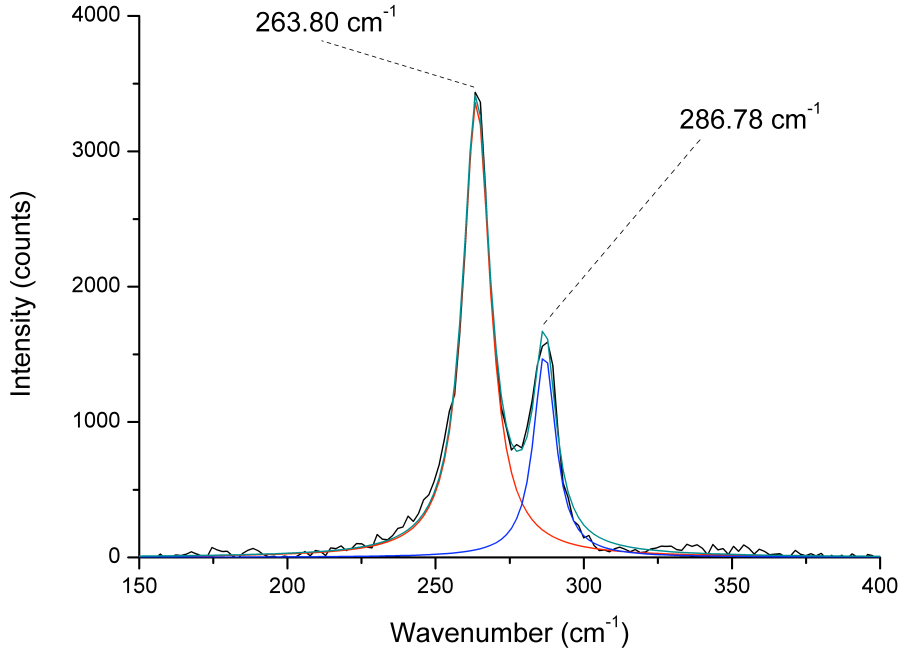

Figure 71: Typical Raman spectra polycrystalline GaAs on glass.

6.1.7.4 Scanning Electron Microscopy (SEM)

SEM images were taken in secondary electron mode at 5 kV and the samples were coated with gold before images were taken. The films are fairly compact and particulate in nature but the surfaces were flat and smooth making it difficult to obtain high quality images (Figure 72 and Figure 73).

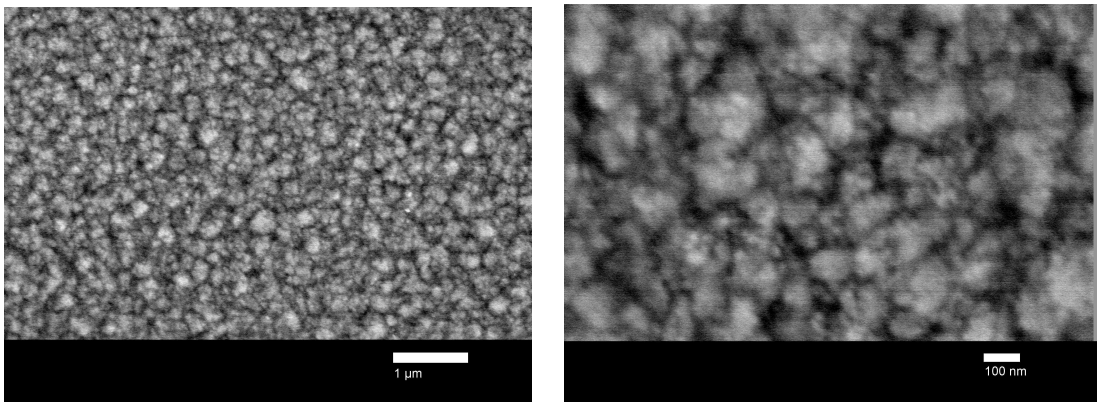

Figure 72: SEM images of films frown under condition 16.

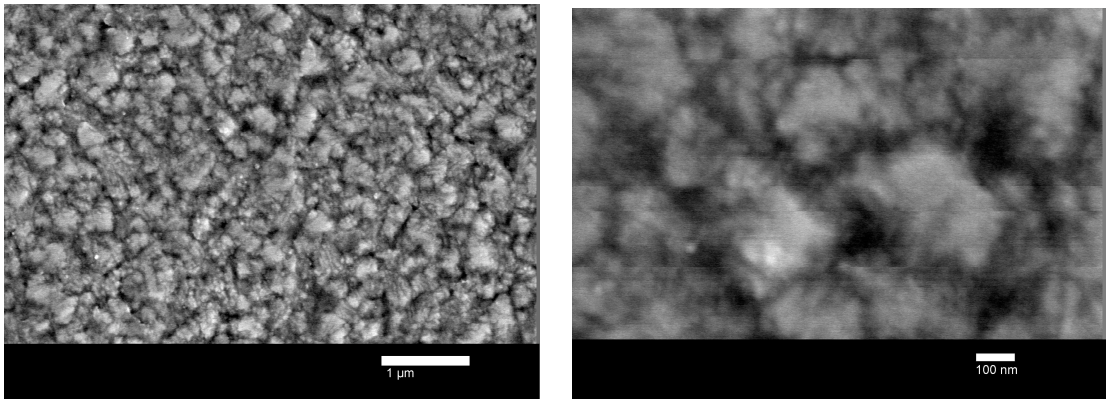

Figure 73: SEM images of films grown under condition 17.

Films grown under condition **16** were deposited at 500 ^oC and films grown under Condition 17 at 550 ^oC with all other variables being constant (Table 18). From the SEMs alone it is difficult to see the individual crystallites that make up the grains (grain = collection of crystallites). Therefore only the grains will be discussed at this point.

From the images it is evident that there is an increase in grain size with increase in temperature and this is as expected. This is due to an increase in the mobility of the

adsorbed species on the substrate surface which allows these adatoms more chance to migrate to the lowest energy site on the substrate before nucleation takes place.[2] Furthermore, in a thermodynamic point of view a crystalline or polycrystalline film with small grains and thus a large amount of grain boundaries is higher in energy than a film of the same material with larger grains. This is because grain boundaries are defects within crystals therefore regions of high energy. Hence there is a thermodynamic driving force to reduce the number of grain boundaries and form larger grains. To achieve this, an 'activation energy' needs to be overcome which can be provided by carrying out the deposition at higher temperatures.

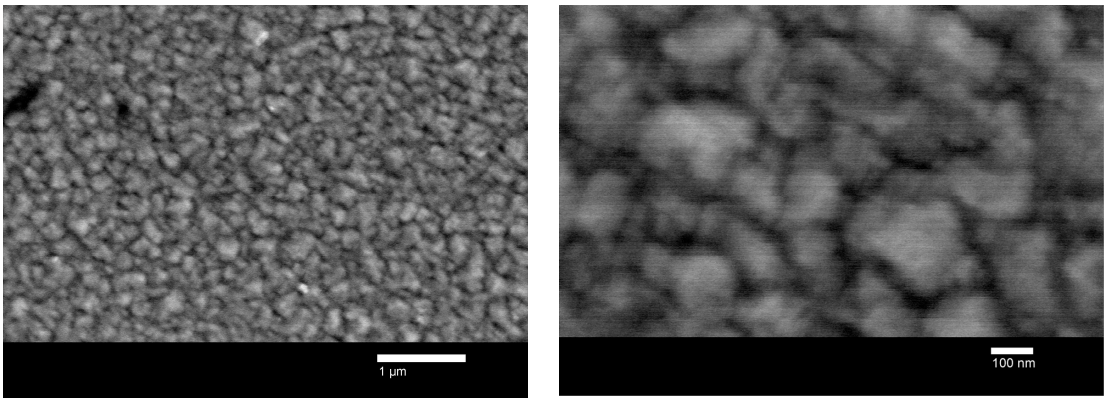

Figure 74 An SEM image of a film grown under condition 12.

A doubling of the deposition time from 1 hour with conditions **16** and **17** to 2 hours with conditions **12** and **18** has caused only a minor change in morphology (Figure 74). It is difficult to say accurately by just using the SEM images but there seems to be only a slight increase in grain size. The films remain compact and the morphology smooth. The increase in grain size is more apparent in the SEM image of the films grown at 550 ^oC (condition **12** and **18**).

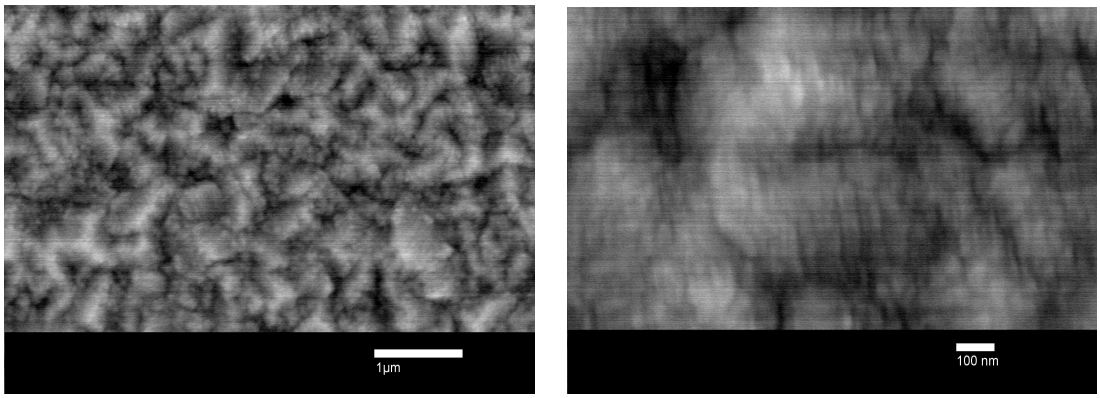

Figure 75: An SEM image of film grown under condition 18.

6.1.7.5 High Resolution Transmission Electron Microscopy (HRTEM)

A more in depth analysis of the morphology and grain structure not only on the surface of the films but also within the bulk of the films is possible using a high-resolution transmission electron microscopy (HRTEM).

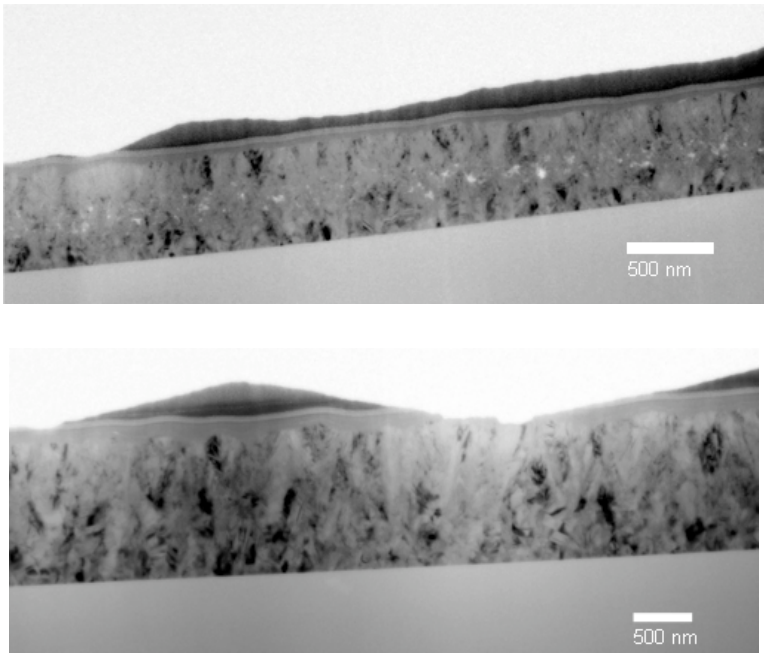

Figure 76: Lightfield TEM **image of film grown under condition 16 (top) and 17 (bottom).**

The lightfield images of films grown under condition **16** and **17** (Figure 76) show that both have uniform thickness. The thickness of film grown under condition **16**

(deposition temperature 500 ^oC) only varies by 40 nm in the region analysed. The thickness variation of the film grown under condition **17** however is slightly more at 70 nm. This is expected with this particular CVD reactor design where the precursor and carrier gas enter the reactor from one direction parallel to the substrate therefore resulting in a thickness gradient. More uniform films are possible if the substrate is moving (i.e. rotating) and the gas/precursor flow from the top. Also, the fact that the deposition is kinetic controlled rather than mass flow controlled, the deposition temperature governs the thickness and uniformity of the films. With increasing deposition temperature the expected thickness variation will also increase.

HRTEM images of a film grown under condition **16** at 500 ^oC show the film to have a good degree of crystallinity with very distinctive lattice fringes (Figure 77 and Figure 78). There are however also regions that have poor crystallinity.

The top region of the film was more crystalline than the central region as it contained fewer regions that were poorly crystalline. From the magnified image (Figure 77c) it possible to see the grain boundaries within the film.

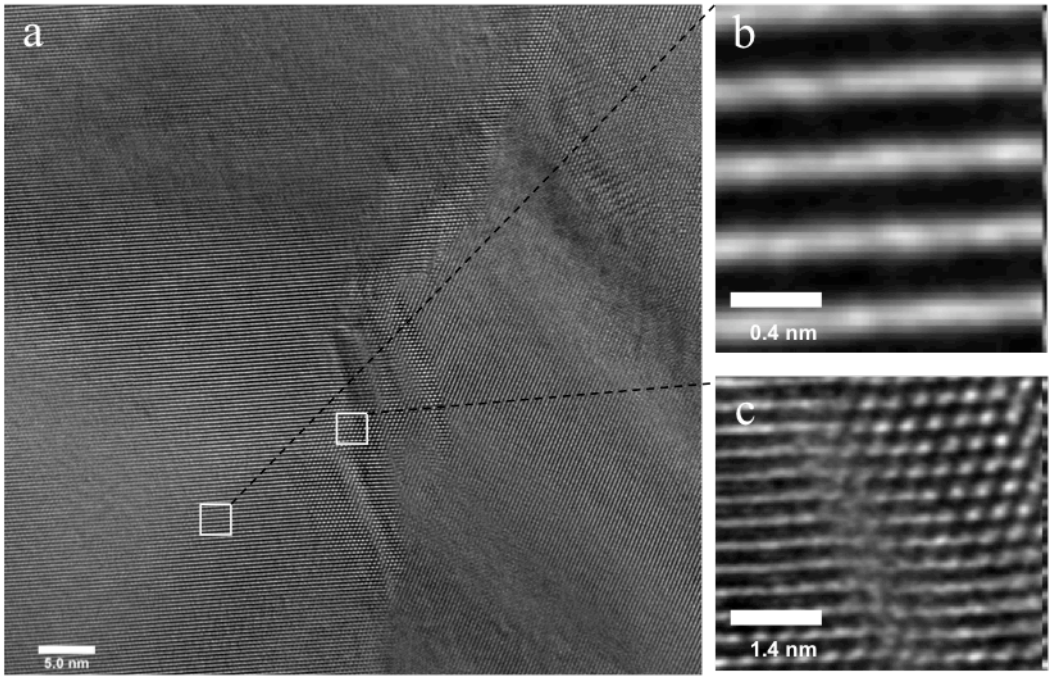

Figure 77: HRTEM of the top region of a film grown under condition 16 at 500 ^oC using $[Me_2GaAs(H)^tBu]_2$ in toluene. There are many grain boundaries in the film. b) The magnified image of a more crystalline region shows that the lattice fringes are well spaced. c) A magnified region showing grain boundaries within the film.

The central region of the film is less crystalline than the top, with more grain boundaries. However the lattice fringes are still very well spaced. This follows the trend see from the HRTEM of the other systems (Chapter 4 and 5) where the top region is always more crystalline than the central.

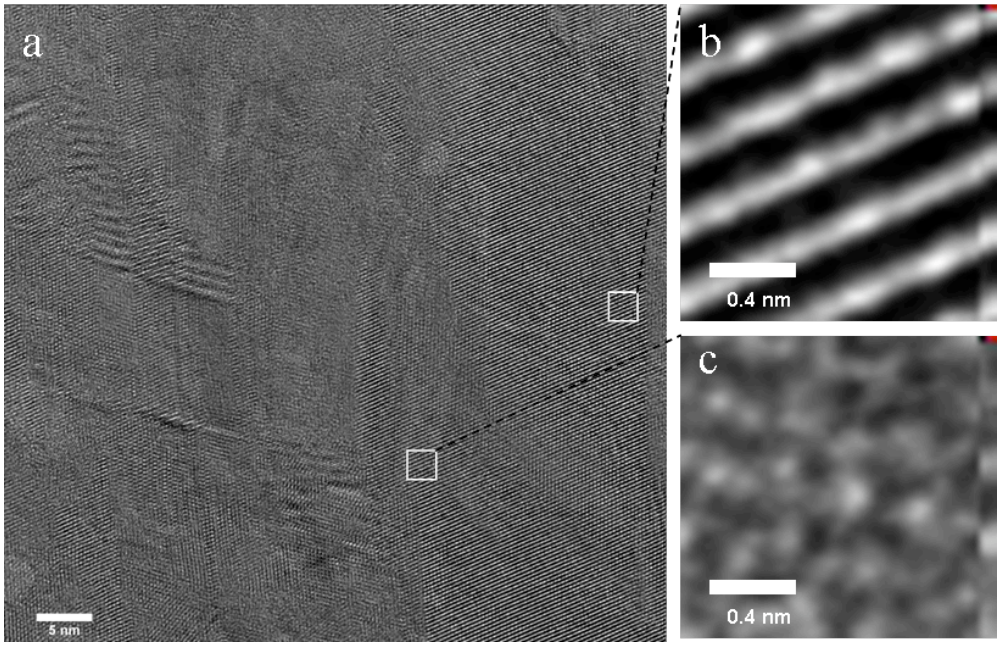

Figure 78: HRTEM of the central region of a film grown under condition 16 at 500 ^oC using $[Me_2GaAs(H)^tBu]_2$ in toluene. There are many grain boundaries in the film. b) The magnified image of a more crystalline region shows that the lattice fringes are well spaced. c) A magnified region showing a poorly crystalline region.

HRTEM images shows that a film grown under condition **17** at 550 ^oC was extremely crystalline with better defined lattice planes than seen for the film grown under condition **15** and any of the other systems seen previously. This is supported by XRD patterns having the narrowest peaks (Figure 68).

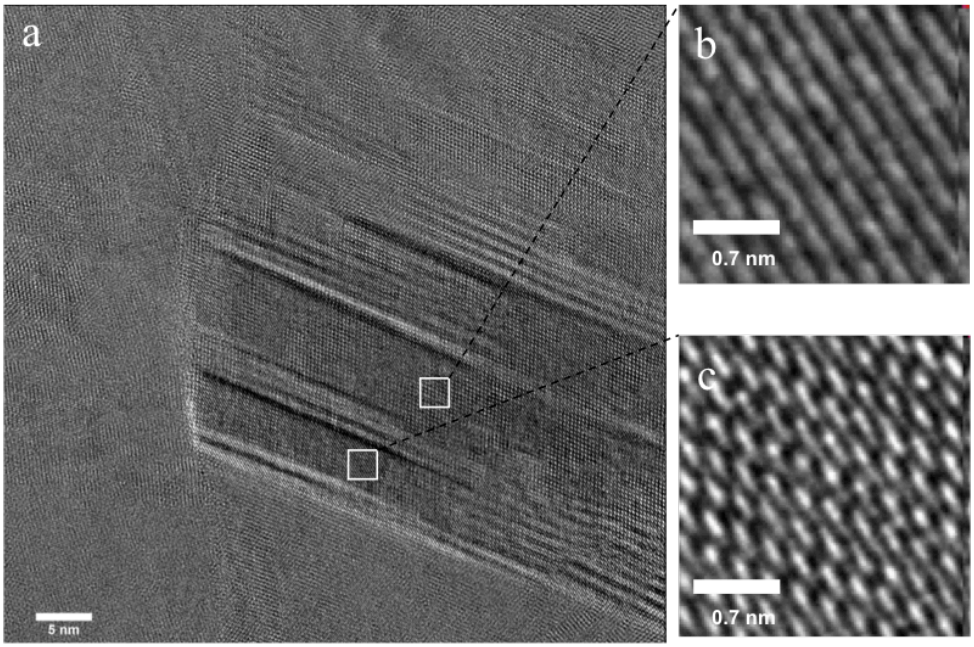

Figure 79: HRTEM of the top region of a film grown under condition 17 at 550 °C using $[Me_2GaAs(H)^tBu]_2$ in toluene. b) The magnified image of a more crystalline region shows that the lattice fringes are well spaced. c) A magnified region of a grain boundary.

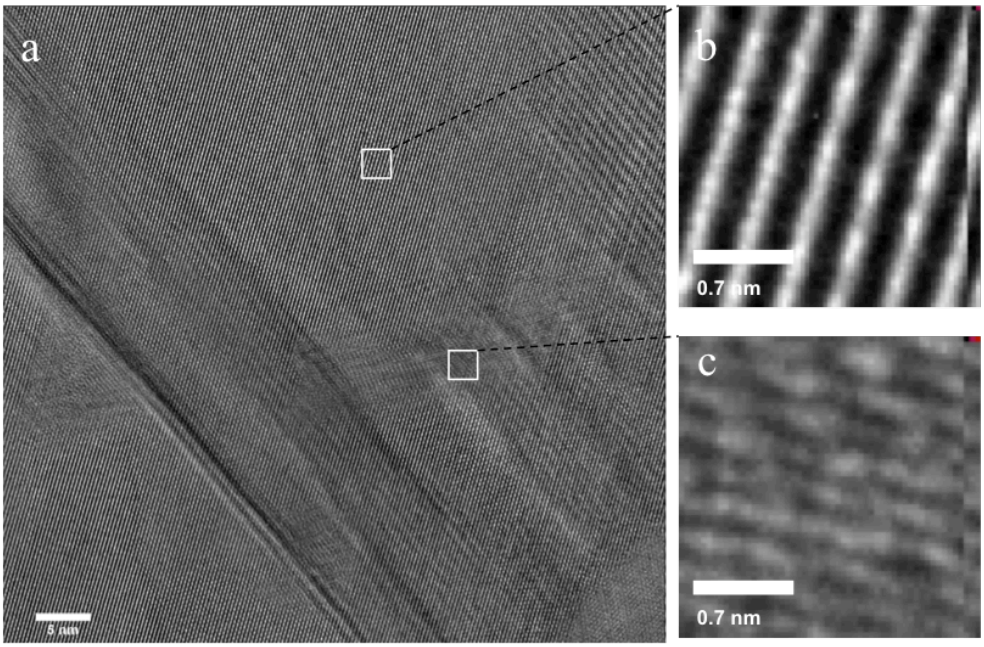

Figure 80: HRTEM of the top region of a film grown under condition 17 at 550 °C using $[Me_2GaAs(H)^tBu]_2$ in toluene. b) The magnified image of a more crystalline region shows that the lattice fringes are well spaced. c) A magnified region showing a poorly crystalline region.

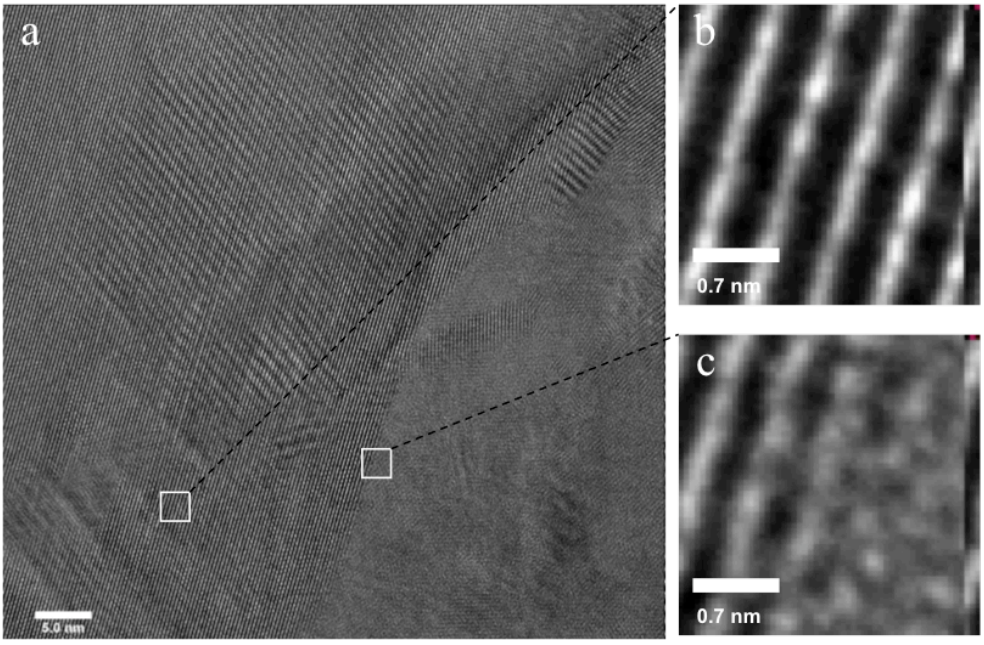

Figure 81: HRTEM of the central region of a film grown under condition 17 at 550 °C using $[Me_2GaAs(H)^tBu]_2$ in toluene. b) The magnified image of a more crystalline region shows that the lattice fringes have good definition. c) A magnified region showing a highly crystalline region mixing with a poorly crystalline area.

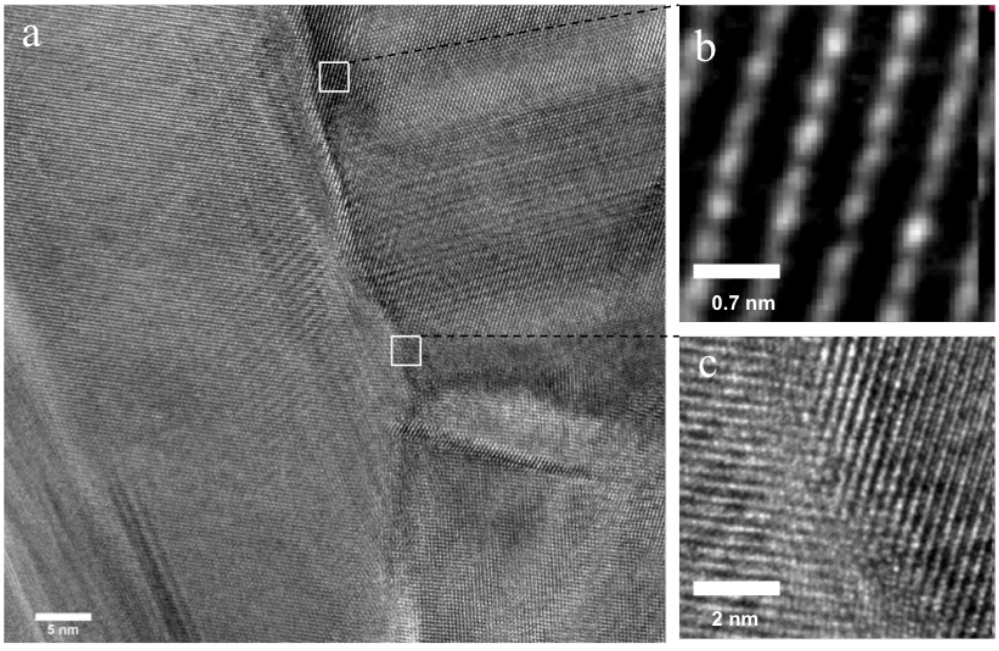

Figure 82: HRTEM of the central region of a film grown under condition 17 at 550 °C using $[Me_2GaAs(H)^tBu]_2$ in toluene. b) The magnified image of a more crystalline region shows that the lattice fringes are well seperated. c) A magnified region showing a grain boundary.

The darkfieled HRTEM images of a film grown under condition **16** and a film grown under condition **17** were obtained (Figure 83). The images show the films to have columnar growth with the film grown at 550 ^oC having more columnar structure, as it is more crystalline than that grown at 500 ^oC. Furthermore, in the film grown under condition **16** there are some voids in the middle of the film. This is most likely specific to just this film and could have occurred due to a disturbance in the aerosol density during the deposition. This is also more apparent in the EDX mapping images that are presented below (Figure 91). Columnar grown structure results in fewer grain boundaries in the vertical direction, which is a favorable property for these films.

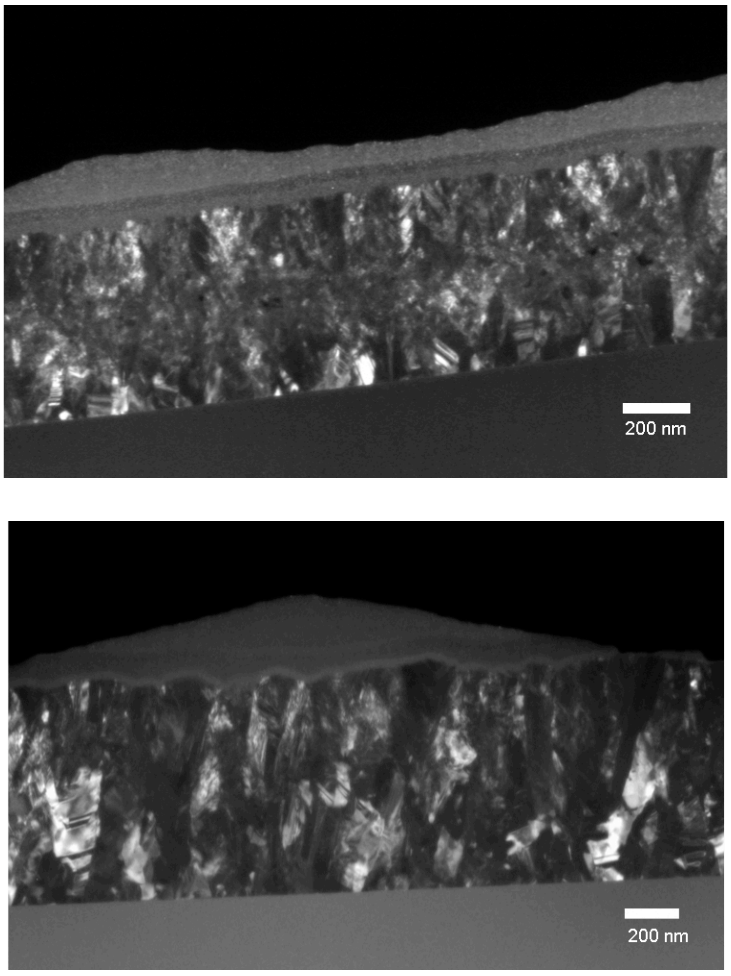

Figure 83: Dark field TEM image of a film grown under condition 16 (top) and 17 (bottom). The film grown at the higher temperature (17) has much better columnar structure.

The grain size distribution in the films was grown under Condition **16** and **17** showed the expected trend (Figure 84 and Figure 85). The grains near the top of the film are larger than those near the bottom. This is expected because the bottom layers act as template and provide a more crystalline surface for growth thus resulting in more crystalline layers.

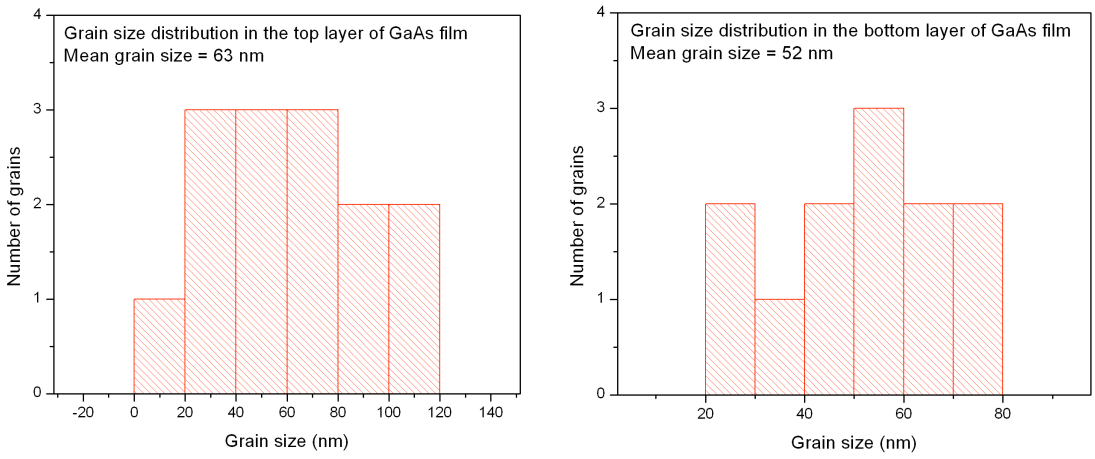

Figure 84: The grain size distribution of in a film grown under condition 16, the grains are larger on the top (right) region of the film compared to the bottom (left).

The average grain size of the bottom region of a film grown under condition **16** is 52 nm and the average grain size near the top of the film is 63 nm.

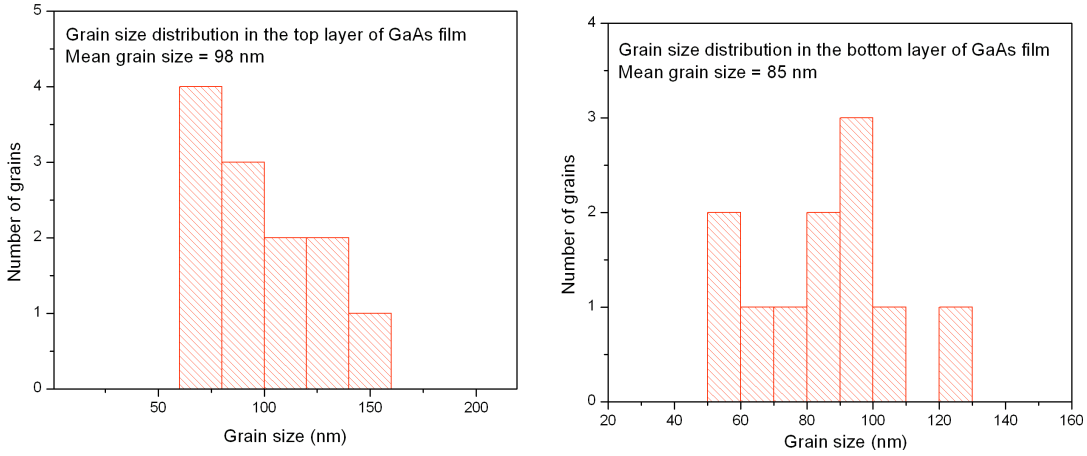

Figure 85: The grain size distribution of in a film grown under condition 17, the grains are larger on the top (right) region of the film compared to the bottom (left).

For film grown under condition **17** at a higher temperature of 550 ^{o}C, compared to 500 ^{o}C for condition **16**, the average grain size near the top of the film is 98 nm. At the bottom region the average grain size is 85 nm. This is much larger than for the film

grown under condition **16** (Figure 84). The increase in grain size is due to the higher temperature of deposition providing the thermal energy needed for crystallites to coalesce together and also during film growth the increased thermal energy enables the adatoms on the surface to diffuse to low energy sites and nucleate to grown films much easier and faster that if the deposition were to take place at lower temperatures.

Comparing the grain sizes calculated *via* the Scherrer equation (Table 23) to those determined *via* HRTEM shows that the Scherrer equation, with all its associated errors has underestimated the sizes. The average grain size calculated *via* the Scherrer equation for a sample grown under condition **16** is 17 nm this is much smaller than the 63 nm value obtained near the surface via HRTEM (Figure 84). For sample grown under condition **17** the Scherrer equation calculated a grain size of 34 nm where as HRTEM gave 98 nm (Figure 85).

6.1.7.6 Energy Dispersive X-Ray (EDX) Mapping

The EDX elemental mapping undertaken on a region (orange box in the annular darkfield STEM image) of a film grown under condition **16** is shown in Figure 84. The lack of colour in the EDX oxygen map shows oxygen only to be present in the substrate and in the void region of the sample possibly due to an interruption in the aerosol flow during deposition. Overall, the gallium and arsenic distribution within the film are very uniform indicating that gallium is only bound to arsenic and vice versa. Also, looking at the gallium and arsenic map only it is possible to see that the oxygen (indicated by the black colour) is only present on the surface. This suggests that contamination is post deposition as expected and seen in literature. In this particular sample there seems to be some carbon contamination throughout the region analysed.

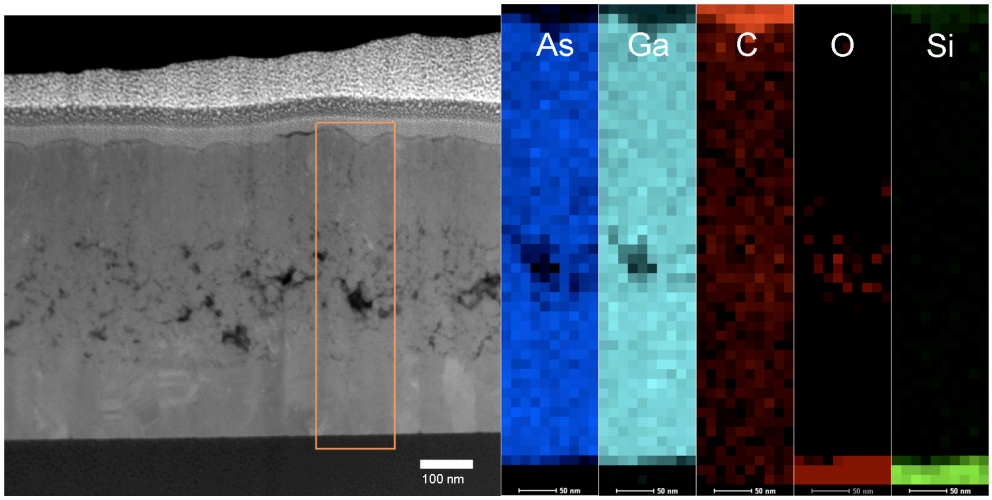

Figure 86: STEM image of a film grown under condition 16 (left) with an orange box to indicate the area used to carry out the EDX mapping shown on the right.

The EDX mapping of a region of a film grown under condition **17** shows much better results than in the previous sample (Figure 91). Due to the lack of the void region in the centre of the film, there is no contamination of impurities within the film. The gallium and arsenic distribution is very uniform therefore suggesting that gallium is bonded to arsenic and vice versa. Again the oxygen and carbon contamination is only present on the surface of the films.

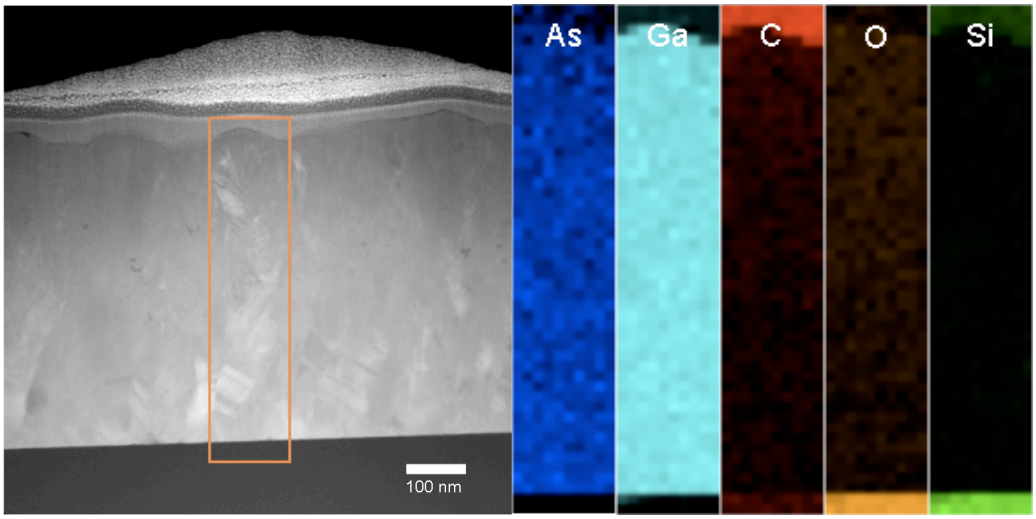

Figure 87: STEM image of a film grown under condition 17 (left) with an orange box to indicate the area used to carry out the EDX mapping shown on the right.

6.1.7.7 X-Ray Photoelectron Spectroscopy (XPS)

XPS analysis was carried out on a sample grown under condition **17** to determine the composition of the Ga and As species in the film. The peak for gallium was deconvoluted to fit two sets of 3d 5/2 and 3d 3/2 peaks (Figure 88). These peaks can be matched for Ga in the 3+ oxidation state in the form of Ga_2O_3 at 20.40 eV and GaAs at 19.02 eV.

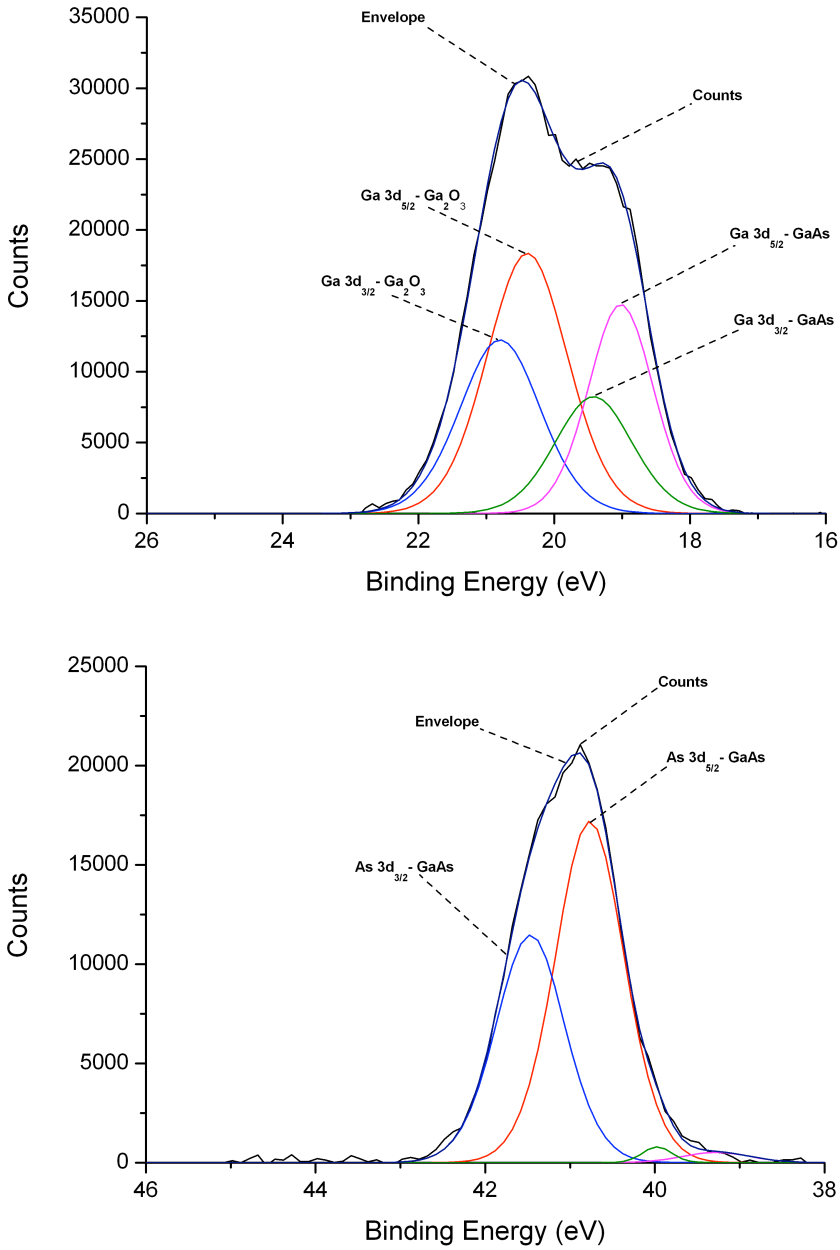

Figure 88: XPS peak for Ga 3d (top) and As 3d (bottom) peak for a film grown under condition 17.

The peak for As was resolved to reveal two different environments (Figure 88). The deconvoluted peak at 40.77 eV belongs to As in the form of GaAs. This matches well

with the literature value of 40.80 eV.[132] The other 3d 5/2 peak in the spectrum appears at 39.27 eV and can not be matched to any As species.

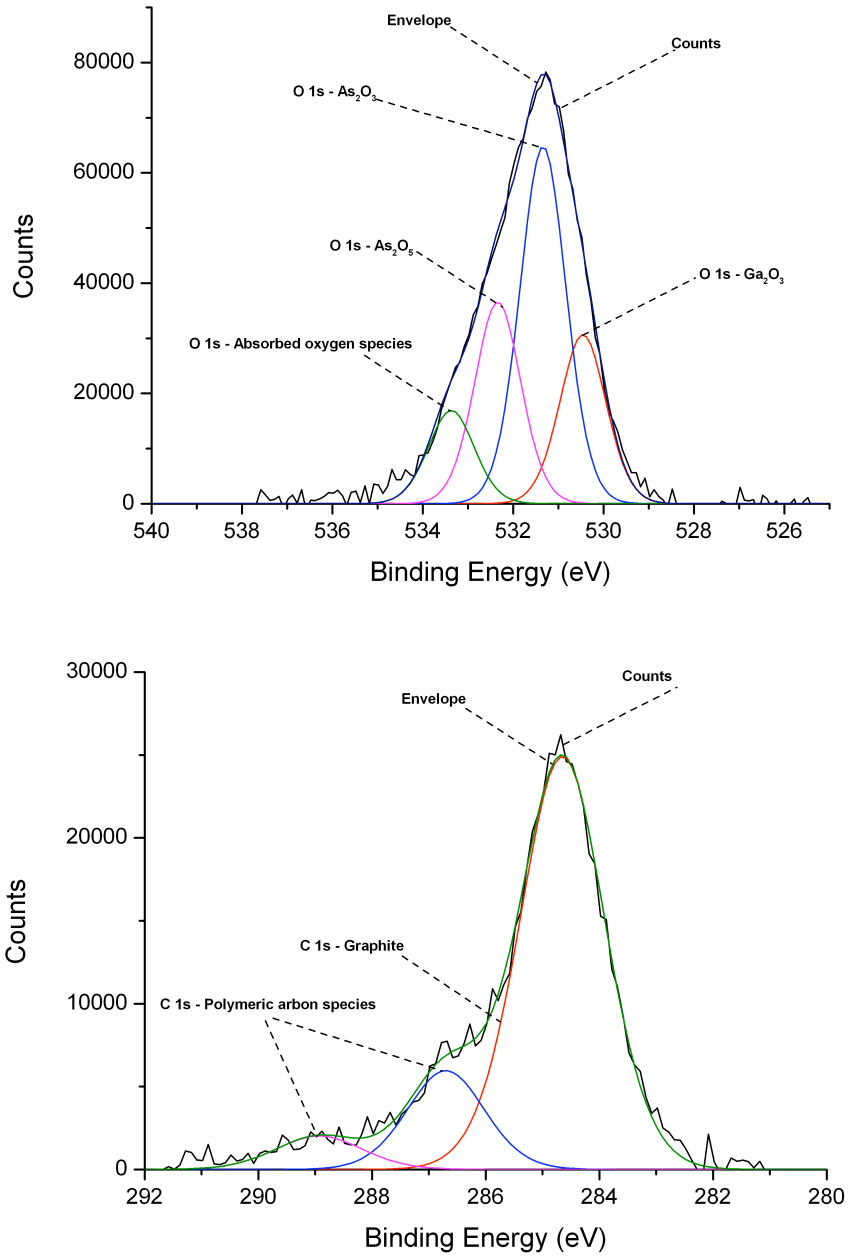

Figure 89: XPS peak for O 1s and C 1s for film grown under conditions 17.

The XPS peak for O 1s was deconvoluted to 4 different environments (Figure 89). The peak at binding energy 530.31 eV corresponds to Ga_2O_3, this agrees well with literature value of 530.70 eV.[133] The peak at 531.19 eV corresponds to As_2O_3. The peak at 532.29 eV corresponds to oxygen in the As_2O_5 environment.[134] The remaining peak at 533.22 eV can be assigned to adsorbed oxygen species on the surface of the film.[135,136]

The XPS peak for carbon 1s was deconvoluted to three peaks. The peak at 285.65 eV belongs to graphitic carbon and the shifts calibrated so that this peak appears at 285.50 eV. The peaks at 286.55 and 288.78 eV belongs to polymeric carbon containing species (Figure 89).[137, 138]

Depth profiling reveals that carbon is only found on the surface of the film and is not present after 30 seconds of sputtering. Also, oxygen is only present on the surface and disappears after 200 seconds of sputtering (Figure 90). Gallium is oxidized only on the surfaces and up to 200 seconds of sputtering into the sample, while As is also only oxidized on the surfaces. Gallium oxidization is more profound than As due to the more oxophilic nature of gallium compared to arsenic. Beyond a certain thickness, there is no oxidation of GaAs. This suggests that oxygen contamination occurs post deposition, which is what is observed in literature.

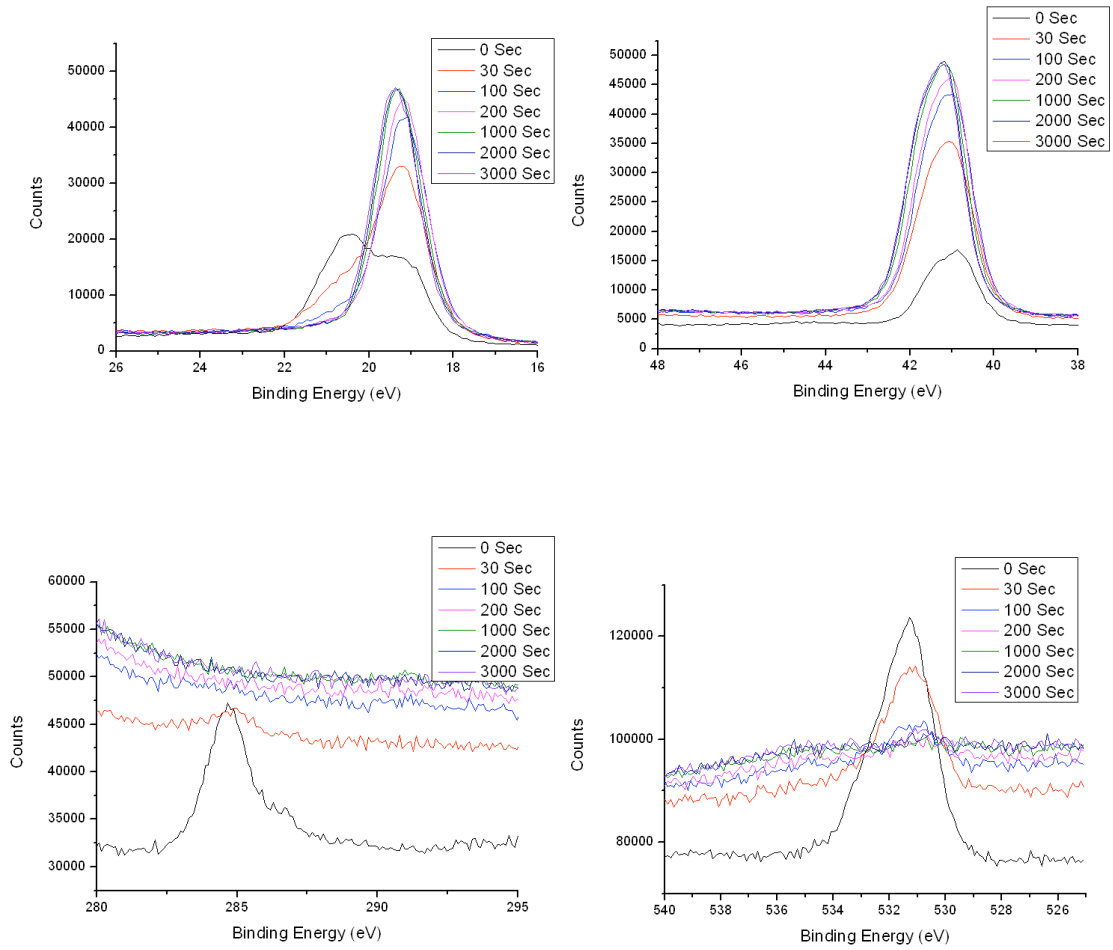

Figure 90: Depth profiling of Ga 3d peak (top left), As (3d) peak (top right), O 1s (bottom left) and C 1s (bottom right) for film grown under Condition 17.

6.1.7.8 Secondary Ion Mass Spectrometry (SIMS)

Secondary ion mass spectrometry was employed to determine the presence of any other impurities that were not detected by XPS and EDX and to determine the concentration of O and C contaminants beneath the surface that may be too low for the detection limit of the other techniques. SIMS is the most sensitive technique for such characterisations with an ability to detect elements in the parts per billion ranges. SIMS is able to detect any elements from the glass substrate such as sodium, calcium and silicon itself that may have diffused into the film during deposition at 500 °C / 550 °C.

Films grow under conditions **16** (Figure 91) and **17** (Figure 92) were analysed using SIMS. The concentration of carbon and oxygen were studied from the surface of the film to the substrate, this was achieved by sputtering.

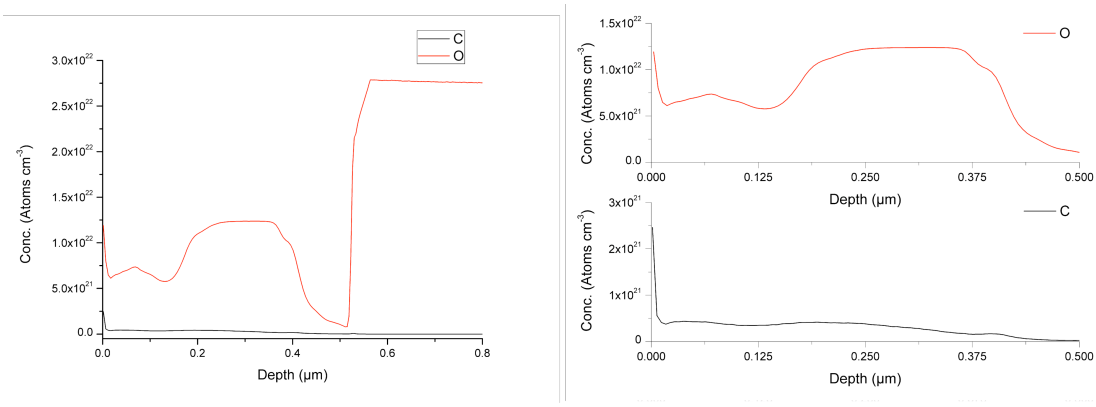

Figure 91: Left - SIMS profile showing carbon and oxygen levels in a film grown under condition 16 (left). Right - A detailed view between a depth of 0 and 0.5 µm of the SIMS profile for a film grown under condition 16.

The carbon concentration starts of at 2.46×10^{21} atoms per cm^3 on the surface of the film grown using condition **16**. It then decreases to 3.75×10^{20} atoms per cm^3 at a depth of 17 nm. It remains at this level until a depth of 400 nm deep into the film where there is the carbon levels start to decrease again to 1.63×10^{19} atoms per cm^3 at a depth of 500 nm. It increases again to 5.86×10^{19} atoms per cm^3 at a depth of 520 nm, close to the substrate.

The oxygen levels start off at 1.19×10^{22} atoms per cm^3 on the surface of the film after 18 nm there is a sudden drop in oxygen levels to 6.11×10^{21} atoms per cm^3. Then there is an increase in the oxygen concentration to 9.93×10^{21} atoms per cm^3 at 185 nm deep into the film. This is followed by a gradual decrease to 9.74×10^{21} atoms per cm^3 after 400

nm. There is a further drop in the concentration to $7.94x10^{20}$ atoms per cm^3 at 512 nm. It remains at this level until the substrate is reached.

This pattern of an increase in oxygen concentration near the middle of the film at about 200 nm matches well with the voids seen along the middle of the film in the HRTEM images. This indicates that these voids within the film are contaminated by oxygen.

The oxygen concentration starts of at $3.60x10^{21}$ atoms per cm^3 for films grown under condition **17**. This quickly drops off to $1.34x10^{21}$ atoms per cm^3 after at a dept of 20 nm into the film. The oxygen concentration remains at this level until the substrate is reached at 1 μm. The carbon concentration follows a similar pattern to the oxygen but starts off at a lower concentration and remains lower until the substrate is reached. On the surface the concentration was $5.89x10^{20}$ atoms per cm^3 it then drops to $6.97x10^{19}$ atoms per cm^3 after 200 nm into the film (Figure 92).

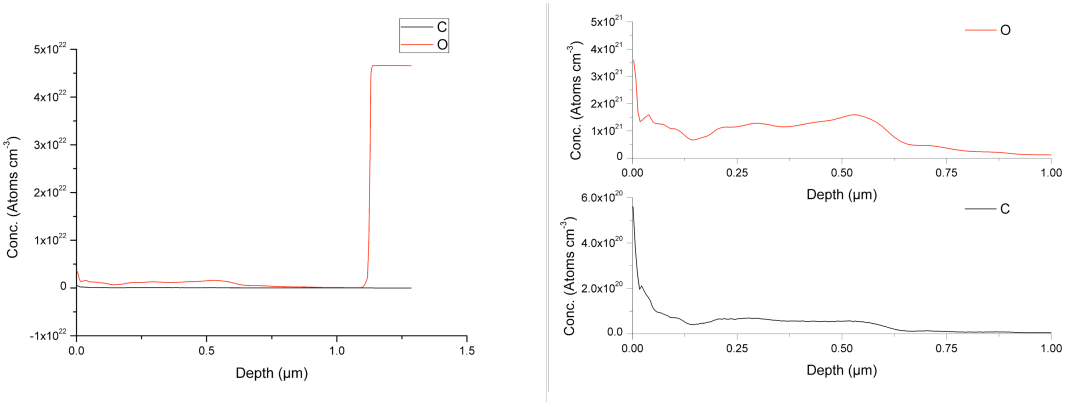

Figure 92: Left - SIMS profile showing carbon and oxygen contamination in film grown under condition 17. Right – A detailed view between a depth of 0 and 1 μm of the SIMS profile for a film grown under condition 17.

6.1.8 Functional Analysis

6.1.8.1 Ultraviolet/Visible (UV/Vis) Spectroscopy

GaAs has a band gap of 1.45 eV and UV/Vis spectroscopy was used in an attempt to determine the bandgap of the films deposited. However, the Tauc plot from UV/Vis data for the GaAs films deposited under all conditions shows up to 3 band edges, including 1.45 eV but also with the dominant edge indicating a band gap of *ca.* 2.5 eV. This could be due to (though highly unlikely) a highly 'efficient' amorphous phase

within the film that is suppressing the gallium arsenide band gap. If this were true, the unknown phase must contain only gallium and/or arsenic along with oxygen, as EDX shows no other impurities.

Furthermore, due to the highly absorbing/reflecting nature of the films, almost all (99-99.99%) of the incident light was absorbed (some was also reflected). This makes the results highly unreliable. Therefore it is best to determine the band gap *via* alternative methods such as photoluminescence or diffuse reflectance UV/Vis spectroscopy.

6.1.8.2 Photoluminescence (PL)

Photoluminescence performed at UCL using the Raman instrument (red laser excitation source) gave some contradicting results to what was obtained using a dedicated PL instrument (Stanford/AMAT). The very broad peak had a maximum at 1.31 eV at room temperature (Figure 93). This was consistent for all the samples (grown under condition **16**, **17**, **12**, **18**). When the PL was performed at close to liquid nitrogen temperature (-180 ^{o}C) the large and very intense broad peak observed at room temperature partially resolved to 3 different peaks of much lower intensity. Two of the peaks were more distinct with maxima at 1.35 eV and 1.42 eV. This shows that the intense peak observed at room temperature was predominantly due to thermal transition and hot bands. The peak at 1.41 eV observed at -180 ^{o}C is close to the band gap of GaAs but cannot be taken as the band gap as this could still be a thermal transition or photoluminescence of an impurity within the film. The experiment has to be carried out at liquid helium temperatures.

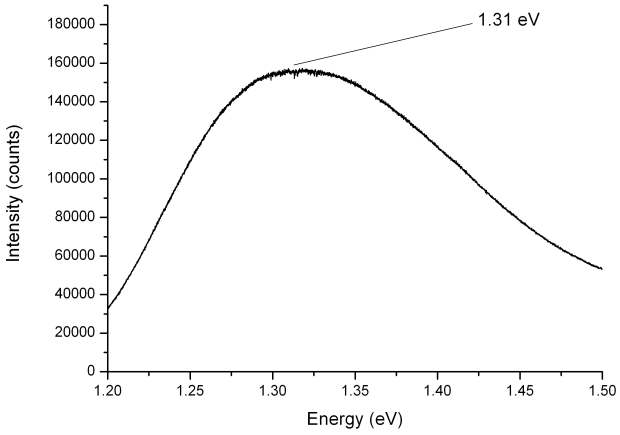

Figure 93: Room temperature photoluminescence spectra for film grown under condition 17.

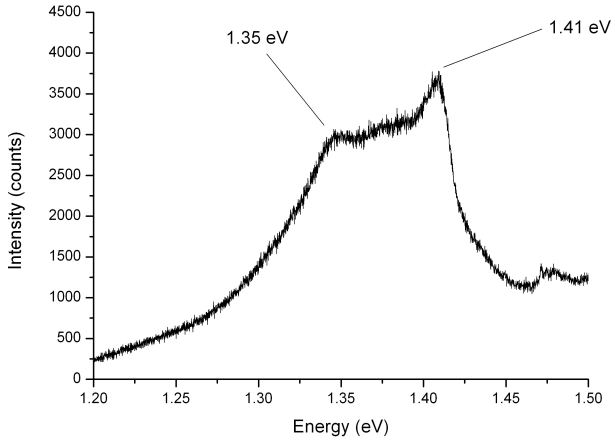

Figure 94: Reduced temperature (-180 °C) photoluminescence spectra for a film grown under condition 17.

The variation in peak position with temperature was studied on the GaAs wafer using the red laser excitation source (Figure 95). As the temperature decreases there is a shift to higher energy starting from 1.41 eV at room temperature, then to 1.46 eV at -130 °C and then finally to 1.48 eV at -180 °C. The intensity of the peaks also decreases with decreasing temperature. Further evidence to show that PL preformed at room temperature shows overshadowed by thermal transitions.

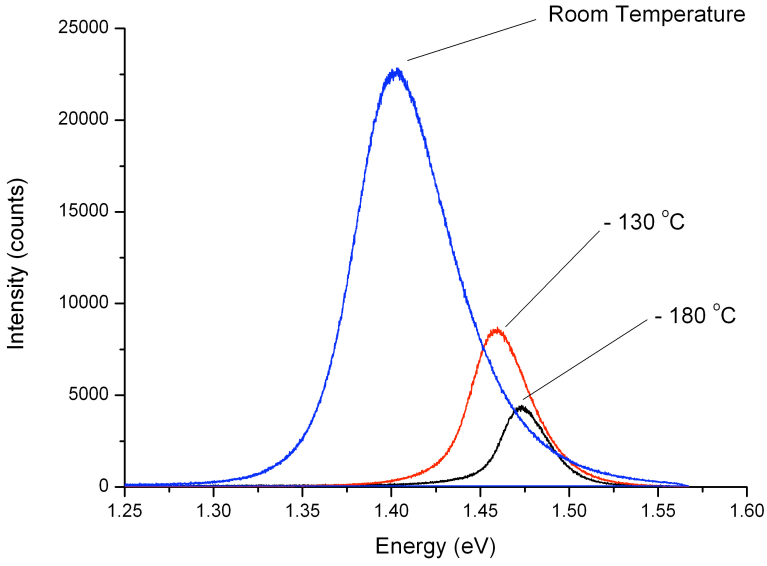

Figure 95: Variable temperature PL of a GaAs wafer using the red laser.

When the PL was performed using the green laser (514.5 nm) excitation source at room temperature the peak maxima was at 1.84 eV for all the samples analysed. This is further evidence that the PL peaks observed from the samples is due to impurities or defects (that are covered by thermal excitations) and not from the band gap as different energy excitation sources give rise to different PL peaks.

Films grown *via* AACVD are highly defective and have relatively small crystallite sizes (therefore having many sites for electron - hole recombination) compared to GaAs wafers. For films grown *via* AACVD, incident light of too high an energy cannot be used as this would result in electrons in the valence band of the film being excited to an electronic state in the conduction band well above the minima. Before the electrons can travel down to the minima of the conduction band and relax radiatively by returning to the valence band (and thus eject a photon corresponding to the energy of the band gap) they undergo non-radiative and radiative recombination. The PL peak observed could arise from any number of electronic defects in the films. This concurs with other literature reports of polycrystalline films on substrates other than GaAs or Ge.

In order to try and determine the band gap *via* PL an excitation source with energy close to the band gap of the gallium arsenide such as 820 nm red laser could be used, unfortunately this is not available.

6.1.9 Device Fabrication

Using the $[Me_2GaAs(H)^tBu]_2$ (**47**) precursor hybrid devices of hydrogenated amorphous silicon *p-i-n* based photovoltaic devices (as detailed in Chapter 1) were fabricated. Thin films of intrinsic GaAs were grown on *p*-type amorphous silicon substrates under various using condition **17** and **18** as these gave the best results on glass substrates.

Films grown using condition 17 (Table 16) resulted in a device that produced a current-voltage (IV) curve as shown in Figure 97. An IV curve typically shows the electrical current through a device and the corresponding voltage (Figure 96). At zero voltage, maximum current is obtained from a solar cell and this is called the short circuit current (I_{sc}). The open circuit voltage (V_{oc}) occurs at maximum voltage where zero current is obtained.

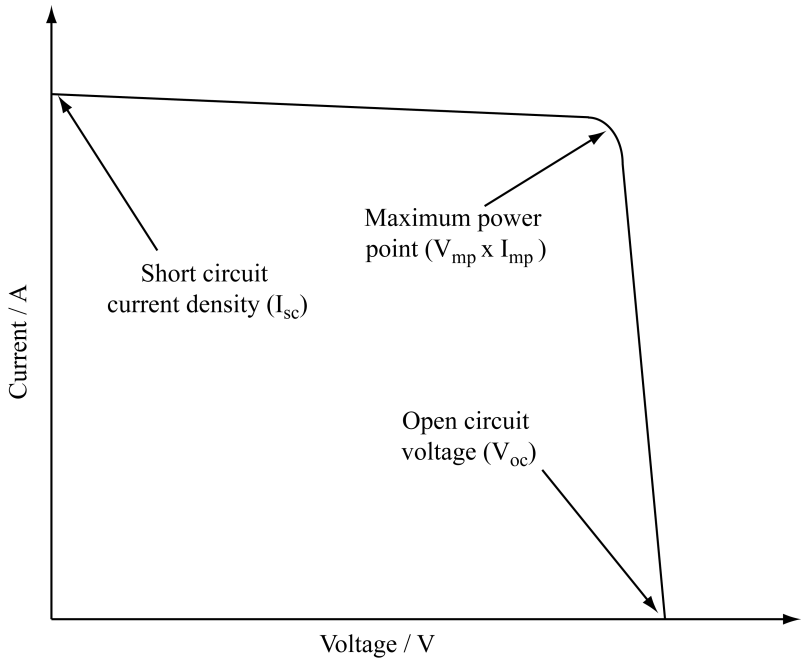

Figure 96: A typical IV curve for a solar device.

Films grown using condition **17** (Table 16) resulted in a device that produced a current response at zero bias. Furthermore, a spectral response of over 30% was achieved at 660 nm. A short circuit current density of 6.9 mA/cm^2 was observed (Figure 97 and Figure 98).

Current at zero bias indicates that the device was able to produce electrical current, i.e. movement of electrons through a circuit without the need of a voltage bias. A spectral response is the ratio of current generated by the device compared to the power incident on the device. The short circuit current density indicates the amount of current passing through a square centimeter of a solar cell when the voltage through the cell is zero. The theoretical maximum short circuit current density for a silicon solar cell is 46 mA/cm^2. Typically for laboratory based devices current densities of 42 mA/cm^2 have been achieved. Commercial products have a current density of about 28 mA/cm^2.

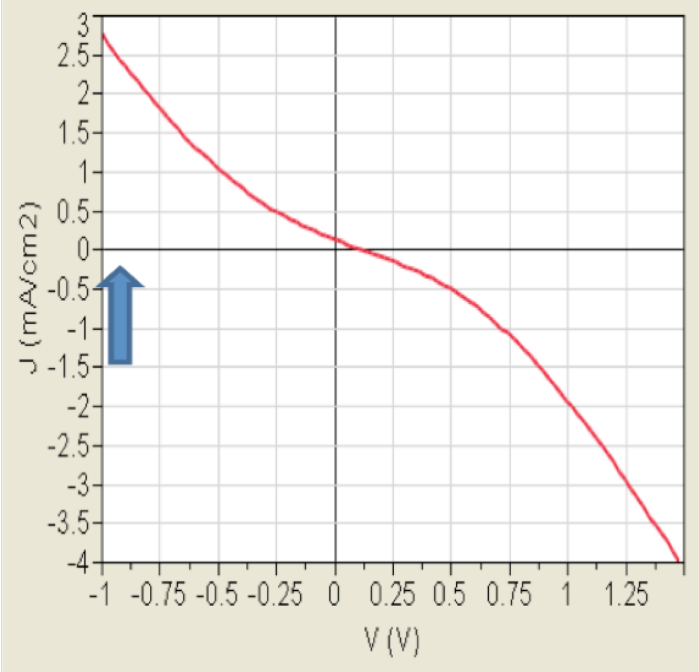

Figure 97: Graph showing the current response of the device at zero bias. Device fabricated under condition 17.

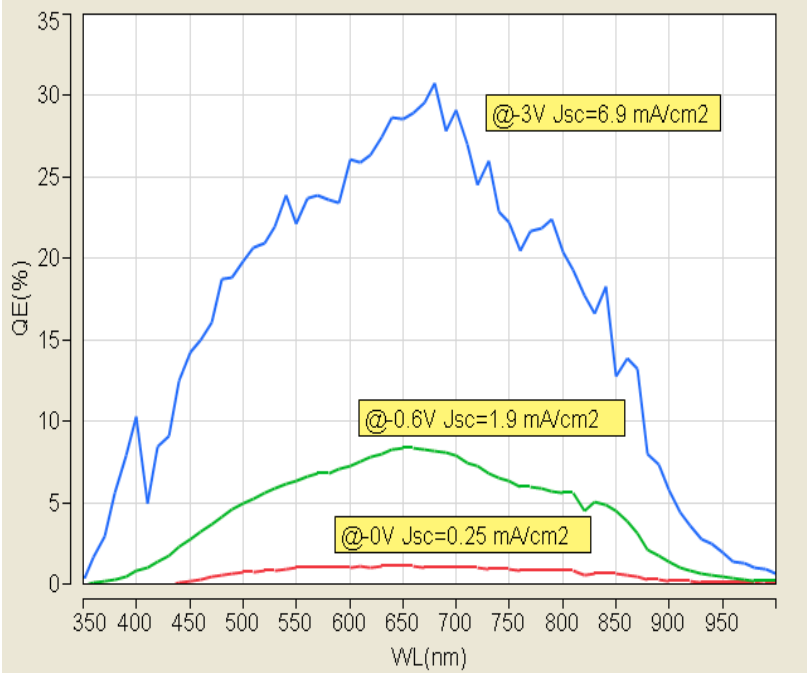

Figure 98: The spectral response and short circuit current density at various applied voltages for device grown under condition 17.

6.1.10 Conclusion

GaAs films have been deposited on glass substrates using the single-source precursors $[Me_2GaAs(H)^tBu]_2$ (**47**) and $[Et_2GaAs(H)^tBu]_2$ (**48**). An initial study between precursors **47** and **48**, taking into account substrate coverage, crystallinity and stoichoimetry found that precursor **47** gave the superior results. Therefore this system was further studied to optimise film properties.

Films produced from $[Me_2GaAs(H)^tBu]_2$ were shown to be stoichoimetric *via* EDX analysis. XPS and EDX mapping showed that carbon and oxygen contamination was only surface bound. SEM showed the films to be smooth, compact and continuous which is ideal for device fabrication.

Devices were fabricated using $[Me_2GaAs(H)^tBu]_2$ on hydrogenated amorphous silicon substrates (*p*-type). These devices showed promising initial results with a current response at zero bias. Furthermore, a spectral response of 30% was obtained at 660 nm and a short circuit current density of 6.9 mA/cm^2 was also obtained at 3 volt applied voltage.

6.1.11 Experimental Procedure

Nitrogen (99.9%, BOC) carrier gas was passed through activated sieves to remove moisture. Tertiary butylarsine (99.99, Strem HAFC Hitech Ltd.) and trimethylgallium and triethylgallium (99.999%, SAFC Hitech Ltd.) were all used as bought. Toluene was stored in alumina columns and dried with anhydrous engineering equipment.

6.1.11.1 Condition 10-12

$[Me_2GaAs(H)^tBu]_2$ (0.5 g, 1.07 mmol) was dissolved in toluene (30 mL) in an AACVD bubbler and deposition carried out at 400, 450 and 500 ^oC. On completion of deposition the reactor was cooled under nitrogen until room temperature. The films were stored under air.

6.1.11.2 Condition 13-15

$[Et_2GaAs(H)^tBu]_2$ (0.5 g, 0.96 mmol) was dissolved in toluene (30 mL) in an AACVD bubbler and deposition carried out at 400, 450 and 500 ^oC. On completion of deposition the reactor was cooled under nitrogen until room temperature. The films were stored under air.

6.1.11.3 Condition 16 and 17

$[Me_2GaAs(H)^tBu]_2$ (0.5 g, 1.07 mmol) was dissolved in toluene (15 mL) in an AACVD bubbler and deposition carried out at 500 and 550 ^oC . On completion of deposition the reactor was cooled under nitrogen until room temperature. The films were stored under air.

6.1.11.4 Condition 18

$[Me_2GaAs(H)^tBu]_2$ (0.5 g, 1.07 mmol) was dissolved in toluene (30 mL) in an AACVD bubbler and deposition carried out at 550 ^oC. On completion of deposition the reactor was cooled under nitrogen until room temperature. The films were stored under air.

6.1.11.5 Condition 17 Deposition on amorphous silicon p-layers

$[Me_2GaAs(H)^tBu]_2$ (0.5 g, 1.07 mmol) was dissolved in toluene (15 mL) in an AACVD bubbler and deposition carried out at 550 ^oC . The AACVD reactor was assembled with the amorphous silicon *p*-layer on glass substrates in the glove box under nitrogen atmosphere. After completion of the depositions the reactor was allowed to reach room temperature under nitrogen atmosphere before being taken into the glove box to be disassembled. The films were stored under a nitrogen atmosphere.

7 References

[1] S.M. Sze, Semiconductor Devices: Physics and Technology 2nd Ed., John Wiley and Sons Inc., New York, 2002, Chapter 2, Page 28-33.

[2] A.R. West, Basic Solid State Chemistry 2nd Ed., John Wiley and Sons Inc., New York, 1999. Chapter 2, Page 110-124.

[3] S. R. Wenham, M.A. Green, M.E. Watt, R. Corkish, Applied Photovoltaics 2nd Ed., Routledge, London, 2006, Chapter 2, Page 36.

S. R. Wenham, M.A. Green, M.E. Watt, R. Corkish, Applied Photovoltaics 2nd Ed., Routledge, London, 2006, Chapter 2, page 43-45.

[4] S. M. Sze, Physics of Semiconductor Devices 2nd Edition, John Wiley and Sons Inc., New York, 2002, Chapter 1, Page 16.

[5] A. Lugue, S. Hegedus, Handbook of Photovoltaic Science and Engineering, John Wiley and Sons Inc., New York, 2003, Chapter 3, Page 71-73.

[6] J.M. Kikkawa, D.D. Awschalom, *Phy. Rev. Lett.,* **80**, 4313, 1998

[7] C. Kittel, Introduction to Semiconductor Physics 7th Ed., John Wiley and Sons Inc., 1996, Chapter 12, Page 428

[8] A. Lugue, S. Hegedus, Handbook of Photovoltaic Science and Engineering, John Wiley and Sons Inc., New York, 2003, Chapter 3, Page 84

[9] T. Markvart, L. Castaner, Practical Handbook of Photovoltaics – Fundamentals and Applications, Elsevier, Oxford, 2003.

[10] Basic Photovoltaic Principles and Methods, U.S Government Print Office, USA, 1982.

[11] R.H. Bube, Photovoltaic Materials, Imperial College Print, London, 1998.

[12] P. T. Landsberg, Recombination in Semiconductors, Cambridge University Press, 2003

[13] A. Lugue, S. Hegedus, Handbook of Photovoltaic Science and Engineering, John Wiley and Sons Inc., New York, 2003, Chapter 3, Page 71-73.

[14] A. Lugue, S. Hegedus, Handbook of Photovoltaic Science and Engineering, John Wiley and Sons Inc., New York, 2003, Chapter 3, page 74-78.

[15] J. S. Blakemore, *J. Appl. Phys.* **53**, 123, 1982

[16] D.J. Fitzgerald, A.S. Grove, *Surface Science*, **9**,1968, 347

[17] R.H. Bube, Photovoltaic Materials, Imperial College Print, London, 1998, Chapter 1, page 23

[18] A.B. Aberle*, Thin Solid Films*, **517**, 2009, 4706

[19] Z. Sen, Solar Energy Fundamentals and Modelling Techniques: Atmosphere, Environment, Climate Change and Renewable Energy, Springer, New York, 2008.

[20] S K. Deb, *Renewable Energy 15*, 1996, **8**, 375

[21] R Brendel, A Goetzberger, Thin Film Crystalline Solar Cells: Physics and Technology, John Wiley and Sons Inc., New York, 2003.

[22] J. Poortmans, V. Arkhipov, Thin film Solar Cells: Fabrication, Characterisation and Applications, John Wiley and Sons Inc., New York, 2006.

[23] M. I. Kabir, Z. Ibarahim, M. Alghoul, K. Sopian, M.D Rezaul Karim, N. Amin, *Chalcogenide Letters*, **9**, 2012, 51

[24] K K. Banger, J A. Holingsworh, J D. Harris, J Cowen, W E. Buhro, A F. Hepp, *Appl. Organomet. Chem.,* 2002, **16**, 617

[25] J L. Pan, J E. McManis, T Osadchy, L Grober, J M. Woodall, P J. Kindlemann, *Nature. Mater.,* 2003, **2**, 375

[26] J.L. Pan, J. E. McManis, T. Osadchy, L. Grober, J. M. Woodall, P. J. Kindlmann, *Nature Mater.*, **2**, 375

[27] A.W. Bett, F. Dimroth, G. Stollwerck, O.V. Sulima, *Appl. Phys. A.,* **69**, 1999, 119

[28] R. H. Bube, Photovoltaic Materials, Imperial College Press, 1998, Chapter 3, Page 113

[29] M. A. Green, R. P. Raffaelle, T. M. Bruton, G. Conibeer, *Prog. Photovolt: Res. Appl*. 2011; **19**, 84

[30] http://education.jlab.org/itselemental/ele031.html on the 29/10/12

[31] Arsenic, Material Safety Data Sheet, 2005

[32] Arsine, Material Safety Data Sheet, 1989

[33] K. Hjort, J. Soderkvist, J. Schweitz., *J. Micromech. Microeng*. **4**, 1994, 1

[34] C Pelosi, the potential of III-V semiconductors as PV devices, *Progress in Photovoltaics Res Appl.,* **15**, 2007, 51

[35] G.B. Stringfellow, *Mat. Sci. Eng. B-Solid*, **87**, 2001, 97

[36] N. I. Buchan, C. A. Larsen, G. B. Stringfellow, *App. Phy. Lett.,* **52**, 1988, 480

[37] C. A. Larsen, C. H. Chen, G.B. Stringfellow, *App. Phys. Lett*., **50**, 1987, 218

[38] C. A. Larsen, N. I Buchan, L. I. Sh, G. B. Stringfellow, *J. Cryst. Growth*, **93**, 1988, 15

[39] S. P. Denbaars, P. M. Petroff, *Superlattice Microst*., **15**, 1994, 15

[40] H. O. Pierson, Handbook of Chemical Vapour Deposition, William Andrew, 2nd ed., 1994, Page 37

[41] O. Reynolds, Phil. *Trans. R. Soc*. **174**, 1993, 935

[42] A. B. Metzner, J. C. Reed., *A.I. Ch. E*., **1**, 1955, 434

[43] X. Hou, K L. Choy, *Chem. Vap. Deposition.*, **12,** 2006,583

[44] R J Lang, *J. Acoust. Soc. Am.*, **34**, 1962, 6

[45] T.T. Kodas, M.J. Hampden-Smith, The Chemistry of Metal CVD, Wiley-VCH, 1st Ed., 1994 Chapter 9, page 492

[46] A. Lugue, S. Hegedus, Handbook of Photovoltaic Science and Engineering, John Wiley and Sons Inc., New York, 2003, Chapter 9

[47] G B Stringfellow, *Appl. Phys. Lett.*, **50**, 1987, 218

[48] H Kuan, K Y Su, Semiconductor Science Technology, **10**, 1995, 540

[49] A. Lugue, S. Hegedus, Handbook of Photovoltaic Science and Engineering, John Wiley and Sons Inc., New York, 2003, Chapter 6, page 305

[50] G B Stringfellow, *Appl. Phys. Lett*, **52**, 1988, 480

[51] K. F. Jensen, *J. Cryst. Growth*, **107**, 1991, 1

[52] A. Lugue, S. Hegedus, Handbook of Photovoltaic Science and Engineering, John Wiley and Sons Inc., New York, 2003

[53] L N. Pfeiffer, K W. West, R L. Willett, H Akiyama, L P. Rokhinson, *Bell Labs Technical Journal*, **10**, 2005,

[54] O P. Pchelyakov, conferences and symposia, *IOP*, 2000, 923

[55] C T. Foxon, Molecular Beam Epitaxy, Tachnische Universiteit Eindhoven

[56] http://www.ringsurf.com/online/2016-epitaxy_mbe.html

[57] R. H. Bube, Photovoltaic Materials, Imperial College Press, Chapter 4 ,113

[58] J.M. Woodall, H.J. Hovel, *J. Vac. Sci. Technol.,* **12**, 1975, 1000

[59] L. L. Kazmerski, *J. Electron., Spectrosc., Relat., Phenom.,* **150**, 2006, 105

[60] N.H. Karam, R.R. King, B. T. Cavicchi, D.D. Krut, J. H. Ermer, M. Haddad, L. Cai, D. E. Joslin, M. Takahashi, J. W. Eldredge, W. T. Nishikawa, D.R. Lillington, B. M. Keyes, R. K. Ahrenkiel, *IEEE Transactions on Electron Devices*, **46**, 1999, 2116

[61] K. L. Ashley, S. W. Beal, *Appl. Phys. Lett*., **32**, 1978, 375

[62] C. Algora, V. Diaz, *Solid State Elec.*, **41**, 1997, 1787

[63] J. Yoon, S. Jo, I. S. Chun, I. Jung, H.S. Kim, M. Meitl, E. Menard, X. Li, J.J. Coleman, U. Paik, J. A. Rogers, *Nature*, **465**, 329, 2010

[64] R. H. Bube, Photovoltaic Materials, Imperial College Press, page 199

[65] M. Imaizumi, *J. Cryst. Growth*, 221, 688, 2000

[66] T. Jimbo, Advanced Nanomaterials and Nanodevices (IUMRS-ICEM 2002, Xi'an, China, 10-14 June 2002

[67] S. Kalem, *App. Phys. A*, 62, 237, 1996

[68] D. P. Norton, *J. Electrochem. Soc.*, **136**, 1989

[69] A H. Cowley, R A. Jones, *Angew. Chem., Int. Engl.* 1989, **28**, 361

[70] D C. Bradley, M M. Faktor, M Scott, E A D. Ehite, *J. Cryst. Growth*, 1989**, 75**, 101

[71] R H. Moss, *J. Cryst. Growth,* 1984, **68**, 78

[72] A Kuczkowski, S Schulz, M Nieger, *Appl. Organometal. Chem*., **18**, 2004, 244

[73] R D. Culp, A H. Cowley, A D. Decken, R A. Jones, M R. Bond, L M. Mokry, C J. Carrano, *Inorg. Chem.,* 1997, **36**, 5165

[74] A. H. Cowley, R A. Jones, *Polyhedron*, 1994, **13**, 1149

[75] A. H. Cowley, R A Jones, M A. Mardones, C M. Nunn, *Organometallics*, 1991, **10**, 1635

[76] R. L. Wells, *Coord. Chem. Rev.,* 1992, **112**, 273

[77] C. Elschenbroich, *Organometallics*, *Wiley*, 2006

[78] J. E. Miller, M A. Mardones, J W. Nail, A H. Cowley, R A. Jones, J G. Ekerdt, *Chem. Mater.,* **4**, 1992, 447

[79] M. A. Arif, B. L. Benac, A. Cowley, R. Geerts, R. A. Jones, K. B. Kidd, C. M. Nunn, *J. Chem. Soc. Chem. Commun.*, 1986, 1543

[80] A H. Cowley B L. Benac, J G. Ekerdt, R A. Jones, K B. Kidd, J Y. Lee, J E. Miller*, J. Am. Chem. Soc.,* 1988, **110**, 6248

[81] J E. Miller, K B. Kidd, A H. Cowley, R A. Jones, J G. Ekerdt, H J. Gysling, A A. Wernberg, T N. Blanton, *Chem. Mater.,* 1990, **2**, 589

[82] F Cheng, K George, A L Hector, M Jura, A Kroner, W Levason, J Nesbitt, G Reid, D C Smith, J W Wilson, *Chem. Mater.*, **23**, 2011, 5217

[83] G E. Coates, J Graham, *J. Chem. Soc.,* 1963, 233

[84] O T Beachley, G E. Coates, *J. Chem. Soc.,* 1965, 3241,

[85] A H. Cowley, B L. Benac, J G. Ekerdt, R A. Jones, K B. Kidd, J Y. Lee, J E. Miller, *J. Am. Chem. Soc.,* 1988, **110**, 6248

[86] J E. Miller, M A. Mardones, J W. Nail, A H. Cowle, R A. Jones, J G. Ekerdt, *Chem. Mater.*, 1992, **4**, 447

[87] C G. Pitt, A P. Purdy, K T. Higa, R L. Wells, *Organometallics,* 1986, **5**, 1266

[88] A C. Jones, *Chem. Soc. Rev.,* 1997, 101

[89] C J. Carmalt, J W. Steed, *Polyhedron*, 2000, **19**, 1639

[90] E E. Foos, R J Jouet, R L. Wells, A L. Rheingold, L M. Liable-Sands, *J. Organometallic Chem.,* 1999, **45**, 582

[91] A Schaller, H D. Hausen, W Schwarz, G Heckmann, J Weidlein, *Z. Anorg. Allg. Chem.,* 2000, 626, 1047

[92] J F. Janik, R L. Wells, V G. Young Jr., A L. Rheingold, I A. Guzei, *J. Am. Chem. Soc.* 1998, **120**, 532

[93] B Neumuller, E Iravani, *Coord. Chem. Rev.,* 2004, **248**, 817

[94] A Dashti-Mommertz, B Neumuller, *Z. Anorg. Allg. Chem*., 1999, **625**, 954

[95] R L. Wells, A. Prudy, A T. McPhail, C G. Pitt, J. *Chem Soc., Chem. Commun.,* 1986, 487

[96] R Brendel, A Goetzberger, Thin film crystalline solar cells: physics and technology *Wiley*, 2003

[97] S. J. S. Qazi, A. R. Rennie, J. K. Cockcroft, M. Vickers*, J. Colloid Interface Sci.,* **338**, 2009, 105

[98] P. Scherrer, Nachr. Ges. Wiss. Gottingen, Math-Phys. Klasse **26**, 1918, 98

[99] C. Suryanarayana, M. G. Norton, X-Ray Diffraction: A Practical Approach, Springer, 1998

[100] A. R. West, Basic Solid State Chemistry, 2nd Ed, John Wiley and Sons, New York, 1999

[101] http://www.chem.qmul.ac.uk/surfaces/scc/scat5_3.htm

[102] C J. Carmalt, J W. Steed, *Polyhedron*, **19**, 2000, 1639

[103] E E. Foos, R J Jouet, R L. Wells, A L. Rheingold, L M. Liable-Sands, J. *Organometallic Chem.,* 1999, **45**, 582

[104] C.J. Carmalt, Coord. *Chem. Rev.,* **223**, 2001, 217

[105] L. K Krannich, C. L. Watkins, D. K. Srivastava, *Polyhedron*, 1990, **9**, 289

[106] C. J. Thomas, L. K. Krannich, C. L. Watkins, *Polyhedron*, 1993, **9**, 89

[107] L. K. *Krannich, Inorg*, 1988, 596

[108] E. Clark, *Ind. Eng. Chem. Anal. Ed.,* **13**, 1941, 820

[109] SAINT+ version 6.45a, Bruker AXS Inc, USA

[110] SADABS version 2.03, Bruker AXS Inc, USA

[111] A.L. Spek*, J.Appl. Cryst.,* 2003, **36**, 7.

[112] L.J. Farrugia, *J. Appl Cryst.,* 1999, **32**, 837.

[113] A. C. Jones*, Chem. Soc. Rev.*, 1997, **26**, 101.

[114] P. Gong, Polytechnic Inst. of Brooklyn, NY, USA., *ICDD*,1981

[115] J. I. Langford, A. J. C. Wilson, *J. Appl. Cryst.,* 1978, **11**, 102

[116] A. Monshi, M. R. Foroughi, M. R. Monshi, *W. J. Nano Sci. & Eng.,* 2012, **2**, 154

[117] I. D. Desnica , M. Ivanda, M. Kranjcec, R. Murri, N. Pinto, *Journal of Non-Crystalline Solids* **170**, 1994 , 263

[118] C.D Wagner, J. F. Moulder, L.E. Davis, W.M. Riggs, Perkin Elmer Corporation, Physical Electronics Division

[119] M.J. Procop, *J. Electron Spectrosc. Relat. Phenom.,* **59**, 1992, R1

[120] B. J. Flinn, N. S. McIntyre, *Surf. Interface Anal.,* **15**, 1990, 19

[121] D. Pirzada, G. J. Cheng, *J. App. Phys.,* 105, 2009

[122] H. Iwakuro, C. Tatsuyama, S. Ichimura., *Jpn. J. Appl. Phys.,* **21**, 1982, 94

[123] M.J. Procop, *J. Electron Spectrosc. Relat. Phenom.,* 59, 1992, R1

[124] F.J. Grunthaner, P.J. Grunthaner, R.P. Vasquez, B.F. Lewis, J. Maserjian, A. Madhukar, *J. Vac. Sci. Technol.***, 16**, 1979, 1443

[125] P.R. Sarode, K.J. Rao, M.S. Hegd, C.N.R. *Rao, J. Phys. C*, **12**, 1979, 4119

[126] B. J. Flinn, N. S. McIntyre, *Surf. Interface Anal.,* **15**, 1990, 19

[127] D.D. Sarma, C.N.R. Rao, *J. Electron Spectrosc. Relat. Phenom.,* **20**, 1980, 25

[128] J. A. Taylor, J. Vac. Sci. Technol. 1982, **20**, 751

[129] D.E. King, J.E. Fernandez, W.E. Swartz*, Appl. Surf. Sci.,* **45**, 1990, 325

[130] K. L. Smith, K. M. Black, *J. Vac. Sci. Technol.,* **A2**, 744, 1984

[131] http://www.ioffe.rssi.ru/SVA/NSM/Semicond/GaAs/optic.html

The Morphology and Microstructure of Thin-Film GaAs on Mo Substrates, K.M. Jones, M.M. Al-Jassim, F.S. Hasoon, and R. Venkatasubramania

[132] C. D. Wagner, J. F Moulder, L. E. Davis, W. M. Riggs, Perkin Elmer, Physical electronics division.

[133] V. I. Nefedov, D. Gati, B.F. Dzhurinskii, N. P. Sergushin, *Y. V. Salyn, Neorg. Khimii.*, **20**, 1975, 2307

[134] D.E. King, J. E. Fernandez, W.E. Swartz, *Appl. Surf. Sci.*, **45**, 1990, 325

[135] C. Poleunis, L. T. Weng, M. Sclavons, P. Bertrand, P. Franquinet, R. Legras, V. Carlier, *J. Adh. Sci. Technol.,* **9**, 1995, 859

[136] D. T. Clark, H. R. Thomas, *Journal of Polymers Science*, **16**, 1978, 791

[137] G. Beamson, D. Briggs, *High Resolution XPS of Organic Polymers: the Scienta ESCA300 Database*, 1992

[138] J. Peeling, F. Hruska, D.M. McKinnon, M. S. Chauhan, N. S. Mclntyre, *Can. J. Chem.,* **56**, 1978, 2407

8 Appendices

Table 1. Crystal data and structure refinement for $[Me_2GaAs(SiMe_2Cy)_2]_2$ (**31**)

Identification code	str0744	
Empirical formula	C42 H94 As2 Ga2 Si4	
Formula weight	1000.81	
Temperature	150(2) K	
Wavelength	0.71073 Å	
Crystal system	Triclinic	
Space group	P-1	
Unit cell dimensions	a = 9.145(4) Å	a= 91.398(8)°.
	b = 9.835(5) Å	b= 90.664(8)°.
	c = 14.547(7) Å	g = 103.042(8)°.
Volume	1274.0(11) $Å^3$	
Z	1	
Density (calculated)	1.304 Mg/m^3	
Absorption coefficient	2.466 mm^{-1}	
F(000)	530	
Crystal size	0.36 x 0.36 x 0.10 mm^3	
Theta range for data collection	1.40 to 28.38°.	
Index ranges	-12<=h<=11, -12<=k<=13, -19<=l<=18	
Reflections collected	10097	
Independent reflections	5635 [R(int) = 0.0467]	
Completeness to theta = 25.00°	95.9 %	
Absorption correction	Semi-empirical from equivalents	
Max. and min. transmission	0.7905 and 0.4705	
Refinement method	Full-matrix least-squares on F^2	
Data / restraints / parameters	5635 / 0 / 233	
Goodness-of-fit on F^2	1.140	
Final R indices [I>2sigma(I)]	R1 = 0.0788, wR2 = 0.2224	
R indices (all data)	R1 = 0.1140, wR2 = 0.3095	
Largest diff. peak and hole	1.787 and -2.605 $e.Å^{-3}$	

Table 2. Atomic coordinates (x 10^4) and equivalent isotropic displacement parameters ($Å^2$ x 10^3) for str0744. U(eq) is defined as one third of the trace of the orthogonalized U^{ij} tensor.

	x	y	z	U(eq)
C(1)	8534(9)	681(9)	5825(6)	30(2)
C(2)	7007(10)	-2376(11)	4793(6)	34(2)
C(3)	4224(10)	-2270(9)	2735(6)	28(2)
C(4)	3990(11)	410(11)	1821(6)	35(2)
C(5)	7010(9)	-450(9)	1885(5)	23(2)
C(6)	8000(10)	-1281(10)	2379(6)	28(2)
C(7)	9412(10)	-1327(12)	1832(6)	37(2)
C(8)	9009(11)	-1938(11)	874(7)	37(2)
C(9)	8058(10)	-1133(11)	377(6)	35(2)
C(10)	6641(10)	-1040(11)	886(6)	33(2)
C(11)	7497(11)	3879(10)	4894(6)	32(2)
C(12)	5440(10)	3971(10)	3250(7)	31(2)
C(13)	8472(8)	3285(9)	2957(6)	23(2)
C(14)	9681(10)	2536(9)	3290(6)	28(2)
C(15)	10989(10)	2735(10)	2637(7)	36(2)
C(16)	11658(10)	4261(10)	2452(7)	35(2)
C(17)	10478(11)	4979(10)	2118(7)	34(2)
C(18)	9159(10)	4797(9)	2793(6)	29(2)
Si(1)	5229(3)	-451(2)	2521(1)	21(1)
Si(2)	6826(3)	3077(2)	3748(2)	21(1)
Ga(1)	6761(1)	-532(1)	5202(1)	20(1)
As(1)	5682(1)	711(1)	3957(1)	18(1)
C(19)	14293(13)	-4815(10)	177(7)	42(3)
C(20)	13751(14)	-3800(13)	-467(7)	54(3)
C(21)	12403(16)	-3283(16)	-71(8)	63(4)

Table 3. Bond lengths [Å] and angles [°] for str0744.

C(1)-Ga(1)	1.979(9)
C(1)-H(1A)	0.9800
C(1)-H(1B)	0.9800
C(1)-H(1C)	0.9800
C(2)-Ga(1)	1.957(9)
C(2)-H(2A)	0.9800
C(2)-H(2B)	0.9800
C(2)-H(2C)	0.9800
C(3)-Si(1)	1.853(9)
C(3)-H(3A)	0.9800
C(3)-H(3B)	0.9800
C(3)-H(3C)	0.9800
C(4)-Si(1)	1.867(9)
C(4)-H(4A)	0.9800
C(4)-H(4B)	0.9800
C(4)-H(4C)	0.9800
C(5)-C(6)	1.533(12)
C(5)-C(10)	1.555(11)
C(5)-Si(1)	1.883(8)
C(5)-H(5)	1.0000
C(6)-C(7)	1.533(12)
C(6)-H(6A)	0.9900
C(6)-H(6B)	0.9900
C(7)-C(8)	1.512(13)
C(7)-H(7A)	0.9900
C(7)-H(7B)	0.9900
C(8)-C(9)	1.493(14)
C(8)-H(8A)	0.9900
C(8)-H(8B)	0.9900
C(9)-C(10)	1.520(12)
C(9)-H(9A)	0.9900
C(9)-H(9B)	0.9900

C(10)-H(10A)	0.9900
C(10)-H(10B)	0.9900
C(11)-Si(2)	1.864(8)
C(11)-H(11A)	0.9800
C(11)-H(11B)	0.9800
C(11)-H(11C)	0.9800
C(12)-Si(2)	1.849(9)
C(12)-H(12A)	0.9800
C(12)-H(12B)	0.9800
C(12)-H(12C)	0.9800
C(13)-C(18)	1.504(12)
C(13)-C(14)	1.540(11)
C(13)-Si(2)	1.882(8)
C(13)-H(13)	1.0000
C(14)-C(15)	1.517(12)
C(14)-H(14A)	0.9900
C(14)-H(14B)	0.9900
C(15)-C(16)	1.519(13)
C(15)-H(15A)	0.9900
C(15)-H(15B)	0.9900
C(16)-C(17)	1.499(13)
C(16)-H(16A)	0.9900
C(16)-H(16B)	0.9900
C(17)-C(18)	1.547(13)
C(17)-H(17A)	0.9900
C(17)-H(17B)	0.9900
C(18)-H(18A)	0.9900
C(18)-H(18B)	0.9900
Si(1)-As(1)	2.343(2)
Si(2)-As(1)	2.355(3)
Ga(1)-As(1)	2.5218(14)
Ga(1)-As(1)#1	2.5328(15)
As(1)-Ga(1)#1	2.5328(15)
C(19)-C(19)#2	1.51(2)

C(19)-C(20)	1.543(17)
C(19)-H(19A)	0.9900
C(19)-H(19B)	0.9900
C(20)-C(21)	1.547(17)
C(20)-H(20A)	0.9900
C(20)-H(20B)	0.9900
C(21)-H(21A)	0.9800
C(21)-H(21B)	0.9800
C(21)-H(21C)	0.9800
Ga(1)-C(1)-H(1A)	109.5
Ga(1)-C(1)-H(1B)	109.5
H(1A)-C(1)-H(1B)	109.5
Ga(1)-C(1)-H(1C)	109.5
H(1A)-C(1)-H(1C)	109.5
H(1B)-C(1)-H(1C)	109.5
Ga(1)-C(2)-H(2A)	109.5
Ga(1)-C(2)-H(2B)	109.5
H(2A)-C(2)-H(2B)	109.5
Ga(1)-C(2)-H(2C)	109.5
H(2A)-C(2)-H(2C)	109.5
H(2B)-C(2)-H(2C)	109.5
Si(1)-C(3)-H(3A)	109.5
Si(1)-C(3)-H(3B)	109.5
H(3A)-C(3)-H(3B)	109.5
Si(1)-C(3)-H(3C)	109.5
H(3A)-C(3)-H(3C)	109.5
H(3B)-C(3)-H(3C)	109.5
Si(1)-C(4)-H(4A)	109.5
Si(1)-C(4)-H(4B)	109.5
H(4A)-C(4)-H(4B)	109.5
Si(1)-C(4)-H(4C)	109.5
H(4A)-C(4)-H(4C)	109.5
H(4B)-C(4)-H(4C)	109.5
C(6)-C(5)-C(10)	110.1(7)

C(6)-C(5)-Si(1)	112.1(6)
C(10)-C(5)-Si(1)	110.3(6)
C(6)-C(5)-H(5)	108.1
C(10)-C(5)-H(5)	108.1
Si(1)-C(5)-H(5)	108.1
C(7)-C(6)-C(5)	111.6(7)
C(7)-C(6)-H(6A)	109.3
C(5)-C(6)-H(6A)	109.3
C(7)-C(6)-H(6B)	109.3
C(5)-C(6)-H(6B)	109.3
H(6A)-C(6)-H(6B)	108.0
C(8)-C(7)-C(6)	111.1(7)
C(8)-C(7)-H(7A)	109.4
C(6)-C(7)-H(7A)	109.4
C(8)-C(7)-H(7B)	109.4
C(6)-C(7)-H(7B)	109.4
H(7A)-C(7)-H(7B)	108.0
C(9)-C(8)-C(7)	110.7(8)
C(9)-C(8)-H(8A)	109.5
C(7)-C(8)-H(8A)	109.5
C(9)-C(8)-H(8B)	109.5
C(7)-C(8)-H(8B)	109.5
H(8A)-C(8)-H(8B)	108.1
C(8)-C(9)-C(10)	113.3(8)
C(8)-C(9)-H(9A)	108.9
C(10)-C(9)-H(9A)	108.9
C(8)-C(9)-H(9B)	108.9
C(10)-C(9)-H(9B)	108.9
H(9A)-C(9)-H(9B)	107.7
C(9)-C(10)-C(5)	111.3(7)
C(9)-C(10)-H(10A)	109.4
C(5)-C(10)-H(10A)	109.4
C(9)-C(10)-H(10B)	109.4
C(5)-C(10)-H(10B)	109.4

H(10A)-C(10)-H(10B)	108.0
Si(2)-C(11)-H(11A)	109.5
Si(2)-C(11)-H(11B)	109.5
H(11A)-C(11)-H(11B)	109.5
Si(2)-C(11)-H(11C)	109.5
H(11A)-C(11)-H(11C)	109.5
H(11B)-C(11)-H(11C)	109.5
Si(2)-C(12)-H(12A)	109.5
Si(2)-C(12)-H(12B)	109.5
H(12A)-C(12)-H(12B)	109.5
Si(2)-C(12)-H(12C)	109.5
H(12A)-C(12)-H(12C)	109.5
H(12B)-C(12)-H(12C)	109.5
C(18)-C(13)-C(14)	110.3(7)
C(18)-C(13)-Si(2)	111.7(6)
C(14)-C(13)-Si(2)	113.1(6)
C(18)-C(13)-H(13)	107.1
C(14)-C(13)-H(13)	107.1
Si(2)-C(13)-H(13)	107.1
C(15)-C(14)-C(13)	111.5(7)
C(15)-C(14)-H(14A)	109.3
C(13)-C(14)-H(14A)	109.3
C(15)-C(14)-H(14B)	109.3
C(13)-C(14)-H(14B)	109.3
H(14A)-C(14)-H(14B)	108.0
C(14)-C(15)-C(16)	112.9(7)
C(14)-C(15)-H(15A)	109.0
C(16)-C(15)-H(15A)	109.0
C(14)-C(15)-H(15B)	109.0
C(16)-C(15)-H(15B)	109.0
H(15A)-C(15)-H(15B)	107.8
C(17)-C(16)-C(15)	111.1(8)
C(17)-C(16)-H(16A)	109.4
C(15)-C(16)-H(16A)	109.4

C(17)-C(16)-H(16B)	109.4
C(15)-C(16)-H(16B)	109.4
H(16A)-C(16)-H(16B)	108.0
C(16)-C(17)-C(18)	111.0(8)
C(16)-C(17)-H(17A)	109.4
C(18)-C(17)-H(17A)	109.4
C(16)-C(17)-H(17B)	109.4
C(18)-C(17)-H(17B)	109.4
H(17A)-C(17)-H(17B)	108.0
C(13)-C(18)-C(17)	112.1(7)
C(13)-C(18)-H(18A)	109.2
C(17)-C(18)-H(18A)	109.2
C(13)-C(18)-H(18B)	109.2
C(17)-C(18)-H(18B)	109.2
H(18A)-C(18)-H(18B)	107.9
C(3)-Si(1)-C(4)	109.1(5)
C(3)-Si(1)-C(5)	109.9(4)
C(4)-Si(1)-C(5)	109.8(4)
C(3)-Si(1)-As(1)	106.9(3)
C(4)-Si(1)-As(1)	108.6(3)
C(5)-Si(1)-As(1)	112.5(3)
C(12)-Si(2)-C(11)	110.0(4)
C(12)-Si(2)-C(13)	108.6(4)
C(11)-Si(2)-C(13)	108.9(4)
C(12)-Si(2)-As(1)	109.5(3)
C(11)-Si(2)-As(1)	108.0(3)
C(13)-Si(2)-As(1)	111.8(3)
C(2)-Ga(1)-C(1)	115.5(4)
C(2)-Ga(1)-As(1)	112.5(3)
C(1)-Ga(1)-As(1)	112.3(3)
C(2)-Ga(1)-As(1)#1	111.1(3)
C(1)-Ga(1)-As(1)#1	114.6(3)
As(1)-Ga(1)-As(1)#1	87.55(5)
Si(1)-As(1)-Si(2)	109.44(9)

Si(1)-As(1)-Ga(1)	116.49(7)
Si(2)-As(1)-Ga(1)	117.29(7)
Si(1)-As(1)-Ga(1)#1	110.15(7)
Si(2)-As(1)-Ga(1)#1	109.55(6)
Ga(1)-As(1)-Ga(1)#1	92.45(5)
C(19)#2-C(19)-C(20)	111.1(10)
C(19)#2-C(19)-H(19A)	109.4
C(20)-C(19)-H(19A)	109.4
C(19)#2-C(19)-H(19B)	109.4
C(20)-C(19)-H(19B)	109.4
H(19A)-C(19)-H(19B)	108.0
C(19)-C(20)-C(21)	112.2(10)
C(19)-C(20)-H(20A)	109.2
C(21)-C(20)-H(20A)	109.2
C(19)-C(20)-H(20B)	109.2
C(21)-C(20)-H(20B)	109.2
H(20A)-C(20)-H(20B)	107.9
C(20)-C(21)-H(21A)	109.5
C(20)-C(21)-H(21B)	109.5
H(21A)-C(21)-H(21B)	109.5
C(20)-C(21)-H(21C)	109.5
H(21B)-C(21)-H(21C)	109.5

Symmetry transformations used to generate equivalent atoms:

#1 -x+1,-y,-z+1 #2 -x+3,-y-1,-z

Table 4. Anisotropic displacement parameters ($Å^2 x\ 10^3$)for str0744. The anisotropic displacement factor exponent takes the form: $-2p^2[\ h^2 a^{*2} U^{11} + ... + 2\ h\ k\ a^*\ b^*\ U^{12}\ ]$

	U^{11}	U^{22}	U^{33}	U^{23}	U^{13}	U^{12}
C(1)	17(4)	37(5)	37(5)	4(4)	-1(3)	11(4)
C(2)	26(5)	57(6)	24(4)	-1(4)	7(4)	20(4)
C(3)	33(5)	27(4)	24(4)	1(3)	5(4)	3(4)
C(4)	33(5)	51(6)	30(5)	3(4)	-3(4)	26(5)
C(5)	20(4)	25(4)	20(4)	1(3)	2(3)	0(3)
C(6)	28(5)	37(5)	24(4)	0(4)	-2(3)	18(4)
C(7)	24(5)	60(7)	31(5)	-9(5)	0(4)	16(5)
C(8)	28(5)	54(6)	36(5)	2(4)	12(4)	22(5)
C(9)	30(5)	47(6)	27(5)	2(4)	11(4)	8(4)
C(10)	28(5)	57(6)	19(4)	5(4)	2(3)	20(5)
C(11)	31(5)	38(5)	23(4)	-11(4)	-3(3)	2(4)
C(12)	25(5)	35(5)	37(5)	7(4)	4(4)	14(4)
C(13)	10(4)	32(4)	27(4)	-2(3)	0(3)	4(3)
C(14)	25(4)	26(4)	33(5)	5(4)	3(4)	6(4)
C(15)	23(5)	38(5)	47(6)	-1(4)	11(4)	8(4)
C(16)	25(5)	30(5)	44(6)	0(4)	5(4)	-5(4)
C(17)	30(5)	32(5)	42(5)	12(4)	6(4)	8(4)
C(18)	27(5)	22(4)	38(5)	-1(4)	-3(4)	4(4)
Si(1)	19(1)	31(1)	15(1)	2(1)	0(1)	8(1)
Si(2)	20(1)	24(1)	21(1)	2(1)	2(1)	6(1)
Ga(1)	16(1)	27(1)	19(1)	1(1)	0(1)	8(1)
As(1)	17(1)	24(1)	15(1)	3(1)	2(1)	6(1)
C(19)	56(7)	33(5)	26(5)	-5(4)	10(4)	-12(5)
C(20)	62(8)	66(8)	28(5)	-13(5)	-1(5)	1(6)
C(21)	65(8)	83(10)	41(7)	-2(6)	-1(6)	17(7)

Table 1. Crystal data and structure refinement for $[Me_2NGaMe_2]_2$ (**40**)

Identification code	2010src0420	
Empirical formula	C8 H24 Ga2 N2	
Formula weight	287.73	
Temperature	120(2) K	
Wavelength	0.71073 Å	
Crystal system	Monoclinic	
Space group	P21/n	
Unit cell dimensions	a = 7.4426(2) Å	a= 90°.
	b = 8.0294(3) Å	b= 99.386(2)°.
	c = 11.2896(2) Å	g = 90°.
Volume	665.63(3) $Å^3$	
Z	2	
Density (calculated)	1.436 Mg/m^3	
Absorption coefficient	4.010 mm^{-1}	
F(000)	296	
Crystal size	0.09 x 0.08 x 0.05 mm^3	
Theta range for data collection	3.56 to 27.49°.	
Index ranges	-9<=h<=9, -9<=k<=10, -13<=l<=14	
Reflections collected	6616	
Independent reflections	1526 [R(int) = 0.0355]	
Completeness to theta = 27.49°	99.5 %	
Absorption correction	Semi-empirical from equivalents	
Max. and min. transmission	0.8247 and 0.7142	
Refinement method	Full-matrix least-squares on F^2	
Data / restraints / parameters	1526 / 0 / 59	
Goodness-of-fit on F^2	1.114	
Final R indices [I>2sigma(I)]	R1 = 0.0215, wR2 = 0.0489	
R indices (all data)	R1 = 0.0247, wR2 = 0.0506	
Largest diff. peak and hole	0.330 and -0.269 e.$Å^{-3}$	

Table 2. Atomic coordinates (x 10^4) and equivalent isotropic displacement parameters ($Å^2$x 10^3) for 2010src0420. U(eq) is defined as one third of the trace of the orthogonalized U^{ij} tensor.

	x	y	z	U(eq)
C(1)	3503(3)	9742(3)	6662(2)	36(1)
C(2)	2204(4)	13089(3)	4868(2)	41(1)
C(3)	1787(3)	7663(3)	4195(3)	45(1)
C(4)	810(3)	9974(4)	2886(2)	42(1)
N(1)	811(2)	9276(2)	4092(1)	24(1)
Ga(1)	1698(1)	10858(1)	5451(1)	19(1)

Table 3. Bond lengths [Å] and angles [°] for 2010src0420.

_____C(1)-Ga(1)

C(1)-H(1A)	0.9800
C(1)-H(1B)	0.9800
C(1)-H(1C)	0.9800
C(2)-Ga(1)	1.966(2)
C(2)-H(2A)	0.9800
C(2)-H(2B)	0.9800
C(2)-H(2C)	0.9800
C(3)-N(1)	1.480(3)
C(3)-H(3A)	0.9800
C(3)-H(3B)	0.9800
C(3)-H(3C)	0.9800
C(4)-N(1)	1.472(3)
C(4)-H(4A)	0.9800
C(4)-H(4B)	0.9800
C(4)-H(4C)	0.9800
N(1)-Ga(1)	2.0180(15)
N(1)-Ga(1)#1	2.0202(17)
Ga(1)-N(1)#1	2.0202(17)
Ga(1)-Ga(1)#1	2.9125(4)
Ga(1)-C(1)-H(1A)	109.5
Ga(1)-C(1)-H(1B)	109.5
H(1A)-C(1)-H(1B)	109.5
Ga(1)-C(1)-H(1C)	109.5
H(1A)-C(1)-H(1C)	109.5
H(1B)-C(1)-H(1C)	109.5
Ga(1)-C(2)-H(2A)	109.5
Ga(1)-C(2)-H(2B)	109.5
H(2A)-C(2)-H(2B)	109.5
Ga(1)-C(2)-H(2C)	109.5
H(2A)-C(2)-H(2C)	109.5
H(2B)-C(2)-H(2C)	109.5
N(1)-C(3)-H(3A)	109.5
N(1)-C(3)-H(3B)	109.5
H(3A)-C(3)-H(3B)	109.5
N(1)-C(3)-H(3C)	109.5
H(3A)-C(3)-H(3C)	109.5

H(3B)-C(3)-H(3C)	109.5
N(1)-C(4)-H(4A)	109.5
N(1)-C(4)-H(4B)	109.5
H(4A)-C(4)-H(4B)	109.5
N(1)-C(4)-H(4C)	109.5
H(4A)-C(4)-H(4C)	109.5
H(4B)-C(4)-H(4C)	109.5
C(4)-N(1)-C(3)	109.41(19)
C(4)-N(1)-Ga(1)	114.47(14)
C(3)-N(1)-Ga(1)	113.30(13)
C(4)-N(1)-Ga(1)#1	113.28(13)
C(3)-N(1)-Ga(1)#1	113.32(14)
Ga(1)-N(1)-Ga(1)#1	92.31(7)
C(2)-Ga(1)-C(1)	120.05(11)
C(2)-Ga(1)-N(1)	112.08(9)
C(1)-Ga(1)-N(1)	110.05(9)
C(2)-Ga(1)-N(1)#1	111.68(9)
C(1)-Ga(1)-N(1)#1	110.66(9)
N(1)-Ga(1)-N(1)#1	87.69(7)
C(2)-Ga(1)-Ga(1)#1	121.11(8)
C(1)-Ga(1)-Ga(1)#1	118.84(7)
N(1)-Ga(1)-Ga(1)#1	43.87(5)
N(1)#1-Ga(1)-Ga(1)#1	43.81(4)

Symmetry transformations used to generate equivalent atoms:

#1 -x,-y+2,-z+1

Table 4. Anisotropic displacement parameters ($Å^2 x\ 10^3$)for 2010src0420. The anisotropic displacement factor exponent takes the form: $-2p^2[\ h^2 a^{*2} U^{11} + ... + 2\ h\ k\ a^*\ b^*\ U^{12}\ ]$

	U^{11}	U^{22}	U^{33}	U^{23}	U^{13}	U^{12}
C(1)	27(1)	47(1)	32(1)	4(1)	-5(1)	5(1)
C(2)	59(2)	26(1)	41(1)	6(1)	15(1)	-8(1)
C(3)	26(1)	35(1)	72(2)	-26(1)	0(1)	8(1)
C(4)	33(1)	73(2)	21(1)	-8(1)	10(1)	-16(1)
N(1)	22(1)	27(1)	23(1)	-5(1)	4(1)	1(1)
Ga(1)	20(1)	19(1)	19(1)	1(1)	2(1)	-1(1)